Dynamics and Radiation from Tidal Disruption Events

ISBN: 978-94-6233-731-2

Dynamics and Radiation from Tidal Disruption Events

Proefschrift

ter verkrijging van
de graad van Doctor aan de Universiteit Leiden,
op gezag van Rector Magnificus prof. mr. C.J.J.M. Stolker,
volgens besluit van het College voor Promoties
te verdedigen op donderdag 5 oktober 2017
klokke 11:15 uur

door

Clément Bonnerot

geboren te Brunoy, Frankrijk
in 1989

Promotiecommissie

Promotor:	Prof. dr. Joop Schaye	
Co-promotor:	Dr. Elena Maria Rossi	
	Dr. Giuseppe Lodato	(University of Milan)
Overige leden:	Prof. dr. Jelle Kaastra	
	Prof. dr. Sera Markoff	(University of Amsterdam)
	Dr. Alessandro Patruno	
	Prof. dr. E. Sterl Phinney	(California Institute of Technology)
	Prof. dr. Enrico Ramirez-Ruiz	(University of California, Santa Cruz)
	Prof. dr. Huub Röttgering	

Cover: artistic view designed by the author depicting the self-crossing shocks involved in the disc formation process during tidal disruption events.

Contents

1 **Introduction** **1**
- 1.1 Tidal disruption events . . . 1
- 1.2 Interests . . . 2
- 1.3 Observational constraints . . . 3
- 1.4 Different phases of a TDE and link to observables . . . 4
  - 1.4.1 Overview . . . 5
  - 1.4.2 Scattering into the loss cone . . . 5
  - 1.4.3 Pericentre passage . . . 9
  - 1.4.4 Stream evolution around the black hole . . . 13
  - 1.4.5 Fallback of the debris . . . 15
  - 1.4.6 Disc formation and accompanying phenomena . . . 16
  - 1.4.7 Formation of relativistic jets . . . 22
  - 1.4.8 Related events . . . 24
- 1.5 Future prospects . . . 25
- 1.6 Thesis summary . . . 26

2 **Disc formation from tidal disruptions of stars on eccentric orbits by Schwarzschild black holes** **35**
- 2.1 Introduction . . . 36
- 2.2 SPH simulations . . . 38
- 2.3 Results . . . 42
  - 2.3.1 Impact of relativistic precession . . . 44
  - 2.3.2 Influence of the cooling efficiency . . . 46
  - 2.3.3 Dependence on the orbit of the star . . . 50
  - 2.3.4 Convergence of the results . . . 53
- 2.4 Discussion and conclusion . . . 53
  - 2.4.1 Thermal energy radiation . . . 54
  - 2.4.2 Viscous evolution . . . 54
  - 2.4.3 Evaluation of the cooling efficiency . . . 55
  - 2.4.4 Extrapolation to parabolic orbits . . . 56

3 **Long-term stream evolution in tidal disruption events** **61**
- 3.1 Introduction . . . 62
- 3.2 Stream evolution model . . . 63
  - 3.2.1 Shocks . . . 64
  - 3.2.2 Magnetic stresses . . . 66
  - 3.2.3 Equivalent differential equation . . . 68
  - 3.2.4 Stream evolution outcome . . . 68
- 3.3 Results . . . 69
  - 3.3.1 Dynamical evolution of the stream . . . 69
  - 3.3.2 Observational appearance . . . 76
  - 3.3.3 Impact of inefficient cooling . . . 80
- 3.4 Discussion and conclusion . . . 85

4 Bad prospects for the detection of giant stars' tidal disruption: effect of the ambient medium on bound debris 91
4.1 Introduction . . . 92
4.2 Gaseous environment model . . . 93
4.3 Tidal stream model . . . 93
4.4 Tidal stream - ambient medium interactions . . . 95
  4.4.1 Hydrodynamical instabilities . . . 95
  4.4.2 Ram pressure . . . 98
  4.4.3 Effect on flare luminosities . . . 98
4.5 Impact on the detectability of TDEs . . . 101
4.6 Discussion and conclusion . . . 102

5 Magnetic field evolution in tidal disruption events 105
5.1 Introduction . . . 106
5.2 SPH simulations . . . 107
5.3 Results . . . 110
  5.3.1 Influence on the field orientation . . . 110
  5.3.2 Dependence on the penetration factor . . . 114
  5.3.3 Impact of the field strength . . . 116
  5.3.4 Resolution study . . . 117
5.4 Discussion and conclusion . . . 119

6 Nederlandse samenvatting 125
6.1 Supermassieve zwarte gaten . . . 125
6.2 Verstoring door getijdenwerking . . . 125
6.3 Dit proefschrift . . . 126

7 Résumé en français 129
7.1 Trous noirs supermassifs . . . 129
7.2 Événement de rupture par effet de marée . . . 129
7.3 Cette thèse . . . 130

Publications 133

Curriculum Vitae 135

Acknowledgements 137

1

Introduction

1.1 Tidal disruption events

It is now commonly believed that all massive galaxies host a supermassive black hole (SMBH) in their centre (Ferrarese & Ford 2005). In the early universe, such massive objects can be detected through their energetic emission. These quasars, first detected in the 60s (Schmidt 1963), remain luminous for millions of years and are now believed to be powered by gas accretion at a high rate. Unfortunately, these accreting black holes are distant and represent only a small fraction of the entire population. Instead, the majority of SMBHs in the local universe are starved from gas and produce an emission too dim to be detectable from Earth. The motion of stars surrounding these black holes provides an alternative technique of study, but is limited to very nearby galaxies for which telescopes can resolve the black hole sphere of influence. For more distant galaxies, another method relies on stellar disruptions. When an unlucky star passes too close to a black hole, the tidal forces of the compact object shred the star apart. The stellar debris can then fuel the SMBH, that becomes luminous for a duration of months to years (Rees 1988) in an event usually referred to as tidal disruption event (TDE). These events represent a powerful technique to study black holes in the centre of both near and far otherwise quiescent galaxies.

The theoretical investigation of TDEs started in the mid-70s. These events were initially studied as a mechanism to provide gas to SMBHs in order to account for the large luminosity of quasars, which had been discovered only a decade before (Hills 1975; Young et al. 1977; Kato & Hoshi 1978; Gurzadyan & Ozernoy 1979). Although stellar disruptions were found to be too rare to efficiently fuel SMBHs, these events then gained interest as probes of black holes in the centre of quiescent galaxies. Rees (1988) and Phinney (1989) made the first prediction of the electromagnetic signal to be expected from a TDE. According to this initial model, TDEs are detectable at UV to soft X-ray wavelengths with a luminosity decreasing with time at a characteristic rate of $t^{-5/3}$. First TDE candidates were detected in X-ray (Bade et al. 1996; Komossa & Bade 1999) with properties consistent with the expectations of this model. Later, discoveries were also made at lower energies, in the UV (Gezari et al. 2006) and optical bands (Komossa et al. 2008; van Velzen et al. 2011).

Numerous additional observations were carried out in the following years. Interestingly, several of these most recent TDE candidates have observational features that cannot be explained within the initial model of Rees (1988). In particular, two categories of events present particularly peculiar characteristics, of which PS1-10jh (Gezari et al. 2012) and *Swift* J1644+57 (Bloom et al. 2011) are typical representatives. TDEs of the first category present a low-energy emission that requires the presence of emitting matter at larger distances from the black hole than originally thought. Instead, the few events belonging to the second category produce a very luminous and energetic emission that can only be explained by the formation of a relativistic jet in the vicinity of the compact object. These discoveries triggered a flurry of theoretical works that revised the original model in order to account for the new observational constraints. Due to the novelty of these new works, there is so far no clear consensus on the exact emission mechanisms at work in TDEs. However, a clear picture should emerge soon given the recent advances on the theoretical side and the development of new observational facilities expected to significantly expand the current sample of TDE candidates.

This introduction is arranged as follows. Section 1.2 motivates the importance of TDEs by describing the main interests. The observational constraints derived from the TDE candidates detected so far are given in Section 1.3. In Section 1.4, a detailed theoretical description of the different phases of a TDE is provided. Future prospects of the field are summed up in Section 1.5. Finally, Section 1.6 gives a summary of the thesis.

1.2 Interests

As mentioned in Section 1.1, TDEs represent a powerful technique to study otherwise quiescent SMBHs at distances too large to resolve the motion of stars orbiting them. These events produce an observational signature for black hole with masses $M_{\mathrm{h}} \lesssim 10^8\,\mathrm{M}_{\odot}$ since above this mass the disruption occurs inside the event horizon. Therefore, TDEs are especially useful to examine the low-mass end of the black hole mass function. In particular, these events can be used to determine the fraction of low-mass galaxies that host a SMBH (Stone & Metzger 2016). Also, tidal disruptions of white dwarfs require an intermediate-mass black hole to be detectable which make them unique probes for the existence of this category of compact objects (Rosswog et al. 2009). In addition to reveal the presence of black holes, the signal emitted from TDEs can in principle be used to put constraints on their mass and spin that both strongly influence the dynamics of tidal disruptions. An alternative use of TDEs is to probe the gaseous environment of black holes in quiescent galaxies, such as its density profile at small scales. This can for example be done for TDEs featuring relativistic jets whose associated radio emission depends on the properties of the surrounding matter (Generozov et al. 2017). Alternatively, this ambient medium density can be estimated by its influence on the stellar debris during its evolution around the black hole prior to accretion (Guillochon et al. 2016; Bonnerot et al. 2016b). The dust content of this environment can also be probed through the heating and associated infrared radiation of dust grains caused by a TDE flare (Lu & Kumar 2016).

TDEs also represent powerful tools to study the numerous physical phenomena occurring near SMBHs. The plunging trajectory of the victim star towards the black hole results from previous scatterings by surrounding stars. Therefore, the rate at which TDEs occur in a given galaxy is a tracer of these dynamical processes (Stone & Metzger 2016). Since the accretion of stellar matter following the disruption can occur in the super-Eddington regime and result in the formation of relativistic jets, tidal disruptions can also be used to examine these two poorly-known physical phenomena. TDEs are unique in this respect because their short duration allows us to observe these processes for their entire duration, which is not possible for long-lived accreting systems such as quasars. These events are for example useful to put constraints on the energy output from this rapid gas accretion and to study state transitions taking place in the accretion disc formed from the debris (e.g. Shen & Matzner 2014). The observation of relativistic jets from birth to shut down can also constrain their formation mechanism, power source and longer-term evolution (Tchekhovskoy et al. 2014; Piran et al. 2015a). In addition, TDEs occur in the proximity of the black hole's event horizon which implies that they are sensitive to relativistic effects. The close encounter between the star and the black hole is expected to produce a burst of gravitational waves potentially detectable with current detectors (Stone et al. 2013). Relativistic effects including spin-related phenomena are also critical in the phase of disc formation from stellar debris (Guillochon & Ramirez-Ruiz 2015;

Bonnerot et al. 2016a) as well as its early evolution (Stone & Loeb 2011; Franchini et al. 2016). These various effects could ultimately be used to test the predictions from the theory of general relativity.

Finally, TDEs are considered as a mechanism to grow SMBHs. They appear to significantly contribute to this process for low-mass black holes with $M_\mathrm{h} < 10^6\,\mathrm{M}_\odot$ (Freitag & Benz 2002; Stone et al. 2016) and possibly also more massive ones with $M_\mathrm{h} > 10^8\,\mathrm{M}_\odot$ for which stars are swallowed before being disrupted (Zhao et al. 2002). Furthermore, these events may contribute to the faint end of the active galactic nuclei (AGN) X-ray luminosity function corresponding to luminosities less than $10^{44}\,\mathrm{erg\,s^{-1}}$ (Milosavljević et al. 2006; Auchettl et al. 2017a).

1.3 Observational constraints

TDEs are identified as large amplitude flares with duration of months to years and localization consistent with the centre of an otherwise quiescent galaxy. The most important sources of confusion are flares from active galactic nuclei (AGN) and supernovae, which have luminosities and timescales similar to TDEs and are expected to be more frequent. Nevertheless, these sources can usually be differentiated from tidal disruptions, in particular because they produce different spectra (van Velzen et al. 2011; Auchettl et al. 2017a). The signal can also be contaminated by atmospheric variations in the case of ground-based observations. This issue is general to the detection of transients and new techniques are currently being developed to circumvent it (Zackay et al. 2016).

The TDE candidates detected to date have been listed by Auchettl et al. (2017b) and the observational data are available online at https://tde.space. They can be classified into three main categories. The first category contains the TDEs emitting in the X-ray band, which are the first to have been detected during the ROSAT all-sky survey (Bade et al. 1996; Komossa & Bade 1999; Komossa & Greiner 1999). Later, several other TDE candidates with similar characteristics were observed with the *XMM-Newton*, *Chandra* and *Swift* satellites (Cappelluti et al. 2009; Esquej et al. 2007; Saxton et al. 2012b; Maksym et al. 2010, 2013; Campana et al. 2015; Lin et al. 2017). Most of these events feature lightcurves with peak luminosity up to a few $10^{44}\,\mathrm{erg\,s^{-1}}$ followed by a temporal decay consistent with $t^{-5/3}$. Their effective temperature is typically $T \approx 10^5\,\mathrm{K}$, slowly increasing with time. The total energy emitted is usually less than a few 10^{51} erg. In addition, some of these TDE candidates show special features in their X-ray emission. For example, the lightcurve from SDSS J120136.02+300305.5 presents several dips of large amplitude (Saxton et al. 2012b). Three outbursts have also been detected in the IC 3599 galaxy, all consistent with accretion of stellar matter (Campana et al. 2015). More recently, the slowly-decaying X-ray source SDSS J150052.07+015453.8 has also been interpreted as a decade-long TDE (Lin et al. 2017).

Another class of TDEs emits at optical and UV wavelengths. The first event of this category has been discovered in UV with the *GALEX* satellite (Gezari et al. 2006). Later, similar events have been observed in optical and UV with surveys such as SDSS, PTF, Pan-STARRS and ASAS-SN (Komossa et al. 2008; van Velzen et al. 2011; Gezari et al. 2012; Arcavi et al. 2014; Chornock et al. 2014; Holoien et al. 2016a,b; Leloudas et al. 2016). These events have peak luminosities up to a few $10^{43}\,\mathrm{erg\,s^{-1}}$ with a lightcurve decay broadly consistent with a $t^{-5/3}$ decrease. Their effective temperatures are $T \approx 10^4\,\mathrm{K}$ and remain remarkably constant in time. As for X-ray events, the total emitted energy is in general less than a few 10^{51} erg. Interestingly, these TDEs are also observed preferentially in E+A galaxies, a rare type of post-starburst galaxies (Arcavi et al. 2014; French et al. 2016). The TDE candidate PS1-10jh is typical of this category of events. Its UV lightcurve follows $t^{-5/3}$ for several years

(Gezari et al. 2012, 2015) with an almost constant effective temperature. Additionally, this event presents an unexpectedly large helium to hydrogen line ratio, a feature shared by several other optical TDEs (e.g. Arcavi et al. 2014). Most TDEs detected in optical and UV also do not emit in X-ray. ASASSN-14li (Holoien et al. 2016a) is one of the few exceptions to this dichotomy for which a significant X-ray emission has been detected (Miller et al. 2015). For this particular event, the X-ray signal was additionally found to lag behind the less energetic optical and UV emissions (Pasham et al. 2017). ASASSN-14li also emits in radio, which likely originates from a weak outflow of gas (van Velzen et al. 2016a; Alexander et al. 2016). In addition, it radiates in infrared due to the heating of surrounding dust particles (Jiang et al. 2016a) which is also the case of other TDEs (e.g. van Velzen et al. 2016b). Finally, the TDE candidate ASASSN-15lh is also particular in this category due to the unexpectedly large mass of $M_{\mathrm{h}} > 10^8\,\mathrm{M}_{\odot}$ inferred for the disrupting black hole (Leloudas et al. 2016; Margutti et al. 2017).

The last category contains the few TDE candidates that have been detected with the *Swift* satellite with a very luminous and energetic emission in the hard X-ray and γ-ray bands accompanied by radio emission (Bloom et al. 2011; Cenko et al. 2012; Brown et al. 2015). These signals can be explained by the presence of a relativistic jet formed during the accretion of stellar matter. The TDE candidate *Swift* J644+57 is the best representative of this category of events (Bloom et al. 2011; Burrows et al. 2011; Levan et al. 2011; Zauderer et al. 2011). It has a peak isotropic X-ray luminosity in excess of $10^{48}\,\mathrm{erg\,s^{-1}}$. This luminosity is orders of magnitude larger than the Eddington luminosity of the black hole, whose mass has been independently inferred to be $M_{\mathrm{h}} \lesssim 10^7\,\mathrm{M}_{\odot}$. This property can be accounted for if the emission is beamed towards our line of sight. This is one of the main indicator for the presence of a relativistic jet, along with the associated radio emission. In the first $\sim$ 10 days after discovery, the X-ray lightcurve features large amplitude variations, with possible quasi-periodicity (Saxton et al. 2012a). It then decays as a power law consistent with $t^{-5/3}$ and finally suddenly drops after $\sim$ 500 days (Zauderer et al. 2013). The event is also emitting in the radio band. Interestingly, the radio lightcurve keeps increasing for a few months after the X-ray emission has started to decay (Berger et al. 2012; Zauderer et al. 2013).

We now summarize the main puzzles based on the above observations, which most theoretical models described in Section 1.4 aim at solving. The first puzzles concern the optical TDEs. While the X-ray emission is usually attributed to the accretion of stellar debris onto the black hole, the origin of the lower energy emission is unclear. Furthermore, the fact that most of these events usually do not emit in X-ray remains to be understood. Additional unexpected features are the large helium to hydrogen line ratio and the almost constant effective temperature detected from these events. Both for X-ray and optical TDEs, the rates derived observationally are an order of magnitude too low compared to theoretical expectations. In addition, this discrepancy is worsened by the preference of optical TDEs for rare E+A galaxies. The amount of total energy emitted from these two classes of events is also problematic since it is much lower than that expected from the accretion of a stellar mass of matter. Finally, theorists are also puzzled by the properties of the radio and X-ray emission from the jetted TDE *Swift* J1644+57.

1.4 Different phases of a TDE and link to observables

A TDE can be naturally divided into distinct phases that involve different physical processes. This section provides a description of these phases from a theoretical point of view. Whenever possible, the physical mechanisms involved are explained with analytical calculations. For each phase of evolution, the link with the observational constraints presented in Section 1.3 is also highlighted.

1.4.1 Overview

Most galactic centres contain a SMBH surrounded by a stellar cluster within which stars interact with each other gravitationally. Occasionally, a star is scattered (Section 1.4.2) from parsec scales on a highly-eccentric orbit that brings it so close to the black hole that the tidal forces from the compact object shred the star apart. This occurs when the star has a pericentre distance R_p lower than a critical value called the tidal radius R_t. Such an event occurs every $10^4 - 10^5$ years in a given galaxy. During pericentre passage (Section 1.4.3), the star is torn apart by tidal forces and its material is launched on different trajectories through a spread in orbital energy imparted to the debris. For weak encounters, the disruption can be partial with a self-gravitating core surviving the interaction. For strong encounters, the star additionally experiences a strong compression possibly associated with prompt X-ray and gravitational wave emissions. As a result of the orbital spread, the debris then evolves (Section 1.4.4) ballistically into an elongated structure with a thin profile confined by self-gravity. Approximately half of the matter is bound to the black hole while the rest escapes the gravitational pull of the compact object. The unbound part is expected to interact with the surrounding environment producing radio and γ-ray emission. Instead, the bound part of the stream falls back (Section 1.4.5) to the black hole about a month after disruption. As a result of stream self-intersections induced by relativistic precession, the bound debris forms an accretion disc (Section 1.4.6) around the black hole within which the gas subsequently spirals inward under the action of viscosity. Most of the signals detected from TDEs are thought to originate from this phase of evolution. The most energetic X-ray emission is produced in the vicinity of the black hole while gas at larger distances contribute to the emission at optical and UV wavelengths. Relativistic jets (Section 1.4.7) can also be launched from the inner regions of the accretion flow producing a beamed X-ray luminosity accompanied by radio emission. To describe the phases of evolution below, we mostly focus on the disruption of a solar-type star by a single black hole. However, other related events are also possible (Section 1.4.8).

1.4.2 Scattering into the loss cone

The first phase of a TDE consists in the scattering of the star on an orbit that takes it inside the tidal radius. The mechanism usually involved to achieve this task is two-body scattering: the victim star is scattered by random encounters with surrounding stars that modify its trajectory until it ultimately crosses the tidal sphere.

We start by presenting an analytical description of this process, based on the loss cone theory (Frank & Rees 1976; Lightman & Shapiro 1977). Consider a star safely orbiting at a distance $R \gg R_\mathrm{t}$ from the black hole. Its velocity v is specified by the black hole's gravity at short distances. However, the gravitational potential is dominated by that of the surrounding stars further away from the compact object. The transition between these two regimes occur at the influence radius

$$R_\mathrm{inf} \equiv \frac{GM_\mathrm{h}}{\sigma^2} = 2\,\mathrm{pc}\left(\frac{\mathrm{M_h}}{10^6\ \mathrm{M}_\odot}\right)^{1/2}, \tag{1.1}$$

where the Keplerian circular velocity is equal to the velocity dispersion σ.[1] The star is disrupted if it is scattered on a trajectory that passes within the tidal sphere. This requires that

---

[1] This definition implies that the mass of stars within the influence radius is similar to the black hole mass. In the second equality of equation (1.1), the $M_\mathrm{h} - \sigma$ relation $M_\mathrm{h} \approx 10^8\,\mathrm{M}_\odot\,(\sigma/200\,\mathrm{km\,s^{-1}})^4$ has been used (e.g. Ferrarese & Merritt 2000).

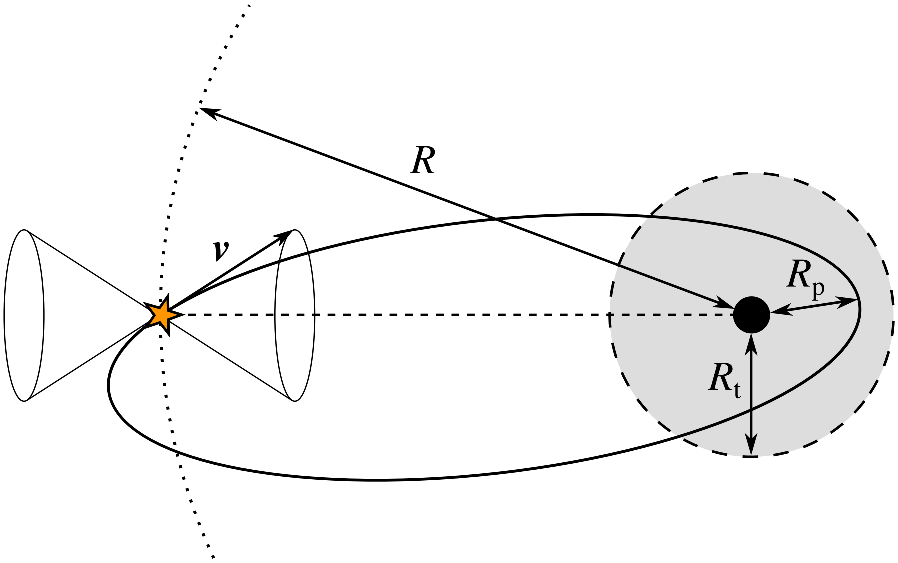

Figure 1.1: Sketch representing a star at a distance R from the black hole with a velocity vector $\mathbf{v}$ at the surface of a loss cone corresponding to a trajectory with pericentre distance R_p lying inside the tidal sphere (grey disc) of radius R_t.

the stellar angular momentum is lower than that J_lc of an orbit with pericentre $R_\mathrm{p} \leq R_\mathrm{t}$, that is

$$J \leq J_\mathrm{lc} \equiv (2GM_\mathrm{h}R_\mathrm{p})^{1/2}, \tag{1.2}$$

where the last equality uses the fact that the potential at R_p is imposed by the black hole's gravity and assumes that the star originates from a weakly bound orbit with an orbital energy satisfying $|\epsilon| \ll GM_\mathrm{h}/R_\mathrm{p}$. The inequality (1.2) imposes that the velocity vector of the star lies into a cone, as illustrated in Fig. 1.1. This region in velocity space is called the loss cone (Frank & Rees 1976; Lightman & Shapiro 1977; Syer & Ulmer 1999). A star that enters it will be destroyed in a dynamical time assuming that it is not further perturbed during the plunge. The opening angle of the loss cone is given by

$$\theta_\mathrm{lc} = \frac{v_\perp}{v} = \frac{J_\mathrm{lc}}{J_\mathrm{c}} \tag{1.3}$$

where the second equality uses angular momentum conservation to express the tangential component $v_\perp$ of the velocity. In the last equality, $J_\mathrm{c} = Rv$ denotes the circular angular momentum of the star, that is the angular momentum that the star would have if it was on a circular orbit with its current position and velocity.

The rate of stellar disruptions can therefore be obtained by computing how fast stars enter the loss cone. The orbital elements of a given star orbiting the black hole vary due to two-body encounters with other stars. A timescale associated with this process is the relaxation time, during which the stellar velocity changes by order unity, such that the velocity variation is $\Delta v \approx v$. It is given by

$$t_\mathrm{r} \equiv \frac{v^3}{G^2 M_\star \rho \ln \Lambda} \approx 10^{10}\,\mathrm{yr} \left(\frac{\mathrm{M_h}}{10^6\,\mathrm{M_\odot}}\right)^{5/4}, \tag{1.4}$$

where ρ is the density of stars, $M_\star$ the stellar mass and $\ln\Lambda$ denotes the Coulomb logarithm, usually a factor of a few (e.g. Merritt 2013). In the second approximate equality, the relaxation time is evaluated at the influence radius making use of equation (1.1). On a relaxation time, the kinetic energy of the star also changes by order unity since is it proportional to v^2. However, the angular momentum J changes by an amount equal to its circular value $J_\mathrm{c} = Rv$. The change in angular momentum over t_r is therefore $\Delta J \approx J_\mathrm{c} = J/(1-e^2) \geq J$, denoting by e the eccentricity of the star. This means that as soon as the stellar orbit becomes eccentric, its angular momentum varies faster than its energy. An important consequence is that stars enter the loss cone due to angular momentum changes, which happen at approximately constant energy. The angular momentum variations experienced by the star due to two-body encounters can be described as a random walk.[2] Since the angular momentum varies by order J_c every relaxation time, the angular momentum change experienced by the star after a dynamical time t_dyn can then be written $\Delta J = (t_\mathrm{dyn}/t_\mathrm{r})^{1/2} J_\mathrm{c}$. The relative size of this angular momentum step can be determined by comparing it to the angular momentum J_lc at the surface of the loss cone (equation (1.2)) from the parameter

$$q \equiv \frac{\Delta J}{J_\mathrm{lc}}. \tag{1.5}$$

At large distances from the black hole, the long dynamical time allows for a larger angular momentum variation ΔJ and therefore a high value of q. A critical radius R_crit therefore exists above which $q > 1$ and below which $q < 1$. This allows us to distinguish two regimes of angular momentum relaxation into the loss cone. If $q < 1$ ($R < R_\mathrm{crit}$), the star takes small steps in angular momentum. Once it enters the loss cone, it is rapidly disrupted on a dynamical timescale. This regime is called *empty loss cone* regime. If instead $q > 1$ ($R > R_\mathrm{crit}$), the star takes large steps in angular momentum and can be scattered in and out of the loss cone during a dynamical time. This regime is referred to as *full loss cone* regime.

The total rate at which stars enter the loss cone can be written as the sum of the rate in each relaxation regime $\dot{N} = \dot{N}_\mathrm{empty} + \dot{N}_\mathrm{full}$ (Frank & Rees 1976; Syer & Ulmer 1999), where

$$\dot{N}_\mathrm{empty} = \int_0^{R_\mathrm{crit}} \frac{\mathrm{d}N}{\ln(2/\theta_\mathrm{lc}) t_\mathrm{r}}, \tag{1.6}$$

$$\dot{N}_\mathrm{full} = \int_{R_\mathrm{crit}}^{+\infty} \frac{\theta_\mathrm{lc}^2}{t_\mathrm{dyn}} \,\mathrm{d}N. \tag{1.7}$$

In the empty loss cone regime, the tip of the velocity vector slowly diffuses in velocity space until it enters the loss cone. The diffusion timescale is simply the relaxation time, which justifies the form of the disruption rate per star $\mathrm{d}\dot{N}_\mathrm{empty}/\mathrm{d}N \approx 1/t_\mathrm{r}$, the logarithmic term only giving a small contribution. In the full loss cone regime, there are always stars inside the loss cone which are disrupted on a dynamical time. The disruption rate per star is therefore $\mathrm{d}\dot{N}_\mathrm{full}/\mathrm{d}N = \theta_\mathrm{lc}^2/t_\mathrm{dyn}$ where θ_lc^2 is the fraction of the total volume that the loss cone occupies. These two relaxation regimes correspond to significantly different likelihoods of disruptions with a given pericentre distance R_p. In the empty loss cone regime, stars are disrupted with an angular momentum just below J_lc favouring grazing encounters with $R_\mathrm{p} \approx R_\mathrm{t}$. Instead, equation (1.7) shows that the disruption rate scales as θ_lc^2 in the full loss cone regime and is therefore proportional to R_p according to equations (1.2) and (1.3). This implies that the probability of tidal disruptions with a pericentre distance lower than a given value R_p is equal to $R_\mathrm{p}/R_\mathrm{t}$ (Luminet & Barbuy 1990). Deep encounters with $R_\mathrm{p} < R_\mathrm{t}$ can therefore represent a significant fraction of all TDEs in this regime. An analysis of the integrals (1.6) and (1.7) gives the contribution of each relaxation regime to the total TDE rate $\dot{N}$, which can in general be accurately approximated as

---

[2] During an encounter, the star has an equally likely chance to experience an increase of its angular momentum than a decrease. This justifies the treatment of the angular momentum evolution as a random walk.

$$\dot{N} \approx \frac{N(R_{\mathrm{e}})}{t_{\mathrm{r}}(R_{\mathrm{e}})}, \tag{1.8}$$

where $R_{\mathrm{e}} = \min(R_{\mathrm{crit}}, R_{\mathrm{inf}})$. This is because the integrand in equation (1.6) reaches a peak around R_{inf} before decreasing at larger distances due to the change of gravitational potential happening at the influence radius. However, since the integral is only made over distances smaller than R_{crit}, its main contribution comes from the minimum of the two characteristic distances, that is R_{e} (Syer & Ulmer 1999).[3] In galaxies relevant to TDEs, $R_{\mathrm{crit}} \approx R_{\mathrm{inf}}$ (Stone & Metzger 2016) which implies that most stars originate from close to the influence radius. The TDE rate can be estimated by

$$\dot{N} \approx \frac{N(R_{\mathrm{inf}})}{t_{\mathrm{r}}(R_{\mathrm{inf}})} = 10^{-4}\,\mathrm{yr}^{-1} \left(\frac{\mathrm{M_h}}{10^6\,\mathrm{M_\odot}}\right)^{-1/4}, \tag{1.9}$$

using equation (1.4) and the fact that $N(R_{\mathrm{inf}}) \approx M_{\mathrm{h}}/M_\star$ by definition of the influence radius (e.g. Bar-Or & Alexander 2016). This means that TDEs are rare events in a given galaxy and tend to be more frequent for low-mass black holes. Note however that if the total rate is evaluated at the critical radius, the dependence on the black hole mass varies with the stellar density profile considered. In particular, the total rate is found to increase with black hole mass for shallow stellar profiles (Wang & Merritt 2004).

The qualitative conclusions drawn from the above analytical calculations have been confirmed by more careful treatments of two-body relaxation. This has been done by treating this mechanism as a Fokker-Planck process (Lightman & Shapiro 1977; Cohn & Kulsrud 1978) and more recently using N-body simulations (Brockamp et al. 2011; Vasiliev & Merritt 2013; Zhong et al. 2014). The TDE rate has been estimated using observed stellar distributions determined from high-resolution surface brightness profiles. These studies find a typical TDE rate per galaxy of $\dot{N} \gtrsim 10^{-4}\,\mathrm{yr}^{-1}$ dominated by low-mass galaxies assuming that they host a SMBH (Magorrian & Tremaine 1999; Wang & Merritt 2004; Stone & Metzger 2016).

Various investigations have also been made to determine the impact of additional effects on the TDE rate. First, the black hole spin can increase the rate of detectable TDEs for $M_{\mathrm{h}} \gtrsim 10^8\,\mathrm{M_\odot}$ owing to a reduced size of the event horizon (Kesden 2012a). Several authors also explored the possibility of tidal disruptions by a binary black hole. In the phase of binary shrinking through stellar interactions, the TDE rate was found to be greatly increased up to $\dot{N} \approx 10^{-2}\,\mathrm{yr}^{-1}$ (Ivanov et al. 2005; Chen et al. 2009, 2011). After the binary has merged, the remnant black hole experiences a velocity kick due to the anisotropic emission of gravitational waves. This causes the black hole to quickly refill its loss cone and can lead to a TDE rate as high as $\dot{N} \approx 10^{-1}\,\mathrm{yr}^{-1}$ (Stone & Loeb 2011). However, Wegg & Bode (2011) argued that TDEs involving a binary black hole represent only a few percent of all TDEs because the phase of TDE enhancement by this mechanism is short compared to the expected rate of galaxy mergers during which binary black holes form. The recoiled black hole is also expected to retain a cluster of stars around it which can result in more tidal disruptions, although with a rate slightly lower than before the kick (Komossa & Merritt 2008; Stone & Loeb 2012b; Li et al. 2017). Interestingly, such TDEs would appear offset with respect to the galactic centre. Various additional stellar dynamical effects have also been proposed that could affect the TDE rate. Several authors studied the impact of resonant relaxation (Rauch & Tremaine 1996). This effect occurs when the stars follow Keplerian ellipses for a large number of periods such that they can be approximated as elliptic wires. In this situation, the torques between wires act coherently which shortens the relaxation time compared to the non-resonant value of equation (1.4). However, this effect on the TDE rate was found to be negligible because stars come from distances similar to $R_{\rm inf}$ where their orbit significantly differ from Keplerian ellipses due to the additional stellar potential (Rauch & Ingalls 1998; Hopman & Alexander 2006; Madigan et al. 2011). The presence of massive perturbers, such as an intermediate-mass black hole or a disrupted globular cluster, is also expected to decrease the relaxation timescale causing an increase of the TDE rate by a factor of ~ 2 (Perets et al. 2007). Similarly, the presence of spiral arms can cause an enhancement of up to 20% (Hamers & Perets 2017). The effect of two-body relaxation is also enhanced for non-spherical stellar distributions. Although the TDE rate increases only by a factor of a few for axisymmetric systems (Vasiliev & Merritt 2013), it can be boosted by several orders of magnitude for triaxial ones(Merritt & Poon 2004). Finally, the TDE rate can be increased by a factor of $\sim$ 100 by the presence of a large-scale accretion disc around the black hole (Karas & Šubr 2007).

---

[3] One exception exists for very steep stellar density profiles where the integrand in equation (1.6) diverges at small distances. In this particular case, a large number of stars could be disrupted on trajectories that originate close to the black hole (Syer & Ulmer 1999).

As mentioned in Section 1.3, the theoretical TDE rate of $\dot{N} \gtrsim 10^{-4}\,\rm yr^{-1}$ is larger than the observed one by about an order of magnitude. The origin of this discrepancy is currently unclear. As shown above, effects additional to pure two-body relaxation tend to further increase this tension. It seems therefore unlikely to originate from inaccurate theoretical TDE rates due to effects unaccounted for. A more natural explanation could come from an underestimate of the observed rate, for example due to selection effects, or to the fact that special conditions are required for a TDE to be detectable, such as a deep encounter with the black hole (Stone & Metzger 2016). Another observational feature is the preference of TDEs for post-starburst E+A galaxies (French et al. 2016). This could be due to the presence of a binary black hole in the centre of the galaxy that is expected to momentarily increase the TDE rate. This scenario is however disfavoured based on the inferred time since starburst (French et al. 2017). A central stellar overdensity could also explain this large rate of disruptions. This latter explanation is favoured by the observation of a particular E+A galaxy, which provides evidence for a very steep stellar density profile (Stone & van Velzen 2016) expected to enhance the TDE rate in the empty loss cone regime (Syer & Ulmer 1999). Finally, this enhanced rate could be due to a triaxiality of the stellar potential in this type of galaxies, which strongly boosts the rate of stellar disruptions (Merritt & Poon 2004).

1.4.3 Pericentre passage

The next phase of evolution concerns the passage of the star at pericentre, a distance $R_{\rm p} \leq R_{\rm t}$ from the black hole. The most important consequence is the disruption of the star, during which an orbital energy spread is imparted to the debris. Additional effects are specific to deep disruptions, where the star passes well within the tidal radius.

By definition, the tidal forces from the black hole become similar to the star's self-gravity at the tidal radius. This critical distance can therefore be obtained by equating the self-gravity acceleration $a_{\rm g} \approx GM_\star/R_\star^2$ and the tidal acceleration $a_{\rm t} \approx GM_{\rm h}R_\star/R^3$, which gives

$$R_{\rm t} \equiv R_\star \left(\frac{M_{\rm h}}{M_\star}\right)^{1/3} = 0.5\,{\rm AU} \left(\frac{\rm M_h}{10^6\,\rm M_\odot}\right)^{1/3} \left(\frac{\rm R_\star}{\rm R_\odot}\right)\left(\frac{\rm M_\star}{\rm M_\odot}\right)^{-1/3}, \tag{1.10}$$

where $M_\star$ and $R_\star$ denote the mass and radius of the star, respectively. A tidal disruption can happen either at the surface of the tidal sphere or deep inside it. The depth of the encounter is parametrized by the penetration factor

$$\beta \equiv \frac{R_{\rm t}}{R_{\rm p}}, \tag{1.11}$$

which must be larger than unity for a TDE to occur. For this disruption to be detectable, it needs to happen outside the event horizon of the black hole, that is twice its gravitational radius

$$R_\mathrm{g} \equiv \frac{GM_\mathrm{h}}{c^2} = 0.01\,\mathrm{AU}\left(\frac{\mathrm{M_h}}{10^6\,\mathrm{M_\odot}}\right), \tag{1.12}$$

for a Schwarzschild black hole. Imposing $R_\mathrm{t} \gtrsim 2R_\mathrm{g}$ translates into an upper limit on the black hole mass

$$M_\mathrm{h} \leq M_\mathrm{H} = 10^8\,\mathrm{M_\odot}\left(\frac{\mathrm{R_\star}}{\mathrm{R_\odot}}\right)^{3/2}\left(\frac{\mathrm{M_\star}}{\mathrm{M_\odot}}\right)^{-1/2}, \tag{1.13}$$

usually referred to as the Hills mass since it was first derived by Hills (1975). For Kerr black holes, the event horizon decreases implying that the Hills mass is larger. For black holes above this critical mass, the star is swallowed whole before being disrupted with no significant emission. For the TDE candidate ASASSN-15lh, a black hole mass of $M_\mathrm{h} > 10^8\,\mathrm{M_\odot}$ has been measured suggesting that the black hole must be rotating for the disruption to be detectable (Leloudas et al. 2016).

We now describe the basic dynamics associated with the passage of the star at pericentre. This process is depicted in Fig. 1.2. Initially in hydrostatic equilibrium, the star starts being deformed under the influence of the black hole's tidal force at a distance of a few R_t from the black hole. Specifically, it is stretched along an almost radial direction because stellar elements closer to the black hole undergo a larger gravitational pull. This deformation reaches order unity when the star reaches the tidal radius. The response of pressure to this deformation causes the stellar debris to experience a spread in orbital energy

$$\Delta\epsilon = \frac{GM_\mathrm{h}}{R_\mathrm{t}^2}R_\star, \tag{1.14}$$

which can be computed from a Taylor expansion of the gravitational potential across the star, as first realized by Lacy et al. (1982) and Evans & Kochanek (1989). The latter calculation can be understood in the impulse approximation. Under this approximation, the star remains unaffected until it reaches the tidal radius, at which point the trajectory of the debris changes instantaneously. This implies that the stellar elements all have the same kinetic energy, equal to that of the star, at the moment of disruption. Instead, each gas parcel has a different potential energy given by its position within the black hole potential. This results in an energy spread across the star given by equation (1.14). Stellar elements closer to the black hole than the centre of mass experience an orbital energy decrease while those further away undergo an increase in orbital energy. In principle, the trajectory of the centre of mass is also affected by heat injection and spin-up of the star, both realized at the expense of the orbital energy. However, this does not affect the subsequent evolution of the debris since the energy loss associated with these processes is similar to the stellar binding energy $\epsilon_\mathrm{b} \approx GM_\star/R_\star$ which satisfies $\epsilon_\mathrm{b}/\Delta\epsilon \approx (M_\mathrm{h}/M_\star)^{-1/3} \ll 1$. In the initial estimates of the energy spread (e.g. Lacy et al. 1982), the tidal radius was actually replaced by the pericentre distance in the denominator of equation (1.14) implying that deep encounters with $R_\mathrm{p} < R_\mathrm{t}$ would lead to large energy spreads. However, it was shown more recently that equation (1.14) is in fact the correct version (Sari et al. 2010; Stone et al. 2013). The reason is that, within the tidal sphere, the gas moves on ballistic trajectories since the gravitational force from the black hole dominates all the other forces. As a result, the orbital energy of the debris is frozen-in at the tidal radius and independent of the penetration factor β.

This orbital energy spread has an important consequence on the following evolution of the debris. As demonstrated in Section 1.4.2, victim stars originate from distances similar to the influence radius given by equation (1.1). This implies that a star typically reaches the

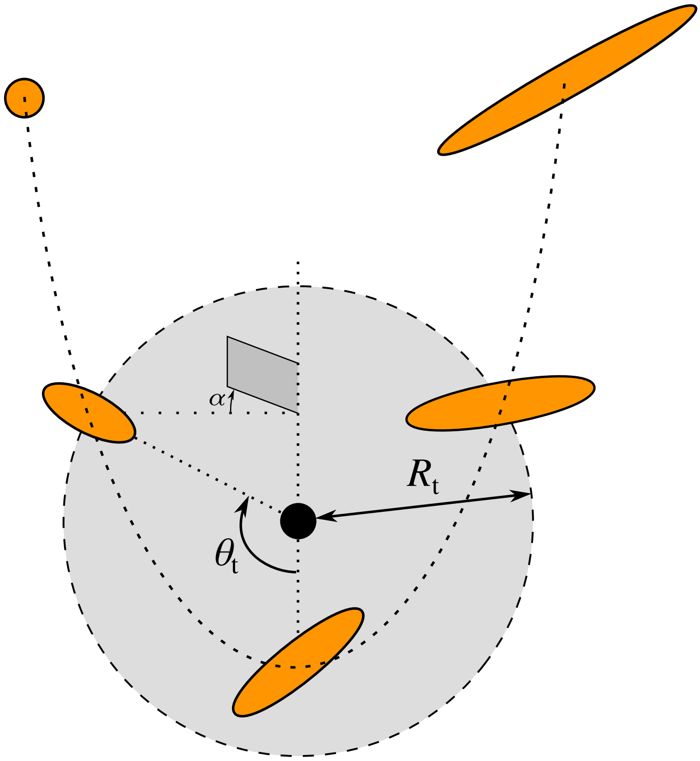

Figure 1.2: Sketch showing the passage of the star (in orange) at pericentre inside the tidal sphere (grey area). At the tidal radius R_t, the star has a true anomaly θ_t. Inside the tidal sphere, it is then confined between two orbital planes inclined by an angle α.

tidal sphere on a highly eccentric orbit with $1 - e \approx R_{\rm inf}/R_t = 10^{-6}$, which can safely be approximated as a parabola with orbital energy $\epsilon \approx 0$. As a consequence, the stellar matter experiencing an energy increase gets unbound from the black hole with an orbital energy $\Delta\epsilon$ while that losing orbital energy becomes bound with an orbital energy $-\Delta\epsilon$ (Rees 1988). In general, the orbital energy is distributed roughly symmetrically within the debris, implying that approximately half of the debris falls in each category. The gas elements subsequently evolve on different trajectories causing the formation of an elongated and eccentric stream with a range of eccentricities given by

$$1 - e = \pm\frac{2}{\beta}\left(\frac{M_{\rm h}}{M_\star}\right)^{-1/3} = \pm\, 0.02\beta^{-1}\left(\frac{M_{\rm h}}{10^6\,{\rm M}_\odot}\right)^{-1/3}\left(\frac{M_\star}{{\rm M}_\odot}\right)^{1/3}, \tag{1.15}$$

using equation (1.14). Within this stream, about half of the matter comes back to black hole while the rest escapes its gravitational pull. The energy distribution within the debris specifies the form of the mass rate at which the bound matter falls back. Deviations from the simple ballistic argument used above to obtain the energy spread of equation (1.14) will be discussed in Section 1.4.5 along with the impact of various effects on the debris energy distribution and corresponding fallback rate.

For penetration factors $\beta \approx 1$, the star only grazes the tidal sphere. As demonstrated in Section 1.4.2, such encounters are in general more likely, especially in the empty loss cone regime. In this case, the disruption can be partial with a self-gravitating core surviving after pericentre passage, a scenario confirmed by numerical simulations (Guillochon & Ramirez-Ruiz 2013; Mainetti et al. 2017). This process is especially likely for giant stars as will be described in Section 1.4.8. Interestingly, partial disruptions can account for the low total energy emitted from most TDEs since the accretion of a hundredth of solar mass with a radiative efficiency η releases an energy of $\eta\, \mathrm{M}_{\odot} \mathrm{c}^2/100 \approx 10^{51}\,\mathrm{erg}\,(\eta/0.1)$, consistent with the observed values (Li et al. 2002; Chornock et al. 2014). Additionally, numerical studies found that mass loss is asymmetric with more matter being lost from the side of the star facing the black hole. Since the gas on this side is more bound to the black hole, the partial disruption results in a velocity kick given to the surviving core similar to the star's escape velocity (Manukian et al. 2013; Gafton et al. 2015).

Numerous additional effects are predicted for tidal disruptions with $\beta \gtrsim 3$. These deep encounters are less likely than grazing ones but can still represent a significant fraction of TDEs, around $1/\beta = 1/3 \approx 33\%$, in the full loss cone regime (Luminet & Barbuy 1990) as demonstrated in Section 1.4.2. In this type of encounters, the star undergoes a strong compression in addition to the shearing along the orbital plane described above. The first study of this process was carried out by Carter & Luminet (1982) based on the following geometrical argument. Consider a star whose trajectory passes well within the tidal radius, as illustrated in Fig. 1.2. Inside the tidal sphere, the stellar matter moves ballistically. As a result, the star is confined between two orbital planes that intersect near pericentre and the star is progressively compressed into a pancake, or "crêpe stellaire". In the limit of large β, the inclination angle between these two planes is $\alpha \approx R_\star/(R_\mathrm{t} \sin\theta_\mathrm{t})$, where θ_t represents the true anomaly of the star at the tidal radius. Since the star moves on a parabolic orbit, $\cos\theta_\mathrm{t} = 2R_\mathrm{p}/R_\mathrm{t} - 1$, which implies $\sin\theta_\mathrm{t} \approx \theta_\mathrm{t} \approx (R_\mathrm{p}/R_\mathrm{t})^{1/2}$ and results in $\alpha \approx R_\star/(R_\mathrm{p} R_\mathrm{t})^{1/2}$. At pericentre, the star therefore undergoes a vertical collapse at a velocity $v_\mathrm{c} \approx v_\mathrm{p}\alpha$ where $v_\mathrm{p} \approx (GM_\mathrm{h}/R_\mathrm{p})^{1/2}$ is the velocity at pericentre. Using the value of α derived above, the collapse velocity takes the form

$$v_\mathrm{c} \approx \beta \left(\frac{GM_\star}{R_\star}\right)^{1/2}. \tag{1.16}$$

This strong vertical compression causes the formation of shocks that convert kinetic energy into heat, increasing the temperature of the stellar core to $T_\mathrm{c} \approx \beta^2 T_\star$. Assuming an adiabatic evolution with the density scaling as $\rho_\mathrm{c} \propto T_\mathrm{c}^{3/2}$, the density reaches a value $\rho_\mathrm{c} \approx \beta^3 \rho_\star$ during the collapse. Here, $T_\star$ and $\rho_\star$ denotes the temperature and density of the stellar core, respectively.

For main sequence stars, the above estimates imply that temperatures and densities of the order of $T_\mathrm{c} \approx 10^9\,\mathrm{K}$ and $\rho_\mathrm{c} \approx 10^4\,\mathrm{g\,cm^{-3}}$ can be attained in the compressed stellar core for $\beta \approx 10$. This led Carter & Luminet (1982) to argue that nuclear reactions, such as helium burning through the triple$-\alpha$ process, could be triggered during the stellar compression of main sequence stars. However, this conclusion is now controversial. Later studies relying on the semi-analytical affine model that describes the compressed star as a time-dependent ellipsoid (Carter & Luminet 1983, 1985; Luminet & Marck 1985; Luminet & Carter 1986) and one-dimensional hydrodynamical calculations (Brassart & Luminet 2008, 2010) confirmed this result. However, three-dimensional hydrodynamical simulations, including more recent ones, tend to return lower values for the temperatures and densities reached (Bicknell & Gingold 1983; Laguna et al. 1993; Kobayashi et al. 2004; Guillochon et al. 2009). The origin of this discrepancy remains unclear: it could be due to purely three-dimensional effects that can prevent an efficient pressure build-up during the collapse (Guillochon et al. 2009) but also be attributed to the too low resolution of the simulations. Although this controversy is still ongoing, it has cast doubt on the possibility of tidally-induced nuclear reactions for main sequence stars. Owing to their larger initial densities, white dwarfs are now preferred candidates for the

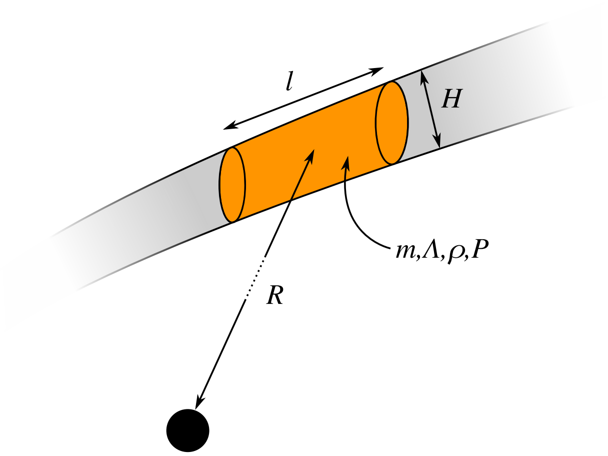

Figure 1.3: Sketch of a gas element (in orange) belonging to the debris stream and located at a distance R from the black hole. It can be approximated as a cylinder with width H and length l. The element has a pressure P, a density $\rho \approx m/(\pi H^2 l)$ and a linear density $\Lambda \approx m/l$ where m denotes the mass of the element.

occurrence of this process as will be discussed in Section 1.4.8.

Even if not strong enough to trigger important nuclear reactions, the vertical compression experienced by the star during a deep tidal disruption has other potentially detectable consequences. Following the collapse, shock waves propagate outward within the star. When the shock front reaches the stellar surface, radiation emitted by the hot outer layers is able to diffuse out. This shock breakout leads to a prompt X-ray signature lasting ~ 10 s with an luminosity of $\sim 10^{44}$ erg s^{-1} (Kobayashi et al. 2004; Guillochon et al. 2009). Another electromagnetic signal could originate from the prompt accretion of stellar matter during a close pericentre passage due to shocks induced by strong relativistic effects (Haas et al. 2012; Evans et al. 2015). These emission mechanisms have the potential to indicate the time of pericentre passage, which is unknown in most TDE candidates. However, they have not so far been detected.

Finally, two categories of gravitational waves emission are expected from the pericentre passage of the star. The first relates to the motion of the star near the black hole. For main sequence star and white dwarf disruptions, the signal lies in the *LISA* frequency range with an expected strain amplitude of $h \gtrsim 10^{-22}$ for a source at 10 Mpc that makes it marginally detectable (Kobayashi et al. 2004; Guillochon et al. 2009). The second signal relates to the change of shape of the star during compression. For main sequence stars, the prospects of detection are dim. The associated frequency is $f \approx 10$ Hz for an extreme penetration factor $\beta = 25$, which only corresponds to the lower bound of the frequency range detectable by Advanced LIGO. The corresponding signal for white dwarfs may however be detectable with this instrument since the frequency increases to $f \approx 10^2$ Hz with a strain amplitude of $h \approx 10^{-23}$ at 10 Mpc for a less extreme value of $\beta \approx 5$ (Guillochon et al. 2009; Stone et al. 2013).

1.4.4 Stream evolution around the black hole

Following the disruption, the stellar matter evolves into an elongated structure. The next phase concerns the evolution of this stream of gas around the black hole. In general, the stream moves ballistically, keeping a narrow profile under the influence of self-gravity. However, special circumstances exist that can make the stream evolution deviate from this prediction.

To a good approximation, the motion of the stream is determined by the different trajectories of the debris set by the energy spread imparted during the disruption process and given by equation (1.14). The stream transverse structure can instead be affected by three different forces: the tidal force from the black hole, the stream pressure force and its self-gravity. For the most likely grazing encounters with $\beta \approx 1$, analytical and numerical studies demonstrate that the stream retains a large enough density for hydrostatic balance between pressure and self-gravity to be maintained in the vertical direction (Kochanek 1994; Coughlin et al. 2016b,a). The evolution of the width H of the stream as a function of distance R from the black hole can be found analytically by modelling the gas distribution by a series of cylindrical debris elements. As illustrated in Fig. 1.3, a given element has a width H, a length l and contains a mass m of gas such that its density can be approximated as $\rho \approx m/(\pi H^2 l)$. Hydrostatic equilibrium states that the outward pressure acceleration $a_{\rm p} \approx P/(H\rho)$ is equal to the inward self-gravity acceleration $a_{\rm g} \approx Gm/(Hl)$. Equating these two accelerations, the stream width is found to scale as

$$H \propto \Lambda^{-1/4}, \tag{1.17}$$

where $\Lambda = m/l$ denotes the linear density of a stream element and assuming an adiabatic evolution with $P \propto \rho^{5/3}$ (Kochanek 1994; Guillochon et al. 2014; Coughlin et al. 2016a). As long as the gas elements remain close to the stream centre of mass, the linear density scales as $\Lambda \propto R^{-2}$, which yields $H \propto R^{1/2}$ (Coughlin et al. 2016a). When the debris trajectory starts significantly deviating from that of the centre of mass after a few months, the scaling changes to $\Lambda \propto R^{-1}$, which implies

$$H \propto R^{1/4}, \tag{1.18}$$

using equation (1.17) (Kochanek 1994; Coughlin et al. 2016a). The width therefore increases slowly with distance due to the confining effect of self-gravity implying that the stream retains a thin shape even far from the tidal radius.

This confinement of the stream transverse profile is prevented if its density is too low, which causes the tidal force from the black hole to dominate self-gravity. In this case, the width of the stream scales as $H \propto R$ because its external parts move on approximately radial orbits. Such a density decrease can occur in several situations. As explained in Section 1.4.3, if the star passes deep inside the tidal radius, it undergoes a thermal energy injection at pericentre that can cause an early expansion of the gas distribution with an associated decrease in density (Kochanek 1994; Coughlin et al. 2016a). If the stream is highly magnetized, expansion can also occur when magnetic pressure overcomes gas pressure that can happen from tens of days following the disruption (Guillochon & McCourt 2017; Bonnerot et al. 2017a). Finally, the stream will also expand if it is heated by any mechanism, such as hydrogen recombination when the temperature drops to $\sim 10^4$ K about a week after disruption (Kasen & Ramirez-Ruiz 2010).

Additionally, the stream can be subject to instabilities during its evolution around the black hole. As it expands, the stream can get cold enough to become gravitational unstable. This results in the formation of self-gravitating clumps that can start appearing from a few days after disruption (Coughlin & Nixon 2015; Coughlin et al. 2016b). Due to its interaction with the surrounding gaseous medium, the stream is also subject to the Kelvin-Helmholtz mixing instability. This affects primarily the disruption of red giants since these evolved stars produce low density streams that are easily affected by the instability. However, it possibly also impacts disruptions involving main sequence stars for an ambient medium of high density (Bonnerot et al. 2016b; Kathirgamaraju et al. 2017).

Finally, when the unbound part of the stream reaches parsec scales, it is decelerated by its interaction with the ambient medium. During this process, shocks can form that drive particle acceleration leading to radio emission via synchrotron radiation and the production of cosmic rays accompanied by γ-ray emission when these particles interact with the surrounding matter (Guillochon et al. 2016; Chen et al. 2016). This mechanism constitutes a possible origin for the radio emission detected from the TDE candidate ASASSN-14li (Krolik et al. 2016).

1.4.5 Fallback of the debris

Since about half of the debris stream produced by the disruption is bound to the black hole, it comes back to the disruption site. In this section, we focus on this phase of evolution in order to evaluate the mass fallback rate of the stellar matter. As derived below, this rate typically decreases with time as $t^{-5/3}$ although deviations from this simple power law decay are expected.

As explained in Section 1.4.4, the stream moves ballistically around the black hole. The most tightly bound debris has an orbital energy $-\Delta\epsilon$, which corresponds to a semi-major axis and orbital period of

$$a_{\rm min} = \frac{R_\star}{2}\left(\frac{M_{\rm h}}{M_\star}\right)^{2/3} = 23\,{\rm AU}\left(\frac{\rm M_h}{10^6\,\rm M_\odot}\right)^{2/3}\left(\frac{\rm M_\star}{\rm M_\odot}\right)^{-2/3}, \tag{1.19}$$

$$t_{\rm min} = \frac{\pi}{\sqrt{2}}\left(\frac{R_\star^3}{GM_\star}\right)^{1/2}\left(\frac{M_{\rm h}}{M_\star}\right)^{1/2} = 41\,{\rm d}\left(\frac{\rm M_h}{10^6\,\rm M_\odot}\right)^{1/2}\left(\frac{\rm R_\star}{\rm R_\odot}\right)^{3/2}\left(\frac{\rm M_\star}{\rm M_\odot}\right)^{-1}, \tag{1.20}$$

making use of equation (1.14) and Kepler's third law. The mass fallback rate, at which the debris reaches the black hole, is given by $\dot{M}_{\rm fb} = {\rm d}M/{\rm d}t$ which, using the chain law, becomes

$$\dot{M}_{\rm fb} = \frac{{\rm d}M}{{\rm d}\epsilon}\frac{{\rm d}\epsilon}{{\rm d}t} = \frac{(2\pi G M_{\rm h})^{2/3}}{3}\frac{{\rm d}M}{{\rm d}\epsilon}t^{-5/3}, \tag{1.21}$$

where the Kepler's third law has again been used to express the orbital energy time derivative ${\rm d}\epsilon/{\rm d}t$. Equation (1.21) implies that the fallback rate decay law is entirely dependent on the energy distribution ${\rm d}M/{\rm d}\epsilon$. Early investigations made the simplifying assumption that this distribution is flat, that is ${\rm d}M/{\rm d}\epsilon$ is independent of ϵ. Under this approximation, the mass fallback rate decays as $\dot{M}_{\rm fb} \propto t^{-5/3}$ (Rees 1988; Phinney 1989) and can be written

$$\dot{M}_{\rm fb} = \dot{M}_{\rm p}\left(\frac{t}{t_{\rm min}}\right)^{-5/3}, \tag{1.22}$$

$$\dot{M}_{\rm p} = \frac{M_\star}{3t_{\rm min}} = 3\,{\rm M_\odot\,yr^{-1}}\left(\frac{M_{\rm h}}{10^6\,\rm M_\odot}\right)^{-1/2}\left(\frac{R_\star}{\rm R_\odot}\right)^{-3/2}\left(\frac{M_\star}{\rm M_\odot}\right)^{2}, \tag{1.23}$$

where the value of the peak fallback rate $\dot{M}_{\rm p}$ comes from imposing that a mass $M_\star/2$ reaches the black hole for $t \geq t_{\rm min}$.

Hydrodynamical simulations of the disruption process have been carried out to test the validity of the flat energy distribution approximation. For a realistic stellar structure, the energy distribution generally peaks at $\epsilon \approx 0$ and decreases for larger values of $|\epsilon|$. This is due to the larger density in the central region of the star compared to its outer layers. As a result, the associated rate of fallback features an initial rise to peak that lasts a few $t_{\rm min}$ before decaying (Lodato et al. 2009). The fallback rate follows $\dot{M}_{\rm fb} \propto t^{-5/3}$ only at late times due to the flatness of the energy distribution for marginally bound debris with $\epsilon \lesssim 0$. Additionally, the energy spread was numerically found to be slightly larger than that of equation (1.14) for

$\beta \approx 1$ (Lodato et al. 2009; Guillochon & Ramirez-Ruiz 2013) which is likely caused by an in-plane compression of the star at pericentre (Coughlin et al. 2016b). This effect is even more severe for deep tidal disruptions due to the vertical compression discussed in Section 1.4.3 (Rosswog et al. 2008). If the disruption is partial, the energy distribution of the debris present instead a deficit of matter at energies $\epsilon \approx 0$ due to the self-gravitating core that survives the disruption. As a result, the mass fallback rate decays faster with $\dot{M}_{\rm fb} \propto t^{-2.2}$ (Guillochon & Ramirez-Ruiz 2013). Finally, relativistic effects lead to a larger and earlier peak in the fallback rate due to a stronger tidal field that produces a wider energy spread (Laguna et al. 1993; Kesden 2012b; Tejeda et al. 2017). Despite these various possible deviations, evaluating the fallback rate using equations (1.22) and (1.23) is in general a good approximation.

It was originally thought that the luminosity of the flare powered by the accretion of debris onto the black hole would directly trace the mass fallback rate leading to a luminosity decay as $t^{-5/3}$ (Rees 1988). However, recent works has cast serious doubt on the validity of this approach as will be explained in Section 1.4.6.

1.4.6 Disc formation and accompanying phenomena

It is commonly believed that most of the electromagnetic emission detected from TDEs originates from the dissipation of the debris orbital energy when the stream comes back to the black hole. Until a few years ago, this energy extraction was assumed to occur via the rapid formation of a standard accretion disc within which the gas spirals inward while radiating away its orbital energy. However, it has recently become clear that significant modifications to this initial model are necessary to account for new theoretical and observational constraints. Despite fast advances, several models for this phase of evolution still coexist and a clear consensus has so far not been reached.

We start by explaining the initial model, due to Rees (1988), that was widely accepted until recently. This initial model assumes that the debris settles into a standard thick accretion disc on a short circularization timescale $t_{\rm circ} \lesssim t_{\rm min}$. Within this disc, most of the mass is located at a distance $R_{\rm d} \approx 2R_{\rm p}$ from the black hole as predicted by angular momentum conservation.[4] The viscous timescale in this torus satisfies

$$\frac{t_{\rm visc}}{t_{\rm min}} = \frac{1}{t_{\rm min}}\alpha^{-1}\left(\frac{R_{\rm d}^3}{GM_{\rm h}}\right)^{1/2} = 10^{-2}\beta^{-3/2}\left(\frac{\alpha}{0.1}\right)^{-1}\left(\frac{M_{\rm h}}{10^6\,{\rm M}_\odot}\right)^{-1/2}\left(\frac{R_{\rm d}}{2R_{\rm p}}\right)^{3/2}, \tag{1.24}$$

using equation (1.20) and where α denotes the viscosity parameter (Frank et al. 2002).[5] Therefore, the infalling matter is accreted shortly after joining the torus such that the mass accretion rate within the disc can a priori be identified to the fallback rate of equation (1.22). Assuming that a fraction η of the available rest mass energy is dissipated and radiated locally, the associated luminosity can be larger than the Eddington luminosity by a factor

$$\frac{\dot{M}_{\rm fb}}{\dot{M}_{\rm Edd}} \equiv \frac{\eta \dot{M}_{\rm fb} c^2}{L_{\rm Edd}} = 10^2\left(\frac{\eta}{0.1}\right)\left(\frac{M_{\rm h}}{10^6\,{\rm M}_\odot}\right)^{-3/2}\left(\frac{t}{t_{\rm min}}\right)^{-5/3}, \tag{1.25}$$

---

[4] Before the disruption, all the stellar elements have an angular momentum similar to that of the star $J \approx (2GM_{\rm h}R_{\rm p})^{1/2}$ corresponding to a parabolic orbit with pericentre distance $R_{\rm p}$. The angular momentum of a circular disc formed from the debris at radius $R_{\rm d}$ is $J_{\rm d} \approx (GM_{\rm h}R_{\rm d})^{1/2}$, which imposes $R_{\rm d} \approx 2R_{\rm p}$ by angular momentum conservation.

[5] In accretion discs, the viscosity inducing the inward transport of mass can be parametrized as $\nu = \alpha c_{\rm s} H$ where $c_{\rm s}$ and H are the sound speed and disc thickness while α is the viscosity parameter (Shakura & Sunyaev 1973). The physical origin of viscosity is commonly attributed to magnetic stresses generated by turbulence induced by the magneto-rotational instability (Balbus & Hawley 1991).

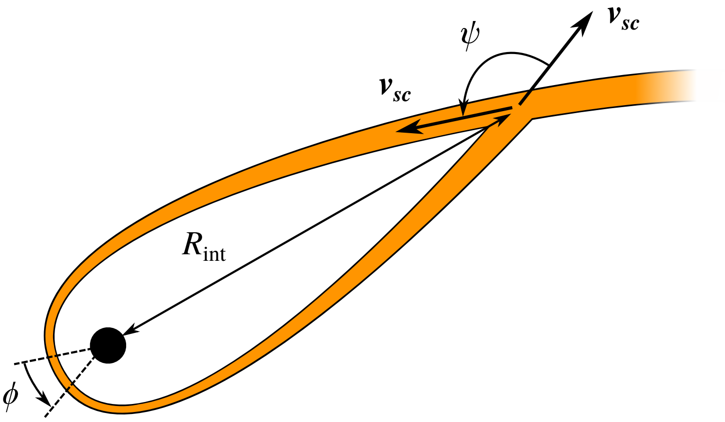

Figure 1.4: Sketch showing the self-crossing of the stream. Due to relativistic precession, the most bound part of the stream precess by an angle ϕ after pericentre passage. As a result, it collides with the part of the stream still approaching the black hole. This intersection occurs at a distance $R_{\rm int}$ from the black hole with a collision angle ψ between the two colliding elements of velocity $\mathbf{v}_{\rm sc}$.

where $\dot{M}_{\rm Edd}$ is the Eddington accretion rate. This ratio exceeds unity initially as long as the black hole mass is $M_{\rm h} \leq 3 \times 10^7\,{\rm M}_{\odot}$. It then decreases with time and becomes lower than one for $t \geq t_{\rm Edd}$ with $t_{\rm Edd}/t_{\rm min} \equiv (\dot{M}_{\rm p}/\dot{M}_{\rm Edd})^{3/5} \approx 20\,(M_{\rm h}/10^6\,{\rm M}_{\odot})^{-9/10}$. The accretion luminosity is therefore capped to $L_{\rm acc} \approx L_{\rm Edd}$ for $t \leq t_{\rm Edd}$. At later times $t \geq t_{\rm Edd}$, the accretion luminosity decays as $L_{\rm acc} = \eta \dot{M}_{\rm fb} c^2 \propto t^{-5/3}$. This model therefore predicts a peak luminosity close to the Eddington value

$$L_{\rm acc} \approx L_{\rm Edd} = 10^{44}\,{\rm erg\,s^{-1}} \left(\frac{{\rm M_h}}{10^6\,{\rm M}_{\odot}}\right), \tag{1.26}$$

and a corresponding effective temperature of

$$T_{\rm acc} = \left(\frac{L_{\rm acc}}{4\pi R_{\rm ph}^2 \sigma_{\rm SB}}\right)^{1/4} = 2 \times 10^5\,{\rm K} \left(\frac{{\rm R_{ph}}}{{\rm R_p}}\right)^{-1/2} \left(\frac{{\rm M_h}}{10^6\,{\rm M}_{\odot}}\right)^{1/4}, \tag{1.27}$$

where $\sigma_{\rm SB}$ denotes the Stefan-Boltzmann constant and the photospheric radius is set to $R_{\rm ph} \approx R_{\rm p}$, that is the size of the torus (Rees 1988; Ulmer 1999; Lodato & Rossi 2011; Miller 2015). This means that most of the energy is radiated in the soft X-ray band. This initial model is able to explain the first TDE candidates detected in soft X-rays with lightcurves peaking at $\sim 10^{44}\,{\rm erg\,s^{-1}}$ and exhibiting a decay law consistent with $t^{-5/3}$. However, it is unable to account for the more recently discovered class of optical TDEs which, as described in Section 1.3, feature lower effective temperatures of $\sim 10^4$ K. Furthermore, recent investigations of the disc formation process from the stellar debris strongly challenged this initial model. Based on this new understanding of the TDE dynamics, alternative emission sources have been proposed to explain these observations.

The initial model assumes the rapid formation of a circular accretion disc around the black hole. It is nevertheless not clear a priori how such a structure forms from the debris stream. We now provide analytical estimates for the main physical effects involved in the disc formation process. The first ingredient needed to achieve disc formation is an efficient dissipation mechanism. Rapid circularization requires to dissipate an energy $\Delta\epsilon_{\rm circ} = GM_{\rm h}/(4R_{\rm p})$ in a dynamical timescale. Two main dissipation mechanisms have been proposed. The first relates to the strong compression of the stream at pericentre. This process is similar to that discussed in

Section 1.4.3 for which the star is strongly compressed in the vertical direction when it passes well within its tidal radius. Since the stream is less dense that the star, its tidal radius is further away. As a result, the stream always passes deep inside its own tidal radius and experiences strong vertical compression. The energy dissipation associated with this nozzle shock turns out to be the same as that experienced by the star (Guillochon et al. 2014). The dissipated energy is therefore

$$\Delta\epsilon_{\rm no} = v_{\rm c}^2 \approx \beta^2 \frac{GM_\star}{R_\star} \tag{1.28}$$

where $v_{\rm c}$ is given by equation (1.16). $\Delta\epsilon_{\rm no}/\Delta\epsilon_{\rm circ} \approx \beta(M_{\rm h}/M_\star)^{-2/3} \approx 10^{-4}$ for $M_{\rm h} = 10^6\,{\rm M}_\odot$ and $\beta = 1$, which implies that this dissipation mechanism cannot drive complete circularization. However, it could still be efficient for large penetration factors and black holes of very low masses $M_{\rm h} < 10^3\,{\rm M}_\odot$. The second dissipation mechanism, illustrated in Fig. 1.4, involves an intersection of the stream with itself. When the most bound part of the stream passes at pericentre, its orbit precesses due to relativistic precession. As a result, it intersects the matter arriving later and still approaching the black hole. This crossing leads to the formation of shocks that can dissipate part of the stream orbital energy into heat. Assuming inelastic collision, the energy dissipated during this self-crossing shock can be estimated by

$$\Delta\epsilon_{\rm sc} = \frac{v_{\rm sc}^2}{2}\sin^2(\psi/2) \approx \frac{GM_{\rm h}}{R_{\rm int}} \tag{1.29}$$

where $v_{\rm sc} \approx (GM_{\rm h}/R_{\rm int})^{1/2}$ is the velocity at the shock location and ψ denotes the collision angle, that is the angle between the velocity vectors of the two colliding stream elements (Dai et al. 2015; Bonnerot et al. 2017b). The approximate equality uses the fact that $\sin(\psi/2) \approx 1$ since the two colliding elements typically move in roughly opposite directions (see Fig. 1.4). Due to the low value of the precession angle $\phi \approx 3\pi R_{\rm g}/R_{\rm p} = 10^\circ \beta(M_{\rm h}/10^6\,{\rm M}_\odot)^{2/3}$, the intersection radius is generally close to the semi-major axis of the most bound debris with $R_{\rm int} \approx a_{\rm min}$. This results in $\Delta\epsilon_{\rm sc}/\Delta\epsilon_{\rm circ} \approx R_{\rm p}/a_{\rm min} \approx 10^{-2}$ for $M_{\rm h} = 10^6\,{\rm M}_\odot$ and $\beta = 1$, which implies that self-crossing shocks cannot completely circularize the debris either. However, the precession angle increases by a factor a few for $M_{\rm h} \geq 10^7\,{\rm M}_\odot$ or $\beta \geq 5$ which is sufficient to decrease the intersection radius to $R_{\rm int} \approx R_{\rm p}$. Complete circularization can therefore be achieved in these more extreme conditions. The above analysis demonstrates that self-crossing shocks represent a more efficient dissipation process than the nozzle shock for black holes masses $M_{\rm h} \approx 10^6\,{\rm M}_\odot$. However, neither of the two dissipation mechanisms are in general able to fully circularize the debris on a dynamical time, as was assumed in the initial model. Complete circularization can still in principle be obtained, but only after several revolutions around the black hole.

The disc formation process is also likely to be affected by the black hole spin. The above estimate for the energy dissipation through self-crossing shocks assumes that only relativistic apsidal precession affects the stream trajectory. In this case, stream self-intersection is unavoidable since all the debris has the same orbital plane. However, the black hole spin induces an additional precession that modifies the gas orbital plane as it passes at pericentre. This nodal precession could therefore prevent the formation of self-crossing shocks with one part of the stream passing above the other. This effect can be estimated by comparing the stream width and the vertical offset induced by nodal precession at the intersection radius. After pericentre passage, the stream width is determined by tidal forces such that $H \propto R$ as explained in Section 1.4.4. Its width as the intersection point is therefore $H_{\rm int} \approx (R_{\rm int}/R_{\rm p})\,R_\star$. The ratio of width to vertical offset is therefore

$$\frac{\Delta z}{H_{\rm int}} \approx \frac{R_{\rm int}\Omega}{H_{\rm int}} = \beta^{1/2} a \sin i \left(\frac{M_{\rm h}}{10^6\,{\rm M}_\odot}\right)^{4/3}, \tag{1.30}$$

where $\Omega \approx 4\pi\, 2^{-3/2} a \sin i\, (R_\mathrm{g}/R_\mathrm{p})^{3/2} \approx 1^\circ \beta^{3/2}\, a \sin i\, (M_\mathrm{h}/10^6\,\mathrm{M}_\odot)$ is used to estimate the nodal precession angle with a denoting the black hole spin parameter and i the angle between the gas and black hole angular momenta (Guillochon & Ramirez-Ruiz 2015; Jiang et al. 2016b). This demonstrates that self-crossing is expected to be prevented for $M_\mathrm{h} \gtrsim 10^6\,\mathrm{M}_\odot$ and $\beta \gtrsim 1$ if the black hole is maximally spinning and the gas has an angular momentum orthogonal to that of the black hole, that is $a = 1$ and $i = 90^\circ$.

The last main major obstacle to complete circularization relates to the fact that radiative cooling is likely inefficient during the disc formation process. As a result, the heat injected, for example by the shocks discussed above, mostly remains trapped in the gas rather than being radiated away. This can be seen by computing the diffusion time out of the gas stream $t_\mathrm{dif} = H\tau/c$, where H represents the stream width and $\tau = \kappa_\mathrm{T}\rho H$ denotes the optical depth with $\kappa_\mathrm{T} = 0.4\,\mathrm{cm}^2\mathrm{g}^{-1}$ being the opacity to Thomson scattering. Using mass conservation, the density of a cylindrical stream element is $\rho \approx \dot{M}_\mathrm{p}/(\pi H^2 v_\mathrm{sh})$. The stream velocity is $v_\mathrm{sh} \approx R_\mathrm{p}/t_\mathrm{dyn}$, setting the lengthscale of the heat injection region to $\sim R_\mathrm{p}$. The ratio of diffusion to dynamical timescale is therefore

$$\frac{t_\mathrm{dif}}{t_\mathrm{dyn}} \approx \frac{\dot{M}_\mathrm{p}\kappa_\mathrm{T}}{\pi R_\mathrm{p} c} = 30\beta \left(\frac{M_\mathrm{h}}{10^6\,\mathrm{M}_\odot}\right)^{-5/6}, \tag{1.31}$$

which demonstrates that gas cooling is generally slow (Metzger & Stone 2016; Bonnerot et al. 2017b). As a result, the most likely consequence of energy dissipation is an expansion of the gas distribution at roughly constant total energy. In fact, this expansion is even likely to result in outflows with a significant amount of unbound matter. This can be anticipated by equating the energy $f\Delta\epsilon_\mathrm{circ}$ dissipated to circularize a fraction f of the infalling gas to the initial energy $\Delta\epsilon$ of the debris (equation (1.14)), which yields $f = \Delta\epsilon/\Delta\epsilon_\mathrm{circ} \approx \beta^{-1}(M_\mathrm{h}/M_\star)^{-1/3} \approx 10^{-2}$. This means that the circularization of $\sim 1\%$ of the debris dissipates enough energy to unbind all the rest. Accretion energy can lead to the same outcome with an even smaller fraction of accreted matter.

The disc formation process has been the subject of several recent investigations that confirm the above qualitative estimates. It is important to notice that the elongated geometry of the stream for the standard values of the parameters $M_\mathrm{h} = 10^6\,\mathrm{M}_\odot$ and $\beta = 1$ implies a huge computational cost that makes a simulation unfeasible for this set of parameters (Ayal et al. 2000). As a result, all hydrodynamical simulations of disc formation have so far been made in simplified cases where the stream length is artificially reduced. This can be achieved either by decreasing the black hole mass to $M_\mathrm{h} \approx 10^3\,\mathrm{M}_\odot$ (Ramirez-Ruiz & Rosswog 2009; Rosswog et al. 2009; Guillochon et al. 2014; Shiokawa et al. 2015) or by setting the star on a bound orbit instead of a parabolic one (Hayasaki et al. 2013; Bonnerot et al. 2016a; Hayasaki et al. 2016). It is nevertheless possible to use these simulations to get insight into the disc formation process in the standard case. The results of these studies confirm that self-crossing is in general the most efficient dissipation mechanism available although simulations with artificially low black hole masses find that the nozzle shock might also affect the gas dynamics (Ramirez-Ruiz & Rosswog 2009; Rosswog et al. 2009; Guillochon et al. 2014; Shiokawa et al. 2015). When radiative cooling is artificially fastened by keeping fixed the thermal energy, complete circularization is found to require tens of orbital times for $\beta \approx 1$ but can happen in a dynamical timescale if $\beta \gtrsim 5$ for a non-rotating $10^6\,\mathrm{M}_\odot$ black hole (Hayasaki et al. 2013; Bonnerot et al. 2016a). In the more realistic case of an inefficient radiative cooling (equation (1.31)), simulations find the formation of a puffed-up disc extending out to distances $\sim a_\mathrm{min}$ within which the gas trajectories remain highly eccentric (Ramirez-Ruiz & Rosswog 2009; Rosswog et al. 2009; Guillochon et al. 2014; Shiokawa et al. 2015; Bonnerot et al. 2016a; Hayasaki et al. 2016; Sadowski et al. 2016). The formation of such a thick structure is confirmed by local radiative transfer simulations focusing on the self-crossing shock region (Kim et al. 1999; Jiang et al. 2016b), which find that less than 10% of the thermal energy injected by shocks is radiated at the shock location while the majority is converted back into expansion kinetic energy. Additionally, they infer that up to $\sim$ 10% of the matter can be unbound during the collision (Jiang et al. 2016b). Finally, calculations taking into account the black hole spin find that the occurrence of the self-crossing shock can be delayed, although an intersection may eventually occur closer to the black hole leading to more dissipation (Dai et al. 2013; Guillochon & Ramirez-Ruiz 2015; Hayasaki et al. 2016).

Different sources of emission have been proposed related to the disc formation process or associated phenomena, whose main motivation is to explain the origin of the low energy optical/UV emission detected from certain TDEs as mentioned in Section 1.3. The most recent emission models have been motivated by the simulations presented above. The first class of models constitutes a generalization of the initial one by Rees (1988) taking into account outflows of matter. Due to the initial super-Eddington fallback rate (equation (1.25)), radiation pressure-driven winds are launched from the disc outer radius. As a result, part of the infalling matter is ejected in an outflow with a photosphere expanding to $R_{\rm ph} \approx 100\,R_{\rm p}$. As can be seen from equation (1.27), this increased photospheric radius decreases the effective temperature of the emission to $\sim 10^4$ K which is consistent with optical TDEs (Strubbe & Quataert 2009; Lodato & Rossi 2011). However, the peak luminosity is somewhat lower than that inferred from observations, especially for large black hole masses where the fallback rate becomes only marginally super-Eddington. Additionally, the outflow is found to become rapidly optically thin with an associated recession of the photosphere to the disc outer radius resulting in a sharp decrease of the optical luminosity inconsistent with observations. In a variant of this model, the optical emission originates instead from line-driven winds which are expected if some metals are present in the stellar matter. These winds induce a decrease of the disc maximal temperature which become luminous in the optical band (Miller 2015). They are also able to strongly weaken the dependence of the temperature on the external mass injection rate. This provides an explanation for the constant effective temperatures detected from optical TDEs as explained in Section 1.3.

Alternatively, other authors argued that the optical light detected from TDEs originates from the reprocessing of the high-energy accretion luminosity by a surrounding envelope formed from the debris and located at a distance of $\sim 100\,R_{\rm p}$ (Loeb & Ulmer 1997; Guillochon et al. 2014; Coughlin & Begelman 2014; Metzger & Stone 2016). The exact origin of this reprocessing layer is not yet clear. However, it is a natural consequence of the gas expansion occurring during the disc formation process and early debris accretion which is expected from the above analytical estimates and confirmed by numerical studies. The most complete model so far has been built by Metzger & Stone (2016) who assume that the surrounding envelope is formed from most of the stellar matter. Under this assumption, they find that reprocessing from this envelope can produce optical luminosities consistent with observations. In addition, since the reprocessing material absorbs the X-ray accretion luminosity at early times, this model naturally explains the optical/X-ray TDE dichotomy discussed in Section 1.3. Another advantage of the reprocessing layer model is that it can also account for the large helium to hydrogen line ratio detected for most optical TDEs through an optical depth effect (Guillochon et al. 2014; Roth et al. 2016). A similar idea has been proposed where the unbound debris acts as the reprocessing material (Bogdanović et al. 2004; Strubbe & Quataert 2009). However, the associated optical luminosity is likely lower than the above mechanism due to the thin geometry of the debris.

The last class of models puts forward shocks as the main optical emission source (Lodato 2012; Piran et al. 2015b). As indicated by numerical simulations, most of the gas is located at distances $\sim a_{\rm min}$ following disc formation. This implies that the energy dissipated by shocks is similar to that given by equation (1.29) with $R_{\rm int} \approx a_{\rm min}$. The associated peak luminosity is then determined by

$$L_{\rm sh} \approx \dot{M}_{\rm p} \Delta\epsilon_{\rm sc} \approx 7 \times 10^{43}\,{\rm erg\,s^{-1}} \left(\frac{\rm M_h}{10^6\,{\rm M_\odot}}\right)^{-1/6} \tag{1.32}$$

which leads to a temperature

$$T_{\rm sh} = \left(\frac{L_{\rm sh}}{4\pi R_{\rm ph}^2 \sigma_{\rm SB}}\right)^{1/4} = 3 \times 10^4\,{\rm K} \left(\frac{\rm M_h}{10^6\,{\rm M_\odot}}\right)^{-3/8} \tag{1.33}$$

assuming that radiation emerges from a photosphere located at $R_{\rm ph} \approx a_{\rm min}$ from the black hole (Piran et al. 2015b). This effective temperature is consistent with that of optical TDEs. In addition, the shock luminosity emitted when freshly returning material joins the newly-formed disc is expected to scale as $\dot{M}_{\rm fb} \propto t^{-5/3}$ as found observationally. To account for the absence of X-ray emission, the authors propose that magnetic stresses acting on the gas within an elliptical accretion disc are able to make a large fraction of it plunge inside the event horizon without emitting any accretion luminosity (Svirski et al. 2017). However, strong self-crossing shocks taking place during this process when the gas passes very close to the gravitational radius are likely to result in at least some X-ray emission (Bonnerot et al. 2017b). Alternatively, self-crossing shocks can scatter a fraction of the debris towards the black hole leading to an X-ray signal when this mass accretes. This mechanism could explain the X-ray emission from the TDE candidate ASASSN-14li (Krolik et al. 2016) and is favoured by the fact that this high-energy emission appears to lag behind the optical/UV signal (Pasham et al. 2017).

The process of viscous accretion is also likely to significantly differ from that assumed in the initial model. Under the action of viscosity, the disc of gas formed from the debris continuously spreads radially due to angular momentum redistribution (Pringle 1981). While the matter moving inward gets accreted onto the black hole, the outer radius of the spreading disc $R_{\rm out}$ increases such that its viscous timescale remains similar to the current time, that is $t_{\rm visc} \approx R_{\rm out}^2/\nu \approx t$. The outer radius therefore increases as $R_{\rm out} \propto t^{2/3}$ using the fact that viscosity scales with distance as $\nu \propto R^{1/2}$ in a thick disc relevant to TDEs.[6] Angular momentum conservation then implies that the disc mass follows $M_{\rm d} \propto R_{\rm out}^{-1/2} \propto t^{-1/3}$ and the mass accretion rate therefore decays as $\dot{M}_{\rm acc} \propto M_{\rm d}/t \propto t^{-4/3}$ (Cannizzo & Gehrels 2009; Shen & Matzner 2014). The accretion rate due to viscous spreading therefore decays slightly shallower than the fallback rate. This regime of accretion could dominate at late times when the disc becomes thinner with a longer viscous timescale. This transition may explain the change in slope seen in the X-ray lightcurve of *Swift* J1644+57 (Cannizzo et al. 2011). As realized more recently, matter is present at distances from the black hole larger than the pericentre distance following disc formation. As can be seen from equation (1.24) by setting $R_{\rm d} \approx 100\,R_{\rm p}$, the viscous timescale at this location becomes similar to the fallback time, that is $t_{\rm visc} \approx t_{\rm min}$. This means that matter accumulates around the black hole rather than being rapidly accreted implying that the early accretion could be set by viscous processes rather than the debris fallback (Guillochon & Ramirez-Ruiz 2015). This mechanism has been proposed to account for the slowly decaying lightcurve of the TDE candidate SDSS J150052.07+015453.8 (Lin et al. 2017).

Finally, the black hole spin also has an effect on the accretion disc formed from a TDE. If the disc and black hole angular momentum differ, torques are exerted on the disc due to nodal

---

[6] Making use of the standard viscosity parametrization (Shakura & Sunyaev 1973), the viscosity can be written $\nu = \alpha c_{\rm s} H$. In a thick disc, $H \approx R$ which implies $c_{\rm s} \approx v_{\rm K}$ imposing hydrostatic equilibrium in the vertical direction, where $v_{\rm K} \propto R^{-1/2}$ is the Keplerian circular velocity. This indicates that the viscosity evolves with radius as $\nu \propto R^{1/2}$.

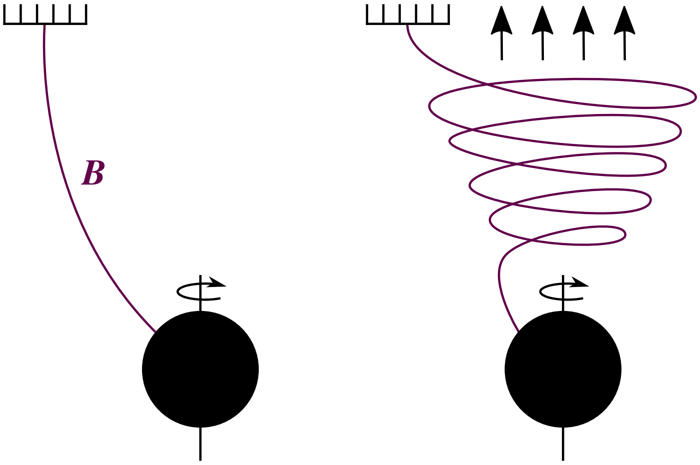

Figure 1.5: Cartoon illustrating the Blandford-Znajek process. Initially (left panel), a magnetic field line (purple line) is attached to the black hole on one side and anchored into the ambient medium on the other. Due to the black hole rotation (right panel), the field line gets tangled, producing a magnetic pressure gradient that pushes any plasma present along the rotational axis into an outflow (black arrows).

precession. Due to the strong radial dependence of the precession rate, these torques tend to create local deformations inside the disc. In the thick disc formed from the debris, these internal stresses are quickly communicated to the neighbouring regions through sound waves. As a result the disc precesses globally like a rigid body around the direction of the black hole spin (Stone & Loeb 2012a; Shen & Matzner 2014; Franchini et al. 2016).

1.4.7 Formation of relativistic jets

Once an accretion disc has formed around the black hole, it is possible that a relativistic jet forms in its inner region. We now discuss this phase of evolution which is supported by the detection of a few TDE candidates with evidence of jet launching.

The first characteristics of jetted TDEs is a beamed X-ray emission that is thought to originate from internal shocks at the base of the jet where shells of accelerated plasma can move at different velocities (Wang & Cheng 2012; De Colle et al. 2012; Crumley et al. 2016). Additionally, particles can be accelerated within these shocks, possibly producing ultra-high energy cosmic rays (Farrar & Piran 2014) as well as high-energy neutrinos (Wang & Liu 2016). One of the mysteries associated with jetted TDEs is the origin of the jet power, which can be magnetic or radiative. In the first option, the jet is powered magnetically via the Blandford-Znajek mechanism (Blandford & Znajek 1977), for which the energy of the jet is extracted from the black hole rotation. This mechanism operates as illustrated in Fig. 1.5. Consider a field line extending from the black hole to much further away in the gaseous environment. One extremity of the field line is attached to the black hole while the other is anchored in the ambient medium. As a result, the black hole rotation leads to the formation of a spring made of magnetic field loops. The accumulation of these field lines causes the formation of a magnetic pressure gradient that ejects any plasma present in this region at high velocities when the lines unwind (Tchekhovskoy 2015). The jet power can be be obtained from a simple dimensional argument by the product of magnetic pressure by the area of the event horizon multiplied by the speed of light, that is $P_{\rm jet} \approx a^2 B^2 R_{\rm g}^2 c = a^2 \Phi^2 c / R_{\rm g}^2$ where B and Φ denote the magnetic field strength and flux through the event horizon, respectively. The spin parameter a also appears in this equation since the jet power originates from the black hole rotation. Using this formula, we can now estimate the magnetic field flux required[7] to produce the jet detected from the TDE candidate *Swift* J1644+57. In this event, the jet power is likely of order $\sim 10^{47}\,\mathrm{erg\,s^{-1}}$ such that it can be converted into a peak X-ray luminosity in excess of $10^{48}\,\mathrm{erg\,s^{-1}}$. This corresponds to a required magnetic flux

$$\Phi \approx 3\times 10^{29}\,\mathrm{G\,cm^2\,a^{-1}}\left(\frac{\mathrm{M_h}}{10^6\,\mathrm{M_\odot}}\right)\left(\frac{\mathrm{P_{jet}}}{10^{47}\,\mathrm{erg\,s^{-1}}}\right)^{1/2}. \qquad (1.34)$$

This magnetic origin is supported by the fact that, if this magnetic field flux is present in the vicinity of the black hole, the magnetic pressure is large enough to balance the ram pressure of the infalling gas such that the jet power scales as $P_{\rm jet} \propto \dot{M}_{\rm fb}$. This provides an explanation for the $t^{-5/3}$ decay of the X-ray lightcurve of *Swift* J1644+57 (Tchekhovskoy et al. 2014). One important issue, however, is that the magnetic field flux of a strongly magnetized star is $\Phi_\star \approx B_\star R_\star^2 = 5\times 10^{24}\,\mathrm{G\,cm^2(B_\star/kG)(R_\star/\,R_\odot)^2}$ which is orders of magnitude too low to account for the jet power inferred from the X-ray emission as can be seen by comparing to equation (1.34). Several mechanisms exist to increase the magnetic flux to the required value such as a dynamo process happening within the accretion disc (Krolik & Piran 2012) and the capture of magnetic field flux by the debris stream from a pre-existing magnetized accretion disc (Kelley et al. 2014). Strongly magnetized stellar matter is also expected if the disrupted star is the remnant of a recent binary merger (Bradnick et al. 2017) or has experienced a previous partial disruption that amplified the magnetic fields of the surviving core (Guillochon & McCourt 2017; Bonnerot et al. 2017a). Alternatively, the jet power could have a radiative origin. The thick disc expected to form during a TDE features funnels of low density along which matter can be accelerated by radiation pressure. This mechanism does not require a strong magnetic flux as the previous one. However, magnetohydrodynamical simulations find that the outflow velocities reached are at most $\sim 0.3c$, too low compared to the values inferred for *Swift* J1644+57 (Jiang et al. 2014; Sadowski & Narayan 2015).

Other features present in the X-ray lightcurve of *Swift* J1644+57 include an initial fast variability in the first $\sim$ 10 days and a sudden decrease in flux at $\sim$ 500 days. The initial variability could be due to a variation in the shock luminosity produced by internal shocks (De Colle et al. 2012). Another possibility is that the jet precesses initially due to the disc rigid precession described in Section 1.4.6 assuming that the jet follows the disc angular momentum (Stone & Loeb 2012a; Lei et al. 2013; Franchini et al. 2016). A last option proposed by Coughlin & Nixon (2015) is that this variability is caused by the accretion of self-gravitating clumps formed within the stream during its evolution around the black hole as described in Section 1.4.4. The sharp decrease in the X-ray flux at late times could be due to the dissolution of the least dense part of the stream into the surrounding medium by Kelvin-Helmholtz instabilities (Bonnerot et al. 2016b; Kathirgamaraju et al. 2017). A change in the disc accretion regime could also account for this feature since a decreased accretion rate induces the formation of a thin disc that does not present the funnels necessary to collimate the jet and within which the field lines cannot reach the black hole vicinity because magnetic diffusion is faster than viscous accretion (Tchekhovskoy et al. 2014; Shen & Matzner 2014).

At larger distances from the black hole, the jet interacts with the gaseous environment causing the formation of shocks within which electrons are accelerated and produce radio synchrotron radiation (Giannios & Metzger 2011). The radio lightcurve from *Swift* J1644+57 also presents an unexpected behaviour that needs to be explained. The X-ray luminosity originating from the jet starts decreasing after $\sim$ 10 days. If the radio emission is due to the jet interaction with the surrounding environment, one would expect the radio lightcurve to decrease as well. Instead, it keeps increasing for a few months. Different explanations for this radio-rebrightening have been proposed. It could be due to a time delay between the turn off of the jet occurring in the black hole vicinity and the end of energy injection into the distant surrounding medium (De Colle et al. 2012). Alternatively, Kumar et al. (2013) argues that the plateau in the radio lightcurve is in fact due to an initial reduction of the radio luminosity due to inverse-Compton cooling of the shocked ambient medium by X-ray photons emitted from the base of the jet. Finally, this feature could be explained if the jet is made of two components with a fast inner core surrounding by a slower sheath. The slow sheath arrives later into the ambient medium causing a delayed energy injection (Mimica et al. 2015).

---

[7] The magnetic field flux is the relevant physical quantity to evaluate since its value through a surface following the fluid is independent of time in ideal magnetohydrodynamics.

1.4.8 Related events

The previous sections mostly focus on the standard TDE scenario involving a solar-type star disrupted by a single black hole. Other types of events exist that are related to this standard setup but differ in a few ways. Such events can for example involve a star in a different evolutionary stage as well as a binary star or black hole.

The first possibility is that the star is not in the main sequence phase, but is instead a white dwarf or red giant. As can be seen from equation (1.13), white dwarfs have a Hills mass of $M_\mathrm{H} \approx 10^5\,\mathrm{M}_\odot$ meaning that their disruption must involve intermediate-mass black holes to be detectable. Equation (1.20) also shows that the typical TDE timescale is shortened to a few hours for the disruption of white dwarfs. Long-lasting γ-ray bursts (e.g. Levan 2015) have been proposed to result from this type of event (MacLeod et al. 2014) as well as other types of high-energy transients with unknown origin (Shcherbakov et al. 2013; Jonker et al. 2013). As pointed out in Section 1.4.3, a deep white dwarf disruption results in a strong compression at pericentre that can lead to explosive thermonuclear reactions. Simulations taking into account the energy injection via nuclear reactions found that it could cause more than half of the debris to become unbound post-disruption and induce the formation of heavy elements (Rosswog et al. 2008, 2009; Haas et al. 2012; Tanikawa et al. 2017). The later radioactive decay of these elements could power an optical transient due to the reprocessing of the emitted $\gamma-$rays by the unbound debris. This signal would look like that of a type Ia supernova except for some characteristic features, such as a strong viewing-angle dependence associated with the elongated geometry of the debris (MacLeod et al. 2016). A new type of calcium-rich supernovae (Kasliwal et al. 2012) could be accounted for by this mechanism (Sell et al. 2015).

Looking at equations (1.13) and (1.20) shows that red giants can be disrupted by virtually any black hole in an event that can last for decades, that is significantly longer than a standard TDE. This duration enables to study the initial rise of the lightcurve to its peak. Such disruptions are also likely to be partial due to the structure of red giants that contain a tenuous envelope more easily affected by tidal forces than the denser core (MacLeod et al. 2012). Accordingly, the giant star could pass several times around the black hole losing a fraction of its mass at each encounter (MacLeod et al. 2014). This mechanism can possibly explain the origin of the three outbursts detected from the IC 3599 galaxy (Campana et al. 2015) as proposed by Mainetti et al. (2015), although an accretion disc instability is another likely origin. The absence of hydrogen lines in the spectrum of the TDE candidate PS1-10jh (Gezari et al. 2012) has also been explained by the disruption of a red giant previously stripped from its envelope (Bogdanović et al. 2014; Strubbe & Murray 2015) although the discovery of more TDEs with the same feature tends to favour the alternative mechanism involving an optical effect in the reprocessing layer (Guillochon et al. 2014; Roth et al. 2016).

The possibility of a TDE involving a binary star has been proposed by Mandel & Levin

(2015). In their picture, the two components of the binary are separated and then sequentially disrupted on the same trajectory. To avoid a situation where the binary is only separated without a subsequent disruption of the components, this mechanism requires that the binary star experiences a large change of angular momentum as expected in the full loss cone regime discussed in Section 1.4.2. The signal associated to this double disruption is expected to resemble that of two independent TDEs separated by a short time delay (Mainetti et al. 2016). Some TDE candidates, such as ASASSN-15lh (Leloudas et al. 2016; Margutti et al. 2017), show evidence of a secondary peak in their lightcurve which could be explained by this mechanism. It is also possible that a TDE involves a binary black hole instead of a single one. Hydrodynamical calculations show that the presence of the secondary black hole affects the stream of debris leading to a fallback rate more variable than for a TDE involving a single black hole (Ricarte et al. 2016; Coughlin et al. 2017). The large dips in the X-ray lightcurve of SDSS J120136.02+300305.5 (Saxton et al. 2012b) have been attributed to the presence of a secondary black hole (Liu et al. 2014), which could represent the first detection of a binary SMBH in a quiescent galaxy. The secondary peak in the lightcurve of ASASSN-15lh could also have a similar origin (Coughlin & Armitage 2017).

1.5 Future prospects

The field of stellar tidal disruptions has been rapidly evolving in the last few years. Recent multi-wavelength observations of TDE candidates allowed us to significantly improve our understanding of these events. Theoretical models now account for these new observational constraints more satisfyingly. Although major advances have been made, numerous puzzles remain to be solved such as the preference of optical TDEs for the rare E+A galaxies and the discrepancy between the disruption rates derived theoretically and observationally. Furthermore, there is still no definite consensus on the precise dynamics of TDEs and the origin of radiation in each energy band. For instance, several competing models exist regarding the origin of the low-energy emission detected from optical TDEs and the outcome of the disc formation process is still debated. An intense theoretical effort is therefore required to keep improving the modelling of these events.

At the same time, more observational data will soon become available from wide-field optical surveys like Pan-STARRS, ZTF as well as the *Gaia* mission. In the future, the TDE sample will also be significantly expanded with hundreds to thousands of more discoveries thanks to new surveys such as LSST in the optical (van Velzen et al. 2011) and eROSITA in the X-ray (Khabibullin et al. 2013). In particular, numerous detections of jetted TDEs will be possible by combining radio and X-ray observations with SKA and ATHENA (Donnarumma & Rossi 2015). These candidates will put strong constraints on theoretical models. Once the dynamics and emission from TDEs is completely understood, these events will become powerful probes of the majority of black holes and the various physical processes occurring in their vicinity. For example, a large sample of jetted TDEs could be used to get insight into the radio-loud/radio-quiet dichotomy of AGN. Once a systematic estimate of the black hole mass and spin from the detected signal can be achieved, such measurements will provide strong insight into pieces currently missing from cosmological models, such as the origin of SMBH seeds in the early universe and the dominant mode of accretion onto these compact objects.

1.6 Thesis summary

The next four chapters of this thesis contain original research works that aim at improving the understanding of the dynamics and associated emission from TDEs using a combination of analytical and numerical tools. A central goal of this thesis, treated in the next two chapters, is to shed light on the disc formation process from the debris stream, about which little was known a few years ago. The following two chapters are instead relevant to other phases of the tidal disruption process, from the passage of the star at pericentre to the formation of relativistic jets.

In **Chapter 2**, we numerically investigate the disc formation process from the debris stream falling back towards the black hole. The study is restricted to stars on initially eccentric orbits for computational tractability and takes into account relativistic effects relevant to a Schwarzschild black hole. Disc formation is driven by stream self-crossings induced by relativistic apsidal precession. This relativistic effect is stronger for deep tidal disruptions resulting in a faster disc formation, taking place in a few revolutions of the debris around the black hole. Relativistic precession is instead weaker for grazing encounters where disc formation requires at least ten orbital periods. The structure of the resulting disc is set by the gas cooling efficiency, varying from a thin ring close to the black hole for an efficient cooling to a thick and extended torus if cooling is inefficient.

Chapter 3 studies the disc formation process for the physically-motivated case of a parabolic stellar orbit around a non-rotating black hole. It makes use of a simplified semi-analytical model that takes into account both self-crossing shocks and viscosity induced by magnetic stresses. If the thermal energy excess imparted by shocks is rapidly radiated away, the stellar debris can completely circularize on a timescale that becomes shorter for deeper encounters and/or more efficient magnetic stresses. For large magnetic stress efficiencies, ballistic accretion of the stream occurring before complete circularization is also a possibility. If the thermal energy is trapped in the gas, the stream evolves into a thick structure or even an envelope that completely engulfs the black hole.

Chapter 4 examines the impact of the gaseous environment of quiescent galaxies on the evolution of the stream of stellar debris around the black hole. Using a semi-analytical model, we demonstrate that the Kelvin-Helmholtz instability can affect a significant fraction of the stellar matter before it is able to come back to the black hole. This effect is particularly strong for the disruption of red giants which produce low-density streams that are more sensitive to the instability. For this type of events, the majority of the debris could be prevented from fuelling the black hole resulting in a corresponding flare much dimmer than previously thought.

The evolution of the stellar magnetic field during the disruption of the star is examined in **Chapter 5** through numerical simulations. Following the disruption, the magnetic field lines align with the stream stretching direction resulting in an increase of the magnetic energy of the gas. For strongly-magnetized stars, the associated magnetic pressure can overcome gas pressure from a few days after disruption likely leading to a thickening of the stream at later times. For partial disruptions, the magnetic field lines get tangled within the surviving self-gravitating core. We find evidence of an associated dynamo process which increases the magnetic field strength by a factor of about 10. This process could be involved in the transport of the magnetic flux required to launch relativistic jets in the TDE candidate *Swift* J1644+57.

Bibliography

Alexander K. D., Berger E., Guillochon J., Zauderer B. A., Williams P. K. G., 2016, ApJ, 819, L25

Arcavi I., et al., 2014, ApJ, 793, 38

Auchettl K., Ramirez-Ruiz E., Guillochon J., 2017a, preprint (arXiv:1703.06141)

Auchettl K., Guillochon J., Ramirez-Ruiz E., 2017b, ApJ, 838, 149

Ayal S., Livio M., Piran T., 2000, ApJ, 545, 772

Bade N., Komossa S., Dahlem M., 1996, A&A, 309, L35

Balbus S. A., Hawley J. F., 1991, ApJ, 376, 214

Bar-Or B., Alexander T., 2016, ApJ, 820, 129

Berger E., Zauderer A., Pooley G. G., Soderberg A. M., Sari R., Brunthaler A., Bietenholz M. F., 2012, ApJ, 748, 36

Bicknell G. V., Gingold R. A., 1983, ApJ, 273, 749

Blandford R. D., Znajek R. L., 1977, MNRAS, 179, 433

Bloom J. S., et al., 2011, Science, 333, 203

Bogdanović T., Eracleous M., Mahadevan S., Sigurdsson S., Laguna P., 2004, ApJ, 610, 707

Bogdanović T., Cheng R. M., Amaro-Seoane P., 2014, ApJ, 788, 99

Bonnerot C., Rossi E. M., Lodato G., Price D. J., 2016a, MNRAS, 455, 2253

Bonnerot C., Rossi E. M., Lodato G., 2016b, MNRAS, 458, 3324

Bonnerot C., Price D. J., Lodato G., Rossi E. M., 2017a, preprint (arXiv:1611.09853)

Bonnerot C., Rossi E. M., Lodato G., 2017b, MNRAS, 15, 1

Bradnick B., Mandel I., Levin Y., 2017, preprint (arXiv:1703.05796)

Brassart M., Luminet J. P., 2008, A&A, 481, 259

Brassart M., Luminet J.-P., 2010, A&A, 511, A80

Brockamp M., Baumgardt H., Kroupa P., 2011, MNRAS, 418, 1308

Brown G. C., Levan A. J., Stanway E. R., Tanvir N. R., Cenko S. B., Berger E., Chornock R., Cucchiaria A., 2015, MNRAS, 452, 4297

Burrows D. N., et al., 2011, Nature, 476, 421

Campana S., Mainetti D., Colpi M., Lodato G., D'Avanzo P., Evans P. A., Moretti A., 2015, A&A, 581, A17

Cannizzo J. K., Gehrels N., 2009, ApJ, 700, 1047

Cannizzo J. K., Troja E., Lodato G., 2011, ApJ, 742, 32

Cappelluti N., et al., 2009, A&A, 495, L9

Carter B., Luminet J. P., 1982, Nature, 296, 211

Carter B., Luminet J.-P., 1983, A&A, 121, 97

Carter B., Luminet J. P., 1985, MNRAS, 212, 23

Cenko S. B., et al., 2012, ApJ, 77, 1

Chen X., Madau P., Sesana A., Liu F. K., 2009, ApJ, 697, L149

Chen X., Sesana A., Madau P., Liu F. K., 2011, ApJ, 729, 13

Chen X., Gómez-Vargas G. A., Guillochon J., 2016, MNRAS, 458, 3314

Chornock R., et al., 2014, ApJ, 780, 44

Cohn H., Kulsrud R. M., 1978, ApJ, 226, 1087

Coughlin E. R., Armitage P. J., 2017, preprint (arXiv:1705.04689)

Coughlin E. R., Begelman M. C., 2014, ApJ, 781, 82

Coughlin E. R., Nixon C., 2015, ApJ, 808, L11

Coughlin E. R., Nixon C., Begelman M. C., Armitage P. J., 2016a, MNRAS, 17, 1

Coughlin E. R., Nixon C., Begelman M. C., Armitage P. J., Price D. J., 2016b, MNRAS, 455, 3612

Coughlin E. R., Armitage P. J., Nixon C., Begelman M. C., 2017, MNRAS, 465, 3840

Crumley P., Lu W., Santana R., Hernández R. A., Kumar P., Markoff S., 2016, MNRAS, 460, 396

Dai L., Escala A., Coppi P., 2013, ApJ, 775, L9

Dai L., McKinney J. C., Miller M. C., 2015, ApJ, 812, L39

De Colle F., Guillochon J., Naiman J., Ramirez-Ruiz E., 2012, ApJ, 760, 103

Donnarumma I., Rossi E. M., 2015, ApJ, 803, 36

Esquej P., Saxton R. D., Freyberg M. J., Read A. M., Altieri B., Sanchez-Portal M., Hasinger G., 2007, A&A, 462, L49

Evans C. R., Kochanek C. S., 1989, ApJ, 346, L13

Evans C., Laguna P., Eracleous M., 2015, ApJ, 805, L19

Farrar G. R., Piran T., 2014, preprint (arXiv:1411.0704)

Ferrarese L., Ford H., 2005, Space Sci. Rev., 116, 523

Ferrarese L., Merritt D., 2000, ApJ, 539, L9

Franchini A., Lodato G., Facchini S., 2016, MNRAS, 455, 1946

Frank J., Rees M. J., 1976, MNRAS, 176, 633

Frank J., King A., Raine D., 2002, Accretion Power in Astrophysics: Third Edition. Cambridge University Press, Cambridge

Freitag M., Benz W., 2002, A&A, 375, 711

French K. D., Arcavi I., Zabludoff A., 2016, ApJ, 818, L21

French K. D., Arcavi I., Zabludoff A., 2017, ApJ, 835, 176

Gafton E., Tejeda E., Guillochon J., Korobkin O., Rosswog S., 2015, MNRAS, 449, 771

Generozov A., Mimica P., Metzger B. D., Stone N. C., Giannios D., Aloy M. A., 2017, MNRAS, 464, 2481

Gezari S., et al., 2006, ApJ, 653, L25

Gezari S., et al., 2012, Nature, 485, 217

Gezari S., Chornock R., Lawrence A., Rest A., Jones D. O., Berger E., Challis P. M., Narayan G., 2015, ApJ, 815, L5

Giannios D., Metzger B. D., 2011, MNRAS, 416, 2102

Guillochon J., McCourt M., 2017, ApJ, 834, L19

Guillochon J., Ramirez-Ruiz E., 2013, ApJ, 767, 25

Guillochon J., Ramirez-Ruiz E., 2015, ApJ, 809, 166

Guillochon J., Ramirez-Ruiz E., Rosswog S., Kasen D., 2009, ApJ, 705, 844

Guillochon J., Manukian H., Ramirez-Ruiz E., 2014, ApJ, 783, 23

Guillochon J., McCourt M., Chen X., Johnson M. D., Berger E., 2016, ApJ, 822, 48

Gurzadyan V. G., Ozernoy L. M., 1979, Nature, 280, 214

Haas R., Shcherbakov R. V., Bode T., Laguna P., 2012, ApJ, 749, 117

Hamers A. S., Perets H. B., 2017, preprint (arXiv:1704.06257)

Hayasaki K., Stone N., Loeb A., 2013, MNRAS, 434, 909

Hayasaki K., Stone N., Loeb A., 2016, MNRAS, 461, 3760

Hills J. G., 1975, Nature, 254, 295

Holoien T. W. S., et al., 2016a, MNRAS, 455, 2918

Holoien T. W.-S., et al., 2016b, MNRAS, 463, 3813

Hopman C., Alexander T., 2006, ApJ, 645, 1152

Ivanov P. B., Polnarev A. G., Saha P., 2005, MNRAS, 358, 1361

Jiang Y.-F., Stone J. M., Davis S. W., 2014, ApJ, 796, 106

Jiang N., Dou L., Wang T., Yang C., Lyu J., Zhou H., 2016a, ApJ, 828, L14

Jiang Y.-F., Guillochon J., Loeb A., 2016b, ApJ, 830, 125

Jonker P. G., et al., 2013, ApJ, 779, 14

Karas V., Šubr L., 2007, A&A, 19, 11

Kasen D., Ramirez-Ruiz E., 2010, ApJ, 714, 155

Kasliwal M. M., et al., 2012, ApJ, 755, 161

Kathirgamaraju A., Duran R. B., Giannios D., 2017, preprint (arXiv:1701.07826)

Kato M., Hoshi R., 1978, Prog. Theor. Phys., 60, 1692

Kelley L. Z., Tchekhovskoy A., Narayan R., 2014, MNRAS, 445, 3919

Kesden M., 2012a, Phys. Rev. D, 85, 024037

Kesden M., 2012b, Phys. Rev. D, 86, 064026

Khabibullin I., Sazonov S., Sunyaev R., 2013, MNRAS, 437, 327

Kim S. S., Park M., Lee H. M., 1999, ApJ, 519, 647

Kobayashi S., Laguna P., Phinney E. S., Meszaros P., 2004, ApJ, 615, 855

Kochanek C. S., 1994, ApJ, 422, 508

Komossa S., Bade N., 1999, A&A, 343, 775

Komossa S., Greiner J., 1999, A&A, 349, L45

Komossa S., Merritt D., 2008, ApJ, 683, L21

Komossa S., et al., 2008, ApJ, 678, L13

Krolik J. H., Piran T., 2012, ApJ, 749, 92

Krolik J., Piran T., Svirski G., Cheng R. M., 2016, ApJ, 827, 127

Kumar P., Duran B., Bošnjak Ž., Piran T., 2013, MNRAS, 434, 3078

Lacy J. H., Townes C. H., Hollenbach D. J., 1982, ApJ, 262, 120

Laguna P., Miller W. A., Zurek W. H., Davies M. B., 1993, ApJ, 410, L83

Lei W.-H., Zhang B., Gao H., 2013, ApJ, 762, 98

Leloudas G., et al., 2016, Nat. Astron., 1, 0002

Levan A., 2015, J. High Energy Astrophys., 7, 44

Levan A. J., et al., 2011, Science, 333, 199

Li L.-X., Narayan R., Menou K., 2002, ApJ, 576, 753

Li S., Liu F. K., Berczik P., Spurzem R., 2017, ApJ, 834, 1

Lightman A., Shapiro S., 1977, ApJ, 211, 244

Lin D., et al., 2017, Nat. Astron., 1, 0033

Liu F. K., Li S., Komossa S., 2014, ApJ, 786, 103

Lodato G., 2012, EPJ Web Conf., 39, 01001

Lodato G., Rossi E. M., 2011, MNRAS, 410, 359

Lodato G., King a. R., Pringle J. E., 2009, MNRAS, 392, 332

Loeb A., Ulmer A., 1997, ApJ, 489, 573

Lu W., Kumar P., 2016, MNRAS, 458, 1071

Luminet J.-P., Barbuy B., 1990, AJ, 99, 838

Luminet J.-P., Carter B., 1986, ApJS, 61, 219

Luminet J.-P., Marck J.-a., 1985, MNRAS, 212, 57

MacLeod M., Guillochon J., Ramirez-Ruiz E., 2012, ApJ, 757, 134

MacLeod M., Goldstein J., Ramirez-Ruiz E., Guillochon J., Samsing J., 2014, ApJ, 794, 9

MacLeod M., Guillochon J., Ramirez-Ruiz E., Kasen D., Rosswog S., 2016, ApJ, 819, 3

Madigan A.-M., Hopman C., Levin Y., 2011, ApJ, 738, 99

Magorrian J., Tremaine S., 1999, MNRAS, 309, 447

Mainetti D., Campana S., Colpi M., Lodato G., D'Avanzo P., Evans P., Moretti A., 2015, preprint (arXiv:1502.07835)

Mainetti D., Lupi A., Campana S., Colpi M., 2016, MNRAS, 457, 2516

Mainetti D., Lupi A., Campana S., Colpi M., Coughlin E. R., Guillochon J., Ramirez-Ruiz E., 2017, preprint (arXiv:1702.07730)

Maksym W. P., Ulmer M. P., Eracleous M., 2010, ApJ, 722, 1035

Maksym W. P., Ulmer M. P., Eracleous M. C., Guennou L., Ho L. C., 2013, MNRAS, 435, 1904

Mandel I., Levin Y., 2015, ApJ, 805, L4

Manukian H., Guillochon J., Ramirez-Ruiz E., O'Leary R. M., 2013, ApJ, 771, L28

Margutti R., et al., 2017, ApJ, 836, 25

Merritt D., 2013, Dynamics and Evolution of Galactic Nuclei. Princeton University Press, Princeton

Merritt D., Poon M. Y., 2004, ApJ, 606, 788

Metzger B. D., Stone N. C., 2016, MNRAS, 461, 948

Miller M. C., 2015, ApJ, 805, 83

Miller J. M., et al., 2015, Nature, 526, 542

Milosavljević M., Merritt D., Ho L. C., 2006, ApJ, 652, 120

Mimica P., Giannios D., Metzger B. D., Aloy M. A., 2015, MNRAS, 450, 2824

Pasham D. R., Cenko B. S., Sadowski A., Guillochon J., Stone N. C., Van Velzen S., Gandhi P., Cannizzo J. F., 2017, ApJ, 837, L30

Perets H. B., Hopman C., Alexander T., 2007, ApJ, 656, 709

Phinney E. S., 1989, in Morris M., ed., Proc. IAU Symposium Vol. 136, The Center of the Galaxy. Kluwer, Dordrecht, p. 543

Piran T., Sądowski A., Tchekhovskoy A., 2015a, MNRAS, 453, 157

Piran T., Svirski G., Krolik J., Cheng R. M., Shiokawa H., 2015b, ApJ, 806, 164

Pringle J. E., 1981, ARA&A, 19, 137

Ramirez-Ruiz E., Rosswog S., 2009, ApJ, 697, L77

Rauch K. P., Ingalls B., 1998, MNRAS, 299, 1231

Rauch K. P., Tremaine S., 1996, New Astron., 1, 149

Rees M. J., 1988, Nature, 333, 523

Ricarte A., Natarajan P., Dai L., Coppi P., 2016, MNRAS, 458, 1712

Rosswog S., Ramirez-Ruiz E., Hix W. R., 2008, ApJ, 679, 1385

Rosswog S., Ramirez-Ruiz E., Hix W. R., 2009, ApJ, 695, 404

Roth N., Kasen D., Guillochon J., Ramirez-ruiz E., 2016, ApJ, 827, 1

Sadowski A., Narayan R., 2015, MNRAS, 453, 3213

Sadowski A., Tejeda E., Gafton E., Rosswog S., Abarca D., 2016, MNRAS, 458, 4250

Sari R., Kobayashi S., Rossi E. M., 2010, ApJ, 708, 605

Saxton C. J., Soria R., Wu K., Kuin N. P. M., 2012a, MNRAS, 422, 1625

Saxton R. D., Read A. M., Esquej P., Komossa S., Dougherty S., Rodriguez-Pascual P., Barrado D., 2012b, A&A, 541, A106

Schmidt M., 1963, Nature, 197, 1040

Sell P. H., Maccarone T. J., Kotak R., Knigge C., Sand D. J., 2015, MNRAS, 450, 4198

Shakura N. I., Sunyaev R. a., 1973, A&A, 24, 337

Shcherbakov R. V., Pe'er A., Reynolds C. S., Haas R., Bode T., Laguna P., 2013, ApJ, 769, 85

Shen R.-F., Matzner C. D., 2014, ApJ, 784, 87

Shiokawa H., Krolik J. H., Cheng R. M., Piran T., Noble S. C., 2015, ApJ, 804, 85

Stone N., Loeb A., 2011, MNRAS, 412, 75

Stone N., Loeb A., 2012a, Phys. Rev. Lett., 108, 061302

Stone N., Loeb A., 2012b, MNRAS, 422, 1933

Stone N. C., Metzger B. D., 2016, MNRAS, 455, 859

Stone N. C., van Velzen S., 2016, ApJ, 825, L14

Stone N., Sari R., Loeb A., 2013, MNRAS, 435, 1809

Stone N. C., Kuepper A. H. W., Ostriker J. P., 2016, preprint (arXiv:1606.01909)

Strubbe L. E., Murray N., 2015, MNRAS, 454, 2321

Strubbe L. E., Quataert E., 2009, MNRAS, 400, 2070

Svirski G., Piran T., Krolik J., 2017, preprint (arXiv:1508.02389)

Syer D., Ulmer A., 1999, MNRAS, 306, 35

Tanikawa A., Sato Y., Nomoto K., Maeda K., Nakasato N., Hachisu I., 2017, ApJ, 839, 81

Tchekhovskoy A., 2015, in Contopoulos I., Gabuzda D., Kylafis N., eds, Astrophysics and Space Science Library Vol. 414, The Formation and Disruption of Black Hole Jets. Springer International Publishing, Switzerland, p. 45

Tchekhovskoy A., Metzger B. D., Giannios D., Kelley L. Z., 2014, MNRAS, 437, 2744

Tejeda E., Gafton E., Rosswog S., 2017, preprint (arXiv:1701.00303)

Ulmer A., 1999, ApJ, 514, 180

Vasiliev E., Merritt D., 2013, ApJ, 774, 87

Wang F. Y., Cheng K. S., 2012, MNRAS, 421, 908

Wang X.-Y., Liu R.-Y., 2016, Phys. Rev. D, 93, 083005

Wang J., Merritt D., 2004, ApJ, 600, 149

Wegg C., Bode J. N., 2011, ApJ, 738, L8

Young P. J., Shields G. A., Wheeler J. C., 1977, ApJ, 212, 367

Zackay B., Ofek E. O., Gal-Yam A., 2016, ApJ, 830, 27

Zauderer B. A., et al., 2011, Nature, 476, 425

Zauderer B. A., Berger E., Margutti R., Pooley G. G., Sari R., Soderberg A. M., Brunthaler A., Bietenholz M. F., 2013, ApJ, 767, 152

Zhao H., Haehnelt M. G., Rees M. J., 2002, New Astron., 7, 385

Zhong S., Berczik P., Spurzem R., 2014, ApJ, 792, 137

van Velzen S., et al., 2011, ApJ, 741, 73

van Velzen S., et al., 2016a, Science, 351, 62

van Velzen S., Mendez A. J., Krolik J. H., Gorjian V., 2016b, ApJ, 829, 19

2

Disc formation from tidal disruptions of stars on eccentric orbits by Schwarzschild black holes

The potential of tidal disruption of stars to probe otherwise quiescent supermassive black holes cannot be exploited, if their dynamics is not fully understood. So far, the observational appearance of these events has been derived from analytical extrapolations of the debris dynamical properties just after disruption. By means of hydrodynamical simulations, we investigate the subsequent fallback of the stream of debris towards the black hole for stars already bound to the black hole on eccentric orbits. We demonstrate that the debris circularize due to relativistic apsidal precession which causes the stream to self-cross. The circularization timescale varies between 1 and 10 times the period of the star, being shorter for more eccentric and/or deeper encounters. This self-crossing leads to the formation of shocks that increase the thermal energy of the debris. If this thermal energy is efficiently radiated away, the debris settle in a narrow ring at the circularization radius with shock-induced luminosities of $\sim 10 - 10^3\, L_{\rm Edd}$. If instead cooling is impeded, the debris form an extended torus located between the circularization radius and the semi-major axis of the star with heating rates $\sim 1 - 10^2\, L_{\rm Edd}$. Extrapolating our results to parabolic orbits, we infer that circularization would occur via the same mechanism in ~ 1 period of the most bound debris for deeply penetrating encounters to ~ 10 for grazing ones. We also anticipate the same effect of the cooling efficiency on the structure of the disc with associated luminosities of $\sim 1 - 10\, L_{\rm Edd}$ and heating rates of $\sim 0.1 - 1\, L_{\rm Edd}$. In the latter case of inefficient cooling, we deduce a viscous timescale generally shorter than the circularization timescale. This suggests an accretion rate through the disc tracing the fallback rate, if viscosity starts acting promptly.

C. Bonnerot, E. M. Rossi, G. Lodato and D. J. Price
2016, *MNRAS*, **Volume 455**, Issue 2, p. 2253-2266

2.1 Introduction

Most galaxies have been found to contain a supermassive black hole (SMBH) at their centre orbited by stars. If one of these stars wanders within the tidal radius of the black hole, the tidal force of the black hole exceeds the star's self-gravity and the star is torn apart. Such an event is called a tidal disruption event (TDE). After the disruption, the stellar debris evolve to form an elongated stream of gas that falls back towards the black hole. In the standard picture of TDEs, these debris then circularize to form an accretion disc where they accrete viscously emitting a thermal flare mainly in the UV to soft X-ray band (Lodato & Rossi 2011). This flare could also be accompanied by a radio signal associated to a relativistic jet originating from the inner region of the disc (Giannios & Metzger 2011). A handful of candidate TDEs have been detected so far in these bands (e.g. Esquej et al. 2008; Komossa et al. 2004; Gezari et al. 2009; van Velzen et al. 2011; Zauderer et al. 2011).

TDEs are powerful tools to detect SMBHs in otherwise quiescent galaxies. Furthermore, they can in principle be used to estimate the properties of both the black hole and the disrupted star and to probe the physics of accretion and relativistic jets. In practice, deriving such constraints from observations is challenging as it requires a precise understanding of the dynamics of TDEs. The latter has been the focus of many analytical and numerical investigations undertaken since the 80s. A distinctive feature of the pioneering works by Lacy et al. (1982), Rees (1988), Evans & Kochanek (1989) and Phinney (1989) is a $t^{-5/3}$ decrease of the rate at which the stellar debris fall back towards the black hole.[1] The same slope is generally fitted to the observed TDE light curves (Esquej et al. 2008; Gezari et al. 2008, 2009; Cappelluti et al. 2009) although it is only expected in the X-ray band (Lodato & Rossi 2011). It assumes that the accretion rate, and therefore the luminosity, traces the fallback rate of the debris. In turn, this requires that the debris circularize to form a disc and that this disc is accreted faster than it is fed from the fallback stream. However, the mechanism driving the circularization is still unknown.

Various effects are likely to be involved in this process, whose common feature is to dissipate the kinetic energy of the debris, injecting a large amount of thermal energy into the newly formed disc. However, the efficiency of this energy transfer is certainly dependent on the mechanism considered. The main candidates are the following (Evans & Kochanek 1989; Kochanek 1994):

1. *Pancake shock*: As the star is disrupted, part of its material is accelerated out of the initial orbital plane. As a result, the debris inside the stream have a range of inclinations. Their orbits are therefore vertically focussed and intersect the orbital plane close to pericentre. At this point, the stream is strongly compressed, leading to the formation of a pancake shock.

2. *Self-crossing*: When they reach pericentre, the debris experience changes of their apsidal angles driven by relativistic apsidal precession or hydrodynamical effects. This can lead to the self-crossing of the stream: as the leading parts move away from the black hole after pericentre passage, they collide with the part that is still falling back, generating shocks.

3. *Shearing*: As the stream comes back to pericentre, the orbits of the debris are radially focussed due to their large range of apocentres but small range of pericentres. This effect is similar to a passage into a nozzle. The debris experience shearing at this point

---

[1] This rate was later shown to be dependent on the stellar structure (Lodato et al. 2009; Guillochon & Ramirez-Ruiz 2013).

as they have a range of apsidal angles and eccentricities induced by the disruption of the star. This effect is enhanced by relativistic apsidal precession: as they have a range of pericentre distances, the orbits of the debris precess by different angles, leading to further shearing.

If an accretion disc forms from the debris, its structure and evolution are two additional uncertainties in the models of TDEs. They depend on the relative efficiency of three processes (Evans & Kochanek 1989): circularization, viscous accretion and radiative cooling. Denoting the timescales of these processes by $t_{\rm circ}$, $t_{\rm visc}$ and $t_{\rm cool}$ respectively, three limiting regimes are to be expected. In the case $t_{\rm visc} < t_{\rm circ}$, viscosity may be important during the circularization process. If instead $t_{\rm visc} > t_{\rm circ}$, accretion begins only once a disc is formed. In this case, if $t_{\rm cool} < t_{\rm circ}$, the disc cools during its formation and is therefore geometrically thin. If instead $t_{\rm circ} < t_{\rm cool}$, the disc puffs up while it forms due to its excess of thermal energy. Many authors have assumed that the disc is geometrically thin or slim (Strubbe & Quataert 2009; Cannizzo & Gehrels 2009; Cannizzo et al. 2011; Lodato & Rossi 2011; Shen & Matzner 2014) using the standard α parametrization (Shakura & Sunyaev 1973). Other investigations considered the possibility of a geometrically thick disc (Loeb & Ulmer 1997; Coughlin & Begelman 2014).

Numerical simulations of tidal disruptions (Evans & Kochanek 1989; Lodato et al. 2009) have often used smoothed particle hydrodynamics (SPH) primarily because of its ability to deal with large regions of space devoid of gas. This technique is also well suited to simulate the subsequent fallback of the debris towards the black hole. The computational cost of such a simulation scales with the total number of SPH particles used to model the stream. To accurately follow their evolution, each part of the stream must contain enough particles. This condition is hard to fulfill for a long stream because the SPH particles are spread on a large volume. The length of the stream increases with the stellar to black hole mass ratio q and with the eccentricity e of the star. The typical values of these parameters are $q = 10^6$ and $e = 1$. This extreme value of e comes from the fact that most disrupted stars are scattered from the sphere of influence of the SMBH, which is much larger than the tidal radius (Frank & Rees 1976). For the Milky Way, the ratio of these two distances is $\sim 10^5$. However, as noted by Ayal et al. (2000), following the fallback of the debris for these typical values of q and e numerically is a computational burden. In their simulation, the leading part of the stream is composed of very few SPH particles that come back almost one by one towards the black hole. As a result, the evolution of these particles cannot be followed accurately. Even if they use a relatively low number of particles ($N = 4295$), this issue is so extreme that it is likely to persist for larger particle numbers. The high computational cost of such a simulation is not limited to SPH but generalizes to other computational techniques.

In the few other investigations of this problem, either q or e has therefore been lowered. The first option has been chosen by several authors (Ramirez-Ruiz & Rosswog 2009; Guillochon et al. 2014) who investigated $q = 10^3$ and $e = 1$. The physical motivation in this case is the tidal disruption of a star by an intermediate mass black hole. Both pancake shock and shearing were shown to be inefficient at circularizing the debris in this case. Instead, the main effect seen in these simulations is the expansion of the stream caused by its pericentre passage. Circularization is more likely driven by self-crossing either induced by this expansion or by relativistic apsidal precession. Hayasaki et al. (2013) made the second choice, as in the present paper, which corresponds to tidal disruptions of bound stars. They considered $q = 10^6$ and $e = 0.8$ and found that self-crossing driven by relativistic precession efficiently drives the circularization of the debris in this case.

Several mechanisms are able to put a star on a bound orbit entering the tidal radius of a SMBH. The first involves a unequal mass SMBH binary interacting with a surrounding stellar cusp. In this situation, bound stars can be scattered inside the tidal radius of the primary black hole through a combination of Kozai interactions and close encounters with the secondary black hole (Chen et al. 2009, 2011). The second mechanism takes place during the coalescence of a SMBH binary. Due to the anisotropic emission of gravitational waves in this phase, the remnant black hole undergoes a kick. It can lead to close encounters between the black hole and the surrounding stars leading to their tidal disruptions (Stone & Loeb 2011). Furthermore, mean-motion resonances can pull surrounding stars inwards during the final phase of the SMBH merger (Seto & Muto 2010) enhancing the rate of tidal disruptions of bound stars by this mechanism. The third mechanism takes place after the tidal separation of a stellar binary by a black hole, which places one of the components on an eccentric orbit. Due to both encounters with the other stars orbiting the SMBH and gravitational wave emission, its orbit shrinks and circularize. Under certain conditions, it can then be tidally disrupted by the SMBH on a bound orbit (Amaro-Seoane et al. 2012).

In this paper, we use SPH simulations to investigate the circularization process leading to the formation of the disc. We also characterize the structure and evolution of this disc. Relativistic apsidal precession, involved in the circularization process, is treated exactly while most previous studies (Ramirez-Ruiz & Rosswog 2009; Guillochon et al. 2014; Hayasaki et al. 2013) used an approximate treatment of this effect. The parameters that are likely to play a significant role in the circularizaton process have also been varied. Two extreme cooling efficiencies, encoded in the equation of state (EOS) of the gas, have been considered. The effect of the orbit of the star has also been examined, by varying both its penetration factor and its eccentricity. Our results demonstrate that circularization is a fast process, happening in a few orbits of the debris around the black hole, and driven mostly by relativistic apsidal precession. They also confirm the expected effect of the cooling efficiency on the structure of the resulting disc. In addition, we found different channels of circularization for different orbits of the star. In particular, by increasing its eccentricity, we got insight into the circularization process at work in the standard parabolic case.

This paper is organized as follows. In Section 2.2, we describe the SPH simulations performed. The results of these simulations are presented in Section 2.3 varying the following parameters: the gravitational potential, the EOS, the depth of the encounter and the eccentricity of the star. The effect of the resolution on these results is also examined. These results are discussed in Section 2.4 and compared to other studies by Shiokawa et al. (2015) and Hayasaki et al. (2015) that appeared at the same time as this paper.

2.2 SPH simulations

We investigate the tidal disruption of a star of mass $M_\star = 1\,\mathrm{M}_\odot$ and radius $R_\star = 1\,\mathrm{R}_\odot$ by a non-rotating black hole of mass $M_\mathrm{h} = 10^6\,\mathrm{M}_\odot$. In this configuration, the tidal radius is $R_\mathrm{t} = R_\star(M_\mathrm{h}/M_\star)^{1/3} = 100\,\mathrm{R}_\odot$. Several initial elliptical orbits of the star are considered. They have different pericentre distances R_p defined via the penetration factor $\beta = R_\mathrm{t}/R_\mathrm{p}$ by setting $\beta = 1$ and $\beta = 5$. It corresponds to pericentre distances $R_\mathrm{p} = 100\,\mathrm{R}_\odot$ and $R_\mathrm{p} = 20\,\mathrm{R}_\odot$ respectively. For $\beta = 1$, only an eccentricity $e = 0.8$ is considered. For $\beta = 5$, two different values $e = 0.8$ and $e = 0.95$ are investigated. For these orbits, all the debris produced by the disruption stay bound to the black hole. This is generally the case if $e < e_\mathrm{crit} = 1 - (2/\beta)(M_\mathrm{h}/M_\star)^{-1/3}$, where $e_\mathrm{crit} = 0.996$ and 0.98 for $\beta = 5$ and $\beta = 1$ respectively. The semi-major axis $a_\star = R_\mathrm{p}/(1-e)$ of these orbits ranges between $100\,\mathrm{R}_\odot$ and $500\,\mathrm{R}_\odot$, corresponding to orbital periods $P_\star = 2\pi\left(GM_\mathrm{h}/a_\star^3\right)^{-1/2}$ between 2.8 h and 31 h.

Both the disruption of the star and the subsequent fallback of the debris towards the disruption site are simulated using SPH. To increase efficiency, the simulations of these two phases are performed separately and make use of two different codes, each adapted to a spe-

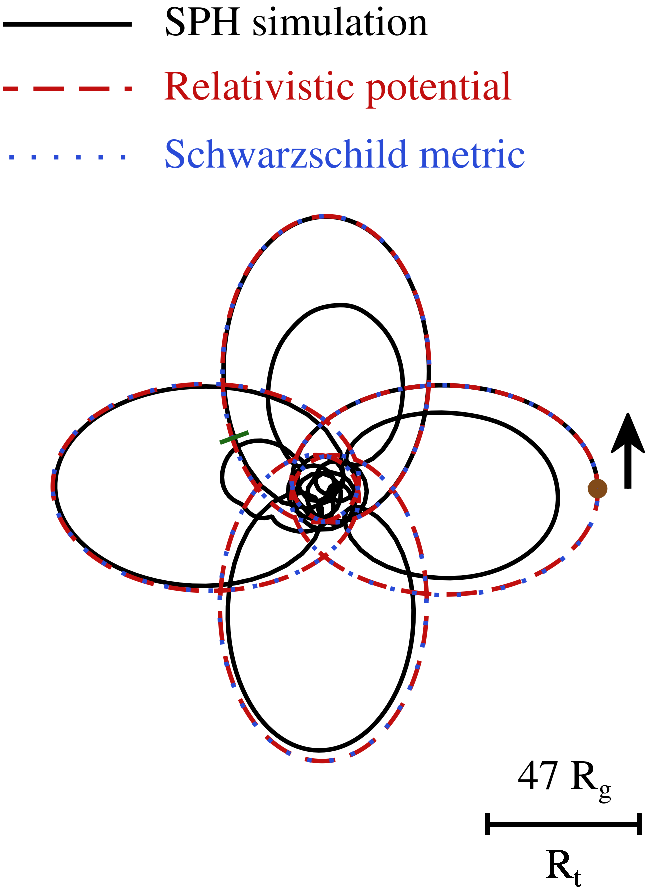

Figure 2.1: Trajectory of the centre of mass of the gas in the simulation corresponding to model RI5e.8 (black solid line) compared to that of a test particle on the same orbit in the relativistic potential (red dashed line) and in the Schwarzschild metric (blue dotted line). All the trajectories start at the initial position of the star indicated by the brown point on the right of the figure. The black arrow specifies the direction of motion. The trajectory of the test particle in the relativistic potential and in the Schwarzschild metric is followed for 4 orbits. That of the centre of mass of the gas in the simulation is followed during the disruption of the star and the fallback of the debris until $t/P_\star = 8$. The transition between the disruption and the fallback phase, treated with two different codes, is indicated by the green dash perpendicular to this trajectory. After a few pericentre passages, the motion of the gas is affected by hydrodynamical effects and the trajectory of its centre of mass differs from that of a test particle.

cific phase. For the disruption phase, we use a code that takes into account self-gravity (Bate et al. 1995). For the fallback phase, we do not consider self-gravity and make use of the highly efficient code PHANTOM (Price & Federrath 2010; Lodato & Price 2010) that is optimized for studying non-self-gravitating problems[2]. This choice is legitimate because the self-gravity force is only needed during the disruption phase where it opposes the tidal force of the black hole. In the fallback phase, the gravitational interactions between the debris is negligible compared to their hydrodynamical interactions and the tidal force of the black hole. The disruption phase is followed until the most bound debris come back to pericentre. Their properties are recorded at this point and constitute the initial conditions for the simulation of the fallback phase. As this paper's primary focus is on the fallback of the debris, the disruption phase is only simulated to get these initial conditions and not discussed in detail.

---

[2] Self-gravity is now implemented into PHANTOM. However, it was not available at the beginning of this work.

The code used for the disruption phase has already been adopted by Lodato et al. (2009) to simulate tidal disruptions of stars on parabolic orbits. In the present paper, we follow the same procedure and numerical setup but consider elliptical orbits instead. Also using the same method, we model the star as a polytropic sphere with $\gamma = 5/3$ containing 100K particles. However, as explained in subsection 2.3.4, the fallback phase is simulated at a higher resolution with the stream of debris containing 500K particles.

In order to resolve the shocks, the code used for the fallback phase, PHANTOM, includes the standard artificial viscosity prescription that depends on the parameters α^{AV} and β^{AV}. In addition, the Morris & Monaghan (1997) switch is implemented to reduce artificial dissipation away from shocks. To this end, α^{AV} is allowed to vary between two values $\alpha^{AV}_{\rm min}$ and $\alpha^{AV}_{\rm max}$ according to a source and decay equation. In this paper, we use $\alpha^{AV}_{\rm min} = 0.01$, $\alpha^{AV}_{\rm max} = 1$ and $\beta^{AV} = 2$.

The orbits considered for the star have pericentre distances comparable with the gravitational radius $R_{\rm g} = GM_{\rm h}/c^2$ of the black hole. More precisely, $R_{\rm p} = 47R_{\rm g}$ and $R_{\rm p} = 9.4R_{\rm g}$ for $\beta = 1$ and $\beta = 5$. Therefore, relativistic effects must significantly affect the motion of the gas when it passes at pericentre. One of these effects is relativistic apsidal precession, a mechanism involved in the circularization process causing the orbit of a test particle to precess at each pericentre passage by a given precession angle. For the orbits considered, the precession angle varies between 13.5 and 89.7 degrees for $\beta = 1$ and $\beta = 5$ respectively. In order to investigate the influence of relativistic effects, the black hole is modelled by an external potential that is either Keplerian or relativistic both in the disruption and the fallback phase. In the following, the variables are labelled by the letter K if they are computed in the Keplerian potential and by the letter R if they are computed in the relativistic potential. These potentials are respectively given by

$$\Phi^{\rm K} = -\frac{GM_{\rm h}}{R}, \tag{2.1}$$

$$\Phi^{\rm R} = -\frac{GM_{\rm h}}{R} - \left(\frac{2R_{\rm g}}{R-2R_{\rm g}}\right)\left[\left(\frac{R-R_{\rm g}}{R-2R_{\rm g}}\right)v_{\rm r}^2 + \frac{v_{\rm t}^2}{2}\right], \tag{2.2}$$

where $v_{\rm r}$ and $v_{\rm t}$ are the radial and tangential velocity of a test particle respectively. We adopt this relativistic potential, designed by Tejeda & Rosswog (2013), because it contains an exact treatment of apsidal precession around a non-rotating black hole. In other words, the value of the precession angle for a test particle on a given orbit is the same in this potential and in the Schwarzschild metric. This is an improvement compared to most previous investigations that used an approximate treatment of this effect (Ramirez-Ruiz & Rosswog 2009; Guillochon et al. 2014; Hayasaki et al. 2013).

For the disruption phase, the star is initially placed at the apocentre of its orbit, a distance $R_{\rm a} = (1+e)R_{\rm p}/(1-e)$ from the black hole. Its initial velocity $v_{\rm a}$ is determined by conservation of specific orbital energy and angular momentum between $R_{\rm a}$ and $R_{\rm p}$. In the Keplerian and relativistic potentials, the specific orbital energy is given by

$$\varepsilon^{\rm K} = \frac{1}{2}\left(v_{\rm r}^2 + v_{\rm t}^2\right) - \frac{GM_{\rm h}}{R}, \tag{2.3}$$

$$\varepsilon^{\rm R} = \frac{1}{2}\left[\left(\frac{R}{R-2R_{\rm g}}\right)^2 v_{\rm r}^2 + \left(\frac{R}{R-2R_{\rm g}}\right)v_{\rm t}^2\right] - \frac{GM_{\rm h}}{R}, \tag{2.4}$$

and the specific angular momentum by

$$l^{\rm K} = Rv_{\rm t}, \tag{2.5}$$

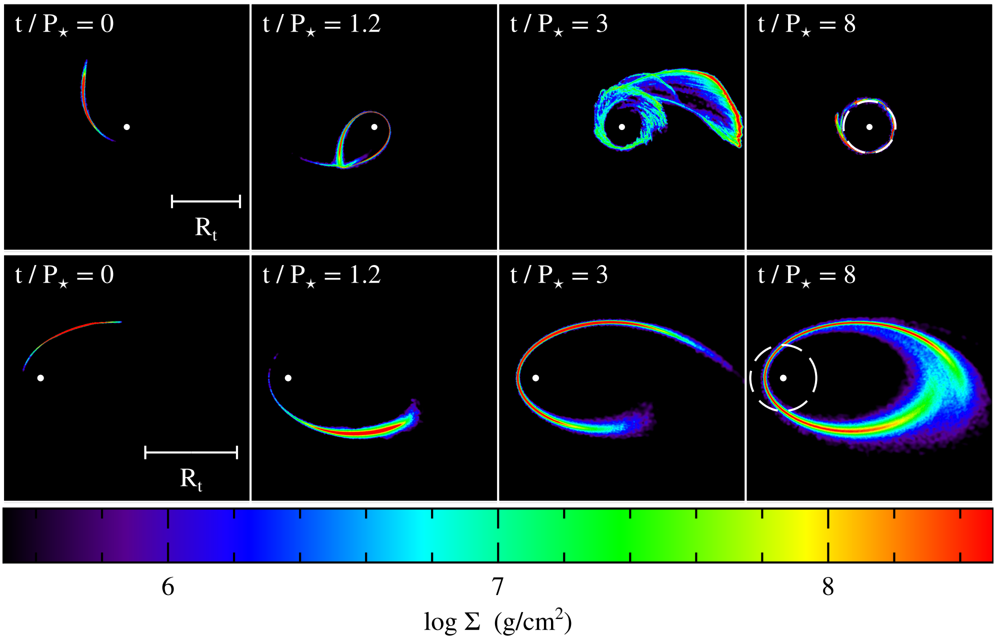

Figure 2.2: Snapshots of the fallback of the debris at different times $t/P_\star = 0, 1.2, 3$ and 8 for models RI5e.8 (upper panel) and KI5e.8 (lower panel). For these models, the period of the star $P_\star$ is 2.8 h. The colours correspond to the column density Σ of the gas whose value is indicated on the colour bar. The white point represents the black hole. The dashed white circle on the last snapshot represents the circularization radius given by equations (2.12) and (2.13) for the Keplerian and relativistic potentials respectively.

$$l^{\mathrm{R}} = \frac{R v_{\mathrm{t}}}{R - 2R_{\mathrm{g}}}, \tag{2.6}$$

respectively. The initial velocity of the star at apocentre is therefore

$$\begin{aligned} v_{\mathrm{a}}^{\mathrm{K}} &= \left(\frac{GM_{\mathrm{h}}}{R_{\mathrm{a}}}\right)^{1/2} \left(\frac{2R_{\mathrm{p}}}{R_{\mathrm{a}} + R_{\mathrm{p}}}\right)^{1/2} && (2.7) \\ &= \left(\frac{GM_{\mathrm{h}}}{R_{\mathrm{a}}}\right)^{1/2} (1-e)^{1/2}, && (2.8) \end{aligned}$$

$$v_{\mathrm{a}}^{\mathrm{R}} = \left(\frac{GM_{\mathrm{h}}}{R_{\mathrm{a}}}\right)^{1/2} \frac{2^{1/2} R_{\mathrm{p}} (R_{\mathrm{a}} - 2R_{\mathrm{g}})}{R_{\mathrm{a}}((R_{\mathrm{a}} + R_{\mathrm{p}})(R_{\mathrm{p}} - 2R_{\mathrm{g}}) + 2R_{\mathrm{g}} R_{\mathrm{p}}^2)^{1/2}}, \tag{2.9}$$

depending on the potential.

In order to demonstrate the correct implementation of the relativistic potential into the SPH codes, we anticipate the next section and analyse the motion of the gas in the simulation associated to model RI5e.8. In this model, the relativistic potential is used and the orbit of the star has a penetration factor $\beta = 5$ and an eccentricity $e = 0.8$. Fig. 2.1 shows the trajectory of the centre of mass of the gas in the simulation corresponding to model RI5e.8 compared to that of a test particle on the same orbit in the relativistic potential and in the Schwarzschild metric. The trajectory of the test particle in the relativistic potential and in the Schwarzschild metric is followed for 4 orbits. That of the centre of mass of the gas is followed during both

Table 2.1: Name and parameters of the different models.

Model	Potential	EOS	β	e
RI5e.8	Relativistic	Locally isothermal	5	0.8
KI5e.8	Keplerian	Locally isothermal	5	0.8
RA5e.8	Relativistic	Adiabatic	5	0.8
KA5e.8	Keplerian	Adiabatic	5	0.8
RI1e.8	Relativistic	Locally isothermal	1	0.8
RA1e.8	Relativistic	Adiabatic	1	0.8
RI5e.95	Relativistic	Locally isothermal	5	0.95
RA5e.95	Relativistic	Adiabatic	5	0.95

the disruption of the star and the fallback of the debris until $t/P_\star = 8$. The trajectory of the test particle is the same in the relativistic potential and in the Schwarzchild metric, confirming that apsidal precession is treated accurately in the relativistic potential as found by Tejeda & Rosswog (2013). During the disruption and the beginning of the fallback phase, the centre of mass of the gas and the test particle have the same trajectory, validating the implementation of the potential into the SPH codes. After a few pericentre passages, the two trajectories start to differ as the hydrodynamical effects on the debris become dominant. This evolution will be investigated in detail in the next section.

The accretion onto the black hole is modelled by an accretion radius fixed at the innermost stable circular orbit of $6R_\mathrm{g}$ for a non-rotating black hole. Particles entering this radius are removed from the simulations.

The simulation of the fallback phase is performed for two different equations of state (EOS) for the gas: locally isothermal and adiabatic. For the locally isothermal EOS, each SPH particle keeps their initial specific thermal energies. Physically, these two EOS represent the two extreme cases for the rate at which an excess of thermal energy is radiated away from the gas. For the locally isothermal one, every increase of thermal energy is instantaneously radiated away while for the adiabatic one, none of this energy is radiated.

Four parameters are therefore considered to simulate the fallback of the debris: the potential, the EOS, the penetration factor β and the eccentricity e. The values of these parameters for the eight models investigated in this paper are shown in table 2.1.

2.3 Results

In this section, we present the results of the simulations for the fallback phase[3]. The time is scaled by the period of the star $P_\star$ with the starting point ($t/P_\star = 0$) being when the most bound debris of the stream come back to pericentre. The circularization process is investigated through the evolution of both the position and the specific orbital energy of the debris. They will be respectively compared to the so called circularization radius and specific circularization energy.

These two quantities are defined as follows. Before the disruption, the distribution of angular momentum of the gas inside the star is sharply peaked around that of the star. As this distribution is not significantly affected by the disruption, the debris still have similar angular momenta. Assuming that they then move from their initial eccentric orbits to circular orbits each of them conserving their angular momentum, these circular orbits will form at similar

---

[3] Movies of the simulations presented in this paper are available at http://home.strw.leidenuniv.nl/~bonnerot/research.html.

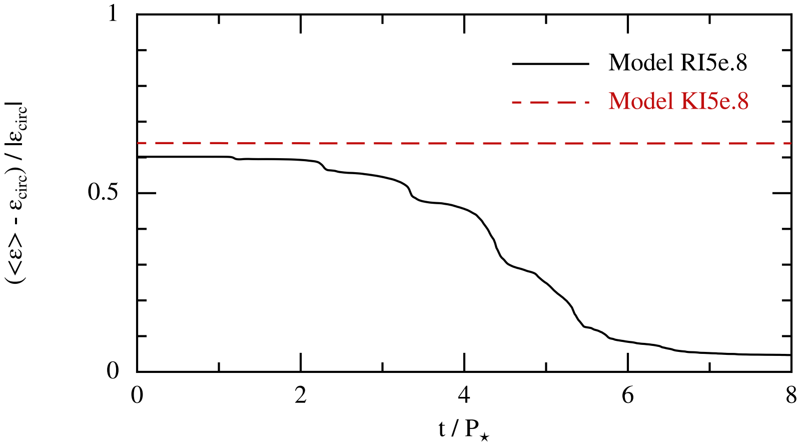

Figure 2.3: Evolution of the average specific orbital energy of the debris for models RI5e.8 and KI5e.8. For these models, the period of the star $P_\star$ is 2.8 h. The average specific orbital energy is shown relative to the specific circularization energy given by equations (2.14) and (2.15) for the Keplerian and relativistic potentials respectively.

radii. It allows to define a characteristic circularization distance, called the circularization radius, obtained by equating the specific angular momentum of the star, given by equations (2.5) and (2.6) evaluated at apocentre, and the specific circular angular momentum given by

$$l_{\mathrm{c}}^{\mathrm{K}} = (GM_{\mathrm{h}}R)^{1/2}, \tag{2.10}$$

$$l_{\mathrm{c}}^{\mathrm{R}} = \frac{(GM_{\mathrm{h}})^{1/2}R}{(R-3R_{\mathrm{g}})^{1/2}}. \tag{2.11}$$

This yields a circularization radius of

$$R_{\mathrm{circ}}^{\mathrm{K}} = \frac{R_{\mathrm{a}}^2 v_{\mathrm{a}}^2}{GM_{\mathrm{h}}} = (1+e)R_{\mathrm{p}}, \tag{2.12}$$

$$R_{\mathrm{circ}}^{\mathrm{R}} = \frac{R_{\mathrm{a}}^4 v_{\mathrm{a}}^2 + (R_{\mathrm{a}}^4 v_{\mathrm{a}}^2(-12GM_{\mathrm{h}}(R_{\mathrm{a}}-2R_{\mathrm{g}})^2 R_{\mathrm{g}} + R_{\mathrm{a}}^4 v_{\mathrm{a}}^2))^{1/2}}{2GM_{\mathrm{h}}(R_{\mathrm{a}}-2R_{\mathrm{g}})^2}, \tag{2.13}$$

where v_{a} is obtained from equations (2.7) or (2.9) depending on the potential. The associated specific orbital energy, called specific circularization energy, is equal to the specific circular orbital energy evaluated at the circularization radius. In the two potentials, it is given by

$$\varepsilon_{\mathrm{circ}}^{\mathrm{K}} = -\frac{GM_{\mathrm{h}}}{2R_{\mathrm{circ}}^{\mathrm{K}}} = -\frac{GM_{\mathrm{h}}}{2(1+e)R_{\mathrm{p}}}, \tag{2.14}$$

$$\varepsilon_{\mathrm{circ}}^{\mathrm{R}} = -\frac{GM_{\mathrm{h}}}{2R_{\mathrm{circ}}^{\mathrm{R}}}\left(\frac{R_{\mathrm{circ}}^{\mathrm{R}}-4R_{\mathrm{g}}}{R_{\mathrm{circ}}^{\mathrm{R}}-3R_{\mathrm{g}}}\right). \tag{2.15}$$

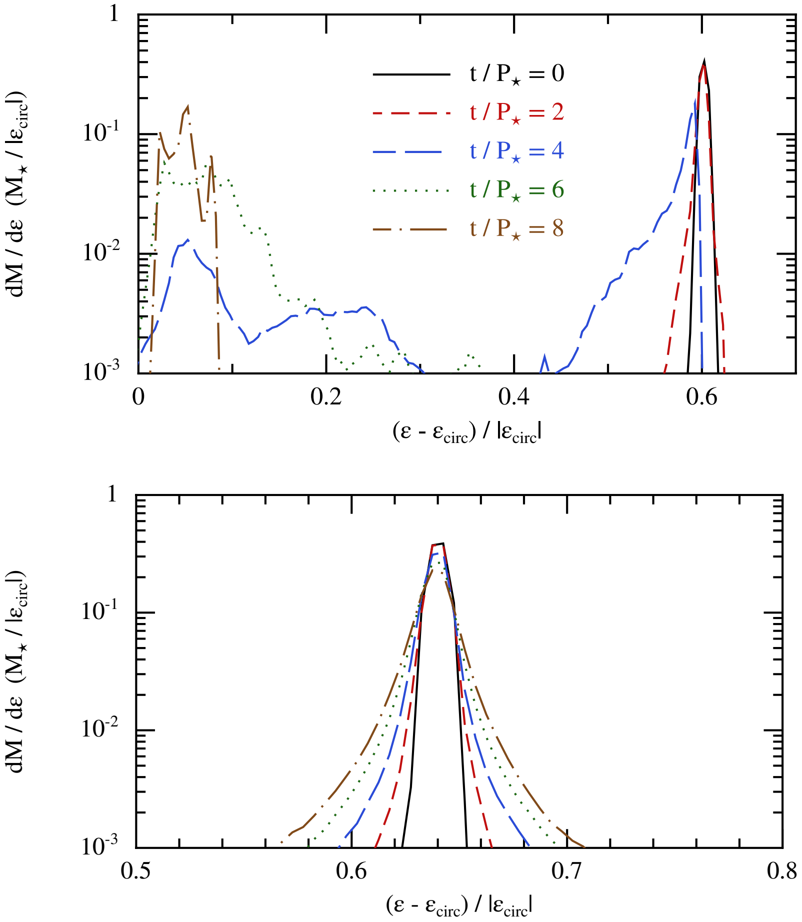

Figure 2.4: Specific orbital energy distributions of the debris at different times $t/P_\star = 0, 2, 4, 6$ and 8 for model RI5e.8 (upper panel) and KI5e.8 (lower panel). For these models, the period of the star $P_\star$ is 2.8 h. The specific orbital energy is shown relative to the specific circularization energy given by equations (2.14) and (2.15) for the Keplerian and relativistic potentials respectively.

2.3.1 Impact of relativistic precession

As mentioned in the previous section, relativistic precession modifies the trajectory of the debris at pericentre. This effect is the strongest for the orbit with $\beta = 5$ and $e = 0.8$ where the precession angle reaches 89.7 degrees. This is because this orbit has the lowest pericentre distance $R_\mathrm{p} = 9.4 R_\mathrm{g}$ and, to a smaller extent, the lowest eccentricity. We investigate the role of relativistic precession for a star on this orbit by comparing models RI5e.8 and KI5e.8. In model RI5e.8, the relativistic potential is used and apsidal precession is taken into account. In model KI5e.8, the debris are forced to move on closed orbits by using a Keplerian potential. In both models, a locally isothermal EOS is adopted for the gas.

We discuss model RI5e.8 first. The evolution of the debris can be seen in Fig. 2.2 (upper panel), which shows snapshots of their fallback towards the black hole at different times $t/P_\star = 0, 1.2, 3$ and 8. The stream remains unaffected until $t/P_\star \simeq 1.2$, corresponding to its second pericentre passage. At this time, the stream self-crosses due to apsidal precession leading to the formation of shocks that convert kinetic energy into thermal energy. However,

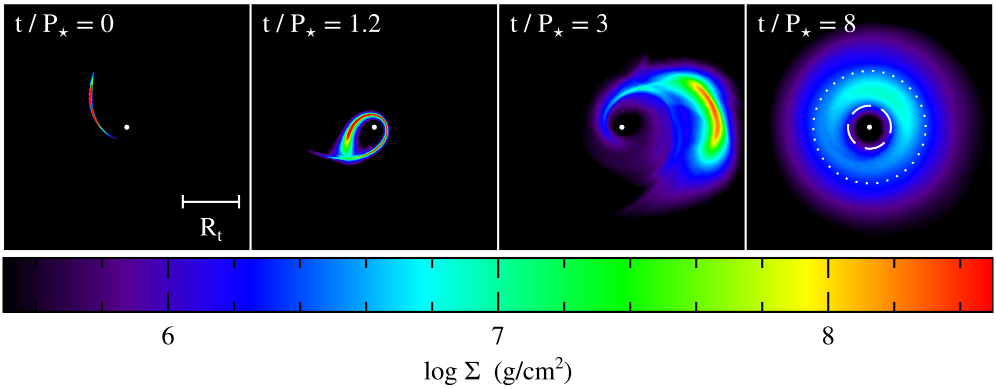

Figure 2.5: Snapshots of the fallback of the debris at different times $t/P_\star = 0, 1.2, 3$ and 8 for model RA5e.8. For this model, the period of the star $P_\star$ is 2.8 h. The colours correspond to the column density Σ of the gas whose value is indicated on the colour bar. The white point represents the black hole. The dashed white circle on the last snapshot represents the circularization radius given by equation (2.13) for the relativistic potential. The dotted white circle represents the semi-major axis of the star.

as a locally isothermal EOS is used, this excess thermal energy is instantaneously removed from the gas. The net effect of these shocks is therefore to reduce kinetic energy. This results in a decrease of the average specific orbital energy of the debris, whose evolution is shown in Fig. 2.3 (solid black line). As self-crossings occur at each pericentre passage, this decrease continues for $t/P_\star \gtrsim 1.2$ through periodic phases. These phases of decrease also become progressively steeper as the self-crossings involve a larger fraction of the stream. Accordingly, the specific orbital energy distribution, shown in Fig. 2.4 (upper panel), shifts towards lower energies. Owing to this orbital energy decrease, the debris progressively move from their initial eccentric orbits to circular orbits. At $t/P_\star \simeq 8$, their average specific orbital energy reaches a value similar to the specific circularization energy (Fig. 2.3, solid black line). By this time, they have settled into a thin and narrow ring of radius comparable to the circularization radius (Fig. 2.2, upper panel).

As can be seen from Figs. 2.2 (upper panel) and 2.3 (solid black line), the final specific orbital energy of the debris is somewhat larger than the specific circularization energy, which results in a ring forming slightly outside the circularization radius. These small discrepancies are due to redistribution of angular momentum between the debris during the shocks where a fraction of them (3 % at $t/P_\star = 8$) loses enough angular momentum to be accreted onto the black hole. This causes an excess angular momentum shared by the remaining debris, that therefore settle into circular orbits at radii larger than the circularization radius. Notably, these discrepancies are reduced when the resolution of the simulations is increased, as will be shown in subsection 2.3.4.

We now discuss model KI5e.8 for which the evolution of the debris, shown in Fig. 2.2 (lower panel), is very different. As there is no apsidal precession, the stream does not self-cross. Therefore, no kinetic energy is removed from the debris and their specific orbital energy remains constant (Fig. 2.3, dashed red line). Their specific orbital energy distribution also stays peaked around its initial value although it spreads somewhat due to tidal effects (Fig. 2.4, lower panel). Consequently, the debris do not move to circular orbits and settle instead at $t/P_\star \simeq 8$ into an elliptical strip centred around the initial orbit of the star (Fig. 2.2, lower panel).

The comparison of models RI5e.8 and KI5e.8 shows the fundamental role of apsidal pre-

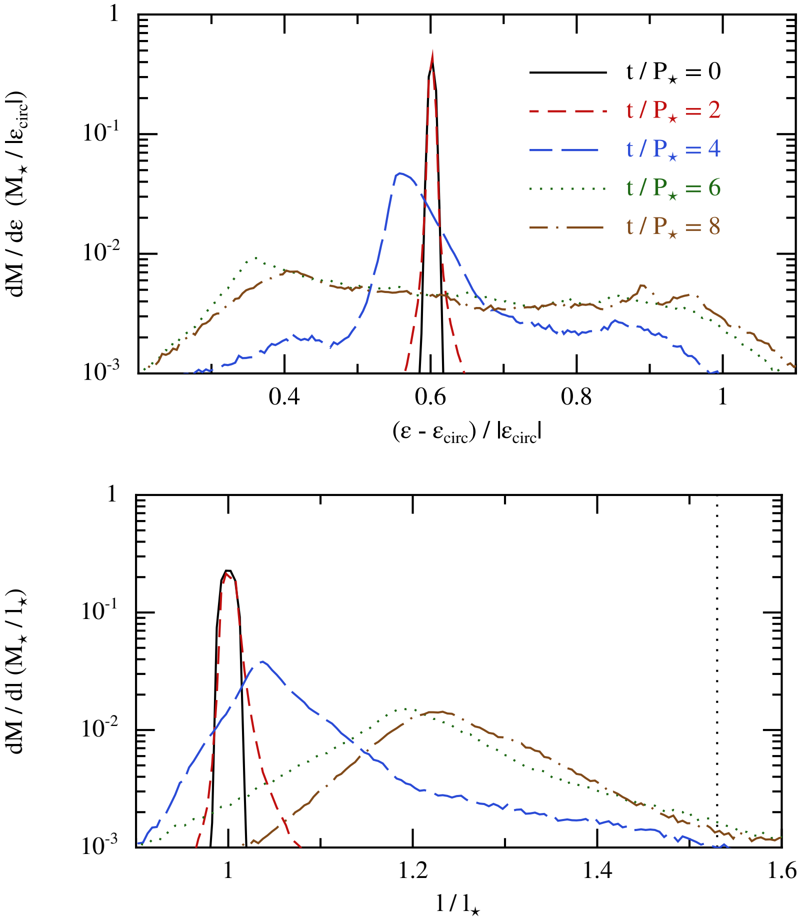

Figure 2.6: Specific orbital energy distribution (upper panel) and specific angular momentum distribution (lower panel) of the debris at different times $t/P_\star = 0, 2, 4, 6$ and 8 for model RA5e.8. For this model, the period of the star $P_\star$ is 2.8 h. The specific orbital energy is shown relative to the specific circularization energy given by equation (2.15) for the relativistic potential. The specific angular momentum is shown relative to that of the star given by equation (2.11) evaluated at apocentre.

cession in the circularization process. Our more accurate treatment of apsidal precession confirms the results of Hayasaki et al. (2013).

2.3.2 Influence of the cooling efficiency

The models discussed in the previous subsection (RI5e.8 and KI5e.8) use a locally isothermal EOS for the gas. We now discuss models RA5e.8 and KA5e.8, that use an adiabatic EOS for the gas instead. The potential used is relativistic for model RA5e.8 and Keplerian for model KA5e.8. The star is on the same orbit as before with $\beta = 5$ and $e = 0.8$.

We discuss model RA5e.8 first. The evolution of the debris as they fall back towards the black hole is shown in Fig. 2.5 at different times $t/P_\star = 0, 1.2, 3$ and 8. The stream self-crosses at $t/P_\star \simeq 1.2$ and experiences shocks which convert kinetic energy into thermal energy. This early evolution is similar to model RI5e.8. However, the subsequent behaviour differs. As the EOS is adiabatic, the thermal energy produced by the shocks is not removed

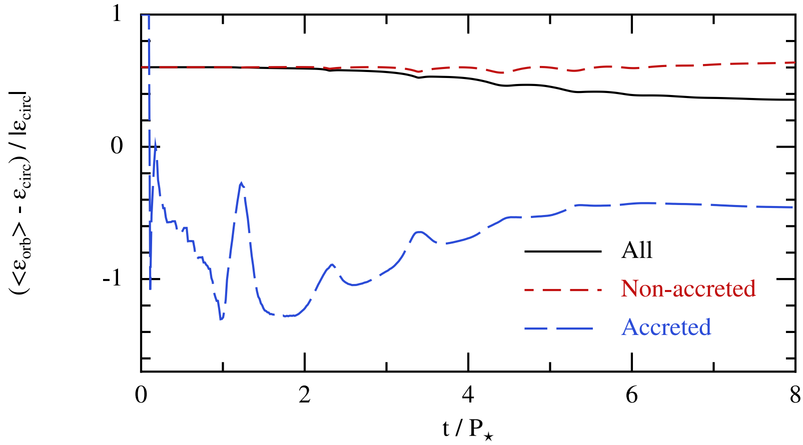

Figure 2.7: Evolution of the average specific orbital energy of all the debris, the non-accreted and accreted ones for model RA5e.8. For this model, the period of the star $P_\star$ is 2.8 h. The average specific orbital energy is shown relative to the specific circularization energy given by equation (2.15) for the relativistic potential.

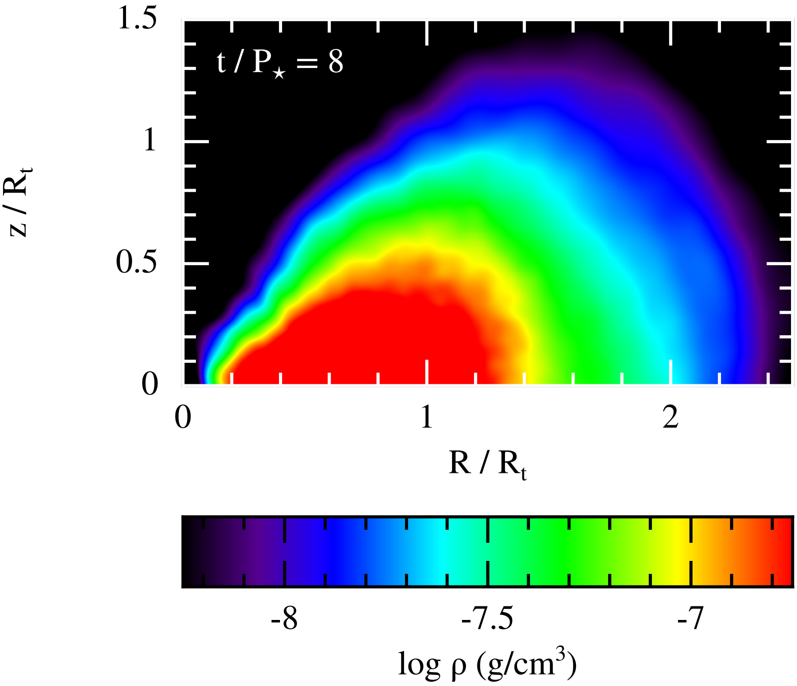

Figure 2.8: Cross-section in the $R - z$ plane of the torus formed at $t/P_\star = 8$ for model RA5e.8. z represents the height with respect to the midplane and R the cylindrical radius. The distances are normalized by the tidal radius. The black hole is at the origin. The colours correspond to the density ρ of the gas whose value is indicated on the colour bar.

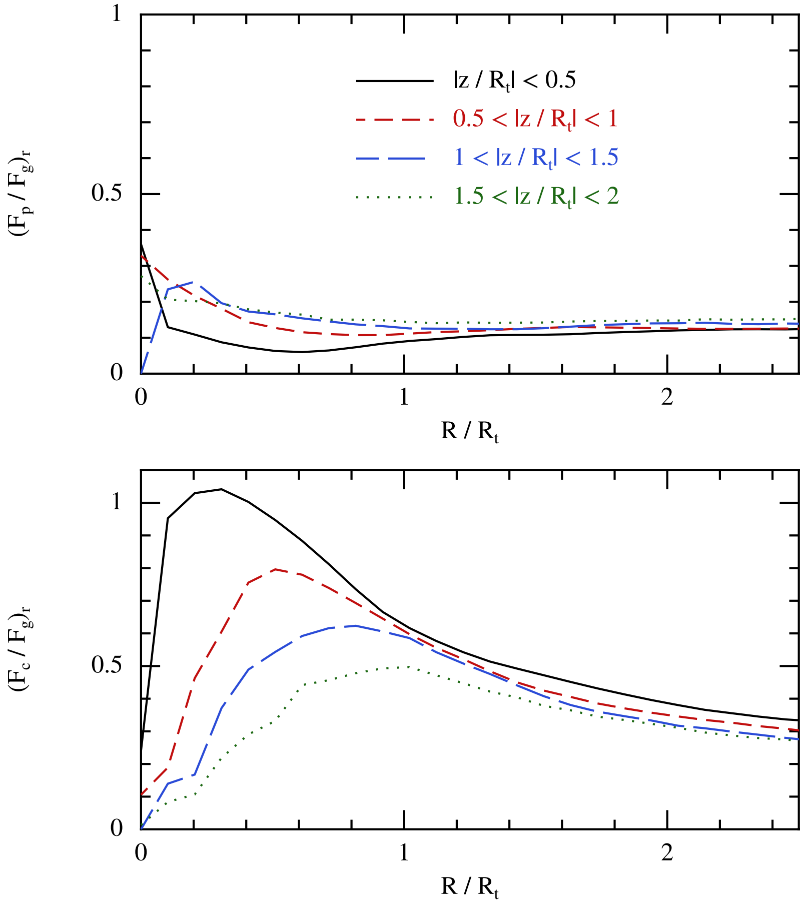

Figure 2.9: Azimuthally-averaged ratios of the pressure (upper panel) and centrifugal (lower panel) forces to the gravitational force projected in the spherical radial direction as a function of the cylindrical radius R at $t/P_\star = 8$ for model RA5e.8. These ratios are shown for different heights z with respect to the midplane: $|z/R_\mathrm{t}| < 0.5$, $0.5 < |z/R_\mathrm{t}| < 1$, $1 < |z/R_\mathrm{t}| < 1.5$ and $1.5 < |z/R_\mathrm{t}| < 2$. The distances are normalized by the tidal radius.

but kept in the debris. As more self-crossings occur, more thermal energy is injected into the stream which expands under the influence of thermal pressure. During the expansion, the ordered motion of the stream is suppressed and the debris depart from their initial eccentric orbits. This is achieved via a redistribution of their orbital parameters which can be seen in Fig. 2.6 by a spread in the distributions of specific orbital energy (upper panel) and angular momentum (lower panel). The latter also presents a tail at large angular momenta that reaches, at $t/P_\star \simeq 8$, the specific circular angular momentum at the semi-major axis of the star, indicated in the lower panel of Fig. 2.6 by a vertical black dotted line. Accordingly, the debris settle into a thick and extended torus with most of the gas located between the circularization radius and the semi-major axis of the star (Fig. 2.5). At this time, the majority of the debris (91%) are still bound to the black hole as indicated by their negative specific orbital energies (Fig. 2.6, upper panel).

Remarkably, a significant fraction of the debris are ballistically accreted onto the black hole during the formation of the torus. The fraction of accreted gas grows roughly linearly

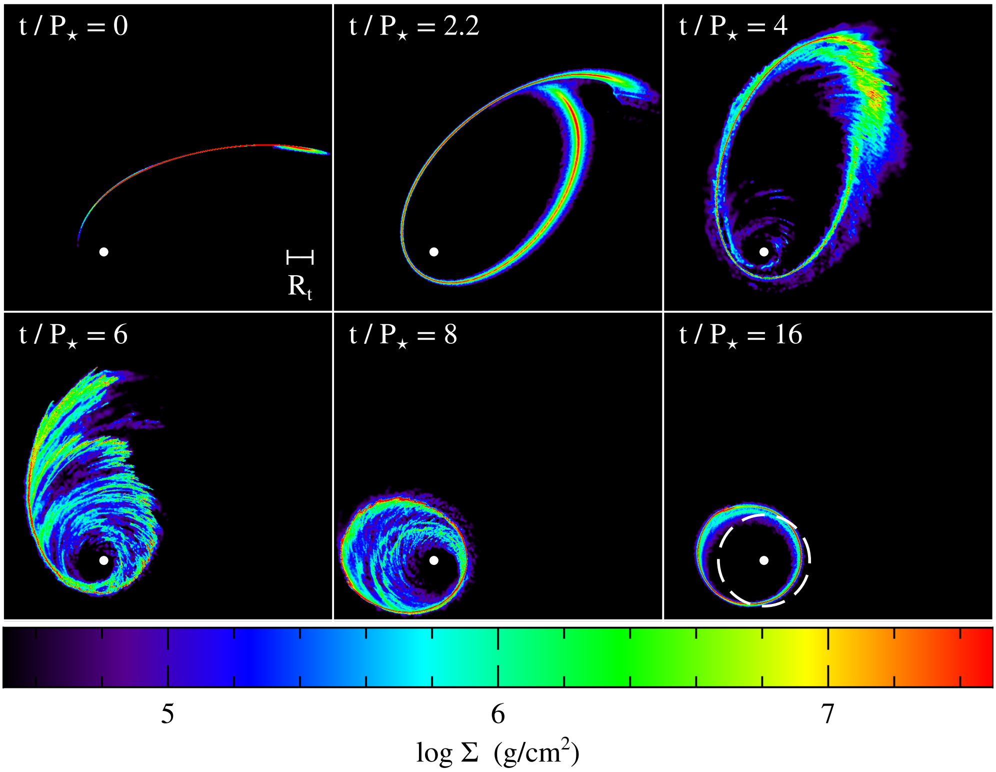

Figure 2.10: Snapshots of the fallback of the debris at different times $t/P_\star = 0, 2.2, 4, 6, 8$ and 16 for models RI1e.8. For this model, the period of the star $P_\star$ is 31 h. The colours correspond to the column density Σ of the gas whose value is indicated on the colour bar. The white point represents the black hole. The dashed white circle on the last snapshot represents the circularization radius given by equation (2.13) for the relativistic potential. Apsidal precession is weaker for this model than for model RI5e.8 owing to a larger pericentre, which causes the stream to self-cross further out from the black hole. At this location, relative velocities are lower, weakening the shocks. The debris therefore move slower to circular orbits.

to reach 26 % at $t/P_\star \simeq 8$. Fig. 2.7 shows the evolution of the average specific orbital energy of all the debris (solid black line), the non-accreted (dashed red line) and accreted (long dashed blue line) ones. When all the debris are considered, their orbital energy decreases due to the shocks where it is converted into thermal energy. However, it does not reach the circularization energy as part of the thermal energy is transferred back into kinetic energy during the expansion. The accreted debris are those which experienced the largest decrease of kinetic energy during the shocks as can be seen from their lower orbital energy. They also have the largest thermal energy which is therefore advected onto the black hole. The thermal energy of the torus is thus reduced due to both its expansion and the accretion of the hottest debris. Instead of decreasing, the orbital energy of the non-accreted debris stays constant. This is due to the accretion of debris with low orbital energies which results in an excess orbital energy shared among the non-accreted debris. As the accreted debris also have the lowest angular momenta, their accretion leads to an increase of the angular momentum of the remaining debris which results in a slight shift of the specific angular momentum distribution to larger values (Fig. 2.6, lower panel).

A more precise analysis of the torus formed at $t/P_\star = 8$ can be done by examining its internal configuration. Fig. 2.8 shows a cross-section in the $R-z$ plane where z represents the height with respect to the midplane and R the cylindrical radius. It exhibits funnels around the rotation axis. It also contains a dense inner region at $z/R_\mathrm{t} \lesssim 0.5$ and $R/R_\mathrm{t} \simeq 1$ that corresponds to the semi-major axis of the star. This dense region is surrounded by a more diffuse one that extends from close to the black hole to $R/R_\mathrm{t} \simeq 2.5$ and $z/R_\mathrm{t} \simeq 1.5$. To assess the internal equilibrium of the torus, we plot in Fig. 2.9 azimuthally-averaged ratios of the pressure force (upper panel) and centrifugal force (lower panel) to the gravitational force projected in the spherical radial direction as a function of R and for different intervals of z: $|z/R_\mathrm{t}| < 0.5$, $0.5 < |z/R_\mathrm{t}| < 1$, $1 < |z/R_\mathrm{t}| < 1.5$ and $1.5 < |z/R_\mathrm{t}| < 2$. The ratio of the pressure force to the gravitational force is roughly $(F_\mathrm{p}/F_\mathrm{g})_r \simeq 0.2$ in the entire torus implying that it is not hydrostatically supported. However, the ratio of the centrifugal force to the gravitational force is larger. For $|z/R_\mathrm{t}| < 0.5$, it presents a maximum of $(F_\mathrm{c}/F_\mathrm{g})_r \simeq 1$ at $R/R_\mathrm{t} \simeq 0.3$ and decreases at larger radii. The same dependence exists for regions further from the midplane but for lower maxima of $(F_\mathrm{c}/F_\mathrm{g})_r \simeq 0.5-0.8$. Therefore, this torus is mostly centrifugally supported against gravity with this support being stronger in its inner region. As they are bound to the black hole, the regions that are not supported against gravity will stop expanding and collapse at a later time. This collapse is likely to cause the formation shocks in the outer part of the torus which would increase hydrostatic support in this region.

For model KA5e.8, the stream does not experience apsidal precession. However, it is heated when it passes at pericentre. This is due to the formation of the pancake shock described in the Introduction. As a result, it expands roughly by a factor of 2 at each pericentre passage both in the radial and vertical directions. It causes the stream to self-cross at $t/P_\star \simeq 4$ that is after its fifth passage at pericentre. The subsequent evolution is similar to model RA5e.8. The debris settle into a thick and extended torus at $t/P_\star \simeq 10$. This channel of disc formation is similar to that found by Ramirez-Ruiz & Rosswog (2009). Therefore, relativistic apsidal precession is not the only factor that can lead to circular orbits of the debris, but it is the most efficient and operates regardless of the EOS used for the gas.

As can be seen by comparing models RI5e.8 and RA5.8, the cooling efficiency determines the structure of the disc formed during the circularization process. While a thin and narrow ring forms at the location of the circularization radius for an efficient cooling, an inefficient cooling leads instead to the formation of a thick and extended torus located between the circularization radius and the semi-major axis of the star.

2.3.3 Dependence on the orbit of the star

So far, the fallback of the debris has been investigated for a fixed orbit of the star with $\beta = 5$ and $e = 0.8$. We now consider two new orbits obtained by decreasing the penetration factor (subsection 2.3.3) and increasing the eccentricity (subsection 2.3.3). Throughout this section, the potential is fixed to relativistic. Models RI5e.8 and RAe.8, discussed above for the initial orbit and this potential, will be used as reference.

2.3.3.1 Decreasing the penetration factor

We start by decreasing the penetration factor to $\beta = 1$ keeping the eccentricity to its initial value $e = 0.8$. This decrease of the penetration factor corresponds to an increase of the pericentre distance from $R_\mathrm{p} = 9.4R_\mathrm{g}$ to $R_\mathrm{p} = 47R_\mathrm{g}$. We investigate the fallback of the debris for a star on this new orbit by discussing models RI1e.8 and RA1e.8. A locally isothermal EOS is used for model RI1e.8 while an adiabatic EOS is used for model RA1e.8. The relativistic potential is used in both models.

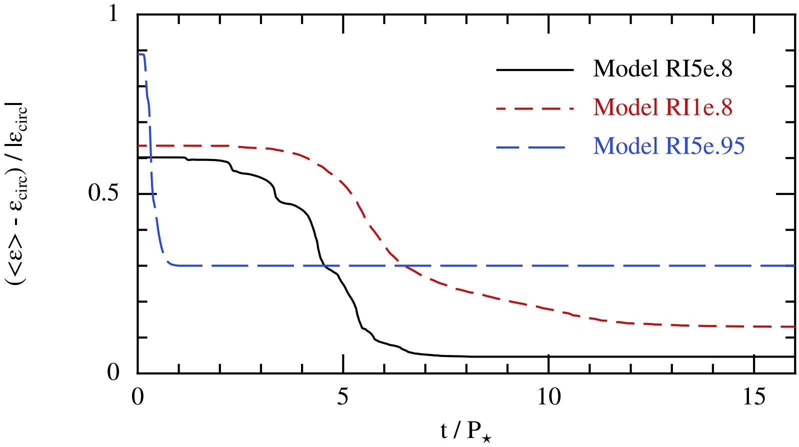

Figure 2.11: Evolution of the average specific orbital energy of the debris for models RI5e.8, RI1e.8 and RI5e.95. For these models, the periods of the star $P_\star$ are respectively 2.8 h, 31 h and 22 h. The average specific orbital energy is shown relative to the specific circularization energy given by equation (2.15) for the relativistic potential.

We discuss model RI1e.8 first. Snapshots of the evolution of the debris are shown in Fig. 2.10 at different times $t/P_\star = 0, 2.2, 4, 6, 8$ and 16. The first self-crossing of the stream occurs at $t/P_\star = 2.2$ that is at its third pericentre passage. It causes the formation of shocks that reduce the kinetic energy of the debris as a locally isothermal EOS is used. However, as the stream passes further from the black hole, relativistic precession is weaker than for model RI5e.8 with a precession angle decreasing from 89.7 to 13.5 degrees. Consequently, the shocks happen further from the black hole and involve parts of the stream with lower relative velocities. For this reason, they are less efficient at removing kinetic energy from the debris. This results in a slower and more gradual decrease of their average specific orbital energy, as seen from Fig. 2.11 that shows its evolution for model RI5e.8 (solid black line) and RI1e.8 (dashed red line). At $t/P_\star \simeq 16$, the average specific orbital energy of the debris stabilizes at a value similar to the circularization energy (Fig. 2.11, dashed red line) and the debris settle into a thin and narrow ring of radius comparable to the circularization radius (Fig. 2.10). As for model RI5e.8, the origin of the small discrepancies with the specific circularization energy and the circularization radius are due to the accretion onto the black hole of a fraction of the debris (3 % at $t/P_\star = 16$) with low angular momenta.

For model RA1e.8, the evolution of the debris is very similar to model RA5.8. The shocks produced by the self-crossings of the stream leads to its expansion. The debris settle into a torus with most of them located between the circularization radius and the semi-major axis of the star. The only effect of modifying the orbit is to change the value of these two limiting radii.

2.3.3.2 Increasing the eccentricity

We now keep the penetration factor to its initial value $\beta = 5$ while increasing the eccentricity to $e = 0.95$. The fallback of the debris is investigated for this new orbit by discussing models RI5e.95 and RA5e.95 which use respectively a locally isothermal and an adiabatic EOS. The relativistic potential is adopted for both of them.

We discuss first model RI5e.95. Fig. 2.12 shows snapshots of the fallback of the debris at different times $t/P_\star = 0, 0.15, 0.25, 0.33, 0.5$ and 1. The stream first crosses itself at $t/P_\star \simeq$

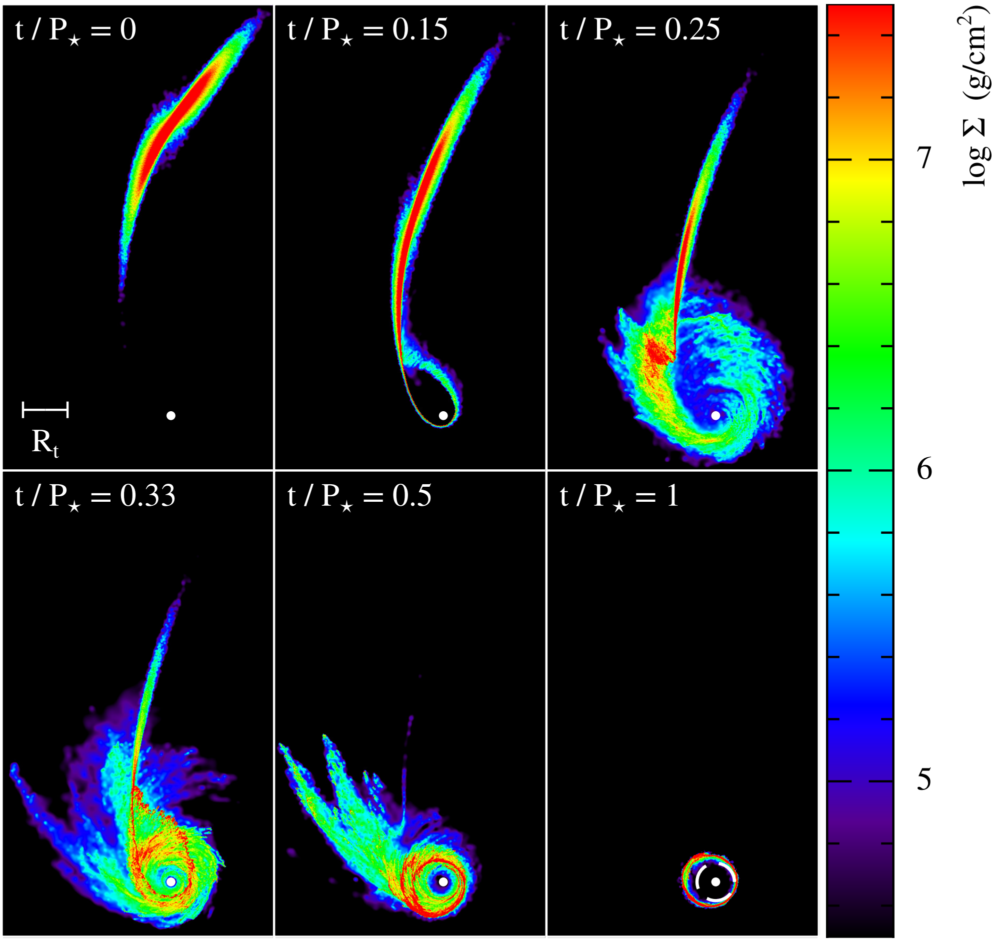

Figure 2.12: Snapshots of the fallback of the debris at different times $t/P_\star = 0, 0.15, 0.5$ and 1 for models RI5e.95. For this model, the period of the star $P_\star$ is 22 h. The colours correspond to the column density Σ of the gas whose value is indicated on the colour bar. The white point represents the black hole. The dashed white circle on the last snapshot represents the circularization radius given by equation (2.13) for the relativistic potential. The stream is longer for this model than for model RI5e.8 as the eccentricity is larger. As a result, the self-crossings involve a larger fraction of the debris, causing them to move faster to circular orbits.

0.15 just after the first passage of its leading part at pericentre. When this occurs, most of the debris are still falling back towards the black hole away from the self-crossing point. This is different from model RI5e.8, for which this self-crossing happens later and when most of the debris are already beyond the self-crossing point (see Fig. 2.2). The reason for these differences is that the stream is longer for model RI5e.95 than for model RI5e.8 owing to the larger eccentricity. After the first self-crossing, the debris located beyond the self-crossing point are expelled leaving the rest of the stream free to move around the black hole. This induces a second self-crossing at $t/P_\star \simeq 0.33$. These self-crossings create shocks that remove kinetic energy from the debris as a locally isothermal EOS is used. As shown in Fig. 2.11 (blue long dashed line), the average specific orbital energy of the debris therefore decreases for $t/P_\star \gtrsim 0.15$. This decrease occurs faster than for model RI5e.8 as the self-crossings involve larger fractions of the debris. At $t/P_\star \simeq 1$, their average specific orbital energy settles at a value similar to the circularization energy (Fig. 2.11, blue long dashed line) and they form a thin and narrow ring of gas located at a distance comparable to the circularization radius (Fig. 2.12). As previously, the discrepancies with the specific circularization energy and the circularization radius are due to the accretion of a fraction of the debris (4 % at $t/P_\star = 1$) with low angular momenta. These discrepancies are larger for this model than for models RI5e.8 and RI1e.8 because more debris are accreted and these debris have lower angular momenta relative to that of the star.

For model RA5e.95, the debris evolve very similarly to model RA5.8. They expand due to shocks produced by the self-crossings of the stream. They settle into a thick and extended torus in which most of the debris are located between the circularization radius and the semi-major axis of the star. Only the value of these two limiting radii differs for the new orbit.

2.3.4 Convergence of the results

The simulations of the fallback phase has been performed for three different resolutions corresponding to about 100K, 500K and 1300K particles. The two larger resolutions have been obtained from the lowest one by using the particle splitting technique (Kitsionas 2003) on the initial condition of the fallback phase. Each particle is split into 5 or 13 additional ones with one at the position of the initial particle and the others distributed on a tetrahedron and on a face-centred cubic structure respectively. In both cases, the distance between each additional particles is fixed to 1.5 times the smoothing length of the initial one. In addition, the particles added outside the volume defined by the initial ones have been removed. The fraction of particles removed in this way is always less than 10%. The mass of the additional particles has then been decreased in order to keep the total mass of the stream constant.

Minor differences have been noticed when the resolution is increased. They are common to the different orbits considered. For a locally isothermal EOS, the time at which the average specific orbital energy of the debris settles is either advanced or delayed by $\Delta t \simeq P_\star$ between the 100K and the 500K simulations. However, this difference becomes negligible between the 500K and 1300K simulations. Both for a locally isothermal and an adiabatic EOS, increasing the resolution also results in a smaller fraction of debris with low angular momenta being accreted onto the black hole. For the isothermal EOS, this causes the average specific orbital energy of the debris to settle at a value closer to the specific circularization energy. The fraction of debris accreted during the disc formation decreases to less than 5% in this case. We therefore attribute it to resolution. For the adiabatic EOS, the torus turns out to be slightly more compact and centrally condensed. However, its internal structure remains the same. The fraction of accreted debris also decreases in this case but remains larger than 25%, and is likely to be physical. The simulations presented in this paper have been performed for 500K particles as both the final configuration of the debris and the time needed to reach it are unchanged above this resolution. Overall, we conclude that the behaviour described in the previous subsections is robust with respect to resolution.

2.4 Discussion and conclusion

By means of SPH simulations, we investigated the circularization process for tidal disruptions of stars on bound orbits by a non-rotating black hole. The formation of an accretion disc from the debris is mostly driven by relativistic apsidal precession that causes the stream to self-cross. If cooling is inefficient, this self-crossing is also partially caused by an expansion of the stream, when it passes at pericentre. In addition, we showed that the structure of the disc depends on the cooling efficiency of the gas by considering two extreme cases. For an efficient cooling, the debris form a thin and narrow ring of gas. For an inefficient cooling, they settle into a thick and extended torus, that at the end of our simulation is still mostly centrifugally supported against gravity. We also demonstrated the existence of different regimes of circularization for different orbits of the star. The circularization timescale $t_{\rm circ}$ varies from $\sim P_\star$ for the largest eccentricity to $\sim 10 P_\star$ for the lowest penetration factor considered (see Fig. 2.11). In physical units, it corresponds to tens to hundreds of hours.

The circularization process in TDEs has been the focus of several other recent works. Shiokawa et al. (2015) simulated the tidal disruption of a white dwarf on a parabolic orbit around a $500\,{\rm M}_\odot$ black hole using a general relativistic simulation while Hayasaki et al. (2015) considered the case of bound orbits around a $10^6\,{\rm M}_\odot$ black hole. The latter use a simulation setup similar to ours but our treatment of apsidal precession is more accurate and we consider a larger range of orbits. Both studies noticed the influence of the cooling efficiency on the disc structure. In addition, Hayasaki et al. (2015) investigated the effect of the black hole spin. As anticipated by Dai et al. (2013), they found that nodal precession can prevent the self-crossing of the stream, delaying circularization. Using Monte-Carlo calculations, Guillochon & Ramirez-Ruiz (2015) found that this delay is of one year on average for a star on a parabolic orbit.

2.4.1 Thermal energy radiation

During the circularization process, thermal energy is injected into the debris at the expense of their kinetic energy. If they cool efficiently, this thermal energy increase can be estimated by subtracting the final circularization energy to the initial orbital energy of the star. It amounts to $\Delta U = M_\star(\varepsilon^{\rm R} - \varepsilon^{\rm R}_{\rm circ}) \simeq$ few $10^{51} - 10^{52}$ erg for the orbits considered, according to equations (2.4) and (2.15). For larger β, ΔU is larger because the circularization energy is lower. Assuming that this excess thermal energy is radiated during the disc formation, it gives rise to a flare of luminosity $L_{\rm circ} = \Delta U / t_{\rm circ} \simeq$ few $10 - 10^3\,{\rm L_{Edd}}$, increasing with β, as $t_{\rm circ}$ is shorter and ΔU is larger.

As described in subsection 2.3.2, if the excess thermal energy is not radiated instantaneously, it is partially transferred back into kinetic energy or advected onto the black hole. As a result, the remaining thermal energy of the torus is $\sim 10\%$ of the above ΔU. The associated heating rate is therefore $\Delta U / t_{\rm circ} \simeq$ few $1 - 10^2\,{\rm L_{Edd}}$. Note that at the end of our simulation, the torus has not yet settled into an equilibrium configuration as we observe outflowing material.

2.4.2 Viscous evolution

Debris on circular orbits are subject to viscous effects which drive their accretion onto the black hole. Viscosity is not explicitly included in the simulations presented above. Nevertheless, its influence can be estimated a posteriori by computing the viscous timescale $t_{\rm visc}$. In our simulations, disc formation is progressive. A fraction of the debris already forms a disc-like structure before complete circularization. An example of such a structure can be seen in Fig. 2.12 at $t/P_\star = 0.33$. We consider that viscosity can start acting on these debris at $t < t_{\rm circ}$ which may lead to their accretion before complete circularization if $t_{\rm visc} < t_{\rm circ}$. For simplicity, $t_{\rm visc}$ is computed for the final configuration of the disc although it is used to evaluate viscous effects as the debris proceed towards this configuration. If the debris cool efficiently, they settle into a thin ring around the circularization radius. At this distance from the black hole,

$$\frac{t_{\rm visc}}{P_\star} = 3 \times 10^3 \left(\frac{\alpha}{0.1}\right)^{-1} \left(\frac{H/R}{10^{-2}}\right)^{-2} \left(\frac{1-e^2}{0.36}\right)^{3/2}, \tag{2.16}$$

where α is the viscosity parameter (Shakura & Sunyaev 1973) and H/R is the aspect ratio of the disc. The circularization radius is obtained from equation (2.12) which is at the origin of the $(1-e^2)^{3/2}$ factor. For all orbits considered, $t_{\rm visc} > t_{\rm circ}$, largely independently of the values of α and H/R. Therefore, viscosity should not have a significant effect during circularization and most of the accretion will occur once the ring is formed. At the end of circularization, the viscous timescale, given by equation (2.16), corresponds to an accretion rate $\dot{M} = M_\star/t_{\rm visc} \simeq$ few $1-100\,\dot{\rm M}_{\rm Edd}$ depending on the orbit, $\dot{M}_{\rm Edd}$ being the Eddington accretion rate for a radiative efficiency of 10%. We therefore speculate that, due to this super-Eddington accretion, the ring will subsequently evolve into a thicker structure under the influence of radiation pressure.

If the gas cools inefficiently, it settles into a thick torus located between the circularization radius and the semi-major axis of the star. At the semi-major axis of the star,

$$\frac{t_{\rm visc}}{P_\star} = 2 \left(\frac{\alpha}{0.1}\right)^{-1} \left(\frac{H/R}{1}\right)^{-2}, \tag{2.17}$$

which does not depend explicitly on the orbit of the star as $P_\star$ cancels out. For the above values of α and H/R, $t_{\rm visc} \lesssim t_{\rm circ}$ which is sensitive to the values chosen for these parameters. However, when evaluated at the circularization radius, $t_{\rm visc}$ is lower by a factor $(1-e^2)^{3/2} \simeq$ few $10^{-2} - 10^{-1}$ depending on the orbit. The precise value of the viscous timescale thus depends on the mass distribution within the torus, being shorter if more mass is close to the circularization radius. We therefore conclude that viscosity may affect the evolution of the debris during the circularization process causing some of them to be accreted. During its subsequent evolution, the torus will keep accreting matter with an accretion rate $\dot{M} = M_\star/t_{\rm visc} \gtrsim 10^4\,\dot{M}_{\rm Edd}$ for the different orbits considered. For these highly super-Eddington accretion rates, the subsequent evolution of the torus is difficult to predict.

2.4.3 Evaluation of the cooling efficiency

In the simulations presented in this paper, two extreme cooling efficiencies have been considered. The ability of the debris to cool can be estimated a posteriori by computing the diffusion timescale $t_{\rm diff}$ defined as the time that photons take to diffuse out of the surrounding gas. As most of the thermal energy is produced by the shocks occurring when the stream self-crosses, the diffusion timescale must be evaluated at the location of these shocks. Since we find that the gas is optically thick to electron scattering, it is given by $t_{\rm diff} = H_{\rm sh}\,\tau/c$ where $\tau = \sigma_{\rm T}\rho_{\rm sh}H_{\rm sh}/\mp$ is the optical depth, $H_{\rm sh}$ and $\rho_{\rm sh}$ are the width and density of the gas at the location of the shocks. When an efficient cooling is assumed, the width of the stream remains $H_{\rm sh} \simeq R_\star$. To ensure self-consistency, the condition $t_{\rm diff} < t_{\rm circ}$ has to be satisfied, which translates into an upper limit on the density

$$\rho_{\rm sh} < 8 \times 10^{-7}\,{\rm g\,cm^{-3}} \left(\frac{\rm n_{circ}}{5}\right)\left(\frac{\rm H_{sh}}{\rm R_\star}\right)^{-2} \left(\frac{\rm a_\star}{100\,R_\odot}\right)^{3/2}, \tag{2.18}$$

where $n_{\rm circ} = t_{\rm circ}/P_\star$. Among the different orbits considered, this condition is satisfied only for that with $\beta = 1$. In general, we estimate that increasing the eccentricity e of the star tends to favour an efficient cooling of the debris. This is because it leads to a more extended and tenuous stream, decreasing $\rho_{\rm sh}$. Condition (2.18) is therefore more easily fulfilled. Instead, increasing the penetration factor β may favour an inefficient cooling. It causes the stream to self-cross closer to the black hole. The debris are therefore located in a smaller volume which increases $\rho_{\rm sh}$. Furthermore, they circularize faster which decreases $n_{\rm circ}$. Condition (2.18) is thus more difficult to fulfill. However, these estimates are only approximate. The ability of radiation to escape depends on the precise location within the stream at which the thermal energy is deposited by the shocks. It also varies with the density distribution of the debris which is highly inhomogeneous at the time when most of the shocks occur. Furthermore, this radiation could also affect the structure of the disc through radiation pressure. A realistic treatment of the interaction between gas and radiation is therefore necessary to determine precisely the influence of cooling during the circularization process.

2.4.4 Extrapolation to parabolic orbits

As mentioned in the Introduction, TDEs typically involve stars on parabolic orbits. In this paper, we chose to simulate the disruption of stars on bound orbits instead. This choice is motivated by a lower computational cost which allows to explore a larger parameter space. However, the results can be extrapolated to get insight into the typical case of parabolic orbits.

The bound orbits considered in the simulations satisfy the condition $e < e_{\rm crit} = 1 - (2/\beta)(M_{\rm h}/M_\star)^{-1/3}$, so that all the debris are bound to the black hole. Furthermore, all the debris have periods similar to that of the star, $P_\star$. Instead, in the case of parabolic orbits, part of the debris become unbound from the black hole. Therefore, the tidal stream has a large range of periods between that of the most bound debris $t_{\rm min}$ and $+\infty$. This means that it features an elongated tail of debris which will continue to fall back towards pericentre long after the most bound ones have reached it. Due to apsidal precession, the leading part of the stream will inevitably collide with this tail after its first passage at pericentre. By means of point particle calculations in the Schwarzschild metric, we found that this prompt self-crossing occurs in general for an eccentricity $e \gtrsim 0.9$ largely independent on β. As discussed in subsection 2.3.3, it happens for model RI5e.95 where $e = 0.95$ and $\beta = 5$ (see Fig. 2.12). In this case, the self-crossing leads to circularization on a timescale $t_{\rm circ} \simeq P_\star$. Therefore, for a parabolic orbit with $\beta = 5$, we expect a disc to form from the most bound debris due to this prompt self-crossing on a timescale $t_{\rm circ} \simeq t_{\rm min}$ where $t_{\rm min}$ replaces $P_\star$ as the period of the most bound debris. In this case, the newly-formed disc is only composed of the tip of the stream, which falls back within $\sim t_{\rm min}$. We expect the debris infalling later to rapidly circularize and join this disc. The timescale $t_{\rm circ}$ for the most bound debris to circularize is less clear for a parabolic orbit with $\beta = 1$ as apsidal precession is weaker. For model RI1e.8 where $e = 0.8$ and $\beta = 1$, it is $t_{\rm circ} \simeq 10P_\star$. However, the presence of a tail of debris would cause the self-crossing to affect the middle of the stream instead of its extremities, which likely makes the shocks more disruptive. On the other hand, the self-crossing happens further out from the black hole. This is because the apocentre of the most bound debris is about ten times larger for a parabolic orbit than for a bound one with $e = 0.8$. Relative velocities are lower at this location, which likely weakens the shocks. Therefore, $t_{\rm circ}$ may remain $\sim 10\,t_{\rm min}$ for a parabolic orbit with $\beta = 1$. In this case, a significant mass of debris falls back within $t_{\rm circ}$, while the most bound ones circularize. Whether all this mass has circularized by $t_{\rm circ}$ is unclear.

Based on our estimates in subsection 2.4.3, conditions for efficient cooling are more easily met for parabolic orbits than for elliptical ones. However, how efficient the cooling is also depends on the penetration factor, as large β favours the formation of denser regions. In general, we expect the cooling efficiency to have the same effect on the disc structure as found in our simulations. If cooling is efficient throughout the evolution, a thin ring forms around the circularization radius. If it is inefficient, a thick torus forms located between the circularization radius and around the semi-major axis of the most bound debris. This allows us to extrapolate to the case of parabolic orbits the discussion in subsections 2.4.1 and 2.4.2.

If cooling is efficient, the increase of thermal energy experienced by the debris during circularization is equal to the total change in orbital energy of the most bound debris. It amounts to $\Delta U = f M_\star(\varepsilon^{\mathrm{R}} - \varepsilon^{\mathrm{R}}_{\mathrm{circ}}) \simeq$ few 10^{51} erg according to equations (2.4) and (2.15). For $\beta = 1$, this estimate assumes that all the debris falling back within t_{circ} have circularized. The factor f accounts for the fact that only a fraction of the debris reaches the black hole within t_{circ} in the parabolic case. Numerically, $f \simeq 0.2 - 0.4$ for $t_{\mathrm{circ}} = 1 - 10\, t_{\mathrm{min}}$ assuming a flat energy distribution. If this thermal energy is radiated during t_{circ}, it leads to a luminosity $L_{\mathrm{circ}} = \Delta U / t_{\mathrm{circ}} \simeq$ few $1 - 10\, \mathrm{L_{Edd}}$. Remarkably, it is comparable or higher than the peak luminosity in the soft X-ray band from the viscous accretion accretion through the disc (Lodato & Rossi 2011). If the thermal energy is not immediately radiated but partly used to expand the disc or advected onto the black hole, the remaining thermal energy of the torus is $\sim 10\%$ of the above ΔU, a percentage extrapolated from the case of bound orbits. The heating rate is then $\Delta U / t_{\mathrm{circ}} \simeq$ few $0.1 - 1\, \mathrm{L_{Edd}}$. This roughly agrees with the value found by Shiokawa et al. (2015) scaling their results to our parameters for the black hole and the star (Piran et al. 2015).

The effect of viscosity can be estimated in the case of parabolic orbits by computing the viscous timescale t_{visc}, obtained from equations (2.16) and (2.17) replacing $P_\star$ and e by the period and eccentricity of the most bound debris t_{min} and e_{crit}. As for bound orbits, we expect the disc to form progressively, with a fraction of the debris rapidly reaching a disc-like structure. For $\beta = 1$, these circularized debris could already be present before most of the final disc mass reaches pericentre. On these debris, viscosity may start acting even before the disc completely settles. If cooling is inefficient, we find that $t_{\mathrm{visc}} \simeq$ few $\mathrm{t_{min}}$ at the semi-major axis of the most bound debris but decreases by a factor $(1 - e^2_{\mathrm{crit}})^{3/2} \simeq$ few $10^{-3} - 10^{-4}$ at the circularization radius. The distribution of mass within the torus thus determines the value of the relevant viscous timescale which decreases if most of the debris are close to the circularization radius. In all cases, we expect $t_{\mathrm{visc}} < t_{\mathrm{circ}}$ since t_{circ} is estimated to be $\gtrsim t_{\mathrm{min}}$. We conclude that a significant fraction of the torus may already be accreted by the end of circularization. If cooling is efficient, $t_{\mathrm{visc}} \simeq$ few $10 - 100\, \mathrm{t_{min}}$ in the thin ring. In this case, $t_{\mathrm{visc}} > t_{\mathrm{circ}}$ which indicates that the ring is not significantly accreted during circularization. However, if the disc geometry changes when accretion starts, the viscous timescale could be different. In particular a thicker disc may result from a super-Eddington accretion rate, shortening the viscous timescale.

The fact that $t_{\mathrm{visc}} \ll t_{\mathrm{min}}$ has often been interpreted as evidence that the accretion rate onto the black hole traces directly the fallback rate of the debris. However, if most of the debris initially form a disc without having the possibility of accreting, then the accretion rate onto the black hole will be driven by viscous processes rather than by infall, which has essentially finished once accretion starts (Cannizzo et al. 1990; Shen & Matzner 2014). If disc accretion is significantly delayed with respect to disc formation, we thus expect a solution a la Cannizzo et al. (1990), that predicts an accretion rate declining as $t^{-4/3}$. If on the other hand accretion already occurs while the disc is forming, we expect at late times a $t^{-5/3}$ decline in the accretion rate. Owing to a progressive disc formation, we consider the latter scenario to be a possibility, which seems favoured if cooling is inefficient, since $t_{\mathrm{visc}} < t_{\mathrm{circ}}$.

The simulations presented in this paper allowed to get insight into the circularization process during TDEs. Several extensions of this work are possible including simulations considering a more eccentric star, the treatment of the interaction between the debris and the radiation emitted during the disc formation and the effect of the black hole spin.

Acknowledgments

We acknowledge the use of SPLASH (Price 2007) for generating the figures. C.B. is grateful to Inti Pelupessi for his help in implementing the particle splitting technique.

Bibliography

Amaro-Seoane P., Miller M. C., Kennedy G. F., 2012, MNRAS, 425, 2401

Ayal S., Livio M., Piran T., 2000, ApJ, 545, 772

Bate M. R., Bonnell I. A., Price N. M., 1995, MNRAS, 277, 362

Cannizzo J. K., Gehrels N., 2009, ApJ, 700, 1047

Cannizzo J. K., Lee H. M., Goodman J., 1990, ApJ, 351, 38

Cannizzo J. K., Troja E., Lodato G., 2011, ApJ, 742, 32

Cappelluti N., et al., 2009, A&A, 495, L9

Chen X., Madau P., Sesana A., Liu F. K., 2009, ApJ, 697, L149

Chen X., Sesana A., Madau P., Liu F. K., 2011, ApJ, 729, 13

Coughlin E. R., Begelman M. C., 2014, ApJ, 781, 82

Dai L., Escala A., Coppi P., 2013, ApJ, 775, L9

Esquej P., et al., 2008, A&A, 489, 543

Evans C. R., Kochanek C. S., 1989, ApJ, 346, L13

Frank J., Rees M. J., 1976, MNRAS, 176, 633

Gezari S., et al., 2008, ApJ, 676, 944

Gezari S., et al., 2009, ApJ, 698, 1367

Giannios D., Metzger B. D., 2011, MNRAS, 416, 2102

Guillochon J., Ramirez-Ruiz E., 2013, ApJ, 767, 25

Guillochon J., Ramirez-Ruiz E., 2015, ApJ, 809, 166

Guillochon J., Manukian H., Ramirez-Ruiz E., 2014, ApJ, 783, 23

Hayasaki K., Stone N., Loeb A., 2013, MNRAS, 434, 909

Hayasaki K., Stone N. C., Loeb A., 2015, preprint (arXiv:1501.05207)

Kitsionas S., 2003, PhD thesis, Cardiff University

Kochanek C. S., 1994, ApJ, 436, 56

Komossa S., Halpern J., Schartel N., Hasinger G., Santos-Lleo M., Predehl P., 2004, ApJ, 603, L17

Lacy J. H., Townes C. H., Hollenbach D. J., 1982, ApJ, 262, 120

Lodato G., Price D. J., 2010, MNRAS, 405, 1212

Lodato G., Rossi E. M., 2011, MNRAS, 410, 359

Lodato G., King A. R., Pringle J. E., 2009, MNRAS, 392, 332

Loeb A., Ulmer A., 1997, ApJ, 489, 573

Morris J., Monaghan J., 1997, Journal of Computational Physics, 136, 41

Phinney E. S., 1989, in Morris M., ed., Proc. IAU Symposium Vol. 136, The Center of the Galaxy. Kluwer, Dordrecht, p. 543

Piran T., Svirski G., Krolik J., Cheng R. M., Shiokawa H., 2015, ApJ, 806, 164

Price D. J., 2007, Publ. Astron. Soc. Australia, 24, 159

Price D. J., Federrath C., 2010, MNRAS, 406, 1659

Ramirez-Ruiz E., Rosswog S., 2009, ApJ, 697, L77

Rees M. J., 1988, Nature, 333, 523

Seto N., Muto T., 2010, Phys. Rev. D, 81, 103004

Shakura N. I., Sunyaev R. A., 1973, A&A, 24, 337

Shen R.-F., Matzner C. D., 2014, ApJ, 784, 87

Shiokawa H., Krolik J. H., Cheng R. M., Piran T., Noble S. C., 2015, ApJ, 804, 85

Stone N., Loeb A., 2011, MNRAS, 412, 75

Strubbe L. E., Quataert E., 2009, MNRAS, 400, 2070

Tejeda E., Rosswog S., 2013, MNRAS, 433, 1930

Zauderer B. A., et al., 2011, Nature, 476, 425

van Velzen S., et al., 2011, ApJ, 741, 73

3

Long-term stream evolution in tidal disruption events

A large number of tidal disruption event (TDE) candidates have been observed recently, often differing in their observational features. Two classes appear to stand out: X-ray and optical TDEs, the latter featuring lower effective temperatures and luminosities. These differences can be explained if the radiation detected from the two categories of events originates from different locations. In practice, this location is set by the evolution of the debris stream around the black hole and by the energy dissipation associated with it. In this paper, we build an analytical model for the stream evolution, whose dynamics is determined by both magnetic stresses and shocks. Without magnetic stresses, the stream always circularizes. The ratio of the circularization timescale to the initial stream period is $t_{\rm ev}/t_{\rm min} = 8.3(M_{\rm h}/10^6 M_{\odot})^{-5/3}\beta^{-3}$, where $M_{\rm h}$ is the black hole mass and β is the penetration factor. If magnetic stresses are strong, they can lead to the stream ballistic accretion. The boundary between circularization and ballistic accretion corresponds to a critical magnetic stresses efficiency $v_{\rm A}/v_{\rm c} \approx 10^{-1}$, largely independent of $M_{\rm h}$ and β. However, the main effect of magnetic stresses is to accelerate the stream evolution by strengthening self-crossing shocks. Ballistic accretion therefore necessarily occurs on the stream dynamical timescale. The shock luminosity associated to energy dissipation is sub-Eddington but decays as $t^{-5/3}$ only for a slow stream evolution. Finally, we find that the stream thickness rapidly increases if the stream is unable to cool completely efficiently. A likely outcome is its fast evolution into a thick torus, or even an envelope completely surrounding the black hole.

C. Bonnerot, E. M. Rossi and G. Lodato
2017, *MNRAS*, **Volume 464**, Issue 3, p. 2816-2830

3.1 Introduction

Two-body encounters between stars surrounding a supermassive black hole occasionally result in one of these stars being scattered on a plunging orbit towards the central object. If this star is brought too close to the black hole, the strong tidal forces exceed its self-gravity force, leading to the star's disruption. About half of the stellar material ends up being expelled. The remaining fraction stays bound and returns the black hole as an extended stream of gas (Rees 1988) with a mass fallback rate decaying as $t^{-5/3}$. This bound material is expected to be accreted, resulting in a luminous flare. Such tidal disruption events (TDEs) contain information on the black hole and stellar properties. While white dwarf tidal disruptions necessarily involve black holes with low masses $M_{\rm h} \lesssim 10^5\,{\rm M}_{\odot}$ (MacLeod et al. 2016), TDEs involving giant stars are best suited to probe the higher end of the black hole mass function, with $M_{\rm h} \gtrsim 10^8\,{\rm M}_{\odot}$ (MacLeod et al. 2012). However, the latter might be averted by the dissolution of the debris into the background gaseous environment through Kelvin-Helmholtz instability, likely dimming the associated flare (Bonnerot et al. 2016b). TDEs also represent a unique probe of accretion and relativistic jets physics. Additionally, they could provide insight into bulge-scale stellar processes through the rate at which stars are injected into the tidal sphere to be disrupted.

The number of candidate TDEs is rapidly growing (see Komossa 2015 for a recent review). Most of the detected electromagnetic signals peak in the soft X-ray band (Komossa & Bade 1999; Cappelluti et al. 2009; Esquej et al. 2008; Maksym et al. 2010; Saxton et al. 2012) and at optical and UV wavelengths (Gezari et al. 2006, 2012; van Velzen et al. 2011; Cenko et al. 2012; Arcavi et al. 2014; Holoien et al. 2016). In addition, a small fraction of candidates shows both optical and X-ray emission (e.g. ASSASN-14li, Holoien et al. 2016). Finally, TDEs have been detected in the hard X-ray to γ-ray band (Cenko et al. 2012; Bloom et al. 2011).

The classical picture for the emission mechanism relies on an efficient circularization of the bound debris as it falls back to the disruption site (Rees 1988; Phinney 1989). In this scenario, the emitted signal comes from an accretion disc that forms rapidly from the debris at $\sim 2R_{\rm p}$, where $R_{\rm p}$ denotes the pericentre of the initial stellar orbit. The argument for rapid disc formation involves self-collision of the stream debris due to relativistic precession at pericentre. This picture is able to explain the observed properties of X-ray TDE candidates, which feature an effective temperature $T_{\rm eff} \approx 10^5$ K with a luminosity up to $L \approx 10^{44}$ erg s^{-1}. However, it is inconsistent with the emission detected from optical TDEs, with $T_{\rm eff} \approx 10^4$ K and $L \approx 10^{43}$ erg s^{-1}. This is because the disc emits mostly in the X-ray, with a small fraction of the radiation escaping as optical light, typically only $\lesssim 10^{41}$ erg s^{-1} in terms of luminosity (Lodato & Rossi 2011, their figure 2).

The puzzling features of optical TDEs have motivated numerous investigations. Several works argue that optical photons are emitted from a shell of gas surrounding the black hole at a distance $\sim 100\,R_{\rm p}$. This envelope could reprocess the X-ray emission produced by the accretion disc, giving rise to the optical signal. This reprocessing layer is a natural consequence of several mechanisms, such as winds launched from the outer parts of the accretion disc (Strubbe & Quataert 2009; Lodato & Rossi 2011; Miller 2015) and the formation of a quasistatic envelope from the debris reaching the vicinity of the black hole (Loeb & Ulmer 1997; Guillochon et al. 2014; Coughlin & Begelman 2014; Metzger & Stone 2016). As noticed by Metzger & Stone (2016), the latter possibility is motivated by recent numerical simulations that find that matter can be expelled at large distances from the black hole during the circularization process (Ramirez-Ruiz & Rosswog 2009; Bonnerot et al. 2016a; Hayasaki et al. 2016; Shiokawa et al. 2015; Sądowski et al. 2016).

Another interesting idea has been put forward by Piran et al. (2015), although it has been proposed for the first time by Lodato (2012). They argue that the optical emission could come from energy dissipation associated with the circularization process, and be produced by shocks occurring at distances much larger than R_p. Furthermore, since the associated luminosity relates to the debris fallback rate, they argue that it should scale as $t^{-5/3}$ as found observationally (e.g. Arcavi et al. 2014). Such outer shocks are expected for low apsidal precession angles, which was shown to be true as long as the star only grazes the tidal sphere (Dai et al. 2015). Owing to the weakness of such shocks, these authors suggest that the debris could retain a large eccentricity for a significant number of orbits. Recently, this picture was claimed to be consistent with the X-ray and optical emission detected from ASSASN-14li (Krolik et al. 2016). Nevertheless, the absence of X-ray emission in most optical TDEs is hard to reconcile with this picture, since viscous accretion should eventually occur, leading to the emission of X-ray photons. For this reason, Svirski et al. (2015) proposed that magnetic stresses are able to remove enough angular momentum from the debris to cause its ballistic accretion with no significant emission in tens of orbital times. In their work, energy loss via shocks has been omitted. However, they are likely to occur as the stream self-crosses due to relativistic precession. This provides an efficient circularization mechanism that could give rise to X-ray emission. This is all the more true that the pericentre distance decreases as magnetic stresses act on the stream, thus strengthening apsidal precession and the resulting shocks.

In this paper, we present an analytical treatment of the long-term evolution of the steam of debris under the influence of both shocks and magnetic stresses. We show that, even if the stream retains a significant eccentricity after the first self-crossing, subsequent shocks are likely to further shrink the orbit. Furthermore, the main impact of magnetic stresses is found to be the acceleration of the stream evolution via a strengthening of self-crossing shocks. If efficient enough, magnetic stresses can also lead to ballistic accretion. However, this necessarily happens in the very early stages of the stream evolution. In addition, we demonstrate that a $t^{-5/3}$ decay of the shock luminosity light curve is favoured for a slow stream evolution, favoured for grazing encounters with black hole masses $\lesssim 10^6\,\mathrm{M}_\odot$. This decay law is in general hard to reconcile with ballistic accretion that occurs on shorter timescales. Finally, we demonstrate that if the excess thermal energy injected by shocks is not efficiently radiated away, the stream rapidly thickens to eventually form a thick structure.

This paper is organised as follows. In Section 3.2, the stream evolution model under the influence of shocks and magnetic stresses is presented. In Section 3.3, we investigate the influence of the different parameters on the stream evolution and derive the observational consequences. In addition, we investigate the influence of inefficient cooling on the stream geometry. Finally, Section 3.4 contains the discussion of these results and our concluding remarks.

3.2 Stream evolution model

A star is disrupted by a black hole if its orbit crosses the tidal radius $R_\mathrm{t} = R_\star(M_\mathrm{h}/M_\star)^{1/3}$, where M_h denotes the black hole mass, $M_\star$ and $R_\star$ being the stellar mass and radius. Its pericentre can therefore be written as $R_\mathrm{p} = R_\mathrm{t}/\beta$, where $\beta > 1$ is the penetration factor. During the encounter, the stellar elements experience a spread in orbital energy $\Delta\epsilon = GM_\mathrm{h}R_\star/R_t^2$, given by their depth within the black hole potential well at the moment of disruption (Lodato et al. 2009; Stone et al. 2013). The debris therefore evolves to form an eccentric stream of gas, half of which falls back towards to black hole.

The most bound debris has an energy $-\Delta\epsilon$. It reaches the black hole after $t_\mathrm{min} = 2\pi GM_\mathrm{h}(2\Delta\epsilon)^{-3/2}$ from the time of disruption, following Kepler's third law. Due to relativistic apsidal precession, it then continues its revolution around the black hole on a precessed orbit. This results in a collision with the part of the stream still infalling. This first self-crossing leads to shocks that dissipate part of the debris orbital energy into heat. The resulting stream moves closer to the black hole, its precise trajectory depending on the amount of orbital energy removed. As the stream continues to orbit the black hole, more self-crossing shocks must happen due to apsidal precession at each pericentre passage.

We therefore model the evolution of the stream as a succession of Keplerian orbits, starting from that of the most bound debris. From one orbit to the next, the stream orbital parameters change according to both shocks and magnetic stresses, as described in Sections 3.2.1 and 3.2.2 respectively. This is illustrated in Fig. 3.1 that shows two successive orbits of the stream, labelled N and $N+1$. Knowing the orbital changes between successive orbits allows to compute by iterations the orbital parameters of any orbit N. This iteration is performed until the stream reaches its final outcome, defined by the stopping conditions presented in Section 3.2.4. In the following, variables corresponding to orbit N are indicated by the subscript “N”.

The initial orbit, corresponding to $N = 0$, is that of the most bound debris. It has a pericentre $R^{\rm p}_0$ equal to that of the star $R_{\rm p}$ and an eccentricity $e_0 = 1 - (2/\beta)(M_{\rm h}/M_\star)^{-1/3}$. Its energy is

$$\epsilon_0 = -\Delta\epsilon \propto M_{\rm h}^{1/3}, \tag{3.1}$$

while, using $e_0 \approx 1$, its angular momentum can be approximated as

$$j_0 \approx \sqrt{2GM_{\rm h}R_{\rm p}} \propto M_{\rm h}^{2/3}\beta^{-1/2}. \tag{3.2}$$

From this initial orbit, the orbital parameters of any orbit N are computed iteratively. Its energy and angular momentum are given by

$$\epsilon_N = -\frac{GM_{\rm h}}{2a_N}, \tag{3.3}$$

$$j_N = \sqrt{GM_{\rm h}a_N(1-e_N^2)}, \tag{3.4}$$

respectively as a function of the semi-major axis a_N and eccentricity e_N of the stream. The apocentre and pericentre distances of orbit N are by definition $R^{\rm a}_N = a_N(1+e_N)$ and $R^{\rm p}_N = a_N(1-e_N)$ respectively. At these locations, the stream has velocities $v^{\rm a}_N = (GM_{\rm h}/a_N)^{1/2}((1-e_N)/(1+e_N))^{1/2}$ and $v^{\rm p}_N = (GM_{\rm h}/a_N)^{1/2}((1+e_N)/(1-e_N))^{1/2}$.

Our assumption of a thin stream moving on Keplerian trajectories requires that pressure forces are negligible compared to gravity. This is legitimate as long as the excess thermal energy produced by shocks is radiated efficiently away from the gas. The validity of this approximation is the subject of Section 3.3.3.

Moreover, our treatment of the stream evolution neglects the dynamical impact of the tail of debris that keeps falling back long after the first collision. This fact will be checked a posteriori in Section 3.3.2. It can already be justified qualitatively here through the following argument. At the moment of the first shock, the tail and stream densities are similar. However, later in the evolution, the tail gets stretched resulting in a density decrease. On the other hand, the stream gains mass and moves closer to the black hole as it loses energy. As a consequence, its density increases. The tail therefore becomes rapidly much less dense than the stream, which allows to neglect its dynamical influence on the stream evolution.

3.2.1 Shocks

Apsidal precession causes the first self-crossing shock that makes the debris produced by the disruption more bound to the black hole. The subsequent evolution of the stream is affected

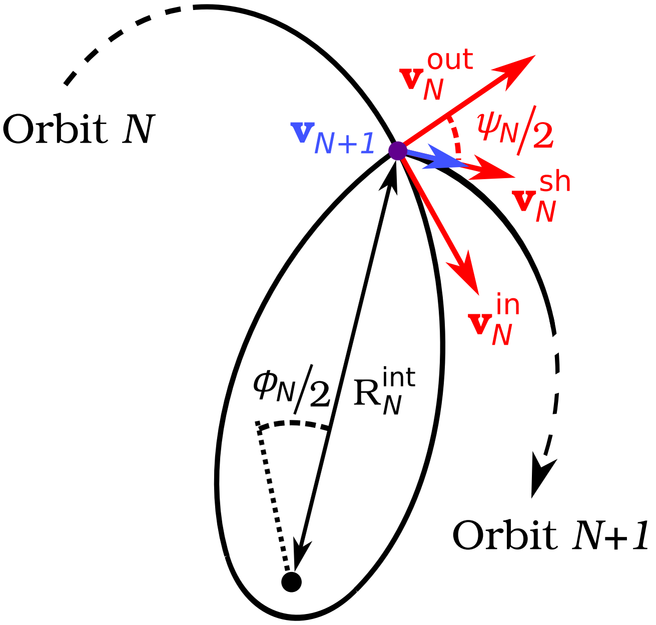

Figure 3.1: Sketch illustrating the stream evolution model as a succession of orbits. Orbit $N+1$ follows orbit N after an energy loss through shocks and an angular momentum loss through magnetic stresses. The associated velocity changes are depicted in red and blue respectively. While the stream is on orbit N, it precesses by an angle ϕ_N, given by equation (3.5). As a result, the stream self-crosses at the intersection point, indicated by the purple point. It occurs at a distance $R_N^{\rm int}$ from the black hole, given by equation (3.6), and with a collision angle ψ_N. The post-shock velocity $\mathbf{v}_N^{\rm sh}$ is obtained from the velocity $\mathbf{v}_N^{\rm in}$ and $\mathbf{v}_N^{\rm out}$ of the two colliding components according to equation (3.7). Immediately after, the stream undergoes magnetic stresses that reduce this velocity to $\mathbf{v}_{N+1}$, given by equation (3.16) and defining the initial velocity of orbit $N+1$.

by a similar process. When an element of the stream passes at pericentre, its orbit precesses, causing its collision with the part of the stream still moving towards pericentre. Once all the stream matter has passed through this intersection point, it continues on a new orbit.

Suppose that the stream is on orbit N. To determine the change of orbital parameters due to shocks as the stream self-crosses, we use a treatment similar to that used by Dai et al. (2015) to predict the orbit resulting from the first self-intersection. This method is also inspired from an earlier work by Kochanek (1994). It is illustrated in Fig. 3.1, with the associated change in velocity shown in red. As orbit N precesses by an angle[1] (Hobson et al. 2006, p. 232)

$$\phi_N = \frac{6\pi G M_{\rm h}}{a_N(1-e_N^2)c^2}, \tag{3.5}$$

it intersects the remaining part of the stream at a distance from the black hole

$$R_N^{\rm int} = \frac{a_N(1-e_N^2)}{1-e_N\cos(\phi_N/2)}. \tag{3.6}$$

The angle in the denominator is computed from a reference direction that connects the pericentre and apocentre of orbit N. At this point, the infalling and outflowing parts of the stream collide. Following Dai et al. (2015), we assume this collision to be completely inelastic. Momentum conservation then sets the resulting velocity to

---

[1] This expression is derived in the small-angle approximation. This is legitimate since our study mainly focuses on outer shocks, for which ϕ_N remains smaller than about 10 degrees. In the case of strong shocks, the stream evolution is fast independently on the precise value of ϕ_N.

$$\mathbf{v}_N^{\rm sh} = \frac{\mathbf{v}_N^{\rm in} + \mathbf{v}_N^{\rm out}}{2}, \tag{3.7}$$

where $\mathbf{v}_N^{\rm in}$ and $\mathbf{v}_N^{\rm out}$ denote the velocity of the inflowing and outflowing components respectively. Equation (3.7) assumes that the two components have equal masses. This is justified since they are part of the same stream. Although this stream might be inhomogeneous shortly after the first shock, inhomogeneities are likely to be suppressed later in its evolution. Note that conservation of momentum implies conservation of angular momentum since this velocity change occurs at a fixed position.

According to equation (3.7), the post-shock velocity is given by $|\mathbf{v}_N^{\rm sh}| = |\mathbf{v}_N| \cos(\psi_N/2)$, where ψ_N is the collision angle between $\mathbf{v}_N^{\rm in}$ and $\mathbf{v}_N^{\rm out}$ and $|\mathbf{v}_N|$ denotes the velocity at the intersection point, equal to $|\mathbf{v}_N^{\rm in}|$ and $|\mathbf{v}_N^{\rm out}|$ because of energy conservation along the Keplerian orbit. Therefore, the energy removed from the stream during the collision is

$$\Delta\epsilon_N = \frac{1}{2}\mathbf{v}_N^2 \sin^2(\psi_N/2). \tag{3.8}$$

Using $\epsilon_N = \mathbf{v}_N^2/2 - GM_{\rm h}/R_N^{\rm int}$ and equation (3.6) combined with $\sin^2(\psi_N/2) = e_N^2 \sin^2(\phi_N/2)/(1 + e_N^2 - 2e_N \cos(\phi_N/2))$, this can be rewritten as

$$\Delta\epsilon_N = \frac{e_N^2}{2}\left(\frac{GM_{\rm h}}{j_N}\right)^2 \sin^2(\phi_N/2), \tag{3.9}$$

which also makes use of the relation $(GM_{\rm h})^2(1 - e_N^2) = -2 j_N^2 \epsilon_N$. Equation (3.9) has the advantage of depending only on the orbital parameters of orbit N. It will be used in Section 3.2.3 to find an equivalent differential equation describing the stream evolution. In addition, equation (3.9) implies that $\Delta\epsilon_N$ is largely independent of N when the stream angular momentum is unchanged, which is the case if magnetic stresses do not affect its evolution. This is because e_N^2 varies only weakly with N while ϕ_N only depends on j_N as can be seen by combining equations (3.4) and (3.5). The constant value of $\Delta\epsilon_N$ can then be obtained by evaluating equation (3.9) at $N = 0$. Simplifying by the small angle approximation $\sin\theta \approx \theta$, it is given by

$$\Delta\epsilon_0 = \left(\frac{9\pi^2}{16c^4}\right) e_0^2 \left(\frac{GM_{\rm h}}{R_{\rm p}}\right)^3 \propto M_{\rm h}^2 \beta^3, \tag{3.10}$$

using equation (3.2) and $e_0 \approx 1$. The fact that $\Delta\epsilon_N \approx \Delta\epsilon_0$ will be used in Section 3.3.1 to find an analytical expression for the circularization timescale of the stream in the absence of magnetic stresses.

3.2.2 Magnetic stresses

Magnetic stresses act on the stream, leading to angular momentum transport outwards. To evaluate the orbital change induced by this mechanism, we follow Svirski et al. (2015). Consider a stream section covering an azimuthal angle $\delta\phi$ and located at a distance $R = j^2/(GM_{\rm h})/(1 + e\cos(\theta))$ from the black hole, j denoting its specific angular momentum and θ its true anomaly. This section loses specific angular momentum at a rate

$$\mathrm{d}j/\mathrm{d}t = (\mathrm{d}\mathcal{G}/\mathrm{d}R)/(\Sigma R \delta\phi). \tag{3.11}$$

In this expression, $\mathcal{G}$ is the rate of angular momentum transport outwards, given by

$$\mathcal{G} = \int_{-\Delta z}^{\Delta z} R \mathcal{M}_{\hat{\mathbf{n}}\hat{\mathbf{t}}} |\hat{\mathbf{r}} \times \hat{\mathbf{t}}| R \delta\phi \mathrm{d}z, \tag{3.12}$$

where Δz denotes the vertical extent of the stream, $\hat{\mathbf{n}}$ and $\hat{\mathbf{t}}$ are unit vectors normal and tangential to the stream section considered while $\hat{\mathbf{r}}$ is in the radial direction. $\mathcal{M}_{\hat{\mathbf{n}}\hat{\mathbf{t}}} = -B_{\hat{\mathbf{n}}} B_{\hat{\mathbf{t}}}/(4\pi)$ denotes the $\hat{\mathbf{n}}$-$\hat{\mathbf{t}}$ component of the Maxwell tensor, $B_{\hat{\mathbf{n}}}$ and $B_{\hat{\mathbf{t}}}$ being the normal and tangential component of the magnetic field. The term $|\hat{\mathbf{r}} \times \hat{\mathbf{t}}| = (1 + e \cos\theta)/(1 + e^2 + 2e\cos\theta)^{1/2}$ is required since only the component of $\hat{\mathbf{t}}$-momentum orthogonal to $\hat{\mathbf{r}}$ contributes to the angular momentum. Combining equations (3.11) and (3.12) then leads to

$$\frac{\mathrm{d}j}{\mathrm{d}t} = \alpha_{\mathrm{mag}} |\hat{\mathbf{r}} \times \hat{\mathbf{t}}| v_{\mathrm{A}}^2, \tag{3.13}$$

where $\alpha_{\mathrm{mag}} = -2B_{\hat{\mathbf{n}}} B_{\hat{\mathbf{t}}}/B^2$ and $v_{\mathrm{A}}^2 = \int_{-\Delta z}^{\Delta z} B^2 \mathrm{d}z/(4\pi\Sigma)$ is the squared Alfvén velocity. The angular momentum Δj lost by the stream section[2] in one period is then obtained by integrating equation (3.13). Using the chain rule to combine equation (3.13) with Kepler's second law $\mathrm{d}\theta/\mathrm{d}t = j/R^2$ and integrating over θ, it is found to be

$$\Delta j = K_e \left(\frac{v_{\mathrm{A}}}{v_{\mathrm{c}}}\right)^2 j, \tag{3.14}$$

where

$$K_e \equiv \alpha_{\mathrm{mag}} \int_0^{2\pi} f_e(\theta) \mathrm{d}\theta, \tag{3.15}$$

with $f_e(\theta) \equiv (1 + e^2 + 2e\cos\theta)^{-1/2}$ and $v_{\mathrm{c}} = (GM_{\mathrm{h}}/R)^{1/2}$ being the circular velocity at R. Equation (3.14) has been obtained by assuming that α_{mag} and $v_{\mathrm{A}}/v_{\mathrm{c}}$ are independent of R. In the following, we set $\alpha_{\mathrm{mag}} = 0.4$, as motivated by magnetohydrodynamical simulations (Hawley et al. 2011). The value of $v_{\mathrm{A}}/v_{\mathrm{c}}$ is varied from 10^{-2} to 1. This range of values relies on the assumption that magneto-rotational instability has fully developed at its fastest rate associated to its most disruptive mode. The former is reached for $v_{\mathrm{A}} k \simeq v_{\mathrm{c}}/R$, k being the wavenumber of the instability (Balbus & Hawley 1998). The latter corresponds to the lowest wavenumber available, that is $k \simeq 1/H$ where H denotes the width of the stream. Therefore, $v_{\mathrm{A}}/v_{\mathrm{c}} \simeq H/R$, which likely varies from 10^{-2} to 1. It is however possible that the MRI did not have time to reach saturation in the early stream evolution since it requires about 3 dynamical times (Stone et al. 1996). This would lead to lower values of $v_{\mathrm{A}}/v_{\mathrm{c}}$. Since $f_e(\pi)/f_e(0) = (1+e)/(1-e) \gg 1$ for $1 - e \ll 1$, the integrand in equation (3.15) is the largest for $\theta \approx \pi$. As noticed by Svirski et al. (2015), this means that the angular momentum loss happens mostly close to apocentre as long as the eccentricity is large, which is true during the stream evolution. Instead, if the stream reaches a nearly circular orbit, angular momentum is lost roughly uniformly along the orbit. This argument will be used in Section 3.2.4 to define one of the stopping criterion of the iteration.

Since magnetic stresses act mostly at apocentre, we implement it as an instantaneous angular momentum loss at this location. The angular momentum removed from orbit N is then obtained from equation (3.14) by $\Delta j_N = K_e (v_{\mathrm{A}}/v_{\mathrm{c}})^2 j_N$. The post-shock velocity given by equation (3.7) has no radial component, which can also be seen from Fig. 3.1. This implies that the apocentre of each orbit is located at the self-crossing point. Angular momentum loss therefore amounts to reducing the post-shock velocity given by equation (3.7) by a factor $1 - \Delta j_N / j_N$. This defines the initial velocity of orbit $N + 1$

---

[2] More precisely, angular momentum is transferred outwards from the bulk of the stream to a gas parcel of negligible mass. It is therefore a fair assumption to assume that this angular momentum is lost.

$$\mathbf{v}_{N+1} = \max\left(0, 1 - \frac{\Delta j_N}{j_N}\right)\mathbf{v}_N^{\mathrm{sh}}, \tag{3.16}$$

where the first term on the right-hand side is required to be positive to prevent change of direction between $\mathbf{v}_{N+1}$ and $\mathbf{v}_N^{\mathrm{sh}}$. Orbit $N+1$ starts from the intersection point given by equation (3.6). Combined with its initial velocity, it allows to compute the orbital elements of orbit $N + 1$.

3.2.3 Equivalent differential equation

As the stream follows the succession of orbits described above, its energy ϵ and angular momentum j vary. In the ϵ-j plane, the stream evolution is equivalent to the differential equation

$$\frac{\mathrm{d}j}{\mathrm{d}\epsilon} = \frac{\Delta j}{\Delta \epsilon} \tag{3.17}$$

as long as the number of ellipses describing the stream evolution is sufficiently large, where $\Delta\epsilon$ and Δj are given by equations (3.9) and (3.14) respectively. Using the scaled quantities $\bar{\epsilon} = -\epsilon/c^2$ and $\bar{j} = j/(R_{\mathrm{g}}c)$, equation (3.17) becomes

$$\frac{\mathrm{d}\bar{j}}{\mathrm{d}\bar{\epsilon}} = -2\left(\frac{K_e}{e^2}\right)\left(\frac{v_{\mathrm{A}}}{v_{\mathrm{c}}}\right)^2 \frac{\bar{j}^3}{\sin^2(3\pi/\bar{j}^2)}. \tag{3.18}$$

In addition, the precession angle has been written as a function of angular momentum combining equations (3.4) and (3.5). This differential equation can be solved numerically for the initial conditions $\bar{\epsilon}_0$ and $\bar{j}_0$, obtained from equations (3.1) and (3.2). The use of scaled quantities makes equation (3.18) independent of M_{h} and β. However, the initial conditions depend on these parameters as $\bar{\epsilon}_0 \propto M_{\mathrm{h}}^{1/3}$ and $\bar{j}_0 \propto M_{\mathrm{h}}^{-1/3}\beta^{-1/2}$.

An analytical solution can be found by slightly modifying equation (3.18). The small angle approximation $\sin\theta \approx \theta$ allows to simplify the denominator. In addition, since K_e/e^2 only varies by a factor of a few with e, it can be replaced by an average value $\tilde{K} \equiv \left\langle K_e/e^2 \right\rangle$. Numerically, we find that this factor can be fixed to $\tilde{K} = 5$ independently on the parameters. The resulting simplified equation is $\mathrm{d}\bar{j}/\mathrm{d}\bar{\epsilon} = -2\tilde{K}(v_{\mathrm{A}}/v_{\mathrm{c}})^2\bar{j}^7/(9\pi^2)$ whose analytical solution is

$$\bar{\epsilon} - \bar{\epsilon}_0 = \frac{3\pi^2}{4\tilde{K}}\left(\frac{v_{\mathrm{A}}}{v_{\mathrm{c}}}\right)^{-2}\left(\bar{j}^{-6} - \bar{j}_0{}^{-6}\right). \tag{3.19}$$

This simplified solution will be used in Section 3.3 to prove interesting properties associated to the stream evolution.

3.2.4 Stream evolution outcome

As described above, the stream evolution is modelled by a succession of ellipses. The orbital elements of any orbit N can be computed iteratively knowing the orbital changes between successive orbits. This iteration is stopped when the stream reaches one of the two following possible outcomes. They correspond to critical values of the orbit angular momentum and eccentricity, below which the computation is stopped.

1. *Ballistic accretion*: if $j_N < j_{\mathrm{acc}} \equiv 4R_{\mathrm{g}}c$, the angular momentum of the stream is low enough for it to be accreted onto the black hole without circularizing.

2. *Circularization*: if $e_N < e_{\mathrm{circ}} = 1/3$, which corresponds to a stream apocentre equal to only twice its pericentre, we consider that the stream has circularized.

Strictly speaking, the expression adopted for j_{acc} is valid only for a test-particle on a parabolic orbit. For a circular orbit, it reduces to $2\sqrt{3}R_{\mathrm{g}}c$ (Hobson et al. 2006), which is lower by a factor of order unity. However, this choice does not significantly affect our results as will be demonstrated in Section 3.3.1. We therefore consider j_{acc} as independent of the stream orbit. Our choice for the critical eccentricity e_{circ} can be understood by looking at the integral term in equation (3.15), below which the function f_e is defined. Our stopping criterion $e < 1/3$ implies $f_e(\pi)/f_e(0) < 2$, which means that the stream loses less than twice as much angular momentum at apocentre than at pericentre. It is therefore legitimate to assume that angular momentum is lost homogeneously along the stream orbit from this point on.

If the computation ends with criterion (i), the stream is accreted. Its subsequent evolution is then irrelevant since it leads to no observable signal. If instead the computation ends with criterion (ii), a circular disc forms from the stream. This disc evolution is driven by magnetic stresses only, which act to shrink the disc nearly circular orbit until it reaches the innermost stable circular orbit, where it is accreted onto the black hole.

3.3 Results

We now present the results of our stream evolution model, which depends on three parameters: the black hole mass M_{h}, the penetration factor β and the ratio of Alfvén to circular velocity $v_{\mathrm{A}}/v_{\mathrm{c}}$.[3] The first two parameters define the initial orbit of the debris through equations (3.1) and (3.2), from which the iteration starts. As can be seen from equation (3.14), the parameter $v_{\mathrm{A}}/v_{\mathrm{c}}$ sets the efficiency of magnetic stresses at removing angular momentum from the stream. The star's mass and radius are fixed to the solar values.

The time required for the stream to reach a given orbital configuration is defined as the time spent by the most bound debris in all the previous orbits, starting from its first passage at pericentre after the disruption. Of particular importance is the time required for the stream to reach its final configuration, corresponding to either ballistic accretion or circularization. This evolution time is denoted t_{ev}.[4]

As in Section 3.2.3, the scaled energy and angular momentum $\bar{\epsilon} = -\epsilon/c^2 > 0$ and $\bar{j} = j/(R_{\mathrm{g}}c)$ will often be adopted in the following. Note that energy loss implies an increase of $\bar{\epsilon}$ due to the minus sign.

3.3.1 Dynamical evolution of the stream

We start by investigating the stream evolution for a tidal disruption by a black hole of mass $M_{\mathrm{h}} = 10^6\,\mathrm{M}_{\odot}$ with a penetration factor $\beta = 1$. Two different magnetic stresses efficiencies are examined, corresponding to $v_{\mathrm{A}}/v_{\mathrm{c}} = 0.06$ and 0.3. The stream evolution is shown in Fig. 3.2 for these two examples. It is represented by the ellipses it goes through, starting from the orbit of the most bound debris whose apocentre is indicated by a green star. The final configuration of the stream is shown in orange. For $v_\mathrm{A}/v_\mathrm{c} = 0.06$ (upper panel), the stream gradually shrinks and becomes circular at $t_\mathrm{ev}/t_\mathrm{min} = 3$. The evolution differs for $v_\mathrm{A}/v_\mathrm{c} = 0.3$ (lower panel) where the stream ends up being ballistically accreted at $t_\mathrm{ev}/t_\mathrm{min} = 0.6$. These evolutions can also be examined using Fig. 3.3 (black solid lines), which shows the associated path in the $\bar{j} - \bar{\epsilon}$ plane. For $v_\mathrm{A}/v_\mathrm{c} = 0.06$ (orange arrow), the stream evolves slowly initially as can be seen from the black points associated to fixed time intervals. As it loses more energy and angular momentum, the evolution accelerates and the stream rapidly circularizes reaching the grey dash-dotted line on the right of the figure that corresponds to $e = e_\mathrm{circ}$. Note that if no magnetic stresses were present, the stream would still circularize but following an horizontal line in this plane. For $v_\mathrm{A}/v_\mathrm{c} = 0.3$ (purple arrow), the stream rapidly loses angular momentum which leads to its ballistic accretion when $j < j_\mathrm{acc}$, crossing the horizontal grey dash-dotted line. The stream evolution outcome therefore depends on the efficiency of magnetic stresses, given by the parameter $v_\mathrm{A}/v_\mathrm{c}$. If they act fast enough, the stream loses enough angular momentum to be accreted with a substantial eccentricity. Otherwise, the energy loss through shocks dominates, resulting in the stream circularization.

---

[3] 3D visualizations of the results presented in this paper can be found at http://home.strw.leidenuniv.nl/~bonnerot/research.html.

[4] If the stream shrinks by a large factor from one orbit to the next, the debris might be distributed on several distinct orbits. It is then possible that the whole stream has not reached its final configuration even though the most bound debris did. This could lead to an underestimate of t_{ev}.

The influence of the magnetic stresses efficiency $v_\mathrm{A}/v_\mathrm{c}$ on the stream evolution can be analysed more precisely from Fig. 3.4, which shows the semi-major axis a_f of the stream at the end of its evolution as a function of $v_\mathrm{A}/v_\mathrm{c}$. The other parameters are fixed to $M_\mathrm{h} = 10^6\,\mathrm{M}_\odot$ and $\beta = 1$. For low values of $v_\mathrm{A}/v_\mathrm{c} \approx 10^{-2}$, the stream circularizes at the circularization radius $(1 + e_0)R_0^\mathrm{p} \approx 2R_\mathrm{t}$ obtained from angular momentum conservation (horizontal dashed line). As $v_\mathrm{A}/v_\mathrm{c}$ increases, the stream circularizes closer to the black hole since its angular momentum decreases due to magnetic stresses during the circularization process. At $v_\mathrm{A}/v_\mathrm{c} \approx 10^{-1}$, the final semi-major axis reaches its lowest value. This minimum corresponds to circularization with an angular momentum exactly equal to j_acc, for which $a_\mathrm{f} = 18R_\mathrm{g} \approx 0.4R_\mathrm{t}$. For $v_\mathrm{A}/v_\mathrm{c} \gtrsim 10^{-1}$, the stream ends its evolution by being ballistically accreted. This demonstrates again the existence of a critical value $(v_\mathrm{A}/v_\mathrm{c})_\mathrm{cr}$ for the magnetic stresses efficiency (vertical solid red line) that defines the boundary between circularization (on the left) and ballistic accretion (on the right). The final semi-major axis reaches a plateau at $v_\mathrm{A}/v_\mathrm{c} \gtrsim 0.4$, for which the stream gets ballistically accreted after its first shock. In this region, $a_\mathrm{f} \approx R_0^\mathrm{int}/2 = 40R_\mathrm{t}$, where $R_0^\mathrm{int} = 80R_\mathrm{t}$ denotes the distance to the first intersection point (see Fig. 3.2). The oscillations visible for $v_\mathrm{A}/v_\mathrm{c} \lesssim 0.4$ are associated to different numbers of orbits followed by the stream before its ballistic accretion. On the left end of the plateau, the stream gets accreted after the first self-crossing shock with an angular momentum just below j_acc. Decreasing $v_\mathrm{A}/v_\mathrm{c}$ by a small amount prevents this ballistic accretion since the stream now has an angular momentum just above j_acc after the first shock. The stream therefore undergoes a second shock, which is strong since the previous pericentre passage occurred close to the black hole with a large precession angle. The stream semi-major axis therefore decreases by a large amount before ballistic accretion. This results in a discontinuity in a_f at the edge of the plateau. Decreasing $v_\mathrm{A}/v_\mathrm{c}$ further, the stream passes further away from the black hole which reduces apsidal precession and weakens the second shock. As a result, a_f increases. When $v_\mathrm{A}/v_\mathrm{c}$ becomes low enough for ballistic accretion to be prevented after the second shock, a strong third shock occurs before ballistic accretion which causes a second discontinuity due to the sharp decrease of a_f. The same mechanism occurs for larger numbers of orbits preceding ballistic accretion, producing the other discontinuities and increases of a_f seen for a decreasing $v_\mathrm{A}/v_\mathrm{c}$ and resulting in this oscillating pattern.

The role of $v_\mathrm{A}/v_\mathrm{c}$ in determining the stream evolution outcome can be understood by looking again at Fig. 3.3. The black solid lines are associated to the succession of ellipses described above. The red dashed line shows the numerical solution of the equivalent differen-

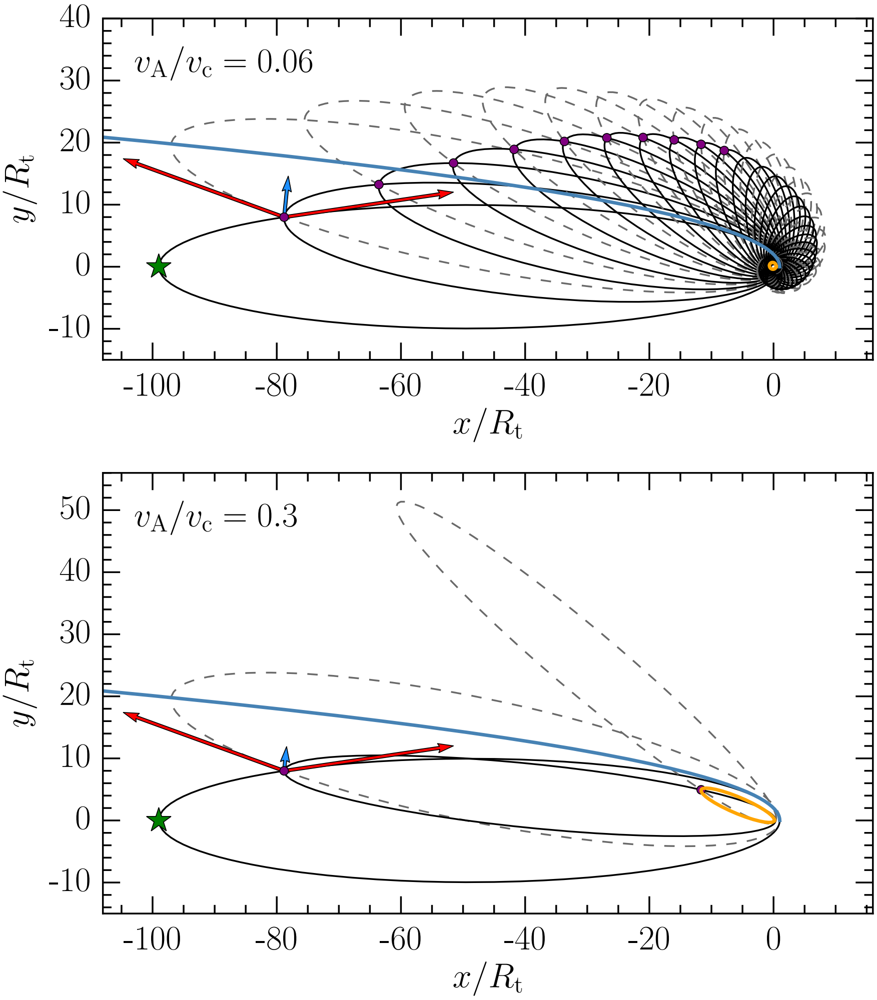

Figure 3.2: Stream evolution for two magnetic stresses efficiencies $v_\mathrm{A}/v_\mathrm{c} = 0.06$ (upper panel) and 0.3 (lower panel). The black hole mass and penetration factor are fixed to $M_\mathrm{h} = 10^6\,\mathrm{M}_\odot$ and $\beta = 1$. The black hole is at the origin. The succession of ellipses starts from the orbit of the most bound debris, whose apocentre is indicated by a green star on the left of the figure. Each stream orbit is divided into two ellipses. The stream elements moving towards the black hole follow the black ellipses. The dashed grey ellipses, precessed with respect to the black ones, are covered by the gas elements moving away from the black hole after pericentre passage. The intersection point is located where the black and grey ellipses cross. At this point, the orbit of the stream changes due to shocks and magnetic stresses. The stream elements then infall towards the black hole on the next solid black ellipse. The first ten self-crossing points are indicated by the purple dots. At the first crossing point, where the transition between orbit 0 and 1 happens, the red arrows show the velocity of the components involved in the associated shock, $\mathbf{v}_0^\mathrm{in}$ and $\mathbf{v}_0^\mathrm{out}$. The blue arrow indicates the initial velocity of orbit 1, $\mathbf{v}_1$, after the debris experienced both shocks and magnetic stresses. This situation is also illustrated in Fig. 3.1 for $N = 0$. The final orbit of the stream, for which one of the two stopping criteria is satisfied, is depicted in orange. For $v_\mathrm{A}/v_\mathrm{c} = 0.06$, the stream circularizes to form a disc. For $v_\mathrm{A}/v_\mathrm{c} = 0.3$, the stream is ballistically accreted before circularizing. The blue line represents a parabolic trajectory with pericentre R_p, equal to that of the star. The trajectories of the debris falling back towards the black hole within the tail are therefore contained between this line and the orbit of the most bound debris.

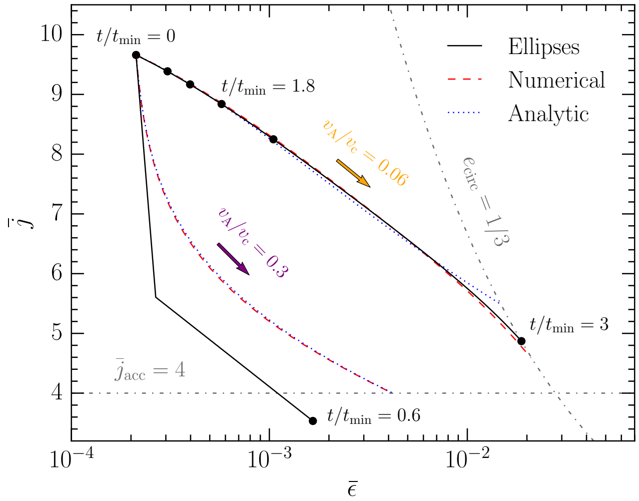

Figure 3.3: Stream evolution shown in the $\bar{j} - \bar{\epsilon}$ plane for two values of $v_{\rm A}/v_{\rm c} = 0.06$ (orange arrow) and 0.3 (purple arrow). The black hole mass and penetration factor are fixed to $M_{\rm h} = 10^6\,{\rm M}_\odot$ and $\beta = 1$. The spatial stream evolution for these two examples is shown in Fig. 3.2. The black solid line corresponds to the succession of ellipses. The red dashed line shows the numerical solution of the differential equation (3.17) while the blue dotted line shows the simplified analytical solution given by equation (3.19) with $\tilde{K} = 5$. The horizontal grey dash-dotted line represents the angular momentum $\bar{j}_{\rm acc} = 4$ below which ballistic accretion occurs while the vertical one shows the eccentricity $e_{\rm crit} = 1/3$ below which circularization happens.

tial equation (3.18) while the blue dotted line corresponds to the simplified analytical version, given by equation (3.19). For $v_{\rm A}/v_{\rm c} = 0.06$, these three descriptions are consistent and able to capture the stream evolution. For $v_{\rm A}/v_{\rm c} = 0.3$, the evolution obtained from the succession of ellipses differs from the two others. This is expected since the stream goes through only three ellipses in this case, not enough for its evolution to be described by the equivalent differential equation. An interesting property of these solutions can be identified from equation (3.19). As soon as $\bar{\epsilon} \gg \bar{\epsilon}_0$ and $\bar{j}^6 \ll \bar{j}_0^6$, the position of the stream in the $\bar{j} - \bar{\epsilon}$ plane becomes independent of the initial conditions $\bar{\epsilon}_0$ and $\bar{j}_0$, given by equations (3.1) and (3.2) respectively. It is therefore dependent on $v_{\rm A}/v_{\rm c}$ only, but not on $M_{\rm h}$ and β anymore. In this case, one expect the critical value $(v_{\rm A}/v_{\rm c})_{\rm cr}$ of the magnetic stresses efficiency to also be completely independent of $M_{\rm h}$ and β. In practice, the first condition $\bar{\epsilon} \gg \bar{\epsilon}_0$ is always satisfied as long as the stream loses energy by undergoing a few shocks since the initial orbit is nearly parabolic with $\bar{\epsilon}_0 \approx 0$. The second one $\bar{j}^6 \ll \bar{j}_0^6$ is however not satisfied in general for low values of $\bar{j}_0$. In fact, $\bar{j}_0$ can be already close to $\bar{j}_{\rm acc} = 4$ for large β or $M_{\rm h}$, since $\bar{j}_0 = j_0/(R_{\rm g}c) \propto \beta^{-1/2} M_{\rm h}^{-1/3}$ (equation (3.2)). To account for this possibility, we define the factor $f_0 \equiv (\bar{j}_0/\bar{j}_{\rm acc})^{-6}$ satisfying $0 < f_0 < 1$. The critical value $(v_{\rm A}/v_{\rm c})_{\rm cr}$, for which the stream circularizes with an angular momentum $\bar{j} = 4$ (see Fig. 3.4), can then be obtained analytically by fixing $e = 1/3$ and $\bar{j} = 4$ in equation (3.19) combined with $1 - e^2 = 2\bar{j}^2\bar{\epsilon}$. This yields $(v_{\rm A}/v_{\rm c})_{\rm cr} = \pi(4096\tilde{K}/27(1 - f_0))^{-1/2}$ whose numerical value is

$$\left(\frac{v_{\rm A}}{v_{\rm c}}\right)_{\rm cr} \approx 10^{-1}\,(1 - f_0)^{1/2} \tag{3.20}$$

using $\tilde{K} = 5$. As anticipated, $(v_{\rm A}/v_{\rm c})_{\rm cr} \approx 10^{-1}$ independently of $M_{\rm h}$ and β as long as $f_0 \ll 1$. This is the case for $M_{\rm h} = 10^6$ and $\beta = 1$, for which $f_0 \approx 5 \times 10^{-3} \ll 1$. We therefore recover

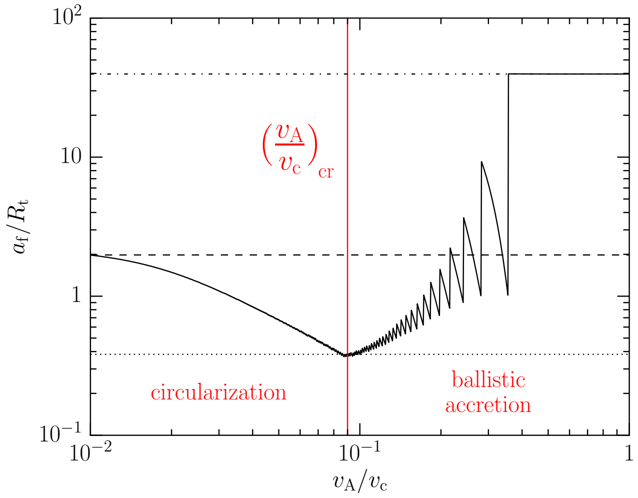

Figure 3.4: Semi-major axis of the stream at the end of the stream evolution as a function of the magnetic stresses efficiency $v_\mathrm{A}/v_\mathrm{c}$. The two other parameters are fixed to $M_\mathrm{h} = 10^6\,\mathrm{M}_\odot$ and $\beta = 1$, for which the spatial stream evolution is shown in Fig. 3.2. From top to bottom, the horizontal lines have the following meanings. The dot-dashed line indicates the semi-major axis of the stream after the first shock $a_1 \approx R_0^\mathrm{int}/2 = 40R_\mathrm{t}$ where R_0^int denotes the distance to the first self-crossing point. The dashed line represents the circularization radius obtained from angular momentum conservation $(1+e_0)R_0^\mathrm{p} \approx 2R_\mathrm{t}$. Finally, the dotted line shows the semi-major axis corresponding to a circular orbit with angular momentum j_acc, equal to $18R_\mathrm{g} \approx 0.4R_\mathrm{t}$.

the value of $(v_\mathrm{A}/v_\mathrm{c})_\mathrm{cr} \approx 10^{-1}$ indicated in Fig. 3.4 (red vertical line). For larger M_h or β, the condition $f_0 \ll 1$ is not necessarily satisfied. For example, $f_0 \approx 0.5$ for $M_\mathrm{h} = 10^7$ and $\beta = 1$. In this case, $(v_\mathrm{A}/v_\mathrm{c})_\mathrm{cr}$ is slightly lower according to equation (3.20), but only by a factor less than 2. In practice, $f_0 \approx 1$ only in the extreme case where the stream is originally on the verge of ballistic accretion with j_0 very close to j_acc. We can therefore conclude that the magnetic stresses efficiency, delimiting the boundary between circularization and ballistic accretion, has a value $(v_\mathrm{A}/v_\mathrm{c})_\mathrm{cr} \approx 10^{-1}$ largely independently on the other parameters of the model, M_h and β. In addition, note that this value is not significantly affected by the choice we made for j_acc as mentioned in Section 3.2.4.

The value of $(v_\mathrm{A}/v_\mathrm{c})_\mathrm{cr}$ derived analytically in equation (3.20) can be confirmed from Fig. 3.5, which shows the stream evolution in the $\bar{j} - \bar{\epsilon}$ plane for various values of the parameters. The different lines have the same meaning as in Fig. 3.3. In each panels, the six sets of lines shows different values of $v_\mathrm{A}/v_\mathrm{c} = 0.01, 0.03, 0.1, 0.3$ and 1 (from top to bottom). The different panels correspond to various choices for M_h and β. The thick set of lines indicates $v_\mathrm{A}/v_\mathrm{c} = 10^{-1}$. As expected from equation (3.20), it corresponds exactly to the boundary between circularization and ballistic accretion for $M_\mathrm{h} = 10^6\,\mathrm{M}_\odot$ (upper left panel) and $10^5\,\mathrm{M}_\odot$ (lower left panel), both with $\beta = 1$. This is because $f_0 \ll 1$ in these cases. However, increasing the black hole mass to $M_\mathrm{h} = 10^7\,\mathrm{M}_\odot$ (lower right panel) or the penetration factor to $\beta = 5$ (upper right panel), the stream is ballistically accreted for $v_\mathrm{A}/v_\mathrm{c} = 10^{-1}$. This comes from the fact that f_0 is not completely negligible in these cases, which implies $(v_\mathrm{A}/v_\mathrm{c})_\mathrm{cr} < 10^{-1}$ according to equation (3.20).

Although the stream evolution outcome only varies with the magnetic efficiency $v_\mathrm{A}/v_\mathrm{c}$, the time required to reach this final configuration and the orbits it goes through in the process are dependent on M_h and β in addition to $v_\mathrm{A}/v_\mathrm{c}$. The effect of varying the black hole mass

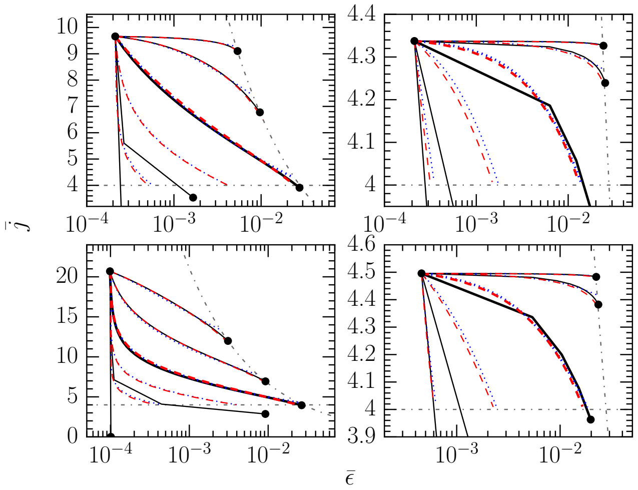

Figure 3.5: Stream evolution shown in the $\bar{j}-\bar{\epsilon}$ plane for various values of the parameters. The meaning of the different lines are the same as in Fig. 3.3. In each panel, the five sets of curves correspond to different values of the magnetic efficiency $v_{\rm A}/v_{\rm c}$ = 0.01, 0.03, 0.1, 0.3 and 1 (from top to bottom). The different panels correspond to different values of $M_{\rm h}$ and β. The two top panels show $M_{\rm h} = 10^6\,{\rm M}_\odot$ for $\beta = 1$ (upper left) and for $\beta = 5$ (upper right). The two bottom panels adopt $\beta = 1$ for $M_{\rm h} = 10^5\,{\rm M}_\odot$ (lower left) and $M_{\rm h} = 10^7\,{\rm M}_\odot$ (lower right). The set of thicker curves is associated to a magnetic stresses efficiency $v_{\rm A}/v_{\rm c} = 0.1$, which approximately corresponds to the critical value (equation (3.20)) defining the boundary between circularization and ballistic accretion, independently on $M_{\rm h}$ and β.

only can be seen by looking at Fig. 3.6, which shows the stream evolution for $M_{\rm h} = 10^5\,{\rm M}_\odot$ (upper panel) and $10^7\,{\rm M}_\odot$ (lower panel) keeping the other two parameters fixed to $\beta = 1$ and $v_{\rm A}/v_{\rm c} = 0.06$. The intermediate case, with $M_{\rm h} = 10^6\,{\rm M}_\odot$, is shown in Fig. 3.2 (upper panel). For larger black hole masses, the time for the stream to circularize is shorter, varying from $t_{\rm ev}/t_{\rm min}$ = 24 to 0.05 from $M_{\rm h} = 10^5\,{\rm M}_\odot$ to $10^7\,{\rm M}_\odot$. Note that this time is also reduced in physical units, from $t_{\rm ev}$ = 310 to 6 days. The reason is that increasing the black hole mass leads to a larger precession angle, which causes the stream to self-cross closer to the black hole and lose more energy. As a result, the stream evolves faster to its final configuration. The same trend is expected if the penetration β is increased since the precession angle scales as $\phi \propto R_{\rm g}/R_{\rm p} \propto \beta M_{\rm h}^{2/3}$. Fig. 3.7 proves this fact by showing the evolution time as a function of black hole mass for several values of β and $v_{\rm A}/v_{\rm c}$. The different colours correspond to different values of $v_{\rm A}/v_{\rm c}$ while the width of the shaded areas represents various values of β from 1 (upper line) to 5 (lower line). Furthermore, it can be seen that the stream evolves more rapidly for larger values of $v_{\rm A}/v_{\rm c}$. For example, $t_{\rm ev}$ decreases by about 2 orders of magnitude for $M_{\rm h} = 10^5\,{\rm M}_\odot$ when the magnetic efficiency is increased from $v_{\rm A}/v_{\rm c}$ = 0 to 0.3. This is because angular momentum loss from the stream at apocentre causes a decrease of its pericentre distance, which results in stronger shocks and a faster stream evolution.

For $v_{\rm A}/v_{\rm c} = 0$, the angular momentum of the stream is conserved. The energy lost by the stream at each self-crossing is then independent of the stream orbit as explained at the end of Section 3.2.1. In this case, the evolution time obeys the simple analytic expression

$$\frac{t_{\rm ev}}{t_{\rm min}} = \frac{2\Delta\epsilon}{\Delta\epsilon_0} = 8.3\left(\frac{M_{\rm h}}{10^6\,{\rm M}_\odot}\right)^{-5/3}\beta^{-3}, \tag{3.21}$$

where $\Delta\epsilon_0$ represents the energy lost at each self-crossing shock, given by equation (3.10).

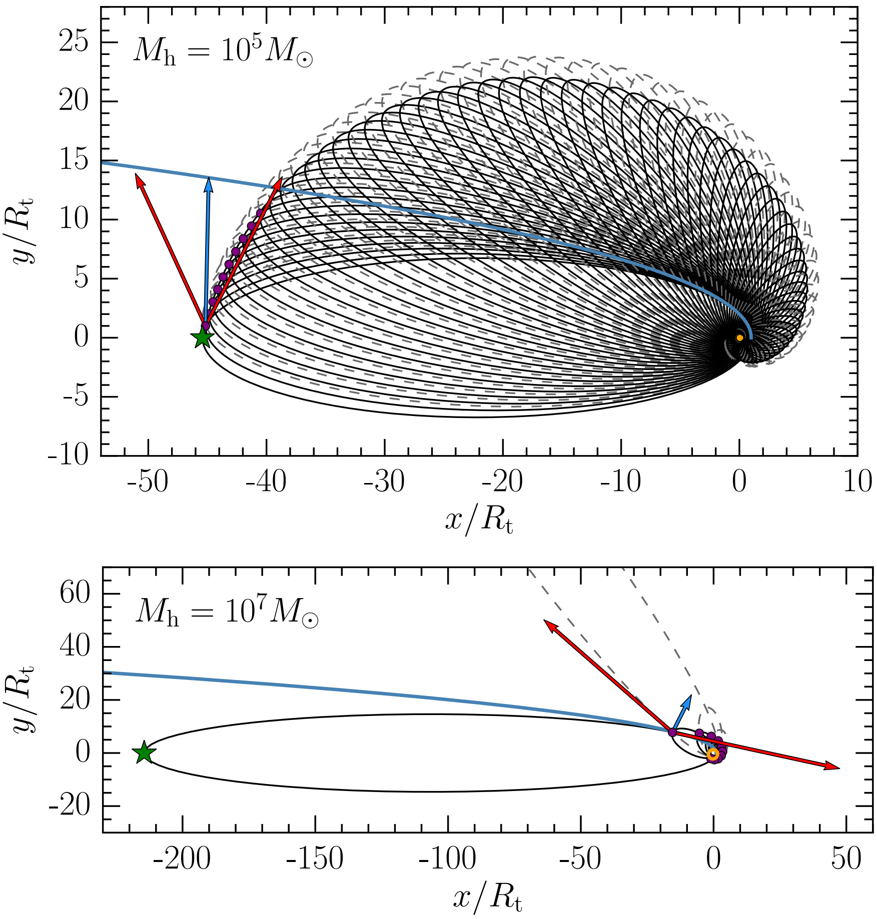

Figure 3.6: Stream evolution for $M_{\rm h} = 10^5\,{\rm M}_\odot$ (upper panel) and $M_{\rm h} = 10^7\,{\rm M}_\odot$ (lower panel) with $\beta = 1$ and $v_{\rm A}/v_{\rm c} = 0.06$. The different elements of this figure have the same meaning as in Fig 3.2, whose upper panel shows the intermediate case with $M_{\rm h} = 10^6\,{\rm M}_\odot$.

It should not be confused with $\Delta\epsilon$, which is the initial energy of the stream equal to that of the most bound debris according to equation (3.1). For clarity, the derivation of equation (3.21) is made in Appendix A. As can be seen from Fig. 3.7, this analytical estimate (dashed black lines) matches very well the value of the evolution time obtained from the succession of ellipses with $v_{\rm A}/v_{\rm c} = 0$ (black solid lines) for both $\beta = 1$ and 5. Equation (3.21) comes from a mathematical derivation but does not have a clear physical reason. Imposing $t_{\rm ev}/t_{\rm min}$ to be constant leads to the relation $\beta \propto M_{\rm h}^{-5/9}$. Interestingly, this dependence is similar although slightly shallower than that obtained by imposing $R_{\rm p}/R_{\rm g}$ to be constant, which gives $\beta \propto M_{\rm h}^{-2/3}$. This latter relation has been used by several authors to extrapolate the results of disc formation simulations from unphysically low-mass black holes to realistic ones (e.g. Shiokawa et al. 2015).

When $v_{\rm A}/v_{\rm c} > (v_{\rm A}/v_{\rm c})_{\rm cr} \approx 10^{-1}$ and the stream is eventually ballistically accreted, the evolution time $t_{\rm ev}$ is always less than a few $t_{\rm min}$ for $M_{\rm h} \approx 10^6\,{\rm M}_\odot$. Moreover, a significant amount of energy is lost before accretion, resulting in a final orbit substantially less eccentric than initially. A typical case of ballistic accretion is illustrated by Fig. 3.2 (lower panel). The

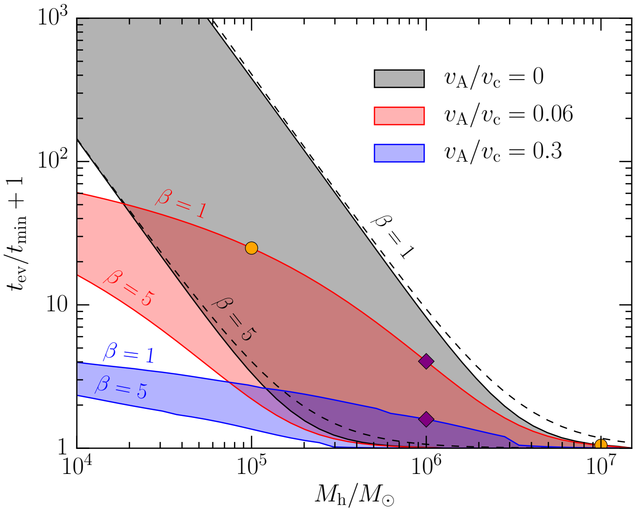

Figure 3.7: Evolution time of the stream as a function of black hole mass. The three shaded areas correspond to three values of the magnetic stresses efficiency $v_{\rm A}/v_{\rm c}$ = 0 (black), 0.06 (red) and 0.3 (blue). Each area is delimited by two lines, which are associated to β = 1 (upper line) and 5 (lower line). The dashed black lines show the analytical estimate for the evolution time in the absence of magnetic stresses given by equation (3.21) for β = 1 (top line) and 5 (bottom line). The cases shown in Fig. 3.2 and 3.6 are represented by the two purple diamonds and orange circles respectively.

only scenario where significant energy loss is avoided is if the stream is accreted immediately after the first shock. However, in this case, $t_{\rm ev}$ is very low. This behaviour is quite different from the evolution described by Svirski et al. (2015), for which the stream remains highly elliptical for tens of orbits progressively losing angular momentum via magnetic stresses before being ballistically accreted. Our calculations demonstrate instead that ballistic accretion happens on a short timescale, most of the time associated with a significant energy loss via shocks.

3.3.2 Observational appearance

We now investigate the main observational features associated to the stream evolution. Two sources of luminosity are identified, which can be evaluated from the dynamical stream evolution presented in Section 3.3.1. The first source is associated to the energy lost by the stream due to self-intersecting shocks. The associated stream self-crossing shock luminosity can be evaluated as

$$L^{\rm s}_{\rm sh} = \eta^{\rm s}_{\rm sh}\dot{M}_{\rm s}\Delta\epsilon_{\rm s}, \tag{3.22}$$

where $\Delta\epsilon_{\rm s}$ is the instantaneous energy lost from the stream, obtained from the succession of orbits described in Section 3.3.1 via a linear interpolation between successive orbits. $\dot{M}_{\rm s}$ represents the mass rate at which the stream enters the shock, obtained from

$$\dot{M}_{\rm s} = M_{\rm s}/\Delta t_{\rm dis}, \tag{3.23}$$

where $M_{\rm s}$ is the mass of debris present in the stream and $\Delta t_{\rm dis}$ denotes the time required for all this matter to go through the shock and dissipate its orbital energy. We explore two different ways of computing the mass of the stream. The first assumes a flat energy distribution within

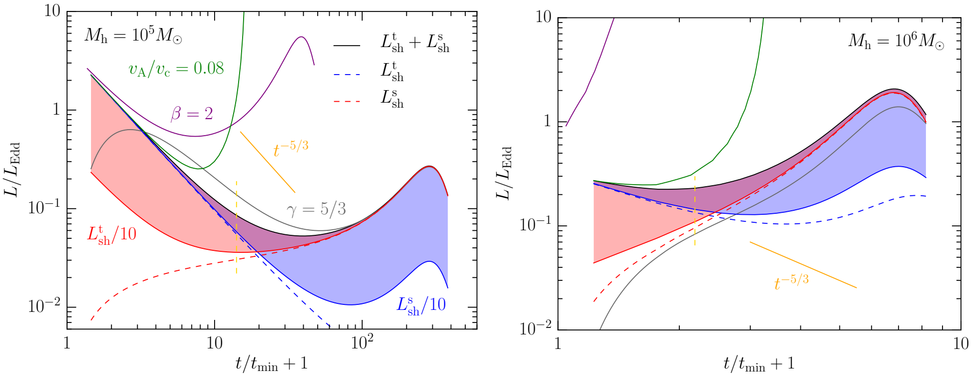

Figure 3.8: Evolution of the stream shock luminosity $L^{\rm s}_{\rm sh}$ (red dashed line), tail shock luminosity $L^{\rm t}_{\rm sh}$ (blue dashed line), given by equations (3.22) and (3.25) respectively, and total shock luminosity $L^{\rm s}_{\rm sh} + L^{\rm t}_{\rm sh}$ (solid black line) for black hole masses $M_{\rm h} = 10^5\,{\rm M}_\odot$ (left panel) and $10^6\,{\rm M}_\odot$ (right panel) assuming a flat energy distribution for the fallback rate and a stream dissipation timescale $\Delta t_{\rm dis} = P_{\rm s}$ in equation (3.23). Equal radiative efficiencies are adopted for the two shock sources, with $\eta^{\rm s}_{\rm sh} = \eta^{\rm t}_{\rm sh} = 1$. The other parameters are fixed to $\beta = 1$ and $v_{\rm A}/v_{\rm c} = 0$. The total luminosity is also shown for $\beta = 2$ (purple solid line), $v_{\rm A}/v_{\rm c} = 0.08$ (green solid line) and using the more precise fallback rate evolution of Lodato et al. (2009) for a polytropic star with $\gamma = 5/3$ (grey solid line) keeping the other parameters fixed. The shaded regions show the areas covered by the total luminosity as $L^{\rm t}_{\rm sh}$ (red area) and $L^{\rm s}_{\rm sh}$ (blue area) are decreased up to a factor of 10 (red and blue solid lines). All the luminosities are scaled by the Eddington value $L_{\rm Edd}$. The orange solid segment indicates the $t^{-5/3}$ slope. The vertical yellow dashed segment marks the time before which the locations of self-crossing and tail shocks remain similar, implying comparable radiative efficiencies $\eta^{\rm s}_{\rm sh} \approx \eta^{\rm t}_{\rm sh}$.

the disrupted star leading to $M_{\rm s} = 0.5 M_\star (1 - (t/t_{\rm min} + 1)^{-2/3})$. The second follows Lodato et al. (2009), which adopts a more precise description of the internal structure of the star, modelled by a polytrope. This latter approach results in a shallower increase of the stream mass. If all the gas present in the stream is able to pass through the intersection point, the time $\Delta t_{\rm dis}$ during which the debris energy is dissipated is equal to the orbital period of the stream $P_{\rm s}$. However, this can be prevented if a shock component, either the infalling or the ouflowing part of the stream, gets exhausted earlier than the other. In this case, part of the stream material keeps its original energy. Nevertheless, this gas will eventually join the rest of the stream and release its energy, only at slightly later times. This effect can therefore be accounted for by setting $\Delta t_{\rm dis} > P_{\rm s}$ by a factor of a few. Finally, the parameter $\eta^{\rm s}_{\rm sh}$ is the shock radiative efficiency, which accounts for the possibility that not all the thermal energy injected in the stream via shocks can be radiated away and participate to the luminosity $L^{\rm s}_{\rm sh}$. Its value depends on the optical thickness of the stream at the shock location and can be estimated by

$$\eta^{\rm s}_{\rm sh} = \min(1, t^{\rm s}_{\rm sh}/t^{\rm s}_{\rm dif}), \tag{3.24}$$

$t^{\rm s}_{\rm dif}$ being the diffusion time at the self-crossing shock location while $t^{\rm s}_{\rm sh}$ denotes the duration of the shock, equal to the dynamical time at this position.

The second luminosity component is associated to the tail of gas constantly falling back towards the black hole. This newly arriving material inevitably joins the stream from an initially nearly radial orbit. During this process, its orbital energy decreases from almost zero to the orbital energy of the stream. The tail orbital energy lost is transferred into thermal energy via shocks and can be radiated. The associated tail shock luminosity is given by

$$L^{\rm t}_{\rm sh} = \eta^{\rm t}_{\rm sh} \dot{M}_{\rm fb} \epsilon_{\rm s}, \tag{3.25}$$

where ϵ_s is the instantaneous energy of the stream obtained from the succession of ellipses by linearising between orbits. $\dot{M}_\mathrm{fb}$ is the mass fallback rate at which the tail reaches the stream. As for $\dot{M}_\mathrm{s}$ in equation (3.22), we investigate two methods to compute the fallback rate. Assuming a flat energy distribution within the disrupted star gives $\dot{M}_\mathrm{fb} = 1/3(M_\star/t_\mathrm{min})(t/t_\mathrm{min}+1)^{-5/3}$, which corresponds to a fallback rate peaking when the first debris reaches the black hole, at $t = 0$, and immediately decreasing as $t^{-5/3}$. Taking into account the stellar structure following Lodato et al. (2009) leads to an initial rise of the fallback rate towards a peak, reached for t of a few t_min, followed by a decrease as $t^{-5/3}$ at later times. The parameter $\eta^\mathrm{t}_\mathrm{sh}$ is the radiative efficiency at the location of the shock between tail and stream present for the same reason as in equation (3.22). It can be evaluated as in equation (3.24) by

$$\eta^\mathrm{t}_\mathrm{sh} = \min(1, t^\mathrm{t}_\mathrm{sh}/t^\mathrm{t}_\mathrm{dif}), \tag{3.26}$$

where $t^\mathrm{t}_\mathrm{dif}$ is the diffusion time at the tail shock location and t^t_sh is the duration of the shock.

Estimating the shock luminosities from equations (3.22) and (3.25) implicitly assumes that most of the radiation is released shortly after the self-crossing points, neglecting any emission close to the black hole. This assumption is legitimate for the following reasons. As will be demonstrated in Section 3.3.3, except in the ideal case where cooling is completely efficient, the stream rapidly expands under pressure forces shortly after its passage through the shock. This expansion induces a decrease of the thermal energy available for radiation as the stream leaves the shock location. Additionally, the radiative efficiency is likely lowered close to the black hole due to an shorter dynamical time, which reduces the emission in this region.

The radiative efficiencies $\eta^\mathrm{s}_\mathrm{sh}$ and $\eta^\mathrm{t}_\mathrm{sh}$ at the location of the self-crossing and tail shocks, given by equations (3.24) and (3.26) respectively, are a priori different since these two categories of shocks can happen at different positions. At early times, we nevertheless argue that they occur at similar locations. A justification can be seen in Fig. 3.2 and 3.6 where the blue solid line represents a parabolic trajectory with pericentre R_p, equal to that of the star. Because the debris in the tail are on elliptical orbits, their trajectories must be contained between this line and the orbit of the most bound debris, whose apocentre is indicated by a green star. The tail shocks therefore occur in the region delimited by these two trajectories. Since the self-crossing points (purple dots) are initially also located in this area, we conclude that the two radiative efficiencies are similar, with $\eta^\mathrm{s}_\mathrm{sh} \approx \eta^\mathrm{t}_\mathrm{sh}$ early in the stream evolution. At late times, when the stream orbit has processed significantly, the self-crossing points leave this region possibly implying a significant difference between the two radiative efficiencies, with $\eta^\mathrm{s}_\mathrm{sh} \neq \eta^\mathrm{t}_\mathrm{sh}$. The time at which this happens is indicated by a vertical yellow dashed segment in Fig. 3.8. Another possibility is that the radiative efficiency decreases as the self-crossing points move closer to the black hole. In the following, we therefore estimate the effect of varying shock radiative efficiencies.

In the remainder of this section, values of $\eta^\mathrm{s}_\mathrm{sh}$ and $\eta^\mathrm{t}_\mathrm{sh}$ close to 1 are adopted, which corresponds to a case of efficient cooling where most of the thermal energy released by shocks is instantaneously radiated. Lower radiative efficiencies would imply lower shock luminosities. However, the shape of the total luminosity $L^\mathrm{s}_\mathrm{sh} + L^\mathrm{t}_\mathrm{sh}$ remains unchanged as long as $\eta^\mathrm{s}_\mathrm{sh} \approx \eta^\mathrm{t}_\mathrm{sh}$. If cooling is inefficient, a significant amount of thermal energy remains in the stream. The influence of this thermal energy excess on the subsequent stream evolution will be evaluated in Section 3.3.3.

The two other contributions to the luminosities given by equations (3.22) and (3.25) are orbital energy losses and mass rates through the shock. It is informative to examine the ratio between these quantities in the two shock luminosity components. The mass rate involved in the self-crossing shocks dominates that of tail shocks, with $\dot{M}_\mathrm{s} \gg \dot{M}_\mathrm{fb}$ typically after the first stream intersection. This tends to increase L^s_sh compared to L^t_sh. Since the velocities involved in the two sources of shocks differ by at most $\sqrt{2} \approx 1.4$, the change of momentum experienced by the stream during tail shocks can be neglected compared to that imparted by self-crossing shocks. This justifies a posteriori our assumption of neglecting the dynamical influence of the tail on the stream evolution. The energy losses, on the other hand, are generally larger for the tail shocks, with $\epsilon_{\rm s} \gg \Delta\epsilon_{\rm s}$. This favours $L^{\rm t}_{\rm sh}$ larger than $L^{\rm s}_{\rm sh}$. It is therefore not obvious a priori which shock luminosity component dominates, which motivates the precise treatment presented below.

Fig. 3.8 shows the temporal evolution of the stream shock luminosity $L^{\rm s}_{\rm sh}$ (red dashed line), tail shock luminosity $L^{\rm t}_{\rm sh}$ (blue dashed line), given by equations (3.22) and (3.25) respectively, and total shock luminosity $L^{\rm s}_{\rm sh} + L^{\rm t}_{\rm sh}$ (solid black line) for $M_{\rm h} = 10^5\,{\rm M}_{\odot}$ (left panel) and $10^6\,{\rm M}_{\odot}$ (right panel) assuming a flat energy distribution for the fallback rate and a stream dissipation timescale $\Delta t_{\rm dis} = P_{\rm s}$ in equation (3.23). Equal radiative efficiencies are adopted for the two shock sources, with $\eta^{\rm s}_{\rm sh} = \eta^{\rm t}_{\rm sh} = 1$. The other two parameters are fixed to $\beta = 1$ and $v_{\rm A}/v_{\rm c} = 0$. For $M_{\rm h} = 10^5\,{\rm M}_{\odot}$, the tail shock luminosity strongly dominates for $t/t_{\rm min} \lesssim 20$. As this luminosity is proportional to the fallback rate $\dot{M}_{\rm fb} \propto t^{-5/3}$, the total shock luminosity also decreases as $t^{-5/3}$ following the solid orange segment. For $t/t_{\rm min} \gtrsim 1$, the stream shock luminosity becomes dominant resulting in an increase of the total shock luminosity. For $M_{\rm h} = 10^6\,{\rm M}_{\odot}$, the tail shock luminosity only weakly dominates initially, leading to a total shock luminosity only slightly decreasing for $t/t_{\rm min} \lesssim 1$ before increasing at later times. The reason for $L^{\rm t}_{\rm sh}$ to drive the total shock luminosity at early times only for $M_{\rm h} = 10^5\,{\rm M}_{\odot}$ relates to the stream dynamical evolution discussed in Section 3.3.1. For lower black hole masses, the stream evolution is slower (see Fig. 3.7). The stream therefore retains a long period $P_{\rm s}$, which translates into a large value of the dissipation timescale $\Delta t_{\rm dis} = P_{\rm s}$. As a result, the stream mass rate $\dot{M}_{\rm s}$ through the shock diminishes (equation (3.23)) leading to a lower stream shock luminosity. On the other hand, the tail shock luminosity is unaffected since its temporal evolution is set by the fallback rate $\dot{M}_{\rm fb}$, independent of the stream evolution timescale. Fig. 3.8 also shows the total luminosity for larger values of the penetration factor $\beta = 2$ (solid purple line) and magnetic stresses efficiency $v_{\rm A}/v_{\rm c} = 0.08$ (solid green line) keeping the other parameters fixed. Since this implies a faster stream evolution (see Fig. 3.7), the duration of the light curve decay is reduced for $M_{\rm h} = 10^5\,{\rm M}_{\odot}$ and even suppressed for $M_{\rm h} = 10^6\,{\rm M}_{\odot}$. A similar behaviour is noticed when the more precise fallback rate evolution of Lodato et al. (2009) is adopted, assuming a polytopic star with $\gamma = 5/3$ (grey solid line). For $M_{\rm h} = 10^5\,{\rm M}_{\odot}$, the only difference is the presence of an initial increase towards a peak in the total luminosity evolution, reached at $t/t_{\rm min} \approx 2$. This peak corresponds to the peak in the fallback rate, which the total luminosity follows initially. For $M_{\rm h} = 10^6\,{\rm M}_{\odot}$, this more accurate fallback rate evolution results in a total luminosity always increasing since the fallback rate peaks at $t/t_{\rm min} \approx 2$, where the stream shock luminosity already dominates.

The shaded regions in Fig. 3.8 show the areas covered by the total luminosity as $L^{\rm t}_{\rm sh}$ (red area) and $L^{\rm s}_{\rm sh}$ (blue area) are decreased up to a factor of 10 (red and blue solid lines). The former can occur if the radiative efficiencies satisfy $\eta^{\rm t}_{\rm sh} < \eta^{\rm s}_{\rm sh}$, which implies a decrease of the tail shock luminosity. The latter can be associated to $\eta^{\rm s}_{\rm sh} < \eta^{\rm t}_{\rm sh}$ or to a stream dissipation timescale such that $\Delta t_{\rm dis} > P_{\rm s}$, which both leads to a lower stream shock luminosity. Decreasing $L^{\rm t}_{\rm sh}$ leads to an initially lower total luminosity. Since the stream shock luminosity dominates earlier, the decay time is also quenched for $M_{\rm h} = 10^5\,{\rm M}_{\odot}$ and even removed for $M_{\rm h} = 10^6\,{\rm M}_{\odot}$. Instead, decreasing $L^{\rm s}_{\rm sh}$ leads to a lower total luminosity at late times with a longer initial decay time. A decrease of the radiative efficiency as self-crossing points get closer to the black hole would instead lead to a steeper decay of the total shock luminosity.

The total shock luminosity computed above remain mostly sub-Eddington. It is significantly lower than that $L_{\rm d}$ associated to the viscous accretion of a circular disc, assum-

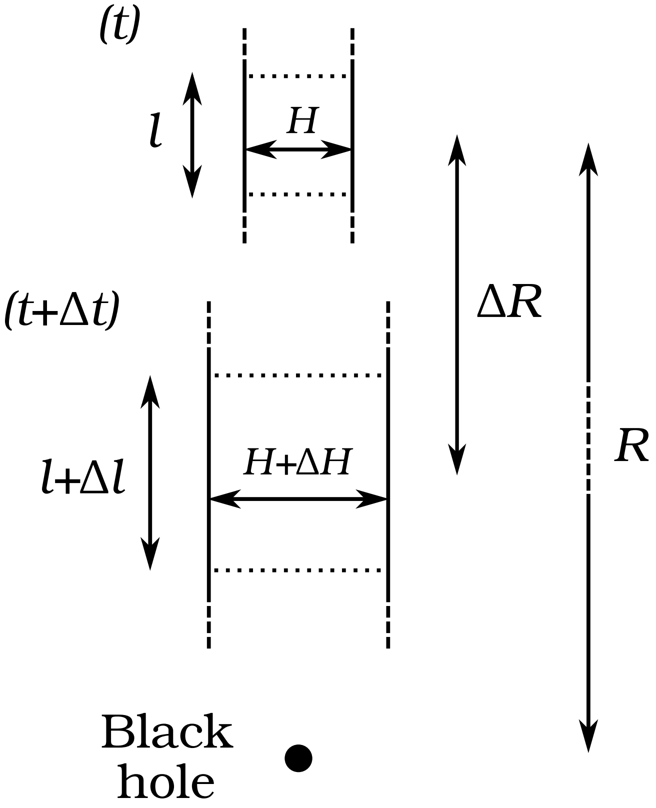

Figure 3.9: Sketch illustrating the width evolution of a stream element as it approaches the black hole. At a time t, the element is located at a distance R from the black hole with a width H and a length l. After a time Δt, the element got closer to the black hole by a distance ΔR while its width and length varied by ΔH and Δl.

ing its rapid formation around to the black hole. For $M_{\rm h} = 10^6\,{\rm M}_\odot$, the former peaks at $L_{\rm d}/L_{\rm Edd} \approx 100$ while the latter only reaches $(L^{\rm t}_{\rm sh} + L^{\rm s}_{\rm sh})/L_{\rm Edd} \approx 0.1$. For this reason, the shock luminosity has been proposed by Piran et al. (2015) as the source of emission from optical TDEs, detected at low luminosities. They also argue that this origin could explain the $t^{-5/3}$ decay of the optical light curve, as detected from this class of TDEs (e.g. Arcavi et al. 2014). However, this is only true if the tail shock luminosity component dominates. According to Fig. 3.8, this requires $M_{\rm h} \lesssim 10^6\,{\rm M}_\odot$ for the most favourable values of the other two parameters, $\beta = 1$ and $v_{\rm A}/v_{\rm c} = 0$. In addition, this luminosity component is suppressed if magnetic stresses are efficient since they cause the stream to evolve faster. This makes the ballistic accretion scenario proposed by Svirski et al. (2015) difficult to realize simultaneously with the decreasing optical luminosity.

3.3.3 Impact of inefficient cooling

In Section 3.3.2, values close to 1 have been adopted for the shock radiative efficiencies $\eta^{\rm s}_{\rm sh}$ and $\eta^{\rm t}_{\rm sh}$, artificially allowing most of the thermal energy injected by shocks to be released instantaneously in the form of radiation. Relaxing this assumption, part of the thermal energy stays in the stream, leading to its expansion through pressure forces. In this Section, we estimate this widening of the stream due to both stream self-crossing shocks and shocks between stream and tail.

We start by deriving differential equations that relate the width of a stream element to its distance from the black hole. The situation is illustrated in Fig. 3.9 in the case where the stream element is moving towards the black hole. At a given time t, the element has a width H and is located at a distance R from the black hole. A time Δt later, its distance from the black hole decreased by $\Delta R < 0$ while its width changed by ΔH. Since the width evolves under the influence of both tidal and pressure forces, its variation can be decomposed into two components $\Delta H = \Delta H_{\rm t} + \Delta H_{\rm p}$, where $\Delta H_{\rm t}$ and $\Delta H_{\rm p}$ denote respectively the change of width due to tidal and pressure forces. As the stream element moves closer to the black hole, tidal forces induce a decrease of its width by $\Delta H_{\rm t} = -v_\perp \Delta t$ where $v_\perp$ is the velocity of the external part of the stream, directed towards the stream centre. For a nearly radial trajectory, $v_\perp$ can be related to the radial velocity $v_{\rm r}$ of the stream via $v_\perp \approx (H/R) v_{\rm r}$, which yields $\Delta H_{\rm t} = (H/R)\Delta R < 0$ using $\Delta R = -v_{\rm r}\Delta t$. Pressure forces cause the stream element to increase by $\Delta H_{\rm p} = c_{\rm s}\Delta t$, where $c_{\rm s}$ is the sound speed. Using $\Delta t = -\Delta R/v_{\rm r}$ then leads to $\Delta H_{\rm p} = -(c_{\rm s}/v_{\rm r})\Delta R > 0$. Putting tidal and pressure components together, $\Delta H = (H/R - c_{\rm s}/v_{\rm r})\Delta R$ if the stream element approaches the black hole. For a stream element moving away from the black hole, this relation becomes $\Delta H = (H/R + c_{\rm s}/v_{\rm r})\Delta R$. The change of sign is required since $\Delta R > 0$ in this case while pressure forces must still induce a increase of H. The evolution of the stream width H as a function of distance R from the black hole therefore obeys the differential equations

$$\frac{\mathrm{d}H}{\mathrm{d}R} = \begin{cases} \dfrac{H}{R} - \dfrac{c_{\rm s}}{v_{\rm r}} & \text{(inwards)} \\ \dfrac{H}{R} + \dfrac{c_{\rm s}}{v_{\rm r}} & \text{(outwards)} \end{cases}, \tag{3.27}$$

The first equation is valid when the stream moves inwards, towards the black hole. Instead, the second one corresponds to an outward motion of the stream, moving away from the black hole. In each equation, the first term on the right-hand side corresponds to the effect of tidal forces. Alone, it leads to an homologous evolution of the stream width, with $H \propto R$. This scaling can also be obtained by combining equations 4 and 13 of Sari et al. (2010). Instead, the second term is associated to pressure forces, which cause the stream expansion. Strictly speaking, our treatment of tidal effects is only valid for a nearly radial trajectory. However, our evaluation of pressure effects also applies to an elliptic orbit as long as $v_{\rm r}$ denotes the radial component of the total velocity. This method is legitimate since the stream trajectory significantly differs from a nearly radial one only at apocentre where pressure effects are found to be dominant.

For later use, we also derive the evolution of the stream element length l with the distance R from the black hole, still in the situation shown in Fig. 3.9. Pressure does not modify the element length since an expansion in the longitudinal direction is prevented by neighbouring stream elements. However, as the stream element moves closer to the black hole, its length increases by Δl due to tidal forces. More precisely, this elongation is caused by the difference of velocity within the stream element, whose parts closer to the black hole move faster. The distance $|\Delta R|$ travelled during Δt therefore becomes a function of R. The relative increase of length is then given by $\Delta l/l = -\mathrm{d}|\Delta R|/\mathrm{d}R$. The equation describing the element length evolution can then be written as a function of the radial velocity $v_{\rm r}$, such that $\mathrm{d}l/l = \mathrm{d}v_{\rm r}/v_{\rm r}$. l therefore follows the same scaling as $v_{\rm r}$ with R, that is $l \propto R^{-1/2}$ for a nearly radial orbit. Again, this scaling can be found from Sari et al. (2010), combining their equations 4 and 14.

Our goal is now to solve equations (3.27) for boundary conditions defined by the dynamical model of Section 3.2 that describes the stream evolution as a succession of orbits. As we show below, this allows to compute iteratively the width evolution of a stream element as it evolves around the black hole. Consider first a given orbit N. The stream element enters this orbit at apocentre, a distance R^{a}_N from the black hole with a velocity v^{a}_N. It then approaches the black hole down to a pericentre distance R^{p}_N where its velocity reaches v^{p}_N. These quantities are directly known from the dynamical model. In addition, the element has an initial width H^{a}_N and a sound speed $c^{\mathrm{a}}_{\mathrm{s},N}$ at apocentre which can also be estimated as explained below. In order to solve equations (3.27), the evolution of the second term $\pm c_{\mathrm{s}}/v_{\mathrm{r}}$ as the element follows orbit N has to be evaluated. It requires to know the dependence on H and R of the sound speed $c_{\mathrm{s},N}$ and radial velocity $v_{\mathrm{r},N}$ in this orbit. These dependencies are obtained as follows. Assuming an adiabatic evolution, $c_{\mathrm{s}} \propto \rho^{1/3}$ with ρ denoting the stream element density. Since the element keeps the same mass, the cylindrical profile of the stream imposes $\rho \propto H^{-2} l^{-1}$. The scaling $l \propto R^{-1/2}$ derived above for the element length then implies $c_{\mathrm{s}} \propto H^{-2/3} R^{1/6}$. The sound speed in orbit N can therefore be written

$$c_{\mathrm{s},N} = c^{\mathrm{a}}_{\mathrm{s},N} \left(\frac{H}{H^{\mathrm{a}}_N} \right)^{-2/3} \left(\frac{R}{R^{\mathrm{a}}_N} \right)^{1/6}. \tag{3.28}$$

Similarly, the radial velocity of the element is obtained from

$$v_{\mathrm{r},N} = \left(v^{\mathrm{a}}_N v^{\mathrm{p}}_N \right)^{1/2} \left(\frac{R^{\mathrm{a}}_N}{R} - 1 \right)^{1/2} \left(1 - \frac{R^{\mathrm{p}}_N}{R} \right)^{1/2}, \tag{3.29}$$

which vanishes at apocentre and pericentre. The evolution of the stream element width H with R as it moves inwards from R^{a}_N to R^{p}_N is then obtained by solving numerically the first of equations (3.27), using equations (3.28) and (3.29) to evaluate the second term. The boundary condition is given by the element width H^{a}_N at $R = R^{\mathrm{a}}_N$. During the outwards motion of the stream away from pericentre to the next crossing point, the width evolution is found by solving the second of equations (3.27), still combined with equations (3.28) and (3.29). In this phase, the boundary condition requires to know the width H^{p}_N at $R = R^{\mathrm{p}}_N$, which is obtained from the continuity of the element width at pericentre.

The last step to compute the element width evolution is to estimate the sound speed $c^{\mathrm{a}}_{\mathrm{s},N}$ at apocentre that appears in equation (3.28). Since shocks and magnetic stresses act at apocentre, both velocity and sound speed undergo discontinuous changes at this location. For the velocity, this discontinuity has already been accounted for in the dynamical model by computing v^{a}_N iteratively from its variation between two successive orbits N and $N+1$, according to equations (3.7) and (3.16). The sound speed $c^{\mathrm{a}}_{\mathrm{s},N}$ can be evaluated in a similar iterative way. This requires to know the relation between the pre-shock sound speed $c^{\mathrm{int}}_{\mathrm{s},N}$ of the stream element as it reaches the intersection point of orbit N to the post-shock sound speed $c^{\mathrm{a}}_{\mathrm{s},N+1}$ of the element as it leaves the shock location from the apocentre of orbit $N+1$. Since sound speed is related to specific thermal energy, this amounts to find the post-shock specific thermal energy u^{a}_{N+1} from its pre-shock value u^{int}_N. This jump in thermal energy corresponds to the fraction of orbital energy lost through shocks from the tail and the stream that is not radiated away. Summing the two thermal energy components, this relation is

$$u^{\mathrm{a}}_{N+1} = (1 - \eta_{\mathrm{sh}}) \frac{\dot{M}^{\mathrm{int}}_{\mathrm{s},N} (\Delta\epsilon_{\mathrm{s},N} + u^{\mathrm{int}}_N) + \dot{M}^{\mathrm{int}}_{\mathrm{fb},N} \epsilon_{\mathrm{s},N}}{\dot{M}^{\mathrm{int}}_{\mathrm{s},N} + \dot{M}^{\mathrm{int}}_{\mathrm{fb},N}}, \tag{3.30}$$

where $\dot{M}^{\mathrm{int}}_{\mathrm{s},N}$ and $\dot{M}^{\mathrm{int}}_{\mathrm{fb},N}$ are the mass rates at which the stream and the tail enters the shocks respectively, evaluated at the intersection point of orbit N. These factors account for the mass difference between the tail and stream components of the shock. $\Delta\epsilon_{\mathrm{s},N}$ and $\epsilon_{\mathrm{s},N}$ are the energies lost by the stream and the tail respectively during the shocks at orbit N, which are computed from the dynamical stream evolution. Equation (3.30) also assumes that the stream self-crossing and tail shocks occur at the same position, leading to a common radiative efficiency

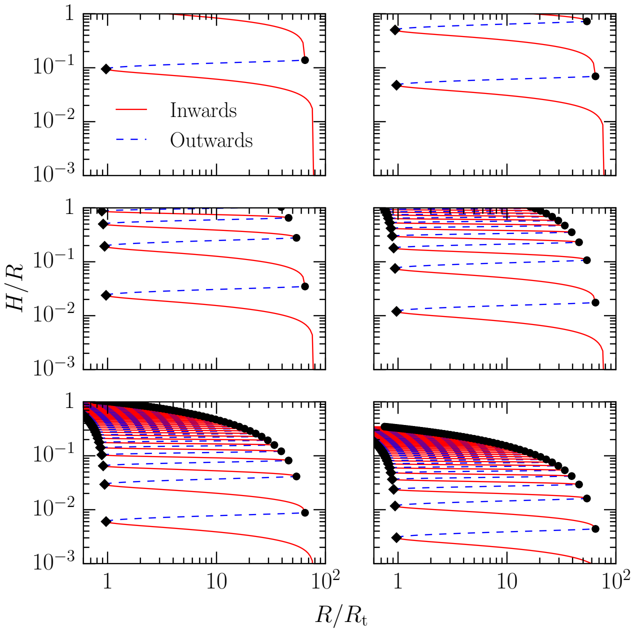

Figure 3.10: Aspect ratio H/R of a stream element as a function of distance from the black hole during the stream evolution. From the upper left to the lower right panel, the shock radiative efficiency increases from $\eta_\mathrm{sh} = 0$ to $1-\eta_\mathrm{sh} = 10^{-1}$, 10^{-2}, 10^{-3}, 10^{-4} and 10^{-5}. The other parameters are fixed to $M_\mathrm{h} = 10^6\,\mathrm{M}_\odot$, $\beta = 1$ and $v_\mathrm{A}/v_\mathrm{c} = 0.06$. The corresponding stream evolution is shown in Fig. 3.2 (upper panel). The solid red lines correspond to an inward motion of the stream element from apocentre (black dot) to pericentre (black diamond), for which H/R is obtained by solving the first of equations (3.27). The dashed blue lines are associated to an outward motion of the stream, for which the second of equations (3.27) is solved to compute H/R.

$\eta_\mathrm{sh} \equiv \eta^\mathrm{s}_\mathrm{sh} = \eta^\mathrm{t}_\mathrm{sh}$ for the two shock sources. As explained in Section 3.3.2, this approximation is legitimate, at least at early times. In general, the relation $u^\mathrm{int}_N \ll \Delta\epsilon_{\mathrm{s},N}$ holds. The numerator of equation (3.30) is therefore $(1-\eta_\mathrm{sh})(L^\mathrm{s}_\mathrm{sh} + L^\mathrm{t}_\mathrm{sh})/\eta_\mathrm{sh}$ (see equations (3.22) and (3.25)), which corresponds as expected to the thermal energy rate released by shocks but not radiated. Sound speed and specific thermal energy are linked via

$$(c^\mathrm{a}_{\mathrm{s},N})^2 = \frac{10}{9} u^\mathrm{a}_N, \tag{3.31}$$

which allows to relate $c^\mathrm{a}_{\mathrm{s},N+1}$ to $c^\mathrm{a}_{\mathrm{s},N}$ using equation (3.30). $c^\mathrm{a}_{\mathrm{s},N}$ can therefore be computed iteratively for any orbit N starting from the pre-shock sound speed of the first shock, which we set to $c^\mathrm{int}_{\mathrm{s},0} = 0$ since the stream element has not experienced any shock yet.

The evolution of the width H of a stream element as a function of R during the stream evolution can now be computed iteratively assuming an initial value for H and its continuity at self-crossing points. At the location of the first self-crossing point, a distance R^int_0 from the black hole, the initial stream element width is fixed to $R_\star$. Although H is imposed to be a continuous function of R, its derivative $\mathrm{d}H/\mathrm{d}R$ is discontinuous at apocentre and pericentre. This is because the differential equation satisfied by $\mathrm{d}H/\mathrm{d}R$ changes at these locations (see equation (3.27)). In addition, c_s increases instantaneously at apocentre where shocks occur and thermal energy is injected into the stream. Furthermore, since the radial velocity cancels at pericentre and apocentre, $\mathrm{d}H/\mathrm{d}R$ becomes infinite at these locations (see equations (3.27)

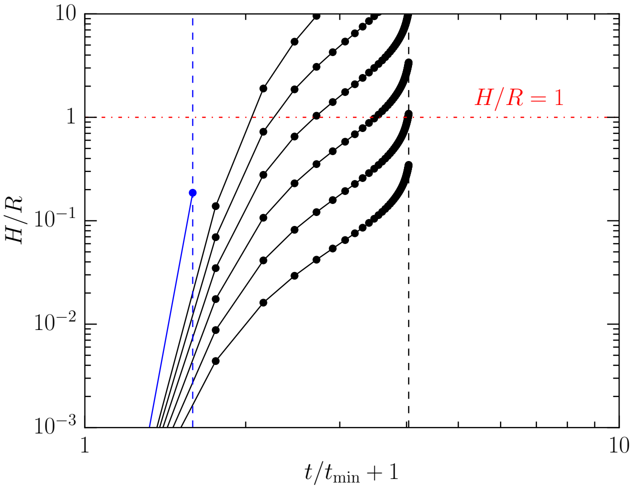

Figure 3.11: Aspect ratio H/R of a stream element as a function of time during the stream evolution. From the top to the bottom solid black line, the shock radiative efficiency $\eta_{\rm sh}$ increases from $\eta_{\rm sh} = 0$ to $1 - \eta_{\rm sh} = 10^{-1}$, 10^{-2}, 10^{-3}, 10^{-4} and 10^{-5} (as in Fig. 3.10). The other parameters are fixed to $M_{\rm h} = 10^6\,{\rm M}_\odot, \beta = 1$ and $v_{\rm A}/v_{\rm c} = 0.06$. The blue line corresponds to a larger magnetic stresses efficiency $v_{\rm A}/v_{\rm c} = 0.3$ for $\eta_{\rm sh} = 0$, keeping the other parameters fixed. The corresponding stream evolutions are shown in Fig. 3.2. The dots indicate apocentre passages. The vertical dashed lines represents the evolution time $t_{\rm ev}$ at which the stream ends its evolution in each case. The horizontal red dash-dotted line shows $H/R = 1$.

and (3.29)) resulting in a vertical tangent for H.

Our evaluation of the stream width evolution assumes that radiation only occurs near the self-crossing points and neglect any emission from the stream when it gets closer to the black hole. This allows to adopt an adabatic evolution for the stream element away from self-crossing points, which has been used to derive equation (3.28). Note that this assumption has already been made in Section 3.3.2 to compute the shock luminosities. It is justified because the radiative efficiency likely decreases close to the black hole due to a shorter dynamical time in that region. If the stream is nevertheless able to cool at this location, pressure forces would be lowered reducing the stream expansion.

Fig. 3.10 shows the aspect ratio H/R of a stream element as a function of distance R from the black hole during the stream evolution for increasing values of the shock radiative efficiency, from $\eta_{\rm sh} = 0$ (upper left panel) to $1 - \eta_{\rm sh} = 10^{-1}$, 10^{-2}, 10^{-3}, 10^{-4} and 10^{-5} (lower right panel). The other parameters are fixed to $M_{\rm h} = 10^6\,{\rm M}_\odot$, $\beta = 1$ and $v_{\rm A}/v_{\rm c} = 0.06$. The corresponding stream evolution is shown in Fig. 3.2 (upper panel). Initially, the stream element is located at the first self-crossing point, a distance $R_0^{\rm int} = 80 R_{\rm t}$ from the black hole (see Fig. 3.2, upper panel). The initial aspect ratio is $R_\star/R_0^{\rm int} \approx 10^{-4}$ that is not visible on the figure. After the first shock, the aspect ratio increases and appears on the lower right part of each panel. It then continues to increase as the stream element successively moves inwards (solid red lines) and outwards (dashed blue line) between apocentre (black points) and pericentre (black diamonds). H/R experiences a sharp increase shortly after each apocentre passage since thermal energy is injected into the stream at these locations (equation (3.30)). Away from self-crossing points, the stream element width follows an almost homologous evolution $H \propto R$ since tidal forces dominate over pressure forces. As mentioned above, if the element was allowed to cool in this region, its width evolution would get even closer to an homologous one since pressure would be reduced. This would result in a slightly slower expansion of the stream. For $\eta_{\rm sh} = 0$ (upper left panel), the aspect ratio becomes $H/R > 1$ after only a few (two) apocentre passages. For larger radiative efficiencies $\eta_{\rm sh}$, the aspect ratio increases more slowly. This is because less thermal energy is injected into the stream, which reduces the impact of pressure forces on the stream widening (equations (3.30), (3.31) and (3.27)). The rapid aspect ratio increase seen for $\eta_{\rm sh} = 0$ persists as long as $1 - \eta_{\rm sh} \gtrsim 10^{-3}$. As can be seen from Fig. 3.11 (solid black lines), the aspect ratio reaches $H/R > 1$ after a time $t \approx t_{\rm min}$, which corresponds to only a third of its evolution time $t_{\rm ev}/t_{\rm min} = 3$. When the shock radiative efficiency satisfies $1 - \eta_{\rm sh} \lesssim 10^{-4}$, the aspect ratio remains $H/R < 1$ after a significant number of apocentre passages. Only for $1 - \eta_{\rm sh} = 10^{-5}$ (lower right panel), the stream circularizes with an aspect ratio $H/R < 1$ (lower right panel of Fig. 3.10 and bottom black solid line of Fig. 3.11).

Although the aspect ratio evolution is only shown for a particular set of parameters, this behaviour is similar for a large range of values for $M_{\rm h}$, β and $v_{\rm A}/v_{\rm c}$. A difference can nevertheless be noticed in the case of a rapid stream evolution, favoured for large values of these parameters (see Fig. 3.7). It can be understood by looking at the blue line of Fig. 3.11, for which the magnetic stresses efficiency is increased to $v_{\rm A}/v_{\rm c} = 0.3$ compared to the top black line that shows $v_{\rm A}/v_{\rm c} = 0.06$, both adopting a shock radiative efficiency $\eta_{\rm sh} = 0$. For $v_{\rm A}/v_{\rm c} = 0.3$, the stream experiences only two self-crossing before being ballistically accreted at $t_{\rm ev}/t_{\rm min} = 0.6$, as can be seen from the corresponding stream evolution shown in of Fig. 3.2 (lower panel). As a result, only a small amount of thermal energy is injected in the stream, which results in an aspect ratio $H/R = 0.6 < 1$ at the end of its evolution, even for $\eta_{\rm sh} = 0$. This trend is also present for an increased black hole mass. For $M_{\rm h} = 10^7\,{\rm M}_\odot$, keeping $\beta = 1$ and $v_{\rm A}/v_{\rm c} = 0.06$, the stream circularizes with $H/R < 1$ for lower radiative efficiencies than $M_{\rm h} = 10^6\,{\rm M}_\odot$, with a critical value $1 - \eta_{\rm sh} \approx 10^{-2} > 10^{-5}$.

When the aspect ratio becomes $H/R \gtrsim 1$, pressure forces cannot anymore be neglected to describe the stream dynamics as we assume in our stream evolution model. This widening of the stream causes a large spread in its orbital parameters. The gas involved in the outward expansion moves to larger orbits while that expanding inwards gets shorter orbits. This is likely to cause complicated interactions between different portions of the stream, which are not captured by our model. The stream is likely to subsequently evolve into a thick torus, or even an envelope surrounding the black hole

3.4 Discussion and conclusion

The dynamical evolution of the debris stream produced during TDEs is driven by two main mechanisms: magnetic stresses and shocks. Although these processes have been considered independently, their simultaneous effect has not been investigated. In this paper, we present a stream evolution model which takes both mechanisms into account. We demonstrate the existence of a critical magnetic stresses efficiency that sets the boundary between circularization and ballistic accretion. Interestingly, its value $(v_{\rm A}/v_{\rm c})_{\rm cr} \approx 10^{-1}$ is found to be largely independent of the black hole mass and penetration factor. In the absence of magnetic stresses, we derive an analytical estimate for the circularization timescale $t_{\rm ev}/t_{\rm min} = 8.3(M_{\rm h}/10^6\,{\rm M}_\odot)^{-5/3}\beta^{-3}$. If magnetic stresses act on the stream, we prove that their dominant effect is to accelerate the stream evolution by strengthening self-crossing shocks. Ballistic accretion therefore necessarily occurs very early in the stream evolution. Instead, we show that a $t^{-5/3}$ decay of the shock luminosity light curve, likely associated to optical emission (Piran et al. 2015), requires a slow stream evolution. This is favoured for low black hole masses $M_{\rm h} \lesssim 10^6\,{\rm M}_\odot$ and hard to reconcile with the strong magnetic stresses necessary for the ballistic accretion scenario proposed by Svirski et al. (2015). Finally, we demonstrate that even marginally inefficient cooling with shock radiative efficiency $\eta_{\rm sh} \lesssim 1$ leads to the rapid formation of a very thick torus around the black hole, which could even evolve into an envelope encompassing it as proposed by several authors (Guillochon et al. 2014; Metzger & Stone 2016). This thick structure could act as a reprocessing layer that intercepts a fraction of the X-ray photons released as debris accretes onto the black hole and re-emit them as optical light. In this picture, the detection of X-ray emission would however be dependent on the viewing angle. For example, the X-ray photons could still be able to escape along the funnels of a thick torus but not along its orbital plane.

In the absence of magnetic stresses, the stream evolution predicted by our model is qualitatively consistent with existent numerical simulations of disc formation from TDEs. Specifically, our model can be compared to Bonnerot et al. (2016a) who consider the disruption of bound stars by a non-rotating black hole of mass $M_{\rm h} = 10^6\,{\rm M}_{\odot}$. For a stellar eccentricity $e = 0.95$ and penetration factor $\beta = 5$, they find that disc formation occurs in less than a dynamical time due to strong apsidal precession. For $\beta = 1$, their simulations predict instead a series of self-crossing shocks that leads to a longer circularization from an initially eccentric disc due to weaker apsidal precession. These two numerical results are in line with our analytic model, which considers the most general case of a parabolic stellar orbit. Finally, the rapid thickening of the stream predicted analytically in this paper in the case of inefficient cooling is consistent with several disc formation simulations that assume an adiabatic equation of state for the debris (Guillochon et al. 2014; Shiokawa et al. 2015; Bonnerot et al. 2016a; Hayasaki et al. 2016; Sądowski et al. 2016). However, these simulations have been performed in the restricted case of either very low black hole masses or bound stars for numerical reasons. Instead, our analytic model treats the standard case.

The range of magnetic stresses efficiencies $v_{\rm A}/v_{\rm c}$ investigated has been set by assuming saturation of the MRI. Although this assumption is legitimate in well-ordered discs after a few dynamical timescales, it is unclear whether it holds in the case of the debris stream that is likely to lose its ordering through shocks. If the MRI has not reached saturation, $v_{\rm A}/v_{\rm c}$ would be lowered thus reducing the dynamical effect of magnetic stresses and preventing ballistic accretion. If it goes down to $v_{\rm A}/v_{\rm c} \lesssim 10^{-2}$, magnetic stresses would even become dynamically irrelevant.

To estimate the widening of the stream, we investigate a wide range of radiative shock efficiencies. The values expected physically for this parameter can be determined by the following calculation. Assuming that the photons propagate in the direction transverse to the stream trajectory, the diffusion time for them to escape the stream is $t_{\rm dif} = c/(\tau H_{\rm sh})$ with τ and $H_{\rm sh}$ the optical depth and width at the shock location. The optical depth can be estimated by $\tau = \Sigma\kappa_{\rm T}$ where Σ denotes the column density at the shock location and $\kappa_{\rm T} = 0.4\,{\rm cm}^2/{\rm g}$ is the Thomson opacity. The column density can be approximated by $\Sigma \approx \dot{M} t_{\rm sh}/H_{\rm sh}^2$, denoting by $\dot{M} = \dot{M}_{\rm d} + \dot{M}_{\rm fb}$ the total mass rate of matter through the shock location. Combining these expressions, the shock radiative efficiency takes the form $\eta_{\rm sh} \equiv t_{\rm sh}/t_{\rm dif} \approx H_{\rm sh} c/(\kappa_{\rm T}\dot{M})$. For the first self-crossing shock, $H_{\rm sh} \approx R_\star$ and $\dot{M} \approx M_\star/(3t_{\rm min})$, which corresponds to the peak fallback rate. This leads to an initial radiative efficiency of $\eta_{\rm sh} \approx 10^{-5}(M_{\rm h}/10^6\,{\rm M}_{\odot})^{1/2}({\rm R}_\star/{\rm R}_{\odot})^{5/2}({\rm M}_\star/{\rm M}_{\odot})^{-2}$, where the parameters adopted assume the disruption of a solar-type star. This implies that a very inefficient cooling is expected in this case. This estimate is consistent with recent radiative transfer simulations by Jiang et al. (2016) focusing on the stream self-intersection region. They obtain values of the shock radiative efficiency of $\eta_{\rm sh} \approx 0.01 - 0.1$ for mass accretion rates roughly three orders of magnitude lower than used in our estimation. This expression also demonstrates that the shock radiative efficiency is expected to increase for disruptions involving red giants, up to $\eta_{\rm sh} \approx 1$ if the stellar radius reaches $R_\star \approx 100\,{\rm R}_{\odot}$. For the following shocks, the dependence $\eta_{\rm sh} \propto H_{\rm sh}\dot{M}^{-1}$

implies the following evolution of the shock radiative efficiency. During the initial expansion of the stream, $H_{\rm sh}$ rapidly increases (see Fig. 3.11) and so does $\eta_{\rm sh}$, most likely by a few orders of magnitude. Later in time, the stream expansion stalls. The increase of $\dot{M} \approx \dot{M}_{\rm d}$ then dominates and eventually induces a drop of $\eta_{\rm sh}$. This temporal dependence of $\eta_{\rm sh}$ is unlikely to significantly affect our results for the width evolution of the stream. However, it induces a modulation of the shock luminosity since the amount of radiation able to diffuse out of the stream depends on the shock radiative efficiency.

The only effect of magnetic stresses considered in our model is angular momentum loss at apocentre, thus increasing further the stream eccentricity. However, another possibility has been pointed out by numerical simulations. It was found that small-scale instability can develop in eccentric discs that damps the eccentricity (Papaloizou 2005; Barker & Ogilvie 2016).

Finally, we neglect for simplicity the black hole spin in our calculations. If the orbital plane of the debris is not orthogonal to the black hole spin, it causes the stream to change orbital plane when it passes at pericentre. One possible consequence is to delay the onset of circularization by preventing the first self-crossing (Dai et al. 2013; Guillochon & Ramirez-Ruiz 2015). However, it can also lead to faster energy dissipation due to complicated interactions between parts of the stream belonging to different orbital planes (Hayasaki et al. 2016).

Our model provides a first attempt at studying the evolution of the debris stream under both shocks and magnetic stresses. It is attractive by its simplicity and points out several solid features about the dynamics, observational appearance and geometry of the stream as it evolves around the black hole. However, given the complexity of this process and the numerous physical mechanisms involved, global simulations are necessary to definitely settle the fate of these debris.

Acknowledgments

CB and EMR acknowledge support from NOVA. CB also thanks Yuri Levin, Chris Matzner and Daniel Price for interesting discussions.

Bibliography

Arcavi I., et al., 2014, ApJ, 793, 38

Balbus S. A., Hawley J. F., 1998, Reviews of Modern Physics, 70, 1

Barker A. J., Ogilvie G. I., 2016, MNRAS, 458, 3739

Bloom J. S., et al., 2011, Science, 333, 203

Bonnerot C., Rossi E. M., Lodato G., Price D. J., 2016a, MNRAS, 455, 2253

Bonnerot C., Rossi E. M., Lodato G., 2016b, MNRAS, 458, 3324

Cappelluti N., et al., 2009, A&A, 495, L9

Cenko S. B., et al., 2012, MNRAS, 420, 2684

Coughlin E. R., Begelman M. C., 2014, ApJ, 781, 82

Dai L., Escala A., Coppi P., 2013, ApJ, 775, L9

Dai L., McKinney J. C., Miller M. C., 2015, ApJ, 812, L39

Esquej P., et al., 2008, A&A, 489, 543

Gezari S., et al., 2006, ApJ, 653, L25

Gezari S., et al., 2012, Nature, 485, 217

Guillochon J., Ramirez-Ruiz E., 2015, ApJ, 809, 166

Guillochon J., Manukian H., Ramirez-Ruiz E., 2014, ApJ, 783, 23

Hawley J. F., Guan X., Krolik J. H., 2011, ApJ, 738, 84

Hayasaki K., Stone N., Loeb A., 2016, MNRAS, 461, 3760

Hobson M., Efstathiou G., Lasenby A., 2006, General Relativity: An Introduction for Physicists. Cambridge University Press, Cambridge

Holoien T. W.-S., et al., 2016, MNRAS, 455, 2918

Jiang Y.-F., Guillochon J., Loeb A., 2016, ApJ, 830, 125

Kochanek C. S., 1994, ApJ, 436, 56

Komossa S., 2015, Journal of High Energy Astrophysics, 7, 148

Komossa S., Bade N., 1999, A&A, 343, 775

Krolik J., Piran T., Svirski G., Cheng R. M., 2016, ApJ, 827, 127

Lodato G., 2012, EPJ Web Conf., 39, 01001

Lodato G., Rossi E. M., 2011, MNRAS, 410, 359

Lodato G., King A. R., Pringle J. E., 2009, MNRAS, 392, 332

Loeb A., Ulmer A., 1997, ApJ, 489, 573

MacLeod M., Guillochon J., Ramirez-Ruiz E., 2012, ApJ, 757, 134

MacLeod M., Guillochon J., Ramirez-Ruiz E., Kasen D., Rosswog S., 2016, ApJ, 819, 3

Maksym W. P., Ulmer M. P., Eracleous M., 2010, ApJ, 722, 1035

Metzger B. D., Stone N. C., 2016, MNRAS, 461, 948

Miller M. C., 2015, ApJ, 805, 83

Papaloizou J. C. B., 2005, A&A, 432, 757

Phinney E. S., 1989, in Morris M., ed., Proc. IAU Symposium Vol. 136, The Center of the Galaxy. Kluwer, Dordrecht, p. 543

Piran T., Svirski G., Krolik J., Cheng R. M., Shiokawa H., 2015, ApJ, 806, 164

Ramirez-Ruiz E., Rosswog S., 2009, ApJ, 697, L77

Rees M. J., 1988, Nature, 333, 523

Sari R., Kobayashi S., Rossi E. M., 2010, ApJ, 708, 605

Saxton R. D., Read A. M., Esquej P., Komossa S., Dougherty S., Rodriguez-Pascual P., Barrado D., 2012, A&A, 541, A106

Sądowski A., Tejeda E., Gafton E., Rosswog S., Abarca D., 2016, MNRAS, 458, 4250

Shiokawa H., Krolik J. H., Cheng R. M., Piran T., Noble S. C., 2015, ApJ, 804, 85

Stone J. M., Hawley J. F., Gammie C. F., Balbus S. A., 1996, ApJ, 463, 656

Stone N., Sari R., Loeb A., 2013, MNRAS, 435, 1809

Strubbe L. E., Quataert E., 2009, MNRAS, 400, 2070

Svirski G., Piran T., Krolik J., 2015, preprint (arXiv:1508.02389)

van Velzen S., et al., 2011, ApJ, 741, 73

Appendix A: Analytic evolution time

Here, we derive the analytical expression for the evolution time in the absence of magnetic stresses, given by equation (3.21). The evolution time is defined by the time spent in all the orbits followed by the stream during the succession of ellipses described in Section 3.2. Mathematically,

$$t_{\rm ev} = \sum_{N=0}^{N_{\rm ev}} P_N, \tag{3.32}$$

where $N_{\rm ev}$ is the total number of orbits followed by the stream and P_N is the period of the stream in orbit N. Since period and energy are related by $P = 2\pi G M_{\rm h}(-2\epsilon)^{-3/2}$ according to Kepler's third law, $\mathrm{d}P^{1/3}/\mathrm{d}\epsilon = (2\pi G M_{\rm h})^{-2/3} P$ whose discretized version can be written

$$\frac{P_{N+1}^{1/3} - P_N^{1/3}}{\Delta\epsilon_N} = -(2\pi G M_{\rm h})^{-2/3} P_N, \tag{3.33}$$

where $\Delta\epsilon_N$ is the energy lost by the stream at each shock. As explained at the end of Section 3.2.1, $\Delta\epsilon_N$ is independent of N if no magnetic stresses act on the stream. Its value is then $\Delta\epsilon_0$, given by equation (3.10). Using $t_{\rm min} = 2\pi G M_{\rm h}(2\Delta\epsilon)^{-3/2}$, equation (3.33) can therefore be rewritten

$$P_{N+1}^{1/3} - P_N^{1/3} = -\frac{\Delta\epsilon_0}{2\Delta\epsilon} \frac{P_N}{t_{\rm min}^{2/3}}. \tag{3.34}$$

Summing both sides from $N = 0$ to $N_{\rm ev}$, the terms on the left-hand side cancel two by two leading to

$$P_{N_{\rm ev}+1}^{1/3} - P_0^{1/3} = -\frac{\Delta\epsilon_0}{2\Delta\epsilon} \frac{t_{\rm ev}}{t_{\rm min}^{2/3}}, \tag{3.35}$$

where equation (3.32) has been used to write $t_{\rm ev}$ on the right-hand side. As demonstrated in Section 3.3, the final outcome of the stream is circularization for $v_{\rm A}/v_{\rm c} = 0$ implying $P_{N_{\rm ev}+1}^{1/3} \ll P_0^{1/3}$. Therefore, equation (3.35) can be simplified to

$$\frac{t_{\rm ev}}{t_{\rm min}} = \frac{2\Delta\epsilon}{\Delta\epsilon_0}, \tag{3.36}$$

using the fact that the initial stream period is $P_0 = t_{\rm min}$. This demonstrates the analytical expression for the evolution time.

4

Bad prospects for the detection of giant stars' tidal disruption: effect of the ambient medium on bound debris

Most massive galaxies are thought to contain a supermassive black hole in their centre surrounded by a tenuous gas environment, leading to no significant emission. In these quiescent galaxies, tidal disruption events represent a powerful detection method for the central black hole. Following the disruption, the stellar debris evolves into an elongated gas stream, which partly falls back towards the disruption site and accretes onto the black hole producing a luminous flare. Using an analytical treatment, we investigate the interaction between the debris stream and the gas environment of quiescent galaxies. Although we find dynamical effects to be negligible, we demonstrate that Kelvin–Helmholtz instability can lead to the dissolution of the stream into the ambient medium before it reaches the black hole, likely dimming the associated flare. This result is robust against the presence of a typical stellar magnetic field and fast cooling within the stream. Furthermore, we find this effect to be enhanced for disruptions involving more massive black holes and/or giant stars. Consequently, although disruptions of evolved stars have been proposed as a useful probe of black holes with masses $\gtrsim 10^8\,\mathrm{M}_\odot$, we argue that the associated flares are likely less luminous than expected.

C. Bonnerot, E. M. Rossi and G. Lodato
2016, *MNRAS*, **Volume 458**, Issue 3, p. 3324-3330

4.1 Introduction

Tidal disruption events (TDEs) occur when a star is scattered into a plunging orbit that brings it so close to a supermassive black hole (SMBH) that it is torn apart by strong tidal forces (Frank & Rees 1976; Rees 1988). During the disruption, the stellar elements are forced into different trajectories, which causes the debris to subsequently evolve into an elongated gas stream. Half of the debris within this stream is bound to the black hole while the other half is unbound. After a revolution around the black hole, the bound debris returns to the disruption site and forms an accretion disc (Shiokawa et al. 2015; Hayasaki et al. 2013, 2015; Bonnerot et al. 2016), from which a powerful flare can be emitted (Komossa et al. 2004, Gezari et al. 2012, see Komossa 2015 for a recent review). This flare represents a unique probe to detect SMBHs in the centres of otherwise quiescent galaxies. Through this signal, it is also in principle possible to put constraints on the black hole properties as well as to investigate the physics of accretion and relativistic jets around these objects.

The debris evolution within the stream from disruption to its return to pericentre has been the focus of several studies, both numerical and analytical. While the debris follows close to ballistic orbits, the transverse structure of the stream is set by the equilibrium between the different forces acting in this direction. During most of its evolution, internal pressure is balanced by self-gravity, which causes the stream to maintain a narrow profile (Kochanek 1994; Ramirez-Ruiz & Rosswog 2009; Guillochon et al. 2014a). However, a recent simulation shows that internal pressure inside the stream may be unable to prevent the fragmentation of the debris into self-gravitating clumps, which can form a few years after disruption (Coughlin & Nixon 2015; Coughlin et al. 2016).

Although it is not associated to substantial emission, a gas component is present around SMBHs in the centre of quiescent galaxies. It is commonly assumed to originate from stellar winds released by massive stars surrounding the black hole (Quataert 2004; Cuadra et al. 2006; Generozov et al. 2015). The impact of this gaseous environment on the stream evolution has so far been largely ignored, owing to a large density contrast between the two components. In a recent study, Guillochon et al. (2015) find that it can affect the trajectories of the unbound debris, resulting in its deceleration on parsec scales. Other authors looked into the influence on the bound part of the stream but in specific contexts, such as a possible origin for the G2 cloud (Guillochon et al. 2014b) and the interaction with a fossil accretion disc (Kelley et al. 2014).

In this paper, we investigate the influence of the ambient gas on the bound debris in a general way. Although dynamical effects are negligible, we demonstrate that hydrodynamical instabilities can lead to the dissolution of a significant part of this debris into the gaseous environment before it returns to pericentre. In this situation, we argue that the associated TDE would be significantly dimmer than expected. This effect is enhanced when the disruption involves a giant star and/or a more massive black hole. As a result, TDEs involving black holes of mass $\gtrsim 10^8\,\mathrm{M}_\odot$ could be difficult to detect. While main sequence stars are swallowed whole by such black holes leading to no substantial emission (MacLeod et al. 2012), disruptions of giant stars could be just as dim owing to the dissolution of the debris into the ambient medium.

This paper is organized as follows. Sections 4.2 and 4.3 present the models used for the SMBH gaseous environment and the debris stream respectively. Section 4.4 investigates the interaction between these two components through both ram pressure and hydrodynamical instabilities. In Section 4.5, we determine the impact on the detectability of TDEs. Our concluding remarks are found in Section 4.6.

4.2 Gaseous environment model

In quiescent galaxies, black holes are surrounded by accretion flows, whose gas is mostly supplied by stellar winds from massive stars. The density distribution within this flow is given by the interplay between their hydrodynamics and the efficiency of the supply mechanism.

The Milky Way is the best example of a quiescent galaxy. It harbours Sgr A*, a central black hole of mass $4.3 \times 10^6\,\mathrm{M}_\odot$, surrounded by a gas environment well studied both theoretically and observationally. Analytical models of stellar winds sources find a density profile in the inner region of the flow decreasing as R^{-1} (Quataert 2004; Generozov et al. 2015), a result consistent with numerical simulations (Cuadra et al. 2006).

Based on this example, we adopt a simple gas density profile for the inner region of quiescent galaxies, given by[1]

$$\rho_\mathrm{g}(R) = \rho_0 \left(\frac{R}{R_0}\right)^{-1}, \tag{4.1}$$

For the Milky Way, the normalization is inferred from Chandra X-ray observations at the Bondi radius, which find a density $\rho_{0,\mathrm{MW}} = 2.2 \times 10^{-22}\,\mathrm{g\,cm^{-3}}$ at $R_{0,\mathrm{MW}} = 0.04\,\mathrm{pc}$.

For galaxies hosting SMBHs of different masses, this profile is scaled using the black hole radius of influence

$$R_\mathrm{inf} = \frac{GM_\mathrm{h}}{\sigma^2} \simeq 3\,\mathrm{pc}\left(\frac{\mathrm{M_h}}{4.3 \times 10^6\,\mathrm{M}_\odot}\right)^{7/15}, \tag{4.2}$$

where M_h is the black hole mass, σ is the velocity dispersion of stars in the bulge and the second equality uses the $M_\mathrm{h} - \sigma$ relation $M_\mathrm{h} = 2 \times 10^8 (\sigma/200\,\mathrm{km\,s^{-1}})^{15/4}\,\mathrm{M}_\odot$ (Gebhardt et al. 2000)[2]. The normalization radius is then obtained from

$$R_0 = \left(\frac{M_\mathrm{h}}{4.3 \times 10^6\,\mathrm{M}_\odot}\right)^{7/15} R_{0,\mathrm{MW}}. \tag{4.3}$$

The normalization density is computed by assuming spherical accretion at a velocity $v \propto v_\mathrm{ff} \propto M_\mathrm{h}^{1/2} R^{-1/2}$, where v_ff is the free-fall velocity. It leads to an accretion rate $\dot{M} \propto R_0^2 \rho_0 v(R_0) \propto \rho_0 M_\mathrm{h}^{6/5}$ using equation (4.3). The gas is supplied to the accretion flow by stellar winds from stars within the black hole sphere of influence. As the mass of stars is similar to that of the black hole within this distance, $\dot{M} \propto M_\mathrm{h}$. This yields

$$\rho_0 = \eta \left(\frac{M_\mathrm{h}}{4.3 \times 10^6\,\mathrm{M}_\odot}\right)^{-1/5} \rho_{0,\mathrm{MW}}, \tag{4.4}$$

where η is a parameter, equal to 1 for the Milky Way. In the following, it is varied up to 1000 to investigate galaxies with denser gas environments. This simple scaling of the gas density profile has also been used by Rimoldi et al. (2015). It leads to a similar dependence on M_h as found from a more detailed treatment (Generozov et al. 2015).

4.3 Tidal stream model

The disruption of a star of mass $M_\star$ and radius $R_\star$ occurs when it reaches the tidal radius $R_\mathrm{t} = R_\star (M_\mathrm{h}/M_\star)^{1/3}$. The resulting debris evolves into an elongated stream owing to an

---

[1] In our galaxy, a density profile scaling as $R^{-1/2}$ may be more consistent with observations of the inner accretion flow (Wang et al. 2013). In other quiescent galaxies, this slope can be derived from observations of TDEs featuring outflows, where it is found to be steeper, decreasing as $R^{-5/2}$ (Alexander et al. 2016) or $R^{-3/2}$ (Berger et al. 2012). However, this could be caused by the propagation of the outflow into a previously evacuated funnel.

[2] The $M_\mathrm{h} - \sigma$ relation can be steeper than this. However, our results are essentially unchanged when using a steeper $M_\mathrm{h} \propto \sigma^{5.3}$ relation (McConnell et al. 2011).

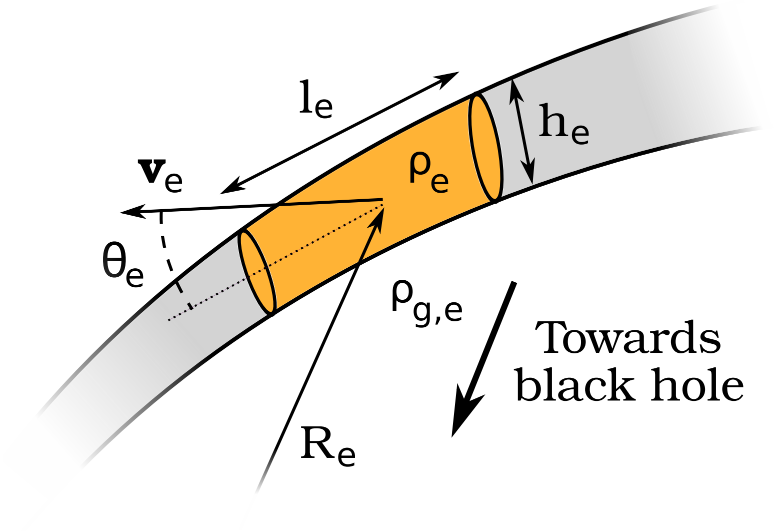

Figure 4.1: Sketch of a portion of debris stream with an element shown in orange. The element has a cylindrical geometry, with length l_e and width h_e. Its density ρ_e is obtained from equation (4.5) knowing its mass. At a distance R_e from the black hole, it moves through a gaseous environment of density $\rho_{g,e} \equiv \rho_g(R_e)$ with a velocity $\mathbf{v}_e$, inclined with respect to its longitudinal axis by an angle θ_e.

orbital energy spread $\delta\epsilon = GM_h R_\star / R_t^2$, acquired during the disruption. In this work, we only focus on the bound debris, with orbital energies ϵ from $-\delta\epsilon$ to 0 and periods T between $t_{\min} = 2\pi G M_h (2\delta\epsilon)^{-3/2}$ and $+\infty$.

To model the stream of bound debris, we divide it into cylindrical elements, an example of which is sketched in Fig. 4.1. In the following, the variables associated to a particular element are indicated by the subscript "e" to differentiate them from those associated to the debris.

An element of period T_e contains debris whose periods satisfy $T_e - \delta T_e < T < T_e + \delta T_e$. Equivalently, it has an average orbital energy $\epsilon_e = -(1/2)(2\pi G M_h / T_e)^{2/3}$ and contains debris with orbital energies in the range $\epsilon_e - \delta\epsilon_e < \epsilon < \epsilon_e + \delta\epsilon_e$. To ensure that each element is composed of debris with similar periods, we set $\delta T_e = 10^{-2}\, t_{\min} \ll T_e$.

Following the disruption, each component of the stream is assumed to follow Keplerian orbits with the same pericentre R_t but different orbital energies ϵ. The position $\mathbf{x}_e$ and velocity $\mathbf{v}_e$ of an element are identified with those of the debris with orbital energy ϵ_e.

Owing to its cylindrical geometry, the density of an element is obtained by

$$\rho_e = \frac{m_e}{\pi h_e^2 l_e}, \tag{4.5}$$

where m_e, h_e and l_e denote the mass, width and length of the element respectively. We explain how these quantities are computed in the remaining of this section.

Knowing the separation $\delta\mathbf{x}_e$ of its two extremities, the length of an element is obtained by $l_e = |\delta\mathbf{x}_e|$. Its velocity $\mathbf{v}_e$ is inclined with respect to its longitudinal direction by an angle θ_e obtained by $\cos\theta_e = \mathbf{v}_e \cdot \delta\mathbf{x}_e / (|\mathbf{v}_e||\delta\mathbf{x}_e|)$.

The mass m_e of an element is obtained from

$$m_e = \int_{\epsilon_e - \delta\epsilon_e}^{\epsilon_e + \delta\epsilon_e} \mathrm{d}M \simeq 2 \left.\frac{\mathrm{d}M}{\mathrm{d}\epsilon}\right|_{\epsilon_e} \delta\epsilon_e. \tag{4.6}$$

where $\mathrm{d}M/\mathrm{d}\epsilon$ is the debris orbital energy distribution. The latter is computed using the analytical model developed by Lodato et al. (2009), which assumes that the debris energy is given by its depth within the black hole potential when the star is disrupted. This yields

$$\frac{\mathrm{d}M}{\mathrm{d}\epsilon} = \frac{R_\star}{\delta\epsilon} \int_{\Delta r}^{R_\star} 2\pi\rho_\star(r) r \mathrm{d}r, \tag{4.7}$$

where $\rho_\star$ is the density inside the star and $\Delta r = (\epsilon/\delta\epsilon)R_\star$. This allows to compute the fallback rate of the debris to pericentre, given by

$$\dot{M}_{\mathrm{fb}} = \frac{\mathrm{d}M}{\mathrm{d}\epsilon}\frac{\mathrm{d}\epsilon}{\mathrm{d}T} = \frac{(2\pi G M_{\mathrm{h}})^{2/3}}{3}\frac{\mathrm{d}M}{\mathrm{d}\epsilon} T^{-5/3}, \tag{4.8}$$

where the relation $T = 2\pi G M_{\mathrm{h}}(-2\epsilon)^{-3/2}$ is used in the second equality.

Based on the work by MacLeod et al. (2012), different density profiles are considered corresponding to the evolution of a 1.4 $\mathrm{M}_\odot$ star. They are obtained from a detailed simulation of the star using the stellar evolution code MESA (Paxton et al. 2011). The evolution of the stellar radius is shown in Fig. 4.2, with the main phases of evolution indicated by filled areas and the five stellar density profiles considered later in the paper shown with coloured points. In the main sequence phase (green area), one profile is considered (MS). Two profiles are chosen in the red giant phase (yellow area): when the star is ascending the red giant branch (RG1) and when it reached the tip of this branch (RG2). For the horizontal branch (orange area) and the asymptotic giant branch (red area) phases, two profiles are selected (HB and AGB).

The width h_{e} is obtained by assuming hydrostatic equilibrium in the stream transverse direction. While pressure tends to expand the stream, the tidal force from the black hole and the stream self-gravity oppose this expansion. Note that the tidal force acts inwards since the stream transverse direction is close to that orthogonal to the direction of the black hole. Hydrostatic equilibrium thus reduces to

$$a_{\mathrm{p,e}} = a_{\mathrm{t,e}} + a_{\mathrm{g,e}} \tag{4.9}$$

where $a_{\mathrm{p,e}} = \nabla P_{\mathrm{e}}/\rho_{\mathrm{e}} \simeq P_{\mathrm{e}}/(\rho_{\mathrm{e}} h_{\mathrm{e}})$ is the pressure acceleration, $a_{\mathrm{t,e}} \simeq G M_{\mathrm{h}} h_{\mathrm{e}}/R_{\mathrm{e}}^3$ is the tidal acceleration and $a_{\mathrm{g,e}} \simeq G m_{\mathrm{e}}/(h_{\mathrm{e}} l_{\mathrm{e}})$ is the self-gravity acceleration within the stream, $R_{\mathrm{e}} = |\mathbf{x}_{\mathrm{e}}|$ being the distance from the black hole and P_{e} the pressure in the stream. For the pressure, we assume an adiabatic evolution with $P_{\mathrm{e}} = K\rho_{\mathrm{e}}^{\gamma}$ where $\gamma = 5/3$. Although the adiabatic constant K should a priori be different for different elements, we adopt a single value averaged over the volume of the star. This is legitimate as the value of K within the star varies only by a factor of a few around this average. The width h_{e} is obtained by solving equation (4.9), making use of equation (4.5). For illustration, in the two limiting cases $a_{\mathrm{g,e}} \gg a_{\mathrm{t,e}}$ and $a_{\mathrm{g,e}} \ll a_{\mathrm{t,e}}$, it scales as $h_{\mathrm{e}} \propto (m_{\mathrm{e}}/l_{\mathrm{e}})^{-1/4}$ and $h_{\mathrm{e}} \propto (R_{\mathrm{e}}^3/M_{\mathrm{h}})^{3/10}(m_{\mathrm{e}}/l_{\mathrm{e}})^{-1/5}$ respectively.

4.4 Tidal stream - ambient medium interactions

4.4.1 Hydrodynamical instabilities

As the stream moves through the ambient medium, it is subject to the Kelvin–Helmholtz (K-H) instability. In this section, we evaluate the effect of this instability on each stream element.

Taking a conservative approach, we only consider the second half of each element orbit, i.e. after apocentre passage. This approach is motivated by the fact that an element reaches its lowest density in this part of the orbit and is therefore more easily affected by its interaction

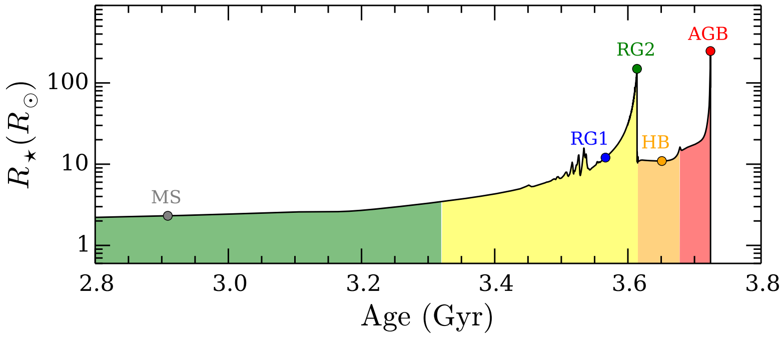

Figure 4.2: Evolution of the radius of a 1.4 $M_\odot$ star. The main evolutionary phases are indicated by filled regions: main sequence (green), red giant (yellow), horizontal branch (orange) and asymptotic giant branch (red). The coloured points correspond to the five stellar density profiles considered.

with the ambient medium. In this portion of the orbit, an element falls almost radially from apocentre to pericentre. In this configuration, the K-H instability develops on a given stream element for wavenumbers k_e which obey the inequality (Clarke & Carswell 2007, p.138)

$$a_\mathrm{e} < \frac{\rho_\mathrm{e}\,\rho_\mathrm{g,e}}{\rho_\mathrm{e}^2 - \rho_\mathrm{g,e}^2}\,k_\mathrm{e}\,v_\mathrm{rel,e}^2 \tag{4.10}$$

where a_e is the inwards acceleration of the element in the transverse direction, $\rho_\mathrm{g,e} \equiv \rho_\mathrm{g}(R_\mathrm{e})$ is the density of gas at the position of the element and $v_\mathrm{rel,e}$ is the relative velocity between the element and the background gas. Although modes with large k_e have fast growth rates, they are also the least disruptive as the associated instability saturates at an amplitude $\sim 1/k_\mathrm{e}$. We therefore consider a wavenumber $k_\mathrm{e} = 1/h_\mathrm{e}$ which has the slowest growth rate but is the most disruptive since it develops on the whole element width. The transverse acceleration a_e has two inwards components. One is the self-gravity acceleration $a_\mathrm{g,e} \simeq G m_\mathrm{e}/(h_\mathrm{e} l_\mathrm{e})$ and the other is the tidal acceleration $a_\mathrm{t,e} \simeq G M_\mathrm{h} h_\mathrm{e}/R_\mathrm{e}^3$. With $a_\mathrm{e} = a_\mathrm{t,e} + a_\mathrm{g,e}$, condition (4.10) reduces to

$$a_\mathrm{t,e} + a_\mathrm{g,e} < \frac{\rho_\mathrm{g,e} v_\mathrm{e}^2}{\rho_\mathrm{e} h_\mathrm{e}} \equiv a_\mathrm{r,e}, \tag{4.11}$$

which uses $\rho_\mathrm{e} \gg \rho_\mathrm{g,e}$. The relative velocity is computed by $v_\mathrm{rel,e} = v_\mathrm{e}\cos\theta_\mathrm{e} \simeq v_\mathrm{e}$ where $v_\mathrm{e} = |\mathbf{v}_\mathrm{e}|$ is the velocity of the element. This uses the approximation $\theta_\mathrm{e} \ll 1$, which is satisfied along an element orbit, as soon as it leaves its apocentre. In addition, this value of $v_\mathrm{rel,e}$ assumes that the background gas is at rest. The possibility of a lower relative velocity caused by radially falling back ground gas has been explored and leads to no significant difference. The right-hand side of equation (4.11) is called $a_\mathrm{r,e}$ as it is equivalent to a ram pressure acceleration.

If condition (4.11) is satisfied, the K-H instability then grows on a timescale

$$\tau_\mathrm{KH,e} = \left(\frac{h_\mathrm{e}}{a_\mathrm{r,e} - a_\mathrm{t,e} - a_\mathrm{g,e}}\right)^{1/2}, \tag{4.12}$$

for a given element. Otherwise, the instability does not develop and $\tau_\mathrm{KH,e} = +\infty$. The K-H instability has time to fully grow before the element reaches pericentre if

$$f_\mathrm{KH,e} \equiv \int_{T_\mathrm{e}/2}^{T_\mathrm{e}} \frac{\mathrm{d}t}{\tau_\mathrm{KH,e}} > 1, \tag{4.13}$$

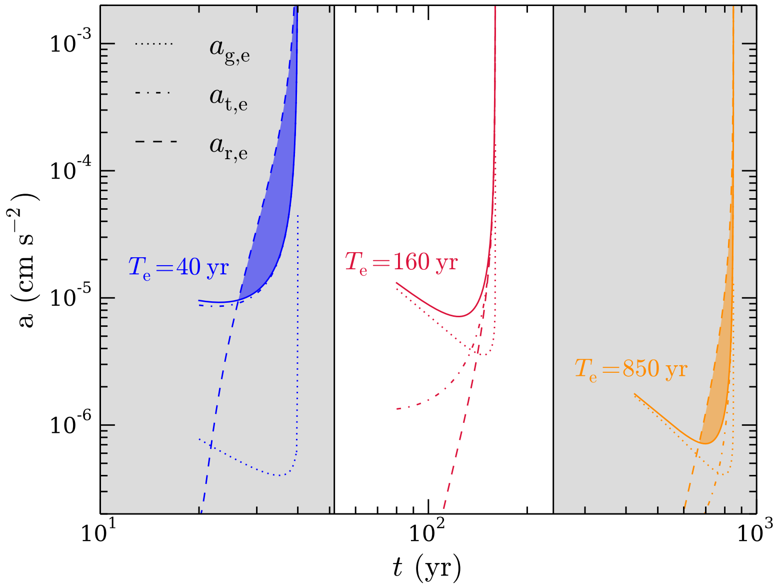

Figure 4.3: Evolution of $a_{g,e}$ (dotted lines), $a_{t,e}$ (dashed dotted lines), $a_{g,e}+a_{t,e}$ (solid line) and $a_{r,e}$ (dashed lines) for three elements of a stream produced by the tidal disruption of the star in the red giant phase (profile RG1) by a black hole of mass $M_h = 10^8\,M_\odot$ in a galaxy with $\eta = 5$. The elements have different periods $T_e = 40$ yr (blue lines), $T_e = 160$ yr (red lines) and $T_e = 850$ yr (yellow lines). For each element, the filled areas indicate the regions where $a_{g,e} + a_{t,e} < a_{r,e}$, that is where condition (4.11) is satisfied. The grey areas indicate the range of periods of elements verifying condition (4.13), for which the K-H instability has time to fully develop before they return to pericentre.

where $T_e/2$ and T_e are the times corresponding to the element apocentre and pericentre passages respectively. Condition (4.13) can be understood by omitting the temporal dependence of $\tau_{KH,e}$. In this case, it reduces to $\tau_{KH,e} < T_e/2$ which clearly implies that the K-H instability has time to fully grow during the portion of orbit considered.

As an example, the evolution of $a_{g,e}$ (dotted lines), $a_{t,e}$ (dashed dotted lines), the left-hand side of equation (4.11) $a_{g,e} + a_{t,e}$ (solid line) and its right-hand side $a_{r,e}$ (dashed lines) is shown in Fig. 4.3 for three different elements of a stream produced by the disruption of the star in the red giant phase (profile RG1) by a black hole of mass $M_h = 10^8\,M_\odot$ in a galaxy with $\eta = 5$. These elements have periods $T_e = 40$ yr (blue lines), $T_e = 160$ yr (red lines) and $T_e = 850$ yr (yellow lines). For all elements, tidal acceleration dominates self-gravity acceleration ($a_{t,e} > a_{g,e}$) in the final part of their orbit, when $R_e < h_e(M_h/m_e)^{1/3}$. The zones where condition (4.11) is true, are indicated by filled regions for each element. They only exist for the most bound (blue lines) and least bound (yellow lines) of the elements considered. For these two elements, condition (4.13) is also satisfied and the K-H instability therefore has time to fully develop before they return to pericentre. For the intermediate element (red lines), condition (4.11) is never verified. This implies $f_{KH,e} = 0$ and condition (4.13) is therefore not satisfied either. The grey areas indicate the range of periods of all the stream elements that satisfy condition (4.13). On these elements, we expect the K-H instability to fully grow over the course of their orbit.

Fig. 4.3 indicates the range of periods of elements that satisfy condition (4.13), but does not show the precise evolution of $f_{KH,e}$ with T_e. Actually, the transition between $f_{KH,e} = 0$ and $f_{KH,e} > 1$ is very sharp. For elements that never satisfy condition (4.11), $f_{KH,e} = 0$.

However, as soon as condition (4.11) is met at some point along an element orbit, $f_{\rm KH,e} \gtrsim 1$, which implies that condition (4.13) is already marginally satisfied. This is because, in the final part of an element orbit where $a_{\rm t,e} \gg a_{\rm g,e}$, the inequality $a_{\rm r,e}/a_{\rm t,e} \gtrsim 2$ implies $\tau_{\rm KH,e} \lesssim (GM_{\rm h}/R_{\rm e}^3)^{-1/2}$, where the right-hand side is the infall time from $R_{\rm e}$ to pericentre. Omitting the time dependence of $\tau_{\rm KH,e}$, this translates to $f_{\rm KH,e} \gtrsim 1$.

The reason why only the most and least bound part of the stream are affected by the K-H instability can be understood by examining condition (4.11) more in detail in the final part of each element orbit, where $a_{\rm t,e} \gg a_{\rm g,e}$. Using $v_{\rm e} \simeq (GM_{\rm h}/R_{\rm e})^{1/2}$, it reduces to

$$m_{\rm e}/l_{\rm e} < \rho_{\rm g,e} R_{\rm e}^2, \tag{4.14}$$

that is a condition on the stream linear density. Note that this condition is also independent on the element width $h_{\rm e}$. Our results are therefore largely independent on the assumption of hydrostatic equilibrium made to compute this width in Section 4.3. Furthermore, this means that physical mechanisms modifying the stream width, such as fast cooling of the debris, are unlikely to affect our results. One can clearly see that condition (4.14), and therefore condition (4.13), is easily satisfied for the most bound part of the stream, which is less massive since it originates from the tenuous outer layer of the star. Although the least bound part of the stream contains more mass, it is stretched owing to different trajectories of neighbouring debris regions and condition (4.14) is also satisfied.

At this point, one can predict how the impact of the K-H instability depends on the other parameters, namely the black hole mass $M_{\rm h}$, the evolutionary stage of the star and η, which relates to the ambient medium density via equation (4.4). Tidal disruptions by more massive black holes lead to more extended streams. Furthermore, the right-hand side of condition (4.14) evaluated at $R_{\rm t}$ scales as $\rho_{\rm g,e} R_{\rm e}^2 \simeq \rho_{\rm g}(R_{\rm t}) R_{\rm t}^2 \propto M_{\rm h}^{9/15}$, which increases with the black hole mass. We therefore anticipate condition (4.11) to be more easily satisfied when $M_{\rm h}$ is larger. The stream is therefore likely to be more sensitive to the K-H instability. This trend is also expected for disruptions of evolved stars as they also lead to more extended streams whose debris originates from a more tenuous outer layer. Finally, we anticipate the same tendency when η is increased, that is for environments with higher gas density, since $\rho_{\rm g,e} R_{\rm e}^2 \propto \eta$. These predictions will be verified explicitly in Section 4.4.3.

4.4.2 Ram pressure

As a stream element sweeps up the ambient medium located on its trajectory, it loses momentum and decelerates. This deceleration affects significantly the trajectory of the element once it has swept a mass of ambient gas larger than its own mass. This is equivalent to

$$f_{\rm ram,e} \equiv \frac{1}{m_{\rm e}} \int_0^{T_{\rm e}} \rho_{\rm e}\, v_{\rm e} A_{\rm e}\, {\rm dt} > 1, \tag{4.15}$$

where $A_{\rm e} = h_{\rm e} l_{\rm e} \sin\theta_{\rm e}$ is the element area sweeping gas from the ambient medium. As for the K-H instability, we find this condition to be satisfied both for the most and least bound part of the stream. However, $f_{\rm ram,e} < f_{\rm KH,e}$ in all cases explored, which means that the debris is affected by the K-H instability before their trajectories change due to ram pressure.

4.4.3 Effect on flare luminosities

We now evaluate the impact of the K-H instability on the flare luminosities produced by the disruption of the star in different evolutionary stages and examine the dependence on the black hole mass $M_{\rm h}$ and ambient gas density, through the parameter η.

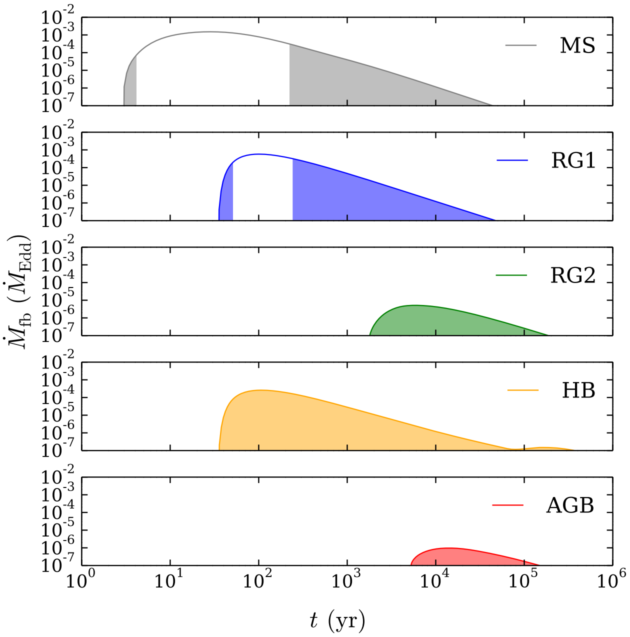

Figure 4.4: Evolution of the debris mass fallback rate after a disruption with $M_{\rm h} = 10^8\, {\rm M}_\odot$ and $\eta = 5$ for the five stellar density profiles considered: MS (grey line), RG1 (blue line), RG2 (green line), HB (yellow line) and AGB (red line). The filled areas correspond to the return times of debris satisfying condition (4.13).

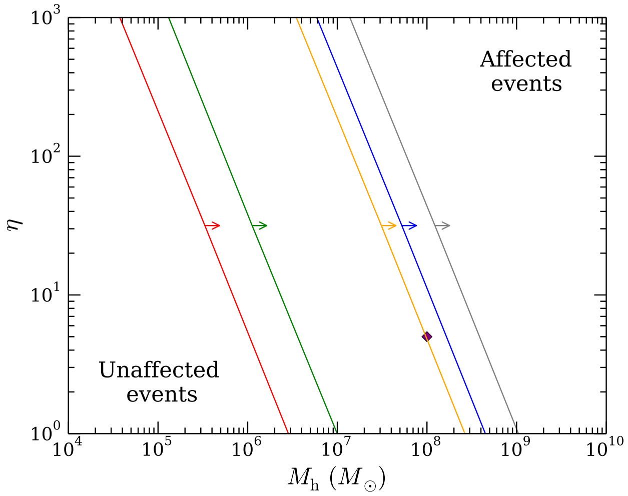

Figure 4.5: $M_{\rm h} - \eta$ plane depicting the effect of the K-H instability on different disruption events. Each line corresponds to one of the stellar density profiles considered. The zone in the direction of the arrow corresponds to events affected by the K-H instability, for which $f_{\rm KH,peak} > 1$. The zone in the opposite direction corresponds to events for which $f_{\rm KH,peak} < 1$, unaffected by the K-H instability. The purple diamond shows the parameters corresponding to Fig. 4.4, $M_{\rm h} = 10^8\, {\rm M}_\odot$ and $\eta = 5$.

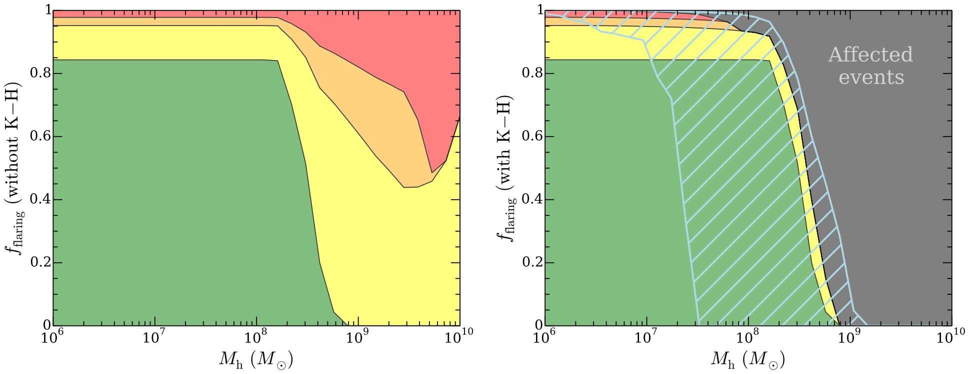

Figure 4.6: Probability for a disruption event to occur in a given evolutionary stage as a function of $M_{\rm h}$. The different coloured areas correspond to different phases in the evolution of the star: main sequence (green), red giant (yellow), horizontal branch (orange) and asymptotic giant branch (red). Only the right panel includes the effect of the K-H instability, with the grey area corresponding to affected events for a galaxy with $\eta = 5$. The zone swept by the boundary of this area is shown by a blue hatched region for values of η varying from 1 to 1000 from right to left.

Fig. 4.4 shows the fallback rate, computed using equation (4.8), of the debris produced by the disruption of the star by a black hole of mass $M_{\rm h} = 10^8\,{\rm M}_\odot$ in a galaxy with $\eta = 5$ for the five stellar density profiles considered. The filled areas indicate the times at which elements satisfying condition (4.13) return to pericentre. For these elements, the K-H instability has time to fully grow over the course of their orbit. For profiles MS and RG1, these zones exist only for the most and least bound debris, as in the example of Fig. 4.3. The debris whose return times correspond to the peak fallback rate are always outside this zone. Instead, for profiles RG2, HB and AGB, all the elements lie in the filled zone, even those returning to pericentre when the fallback rate peaks. It means that the K-H instability has time to fully grow in the whole stream. This confirms our expectation that streams produced by the disruption of evolved stars are more sensitive to the K-H instability.

So far, we have examined for which elements condition (4.13) is satisfied, that is for which debris the K-H instability fully develop before it reaches pericentre. As these instabilities involve the whole width of the stream, we infer that this debris subsequently dissolves into the ambient medium and does not return to pericentre.

Only the elements reaching pericentre intact can participate to the luminosity emitted from the event. Therefore, if all the stream dissolves into the ambient medium due to the K-H instability, the appearance of the event is likely to be affected, emitting a significantly lower luminosity. We take a conservative approach and state that an event is affected by this instability if even the element corresponding to the peak of the mass fallback rate dissolves into the background gas. According to our criterion, this requires condition (4.13) to be satisfied for this element, that is $f_{\rm KH,peak} > 1$. Fig. 4.5 shows the regions of the $M_{\rm h} - \eta$ plane corresponding to events affected by the K-H instability. Each line is associated to one of the stellar density profiles considered. The zone in the direction of the arrow corresponds to affected events while the zone in the opposite direction corresponds to unaffected events. The example discussed above ($M_{\rm h} = 10^8\,{\rm M}_\odot$ and $\eta = 5$), where events corresponding to profiles RG2, HB and AGB are affected, is indicated by a purple diamond. As predicted above, events involving more massive black holes or occurring in galactic nuclei with denser gaseous environment are more sensitive to the K-H instability.

4.5 Impact on the detectability of TDEs

In the previous section, we argued that the K-H instability can lead to the dissolution of a significant part of the stream before it comes back to pericentre, which could significantly reduce the luminosity emitted from the associated event. Furthermore, we showed that events involving more massive black holes and/or evolved stars are more sensitive to this effect. In this section, we examine the consequence on the detectability of TDEs produced by the disruption of a $1.4\,\mathrm{M}_\odot$ star in different evolutionary stages and by black hole of different masses.

For an event to lead to a substantial flare, the star must be disrupted outside the black hole's Schwarzschild radius R_s. Otherwise, it is swallowed whole without significant emission. We investigate the effect of the K-H instability on the detectability of events satisfying this condition. To this aim, we define the probability of such events to occur when the star is in a given evolutionary stage by

$$f_\mathrm{flaring}^\mathrm{stage} = N_\mathrm{stage}/N_\mathrm{lifetime}, \tag{4.16}$$

where N_stage and N_lifetime are the number of events occurring during the evolutionary stage and the whole stellar lifetime respectively. The possibility of an event to be affected by the K-H instability is only included in N_stage. These numbers are obtained by

$$N_\mathrm{stage} = \int_{t_\mathrm{start}}^{t_\mathrm{end}} \dot{N} \chi_\mathrm{swa} \chi_\mathrm{KH}\, \mathrm{dt}, \tag{4.17}$$

$$N_\mathrm{lifetime} = \int_0^{t_\mathrm{lt}} \dot{N} \chi_\mathrm{swa}\, \mathrm{dt}, \tag{4.18}$$

where t_start and t_end are the starting and ending times of the stage respectively, while t_lt is the lifetime of the star. $\dot{N}$ is the disruption rate, which we assumed to scale as $\dot{N} \propto R_\mathrm{t}^{1/4}$ following MacLeod et al. (2012). χ_swa and χ_KH are binary functions given by

$$\chi_\mathrm{swa} = \begin{cases} 0 & \text{if } R_\mathrm{t} \leq R_\mathrm{s} \\ 1 & \text{if otherwise} \end{cases}, \tag{4.19}$$

$$\chi_\mathrm{KH} = \begin{cases} 0 & \text{if } f_\mathrm{KH,peak} \geq 1 \\ 1 & \text{if otherwise} \end{cases}, \tag{4.20}$$

which are respectively zero if the star is swallowed whole and if the stream is affected by the K-H instability according to the criterion defined in Section 4.4.

This probability is shown in Fig. 4.6 as a function of the black hole mass for different evolutionary stages. The left panel does not take into account the K-H instability, artificially fixing $\chi_\mathrm{KH} = 1$ in equation (4.17). It reproduces figure 14 (right panel) of MacLeod et al. (2012). For $M_\mathrm{h} \gtrsim 10^8\,\mathrm{M}_\odot$, the evolutionary stage of most disrupted stars switches from main sequence stars to giant stars. This is because $R_\mathrm{t} < R_\mathrm{s}$ for main sequence stars above this mass. Instead, the right panel of Fig. 4.6 includes the effect of the K-H instability. The grey zone indicates affected events in a galaxy with $\eta = 5$. For $M_\mathrm{h} \gtrsim 10^8\,\mathrm{M}_\odot$, giant stars as previously become more likely to be tidally disrupted than main sequence stars. However, as giant stars are more sensitive to the K-H instability, all the events are affected by the K-H instability for $M_\mathrm{h} \gtrsim 10^9\,\mathrm{M}_\odot$, which could significantly hamper their detection. The blue hatched region indicates the zone swept by the boundary of the grey area for values of η varying from 1 to 1000 from right to left. For $\eta \gtrsim 10$, even the events involving main sequence stars are affected by the K-H instability.

4.6 Discussion and conclusion

The interaction between the debris stream produced by TDEs and the background gas of quiescent galaxies has often been neglected, on the basis of their large difference in density. In this paper, we have investigated this interaction for the bound part of the stream, involved in the flaring activity of these events. Through an analytical argument, we have demonstrated that the K-H instability can affect the debris, especially for disruptions involving an evolved star and/or a massive black hole. In this case, a substantial fraction of the tidal stream can dissolve into the background gas before it reaches pericentre, likely leading to a flare dimmer than previously expected.

In order to model the stream, we have used the analytical model of Lodato et al. (2009) for the specific energy distribution within the stream, which assumes that the star is unperturbed until it reaches pericentre. Actually, numerical simulations have shown that the stellar structure is perturbed at pericentre (Lodato et al. 2009; Guillochon & Ramirez-Ruiz 2013). However, this effect can be easily accounted for within the same analytical model, by applying a homologous expansion of the unperturbed model by a factor ~ 2 (Lodato et al. 2009), which makes the energy distribution very close to the one obtained through simulations. This leads to a stream slightly more resistant to the K-H instability but does not affect our main conclusions.

Another assumption of the model is a total disruption of the star by the black hole. However, simulations have shown that a surviving core can remain after the disruption (Guillochon & Ramirez-Ruiz 2013), which keeps following the initial stellar orbit. This likely causes the marginally bound part of the stream to contain less mass than expected from Lodato et al. (2009). The debris returning to pericentre at late times would therefore be even more sensitive to the K-H instability.

We also note that we have neglected the effects of magnetic fields in the stream. Such effects might prevent the dissolution of the stream by the K-H instability (McCourt et al. 2015). We can address this issue analytically by adding a term $a_{\rm m,e} \simeq B_{||}^2/(\rho_{\rm e} h_{\rm e})$ to the left-hand side of condition (4.11), where $B_{||}$ is the component of the magnetic field parallel to the stream (Chandrasekhar 1961, section 106). This term is significant only if $a_{\rm m,e} \gtrsim a_{\rm r,e}$, which translates to $B_{||} \gtrsim \rho_{\rm g,e}^{1/2} v_{\rm e} \simeq 3\,{\rm G}\,(\eta/1)^{1/2}(R_\star/12\,{\rm R}_\odot)^{-1}(M_{\rm h}/10^8\,{\rm M}_\odot)^{3/10}$, evaluating the right-hand side at $R_{\rm t}$ and for a stellar radius corresponding to profile RG1. Such values of $B_{||}$ correspond to typical surface magnetic fields for main sequence stars. They probably exceed typical surface magnetic fields in red giants, estimated from magnetic flux conservation in the expansion phase. For example, a expansion by a factor of 10 implies a magnetic field reduced by a factor of 100. In the stream, the critical value for $B_{||}$ is unlikely to be reached for several reasons. Firstly, they require that the star is exactly stretched in the direction of its magnetic field, which is unlikely since the magnetic field orientation is random. Secondly, the magnetic field in the inner region of a star is likely tangled and not ordered in the same direction. In this configuration, magnetic reconnection may also occur in the stretching process, lowering the total magnetic field. In addition, although flux conservation imposes that the magnetic field in the direction of the stream is conserved since the stream stays thin, magnetic diffusion could lead to a decrease of this component as the stream orbits around the black hole. A caveat in these arguments is the ill-known value of the magnetic field strength inside giant stars. Nevertheless, we consider it unlikely that magnetic fields would prevent the K-H instability from developing. However, a definite answer would require to follow the evolution of the stellar magnetic field during the disruption and the fallback of the debris.

Finally, our calculations are made in an ambient medium at rest although an inward velocity of the gas environment could diminish the effect of the K-H instability. We have tested the dependence of our results on this assumption by introducing an radial velocity of the gas, which results in a lower relative velocity in equations (4.11) and (4.12). We find that our main conclusions remain unchanged for an infall velocity up to the Keplerian velocity, thus confirming the solidity of our analysis.

The main implication of this study is that any TDEs involving black holes with masses $\gtrsim 10^8\,\mathrm{M}_\odot$ might be difficult to detect, a conclusion largely independent of our scaling for the background gas density with black hole mass. This was already known for main sequence stars, which are swallowed whole for this range of masses (MacLeod et al. 2012). Here, we show that this is also the case for giant stars, which have their debris stream dissolved into the background gas through the K-H instability.

Acknowledgments

C.B. is grateful to Giovanni Dipierro for hosting him during the completion of this work.

Bibliography

Alexander K. D., Berger E., Guillochon J., Zauderer B. A., Williams P. K. G., 2016, ApJ, 819, L25

Berger E., Zauderer A., Pooley G. G., Soderberg A. M., Sari R., Brunthaler A., Bietenholz M. F., 2012, ApJ, 748, 36

Bonnerot C., Rossi E. M., Lodato G., Price D. J., 2016, MNRAS, 455, 2253

Chandrasekhar S., 1961, Hydrodynamic and hydromagnetic stability. Dover Press, New York

Clarke C., Carswell B., 2007, Principles of Astrophysical Fluid Dynamics. Cambridge University Press, Cambridge

Coughlin E. R., Nixon C., 2015, ApJ, 808, L11

Coughlin E. R., Nixon C., Begelman M. C., Armitage P. J., Price D. J., 2016, MNRAS, 455, 3612

Cuadra J., Nayakshin S., Springel V., Di Matteo T., 2006, MNRAS, 366, 358

Frank J., Rees M. J., 1976, MNRAS, 176, 633

Gebhardt K., et al., 2000, ApJ, 539, L13

Generozov A., Stone N. C., Metzger B. D., 2015, MNRAS, 453, 775

Gezari S., et al., 2012, Nature, 485, 217

Guillochon J., Ramirez-Ruiz E., 2013, ApJ, 767, 25

Guillochon J., Manukian H., Ramirez-Ruiz E., 2014a, ApJ, 783, 23

Guillochon J., Loeb A., MacLeod M., Ramirez-Ruiz E., 2014b, ApJ, 786, L12

Guillochon J., McCourt M., Chen X., Johnson M. D., Berger E., 2015, preprint (arXiv:1509.08916)

Hayasaki K., Stone N., Loeb A., 2013, MNRAS, 434, 909

Hayasaki K., Stone N. C., Loeb A., 2015, preprint (arXiv:1501.05207)

Kelley L. Z., Tchekhovskoy A., Narayan R., 2014, MNRAS, 445, 3919

Kochanek C. S., 1994, ApJ, 436, 56

Komossa S., 2015, Journal of High Energy Astrophysics, 7, 148

Komossa S., Halpern J., Schartel N., Hasinger G., Santos-Lleo M., Predehl P., 2004, ApJ, 603, L17

Lodato G., King A. R., Pringle J. E., 2009, MNRAS, 392, 332

MacLeod M., Guillochon J., Ramirez-Ruiz E., 2012, ApJ, 757, 134

McConnell N. J., Ma C.-P., Gebhardt K., Wright S. A., Murphy J. D., Lauer T. R., Graham J. R., Richstone D. O., 2011, Nature, 480, 215

McCourt M., O'Leary R. M., Madigan A.-M., Quataert E., 2015, MNRAS, 449, 2

Paxton B., Bildsten L., Dotter A., Herwig F., Lesaffre P., Timmes F., 2011, ApJS, 192, 3

Quataert E., 2004, ApJ, 613, 322

Ramirez-Ruiz E., Rosswog S., 2009, ApJ, 697, L77

Rees M. J., 1988, Nature, 333, 523

Rimoldi A., Rossi E. M., Piran T., Portegies Zwart S., 2015, MNRAS, 447, 3096

Shiokawa H., Krolik J. H., Cheng R. M., Piran T., Noble S. C., 2015, ApJ, 804, 85

Wang Q. D., et al., 2013, Science, 341, 981

5

Magnetic field evolution in tidal disruption events

When a star gets tidally disrupted by a supermassive black hole, its magnetic field is expected to pervade its debris. In this paper, we study this process via smoothed particle magnetohydrodynamical simulations of the disruption and early debris evolution including the stellar magnetic field. As the gas stretches into a stream, we show that the magnetic field evolution is strongly dependent on its orientation with respect to the stretching direction. In particular, an alignment of the field lines with the direction of stretching induces an increase of the magnetic energy. For disruptions happening well within the tidal radius, the star compression causes the magnetic field strength to sharply increase by an order of magnitude at the time of pericentre passage. If the disruption is partial, we find evidence for a dynamo process occurring inside the surviving core due to the formation of vortices. This causes an amplification of the magnetic field strength by a factor of ~ 10. However, this value represents a lower limit since it increases with numerical resolution. For an initial field strength of 1 G, the magnetic field never becomes dynamically important. Instead, the disruption of a star with a strong 1 MG magnetic field produces a debris stream within which magnetic pressure becomes similar to gas pressure a few tens of hours after disruption. If the remnant of one or multiple partial disruptions is eventually fully disrupted, its magnetic field could be large enough to magnetically power the relativistic jet detected from Swift J1644+57. Magnetized streams could also be significantly thickened by magnetic pressure when it overcomes the confining effect of self-gravity.

C. Bonnerot, D. J. Price, G. Lodato and E. M. Rossi
2017, *MNRAS*, **Volume 469**, Issue 4, p. 4879-4888

5.1 Introduction

A tidal disruption event (TDE) happens when a star gets destroyed by the strong tidal forces of a supermassive black hole. Following the disruption, the stellar debris evolves into an extended stream of gas composed of a bound part that falls back towards the disruption site and an unbound part that escapes the black hole's gravity (Rees 1988). The central region of this stream can also contain a surviving self-gravitating core after the encounter if the star is only partially disrupted.

Stars commonly have a magnetic field that is expected to be transferred to the debris during a TDE. This magnetic field has several potentially interesting consequences on the debris subsequent evolution. Magnetic stresses within the stream can accelerate the circularization of its bound part into an accretion disc (Bonnerot et al. 2017). Alternatively, they can cause a fraction of the debris to pass beyond the event horizon of the black hole and be ballistically accreted (Svirski et al. 2017). If field lines are oriented along the stream longitudinal direction, the associated magnetic tension can make the stream more resistant to hydrodynamical instabilities, predicted to otherwise affect the low-density streams produced by the disruption of giant stars (McCourt et al. 2015; Bonnerot et al. 2016). This magnetic effect could also prevent the stream fragmentation into self-gravitating clumps (Coughlin & Nixon 2015). Finally, while the stream is commonly thought to maintain a narrow profile set by hydrostatic equilibrium between gas pressure and self-gravity (Kochanek 1994; Coughlin et al. 2016b), magnetic pressure could provide an additional outward force that can affect the stream structure, likely making it thicker than previously thought.

Among the few dozen TDE candidates detected so far, a small fraction shows evidence of a relativistic jet, the most famous example being Swift J1644+57 whose X-ray radiation is thought to be beamed along our line of sight (Bloom et al. 2011; Burrows et al. 2011). One mechanism to power a relativistic jet is the Blandford-Znajek mechanism (Blandford & Znajek 1977) which allows to extract rotational energy from the black hole. A necessary ingredient for this mechanism to operate is a large-scale magnetic field threading the black hole. The field lines then get twisted by the black hole rotation. As they unwind and expand, plasma gets ejected at high velocities along the direction of the black hole spin. However, in the case of Swift J1644+57, the stellar magnetic flux alone is far too small to launch a jet powerful enough to account for the measured X-ray luminosity (Tchekhovskoy et al. 2014). Alternative origins have been proposed that involve an in-situ dynamo process creating regions of large magnetic flux within the disc (Krolik & Piran 2012; Piran et al. 2015), the interaction with a fossil disc whose magnetic field is collected by the stream in its fallback (Kelley et al. 2014) and the disruption of a strongly-magnetized star resulting from a recent binary merger (Mandel & Levin 2015). Another possibility is that TDE jets are powered radiatively (Sądowski & Narayan 2015; Jiang et al. 2014; Kara et al. 2016), in which case a large magnetic flux is not required.

In this paper, we study the evolution of the stellar magnetic field as the star is tidally disrupted by a black hole by means of simulations using the smoothed particle magnetohydrodynamics (SPMHD) numerical method (see Price 2012 for a review), a generalization of the smoothed particle hydrodynamics (SPH) technique (Monaghan 2005). This approach is complementary to a recent study by Guillochon & McCourt (2017) which was carried out using a grid-based code and for different initial configurations. Depending on the orientation of the magnetic field with respect to the stream stretching direction, we find that the magnetic field distribution within the debris varies significantly. As expected from flux conservation, the stream magnetic field strength only slowly decreases if the field lines align with the direction of stretching resulting in a magnetic energy increase. For a partial disruption, we find evidence of a dynamo process occurring due to the formation of vortices at the interface between the surviving core and the recollapsing material. The magnetic field strength gets amplified within the core via this mechanism by about an order of magnitude. Instead, the star compression occurring for deep tidal disruptions lead to a sharp peak in the magnetic field strength at pericentre passage. Finally, the disruption of a strongly magnetized star results in a stream inside which magnetic pressure becomes comparable to gas pressure, providing an additional support against self-gravity.

The outline of the paper is as follows. In Section 5.2, we describe the numerical setup and method used to perform the simulations. The results are presented in Section 5.3 which successively treats the influence of the magnetic field orientation, depth of the encounter and strength of the initial stellar magnetic field. The impact of the numerical resolution on these results is also evaluated. Finally, Section 5.4 contains a discussion of these results and our concluding remarks. In particular, we compare our results to that of Guillochon & McCourt (2017).

5.2 SPH simulations

We simulate the interaction between a star of mass $M_\star = \mathrm{M}_\odot$ and radius $R_\star = \mathrm{R}_\odot$ and a black hole of mass $M_\mathrm{h} = 10^6\,\mathrm{M}_\odot$. For this choice of parameter, the tidal radius, within which the tidal force from the black hole exceeds the self-gravity force of the star, is $R_\mathrm{t} = R_\star (M_\mathrm{h}/M_\star)^{1/3} = 100\,\mathrm{R}_\odot$. The star is set on a parabolic orbit at a distance of $3R_\mathrm{t}$ from the black hole, where the tidal force represents only 4% of the self-gravity force. Its pericentre distance R_p is defined via the penetration factor $\beta \equiv R_\mathrm{t}/R_\mathrm{p}$, which we set to different values. We investigate $\beta = 0.7$, for which the star is expected to be only partially disrupted with a surviving core continuing to orbit the black hole after the encounter (Guillochon & Ramirez-Ruiz 2013). Larger values of the penetration factor $\beta = 1$ and $\beta = 5$ are also considered that both correspond to a full disruption of the star.

The star is modelled as a polytropic sphere with $\gamma = 5/3$ containing one million SPH particles. A resolution study is presented in Section 5.3.4 where different numbers of particles are considered. To achieve the desired density profile, the SPH particles are first positioned according to a close sphere packing and then differentially stretched along their radial direction. This structure is then evolved in isolation until its internal properties settle down. This technique has also been used by Lodato et al. (2009). In addition, an initial magnetic field is imposed to the star, which we choose to be uniform and linear for a clearer interpretation of the results, especially their dependence on varying magnetic field orientations. This choice is different from that of Guillochon & McCourt (2017) who consider a unique orientation of the field. Little is known about the strength of magnetic fields in stellar interiors. The magnetic field observed on stellar surfaces have strengths varying between the solar value of $\sim 1\,\mathrm{G}$ and $\sim 10\,\mathrm{kG}$ for rapidly rotating stars (Oksala et al. 2010). In stellar interiors, evidence of magnetic fields with strengths of $\sim 1\,\mathrm{MG}$ are found through asteroseismology measurements in red giants (Fuller et al. 2015). We therefore adopt this range of values to model the stellar magnetic field in this paper. The dynamical importance of the magnetic field is measured by the plasma beta $\beta_\mathrm{M} \equiv P_\mathrm{gas}/P_\mathrm{mag}$, defined as the ratio of gas pressure to magnetic pressure. The latter is given as a function of magnetic field strength as $P_\mathrm{mag} \equiv |\mathbf{B}|^2/(8\pi)$ cgs. The magnetic field strength is set to $|\mathbf{B}| = 1\,\mathrm{G}$ in most of our models. For this choice, the initial plasma beta within the star is $\beta_\mathrm{M,ini} \approx 10^{16} \gg 1$, which implies that the magnetic field is not dynamically relevant. We investigate two different orientations of the field, pointing in the $\mathbf{x}$ and $\mathbf{z}$ directions illustrated on the upper left panel of Fig. 5.1. Note that the $\mathbf{x}$ direction is along the initial stellar orbit while the $\mathbf{z}$ direction is orthogonal to the orbital plane of the star. We also test the effect of increasing the magnetic field strength to $|\mathbf{B}| = 1\,\mathrm{MG}$ and $|\mathbf{B}| = 2\,\mathrm{MG}$, which corre-

Table 5.1: Name and parameters of the different models.

Model [a]	Disruption	β	Strength	Orientation
F1B0G	Full	1	0 G	–
F1B1G-x	Full	1	1 G	**x**
F1B1G-z	Full	1	1 G	**z**
F1B1MG-x	Full	1	1 MG	**x**
F1B2MG-x	Full	1	2 MG	**x**
F5B1G-x	Full	5	1 G	**x**
P.7B1G-x	Partial	0.7	1 G	**x**

[a] The first letter "F" and "P" in the name of the models refer to full and partial tidal disruptions. The following two numbers indicates the value of the penetration factor β and the magnetic field strength. Finally, the last letter refers to the magnetic field orientation.

sponds to a strongly magnetized star. In this case, the initial plasma beta reaches $\beta_{\mathrm{M,ini}} \approx 10^4$. The magnetic fields considered are therefore never dynamically relevant initially. This justifies the method used to produce the initial condition where the magnetic field is added to the star after its evolution in isolation. Finally, we also perform a control simulation for which the star is not magnetized. The different models and the associated choice of parameters are summarized in table 5.1.

The magnetic field is defined only on the SPH particles and not outside the star initially. A problem with this approach is that we therefore do not explicitly specify the boundary condition on the stellar magnetic field. In reality, the magnetic pressure outside the star far exceeds the ram pressure from the ambient medium, so the field lines should move freely with the star, which is what occurs in the simulation because the field is frozen to the fluid. In other words, the interior field evolves due to the deformation of the initial Lagrangian particle distribution, a mapping process that can be reproduced in post-processing since we find the dynamical influence to be unimportant. We thus preferred to leave the boundary condition free, and the similarity of our results to those shown by Guillochon & McCourt (2017) shows that this does not strongly affect the outcome.

The simulations are performed using the SPMHD code PHANTOM (Price & Federrath 2010; Lodato & Price 2010; Price et al. 2017). The self-gravity implementation makes use of a k-D tree algorithm (Gafton & Rosswog 2011). Direct summation is performed to handle short-range interactions according to an opening angle criterion with a critical value of 0.5. The magnetic field is evolved according to the constrained hyperbolic divergence cleaning algorithm developed by Tricco & Price (2012) and Tricco et al. (2016). This algorithm imposes the condition $\nabla \cdot \mathbf{B} = 0$ in accordance with the non-existence of magnetic monopoles. This is achieved by imposing this divergence term to obey a damped propagation equation that efficiently reduces the divergence errors as they are transported with the fluid. With this technique, our divergence errors obey $h|\nabla \cdot \mathbf{B}|/|\mathbf{B}| < 0.1$ during the entire simulations where the left hand side is averaged on the SPH particles and h denotes the smoothing length. In addition, the gas thermodynamical quantities are evolved according to an adiabatic equation of state. To accommodate for shocks, we make use of the standard artificial viscosity prescription in combination with the switch developed by Cullen & Dehnen (2010) to strongly reduce artificial viscosity away from shocks.

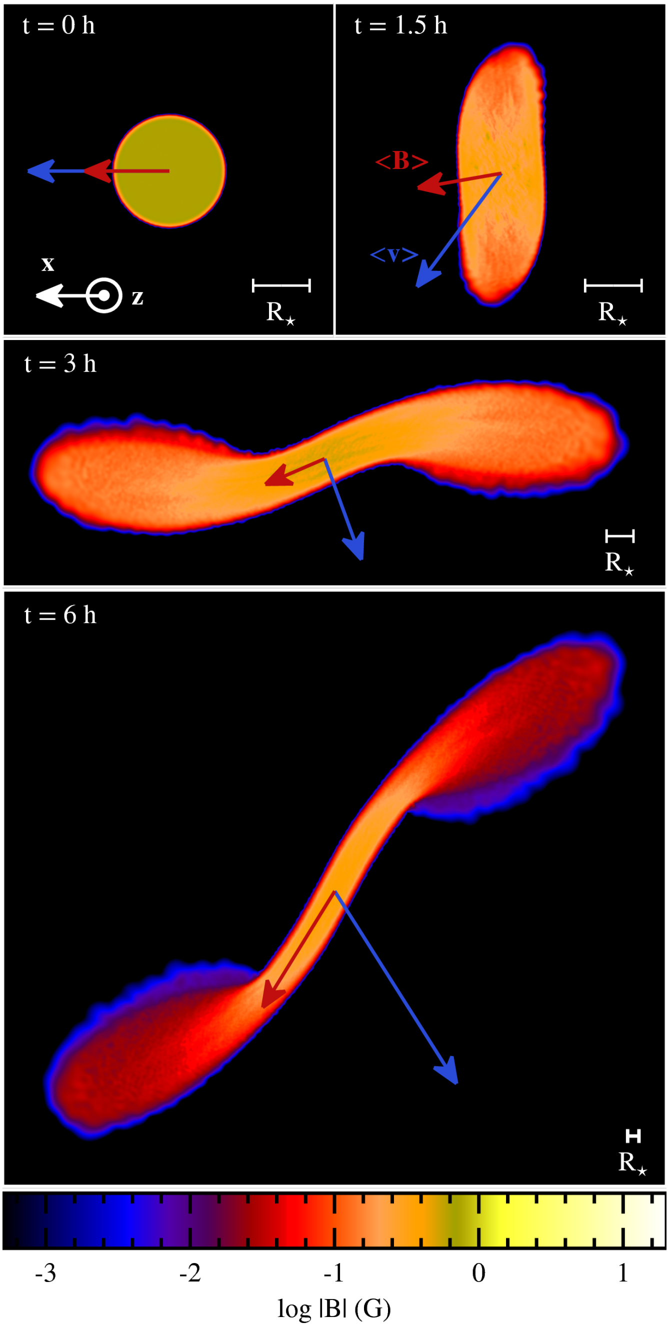

Figure 5.1: Snapshots of the tidal disruption process showing the magnetic field strength of the gas for model F1B1G-x at different times $t = 0$, 1.5, 3 and 6 h in a reference frame that follows the centre of mass. The penetration factor is fixed to $\beta = 1$. The blue arrows indicate the direction of the centre of mass velocity while the red ones represent the direction of the mean magnetic field. Their length does not have a physical meaning. The scale is different in each panel as indicated by the segment on the bottom right which represents the stellar radius. The white arrows on the upper left panel define the **x** and **z** directions.

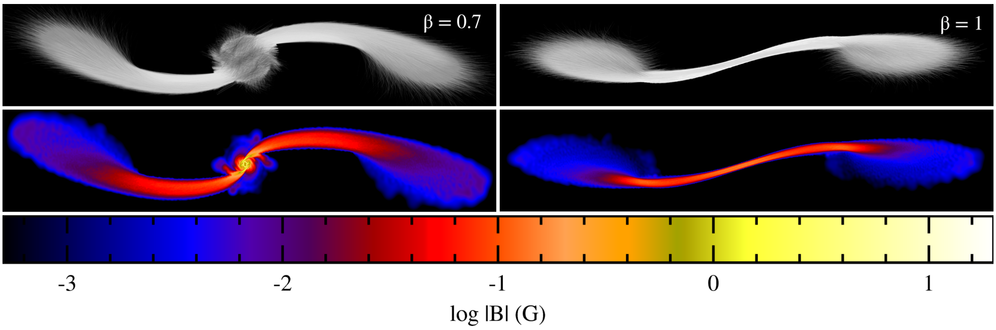

Figure 5.2: Snapshots showing the magnetic field lines (upper panels) and strength (lower panels) at $t = 20\,\mathrm{h}$ in the entire gas distribution for model P.7B1G-x (left panels) and F1B1G-x (right panels), for which the star is partially and fully disrupted respectively.

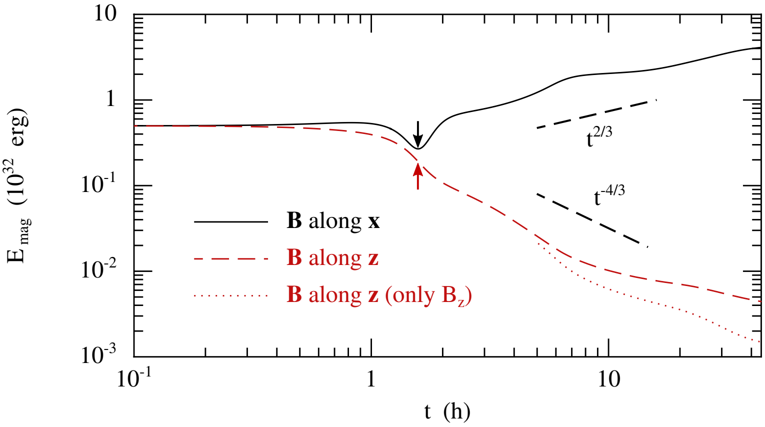

Figure 5.3: Magnetic energy evolution for models F1B1G-x (black solid line) and F1B1G-z (red dashed line), for which the penetration factor is $\beta = 1$. The dotted red line shows the magnetic energy computed from the **z** component of the field only for model F1B1G-z. The times of pericentre passage are indicated by the arrows on each curve. The two solid dashed segments indicate the scalings that the magnetic energy is expected to follow after the disruption.

5.3 Results

In this section, we present the results of the simulations.[1] The analysis is made by evaluating the evolution of the magnetic field strength of the debris and the total magnetic energy. The latter is given as a function of the field strength via $E_{\mathrm{mag}} \equiv \int P_{\mathrm{mag}}\,\mathrm{dV} \approx |\mathbf{B}|^2\mathrm{V}$ where V represents the volume of the gas distribution. The initial magnetic energy is $E_{\mathrm{mag}} \approx 10^{32}$ erg and 10^{44} erg for $|\mathbf{B}| = 1\mathrm{G}$ and $1\mathrm{MG}$ respectively.

5.3.1 Influence on the field orientation

First, we evaluate the impact of the stellar magnetic field orientation on its distribution within the debris, focusing on full disruptions with a fixed penetration factor $\beta = 1$ and magnetic

---

[1] Movies of the simulations presented in this paper are available at http://home.strw.leidenuniv.nl/~bonnerot/research.html.

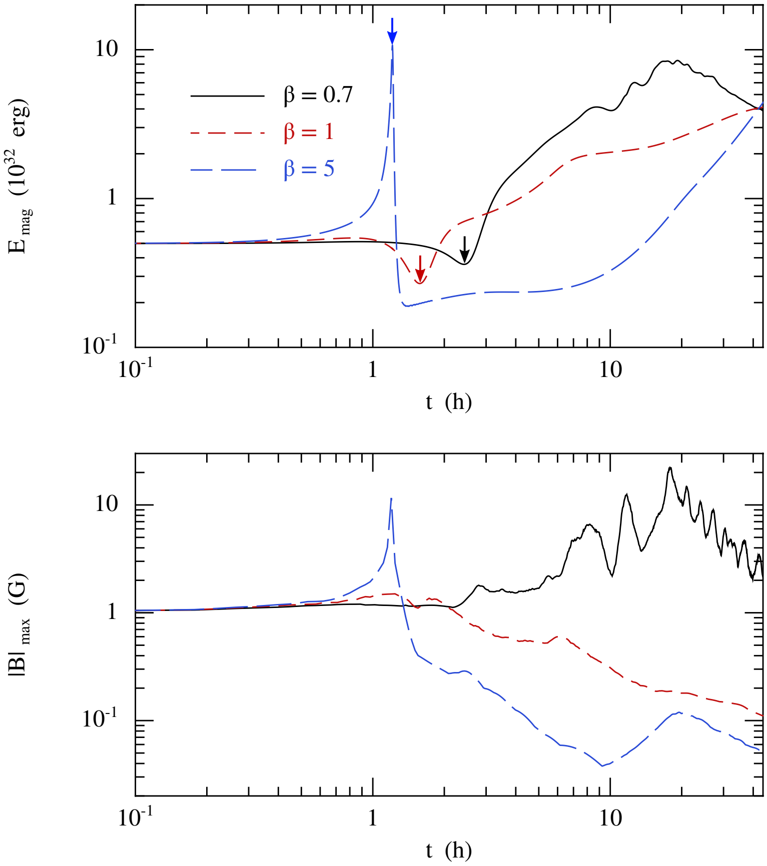

Figure 5.4: Magnetic energy (upper panel) and maximal magnetic field strength (lower panel) evolution for models P.7B1G-x (black solid line), F1B1G-x (red dashed line) and F5B1G-x (long-dashed blue line). The times of pericentre passage are indicated by the arrows on each curve.

field strength $|\mathbf{B}| = 1$G. For this purpose, we compare models F1B1G-x and F1B1G-z, for which the stellar magnetic field is linear and oriented in the **x** and **z** directions respectively. Recall that the **x** direction is aligned with the initial trajectory of the star while the **z** direction is orthogonal to the orbital plane.

The hydrodynamics is indistinguishable between the two models since the magnetic field is dynamically irrelevant owing to the large value of the plasma beta $\beta_{\rm M} \simeq 10^{16} \gg 1$. The gas evolution is presented in Fig. 5.1 which shows snapshots of the tidal disruption process following the centre of mass of the star at different times $t = 0$, 1.5, 3 and 6 h. The colours represent the magnetic field strength for model F1B1G-x while the arrows indicate the direction of the centre of mass velocity (blue arrow) and the direction of the mean magnetic field (red arrow). Initially, the orientation of the magnetic field is imposed by the initial conditions. At $t = 1.5$ h, the star reaches pericentre where it gets stretched by a factor of ~ 2 due to the velocity difference between material on each side of the trajectory, the gas closer to the black hole moving faster than the matter further away. This elongation takes place in the direction perpendicular to the magnetic field for model F1B1G-x. The stellar debris then evolves into a stream that keeps stretching at later times. For model F1B1G-x, the magnetic field gets

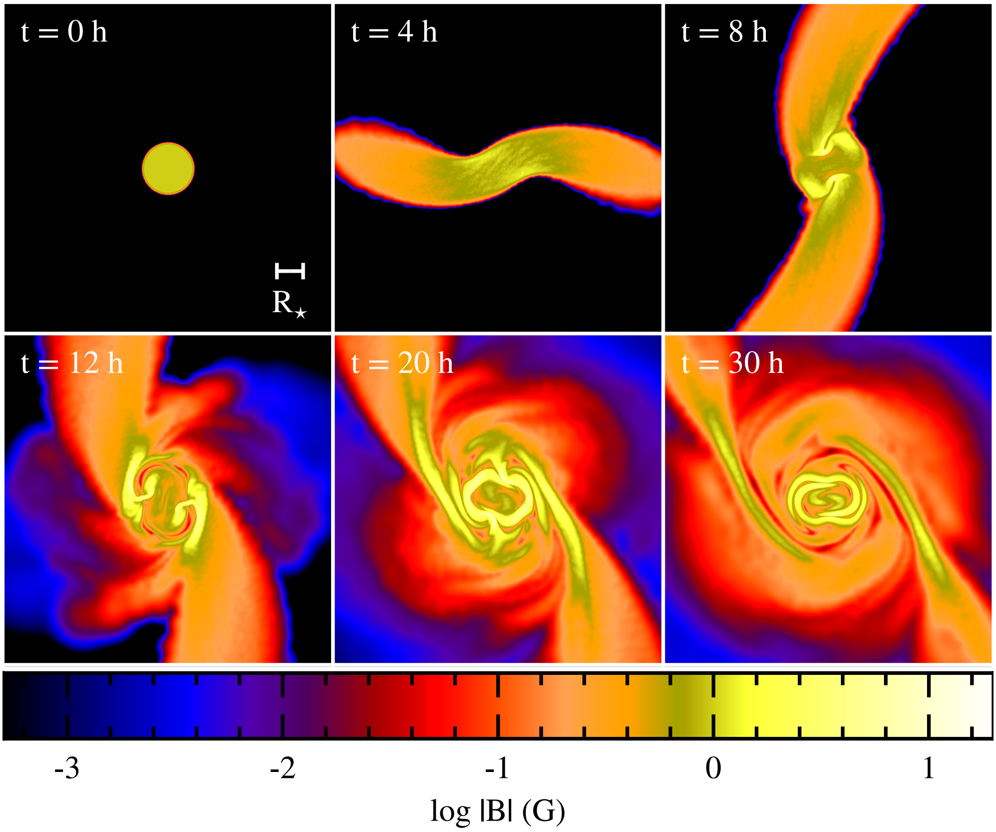

Figure 5.5: Snapshots showing the magnetic field strength at different times t = 0, 4, 8, 12, 20 and 30 h for model P.7B1G-x, corresponding to a partial disruption of the star. The reference frame follows the centre of mass of the gas distribution. The star reaches pericentre at $t \approx 2.5$ h. The magnetic field gets amplified within the surviving core to values up to $|\mathbf{B}| \approx 10$ G

re-oriented in the direction of stretching as the stream continues to expand as can be noticed from the red arrows on the two lowermost panels of Fig. 5.1. This is because, in absence of magnetic diffusion, each magnetic field line must pass through the same fluid elements at all times. Therefore, as the gas distribution gets stretched, so do the field lines causing the magnetic field to re-orient in the stretching direction. For this model (F1B1G-x), the magnetic field lines orientation and strength within the debris are shown in the right panel of Fig. 5.2 at t = 20 h. It illustrates the alignment of the field lines with the direction of stretching and the magnetic strength mild decrease to an average of $|\mathbf{B}| \approx 0.1$G

For model F1B1G-z, the direction of the magnetic field is unaffected by the gas evolution and remains in the initial **z** direction. Also in this case, the field lines are frozen in the flow and follow the stream elongation. However, since the star's stretching occurs in the orbital plane, this is not accompanied by a re-orientation of the field lines. The magnetic field therefore remains orthogonal to the direction of stretching at all times.

The evolution of the magnetic energy is shown in Fig. 5.3 for models F1B1G-x (solid black line) and F1B1G-z (dashed red line) with the time of pericentre passage indicated by an arrow on each curve. Using the gas and magnetic field evolution described above, each trend can be understood from magnetic flux conservation that imposes $|\mathbf{B}| \propto 1/S$, where

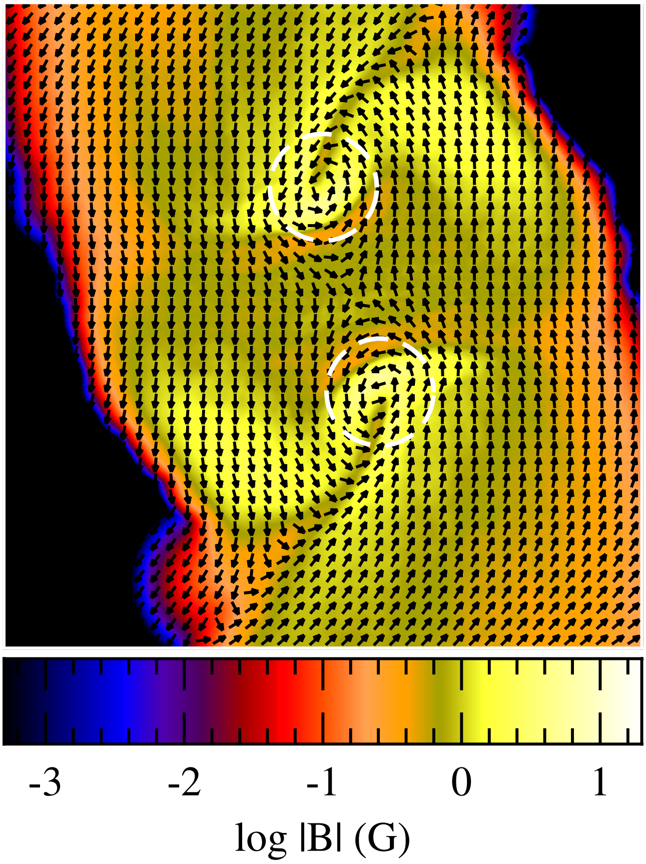

Figure 5.6: Close-up on the centre of mass of the gas distribution showing the magnetic field strength at $t = 8\,\mathrm{h}$ for model P.7B1G-x. The arrows denote the velocity field, which features two zones of rotational motion corresponding to vortices. The location of these vortices correspond to the zones of largest magnetic field strength.

S is the surface orthogonal to the field direction. The magnetic energy therefore scales as $E_{\mathrm{mag}} \approx |\mathbf{B}|^2\, V \propto V/S^2$. For model F1B1G-x, the magnetic energy drops slightly at the moment of disruption. This is due to the elongation experienced by the star in the direction orthogonal to the magnetic field, seen in the upper right panel of Fig. 5.1. Afterwards, the energy increases until the end of our simulation. This increase is caused by the stretching of the stellar debris in the direction parallel to the magnetic field, also visible on the two lowermost panels of Fig. 5.1. The rate of increase can be understood as follows from magnetic flux conservation. The surface through which the field lines pass is orthogonal to the stretching direction and scales as $S_\perp \propto H^2$ while the volume of the gas distribution evolves like $V \propto H^2 l$. H and l represent the width and length of a fluid element belonging to the stream respectively. This implies that the magnetic energy evolves as $E_{\mathrm{mag}} \propto V/S_\perp^2 \propto l/H^2$. Using the scalings $H \propto t^{1/3}$ and $l \propto t^{4/3}$ derived by Coughlin et al. (2016b) during this phase of evolution, the magnetic energy scales as $E_{\mathrm{mag}} \propto t^{2/3}$. This scaling is indicated by the upper black dashed segment in Fig. 5.3 and provides an accurate description of the magnetic energy evolution for model F1B1G-x. Note that, even if the magnetic energy increases, the magnetic field strength decreases since $|\mathbf{B}| \propto 1/H^2 \propto t^{-2/3}$ as illustrated in the bottom panel of Fig. 5.4 (red dashed line).

For model F1B1G-z, the evolution is significantly different since the magnetic energy decreases during the whole simulation. This is because, as explained above, the magnetic field remains orthogonal to the stretching direction in this case. The surface parallel to the stream stretching scales as $S_{\parallel} \propto lH$. As a result, magnetic flux conservation imposes $E_{\rm mag} \propto V/S_{\parallel}^2 \propto 1/l$. Since $l \propto t^{4/3}$, the magnetic energy evolves as $E_{\rm mag} \propto t^{-4/3}$. As can be seen from Fig. 5.3 by comparing the dashed red line to the lower black dashed segment, the magnetic energy follows this scaling closely for model F1B1G-z. At $t \gtrsim 5$ h, the magnetic energy can however be seen to decrease slightly slower than the scaling. This is due to small components of the magnetic field along the orbital plane originating from the shearing experienced by the debris during the tidal disruption process. These additional components of the magnetic field tend to increase the total magnetic energy, making the decrease slower than expected. This interpretation is demonstrated by computing the magnetic energy including only the **z** component of the magnetic field. As can be seen from the red dotted line in Fig. 5.3, this partial magnetic energy follows the expected scaling. At late times, the magnetic energy is small enough to be affected by the presence of low-density regions where the magnetic field is overestimated due to divergence errors, with $h|\nabla \cdot \mathbf{B}|/|\mathbf{B}| \gtrsim 0.1$. This artificially causes the magnetic energy to reach a plateau at $t \gtrsim 20$ h. The SPH particles leading to this unphysical behaviour have densities three orders of magnitude lower than the mean and represent only $\sim 1\%$ of the whole distribution. They have been removed to compute the magnetic energy shown in Fig. 5.3 for model F1B1G-z.

It can also be noticed from Fig. 5.3 that the magnetic energy evolution for both models F1B1G-x and F1B1G-z slightly differs from the above scalings at $t \approx 7$ h where it experiences a small oscillation, also seen in the density evolution. This density oscillation has already been identified in the simulations performed by Coughlin et al. (2016a) and was also found to happen around 5.5 h after pericentre passage for the set of parameters considered here (see their figure 8). It is triggered by a compression of the debris along the orbital plane due to the differential motion of the front and back of the star at the moment of disruption. The density variation is accompanied by a modification of the stream profile causing H to increase slightly slower than the previous scaling and l slightly faster. As a result, the magnetic energy $E_{\rm mag} \propto l/H^2$ for model F1B1G-x increases faster, creating a bump. Similarly, the magnetic energy $E_{\rm mag} \propto 1/l$ for model F1B1G-z decreases faster, producing a hollow.

5.3.2 Dependence on the penetration factor

We investigate the effect of the penetration factor on the magnetic field evolution by comparing models P.7B1G-x and F5B1G-x with model F1B1G-x, already discussed in Section 5.3.1. For model P.7B1G-x, the penetration factor is fixed to $\beta = 0.7$, for which the disruption is expected to be partial. It is increased to $\beta = 1$ and 5 for models F1B1G-x and F5B1G-x, both leading to full disruptions. These three models adopt the same initial magnetic field strength of $|\mathbf{B}| = 1$ G and a common orientation along the **x** direction.

We look at model P.7B1G-x first. Fig. 5.5 shows the gas evolution and its magnetic field strength for this model in a frame of reference following the centre of mass. The star reaches pericentre at $t \approx 2.5$ h, after which it gets stretched to form an elongated structure. This initial phase of evolution is similar to that of model F1B1G-x, shown on the three uppermost panels of Fig. 5.1. However, the subsequent evolution differs due to the lower value of the penetration factor $\beta = 0.7$. Starting from $t \approx 8$ h, matter starts to collapse towards the centre of mass to form a self-gravitating core. The interaction of this re-collapsing gas with the rotating core leads to the formation of two vortices close to the core surface. It is important

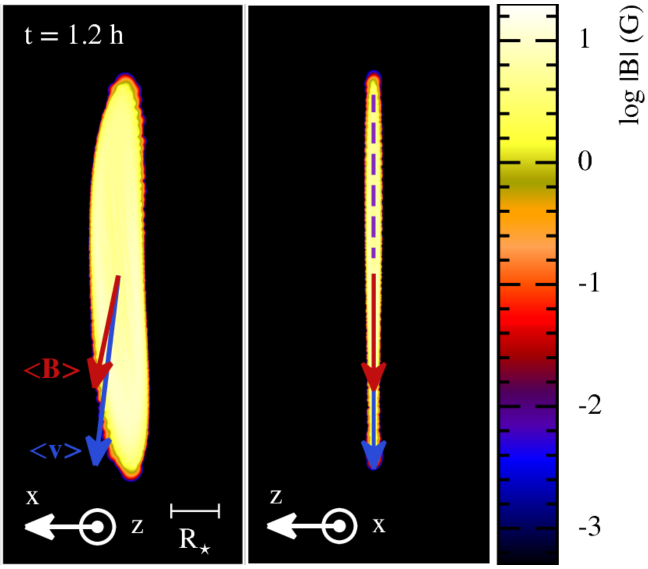

Figure 5.7: Magnetic field strength of the gas for model F5B1G-x at the time of pericentre passage $t = 1.2$ h along a line of sight orthogonal (left panel) and parallel (right panel) to the orbital plane of the star. The blue arrows indicate the direction of the centre of mass velocity while the red ones represent the direction of the mean magnetic field. On the right panel, the vertical dashed purple segment indicates the orbital plane of the star.

to notice that these vortices have a purely hydrodynamical origin since the magnetic field is never dynamically relevant in our simulation. These features can be seen by looking at Fig. 5.6 which shows a close-up on the surviving core at $t = 8$ h where the velocity field computed in the reference frame of the centre of mass is indicated as black arrows. Clearly, this velocity field exhibits two zones of rotational motion, highlighted by the dashed white circles. Inside these vortices, the magnetic field gets amplified to reach strengths up to $|\mathbf{B}| \approx 10$ G. Note that even after this amplification, the magnetic field remains dynamically irrelevant in the core with a plasma beta of $\beta_{\rm M} \approx 10^{13} \gg 1$. Later in time, the core keeps rotating causing the formation of a more complex magnetic structure as can be seen in Fig. 5.5 for $t \geq 12$ h. We also notice that the rotational motion associated to the vortices progressively disappears until the only gas motion identifiable in the core is that due to its rigid rotation.

This evolution is fundamentally different from that of model F1B1G-x described in Section 5.3.1, for which the disruption was total. A comparison can be made by looking at Fig. 5.2 that shows the magnetic field lines and strength within the whole gas distribution at $t = 20$ h for models P0.7B1G-x (left panels) and F1B1G-x (right panels). The magnetic field strength is comparable for the two models away from the centre of mass of the stellar debris, where it is always $|\mathbf{B}| \lesssim 0.1$ G. The field lines are also similar, directed along the stream longitudinal direction. Instead, the magnetic field structure differs significantly near the centre of mass. At this location, model P.7B1G-x features a complex magnetic configuration due to the formation of a self-gravitating core. The magnetic field strength gets amplified and the field lines become tangled. For model F1B1G-x, there is instead no of magnetic field amplification and the field lines are directed along the stretching direction everywhere through the debris.

Fig. 5.7 shows the gas distribution and its magnetic field strength for model F5B1G-x when the star reaches pericentre, at $t = 1.2$ h. As in Fig. 5.1, the left panel adopts a line of sight orthogonal to the orbital plane. On the right panel, the orbital plane is indicated by the dashed purple segment along the gas distribution and the line of sight is parallel to it. This allows to see the gas elements above and below the orbital plane. The red arrow denotes the direction of the mean magnetic field while the blue arrow shows the centre of mass velocity. The star gets elongated along its orbital plane by a factor of ~ 8 as it passes at pericentre. This elongation is analogous to that seen for model F1B1G-x. However, it is more pronounced due to the larger penetration factor $\beta = 5$ that causes the star to pass closer to the black hole where tidal forces are stronger. This larger elongation for model F5B1G-x has a consequence on the magnetic field evolution. As can be seen from Fig 5.7, the magnetic field gets re-oriented in the direction of elongation by the time of pericentre passage. This re-orientation of the field lines has the same origin as for model F1B1G-x, discussed in Section 5.3.1. However, it occurs earlier due to the larger elongation factor. At pericentre passage, the mean magnetic field is still close to its initial orientation for model F1B1G-x (upper right panel of Fig. 5.1) but it is already re-oriented along the direction of stretching for model F5B1G-x. The right panel of Fig. 5.7 shows that the star is additionally compressed by factor of ~ 3 in the direction orthogonal to its orbital plane. This strong vertical collapse is expected for deep-penetrating encounter, for which the matter passes well within the tidal radius (Carter & Luminet 1983; Stone et al. 2013).

A more quantitative analysis can be done using Fig. 5.4 that shows the magnetic energy (upper panel) and maximal magnetic field strength (lower panel) for models P.7B1G-x (solid black line), F1B1G-x (dashed red line) and F5B1G-x (long-dashed blue line). The times of pericentre passage, different for each model, are indicated by the arrows on each curve. For model P.7B1G-x, the magnetic energy increases the fastest shortly after the disruption due to the dynamo process at play in the surviving core. It scales as $E_{\rm mag} \propto t^p$ where $p \approx 1.4$ compared to $E_{\rm mag} \propto t^{2/3}$ for model F1B1G-x. The maximal magnetic field strength also increases to reach $|\mathbf{B}|_{\rm max} \approx 20\,\mathrm{G}$ at $t \approx 18\,\mathrm{h}$. At $t \gtrsim 20\,\mathrm{h}$, the magnetic energy starts decreasing. However, this late stage of evolution appears to be strongly resolution dependent and will be discussed later in Section 5.3.4. For model F1B1G-x, the magnetic field strength continuously decreases down to $|\mathbf{B}| \approx 0.1\,\mathrm{G}$ while the magnetic energy increases. For model F5B1G-x, the evolution is similar except for a large peak at the time of pericentre passage where the maximal magnetic field strength reaches $|\mathbf{B}|_{\rm max} \approx 10\,\mathrm{G}$. This is due to the strong compression experienced by the star in the direction perpendicular to its orbital plane (right panel of Fig. 5.7). Since the magnetic field is orthogonal to the direction of compression, flux conservation imposes an associated increase of the magnetic field strength which explains the peak seen in Fig. 5.4 for model F5B1G-x (long-dashed blue line). At later times, the evolution is similar to that of model F1B1G-x.

5.3.3 Impact of the field strength

We now focus on the impact of the field strength on the debris evolution by analysing model F1B1MG-x, for which the stellar magnetic field strength is increased to $|\mathbf{B}| = 1\,\mathrm{MG}$. This is six orders of magnitude larger than for model F1B1G-x discussed in Section 5.3.1, where the strength was $|\mathbf{B}| = 1\,\mathrm{G}$. However, the initial field remains oriented in the $\mathbf{x}$ direction and the penetration factor is fixed to $\beta = 1$.

Fig. 5.8 (upper panel) shows the evolution of the magnetic (black solid line) and thermal (red dashed line) energies for model F1B1MG-x. As expected, the magnetic energy evolution is identical to that of model F1B1G-x with an energy increase that follows $E_{\rm mag} \propto t^{2/3}$. It is only shifted upwards by twelve orders of magnitude owing to the larger initial magnetic field strength. On the other hand, the thermal energy decreases after disruption due to the expansion of the stream. This energy is given by $E_{\rm th} \equiv (3/2) \int P_{\rm gas}\,\mathrm{dV} \approx \mathrm{P_{gas}V}$. Since the evolution is adiabatic, the gas pressure scales as $P_{\rm gas} \propto \rho^{5/3} \propto V^{-5/3}$ where $\rho \propto 1/V$ represents the gas density. As a result, $E_{\rm th} \propto V^{-2/3} \propto t^{-4/3}$ using $V = H^2 l$ and the temporal dependence of H and l derived by Coughlin et al. (2016b). This slope is indicated by the upper dashed black segment in Fig. 5.8 (upper panel) that is followed closely by the thermal energy. After the disruption, the magnetic energy therefore approaches the thermal energy until, at $t \approx 20$ h, they only differ by an order of magnitude. By that time, the plasma beta $\beta_{\rm M} \approx E_{\rm th}/E_{\rm mag}$ has decreased by three orders of magnitude, from $\beta_{\rm M,ini} \approx 10^4$ initially to $\beta_{\rm M} \approx 10$. This suggests that magnetic pressure is starting to have an dynamical impact on the stream structure. The area indicated by the dotted purple rectangle is zoomed-in on the lower panel of Fig. 5.8, which shows the late time evolution of the thermal energy for model F1B1MG-x (red dashed line) compared to the control model F1B0G (solid black line) with hydrodynamics only and model F1B2MG-x (blue long-dashed line) for which the star has a larger initial magnetic field strength of $|\mathbf{B}| = 2\,$MG. The thermal energy is reduced for increasing magnetic field strengths compared to the non-magnetized case. We interpret this variation as the effect of magnetic pressure that provides an additional support to thermal pressure against self-gravity to ensure hydrostatic equilibrium. To test this interpretation, we compare the variation $\Delta E_{\rm th}$ in thermal energy to the magnetic energy. For both models F1B1MG-x and F1B2MG-x, the ratio of these two quantities is found to be $\Delta E_{\rm th}/E_{\rm mag} = 1.02 \approx 1$ at $t = 20\,$h, which confirms that the decrease in thermal energy compared to the non-magnetized case is due to the presence of magnetic pressure. For model F1B1G-x where the magnetic field strength is of only $|\mathbf{B}| = 1$ G, we find that the thermal energy is identical to model F1B0G, meaning that the magnetic field does not affect the stream structure at any time.

This late-time impact of the magnetic pressure only results from the evolution of magnetic and thermal energies, which increases and decreases respectively during to the stream stretching. This effect is therefore general to every tidal disruption of magnetized stars as long as the magnetic field has an initial component in the direction of stretching. The latter condition is necessary to ensure an increase of the magnetic energy as demonstrated in Section 5.3.1. In this situation, the magnetic pressure is expected to become significant at a finite time $t_{\rm mag}$ after disruption. Since the plasma beta satisfies $\beta_{\rm M} \equiv E_{\rm th}/E_{\rm mag} \propto t^{-2}$, this characteristic timescale is given by

$$t_{\rm mag} = t_{\rm str}\, \beta_{\rm M,ini}^{1/2}, \tag{5.1}$$

where $t_{\rm str}$ denotes the stretching timescale, after which the stream has expanded by a significant amount. As physically expected, the magnetic pressure becomes significant earlier for more magnetized stars since $t_{\rm mag}$ increases with $\beta_{\rm M,ini}$. The stretching timescale can be obtained from $t_{\rm str} = R_\star/\Delta v$ where Δv denotes the velocity difference within the stellar debris imparted by tidal forces at the time of pericentre passage. For $\beta \approx 1$, $\Delta v \approx (GM_\star/R_\star)^{1/2}$ and the stretching timescale is simply the stellar dynamical time, $t_{\rm str} = 0.4\,$h for a solar-type star. This is consistent with the time delay found in our simulations between the disruption of the star and a significant stretching of the debris. Injecting this expression into equation (5.1) leads to

$$t_{\rm mag} = 44\,{\rm h} \left(\frac{\beta_{\rm M,ini}}{10^4}\right)^{1/2} \left(\frac{\rm M_\star}{\rm M_\odot}\right)^{-1/2} \left(\frac{\rm R_\star}{\rm R_\odot}\right)^{3/2}, \tag{5.2}$$

consistent with the time at which the magnetic pressure becomes comparable to the gas pressure.

5.3.4 Resolution study

We now evaluate the effect of numerical resolution on the results of our simulations. This is done by focusing on model P0.7B1G-x such that both the magnetic field evolution imposed

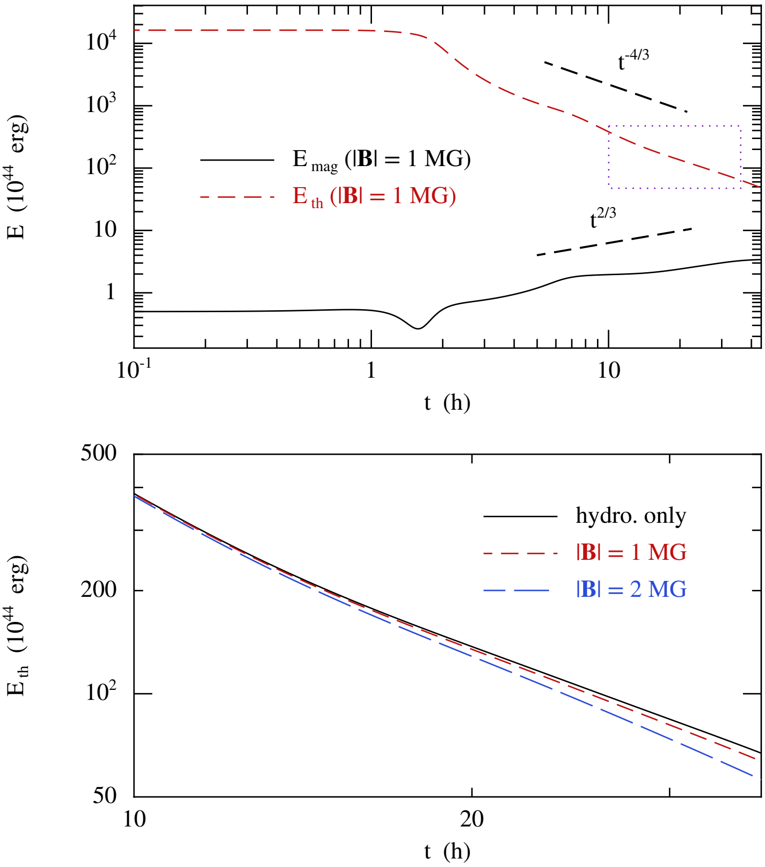

Figure 5.8: Evolution of the magnetic (black solid line) and thermal (red dashed line) energies for model F1B1MG-x (upper panel). The dashed black segments indicate the scaling that these energies are expected to follow after the disruption. The area delimited by the dotted purple rectangle is zoomed-in on the lower panel, which shows the late time thermal energy evolution for models F1B0G (solid black line), F1B1MG-x (dashed red line) and F1B2MG-x (long-dashed blue line).

by stream stretching and the dynamo process at play in the surviving core can be analysed. The magnetic energy evolution is shown in Fig. 5.9 for model P0.7B1G-x adopting three different numbers of SPH particles: 10^5 (black solid line), 10^6 (dashed red line) and 10^7 (long-dashed blue line). Small differences in the initial magnetic energy can be noticed between different resolutions. They are only due to slight variations in the volume of the initial particle distribution within the star. The magnetic energy evolution close to pericentre passage and shortly after is identical for the three resolutions. For $t \gtrsim 4$ h, the initial magnetic field growth is the same for the two largest resolutions but the magnetic energy starts to differ for the lowest resolution. Up to this time, our simulations have therefore already reached convergence for 10^6 particles, the number used for the results presented in this paper. When $t \gtrsim 10$ h, the magnetic energy significantly diverges for the three resolutions. Magnetic field amplification is sustained for a longer time at higher resolutions which results in a larger peak value for the magnetic energy. Between the two lower (larger) resolutions, the peak in magnetic energy is delayed by ~ 3 h (~ 7.6 h) and larger by 89% (54%). We connect this longer magnetic

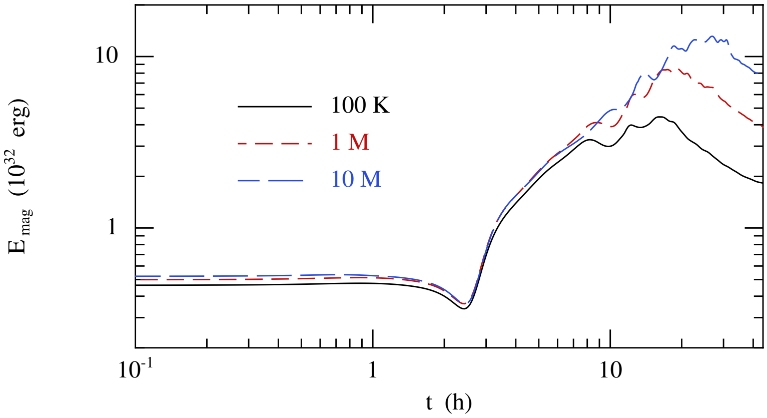

Figure 5.9: Magnetic energy evolution for model P0.7B1G-x using 10^5 (black solid line), 10^6 (red dashed line) and 10^7 (blue long-dashed line) SPH particles for the simulation.

field amplification observed at higher resolution to the fact that the vortices within which the dynamo process operates are longer-lived. Given the dependence on resolution, we interpret this effect as being due to numerical dissipation. At higher resolution, numerical dissipation is reduced and the vortices disappear later in time. Therefore, we conclude that the magnetic field amplification seen in our simulations must be understood as a lower limit. A physical upper limit will be estimated in Section 5.4.

5.4 Discussion and conclusion

The evolution of the magnetic field of the star during its tidal disruption has not received significant attention despite its potentially fundamental importance. In this paper, we perform magnetohydrodynamical simulations of the tidal disruption process considering the stellar magnetic field. We find that the initial magnetic field orientation significantly affects the post-disruption magnetic energy evolution because it determines the inclination of the magnetic field with respect to the stream stretching direction. As expected from flux conservation, the magnetic field strength of the debris decreases slowly when the field lines are aligned with the stretching direction resulting in an increase of the magnetic energy. Instead, the magnetic energy decreases when the magnetic field is perpendicular to the direction of stretching. We also find that varying the depth of the encounter leads to qualitative differences in the magnetic field evolution. For a deeply penetrating encounter, the magnetic field strength undergoes a sharp increase close to pericentre passage caused by a strong compression of the star. Instead, a partial disruption leads to the formation of a surviving core inside which vortices form. We find clear evidence of a dynamo process at play within these vortices, which induces an increase of the magnetic field strength by about an order of magnitude. For the disruption of strongly magnetized stars, we show that magnetic pressure provides an additional support against self-gravity in the stream transverse direction after a few tens of hours for an initial magnetic field strength $|\mathbf{B}| \geq 1\,\mathrm{MG}$. This action of magnetic pressure is also to be expected for less magnetized stars, but on a longer timescale (equation (5.2)).

In our simulations, we find that magnetic pressure provides an additional although marginal support to gas pressure against self-gravity. Since the magnetic energy can increase with time, a possibility is that, in highly magnetized stars, magnetic pressure may exceed self-gravity at later times. As a result, the width of the stream would no longer be confined by self-gravity but would become thicker with a transverse profile entirely determined by magnetic pressure. Several other mechanisms have so far been proposed to counteract the effect of self-gravity which include thermal energy injection at the moment of disruption for large penetration factors $\beta \gtrsim 3$ and hydrogen recombination, which occurs about a week after the disruption (Kasen & Ramirez-Ruiz 2010). The thickening effect of magnetic pressure on the stream could also affect its subsequent circularization. In particular, disc formation might not be delayed by Lense-Thirring precession, thought to prevent an early self-crossing shock for narrow streams revolving around spinning black holes (Guillochon & Ramirez-Ruiz 2015). In addition, circularization can be accelerated since magnetic stresses are able to strengthen self-crossing shocks during the disc formation process (Bonnerot et al. 2017).

Hydrodynamical instabilities can significantly affect the low-density stream of debris expected from tidal disruptions involving giant stars or massive black holes. However, these instabilities are prevented by magnetic tension if the stream has a longitudinal magnetic field component of strength $|\mathbf{B}_{||}| \approx 1-10\,\mathrm{G}$ (Bonnerot et al. 2016). In our simulations, the magnetic field lines naturally align with the stream longitudinal direction as long as the initial magnetic field has a component along the stretching direction. If stars host strongly-magnetized cores with $|\mathbf{B}| \gg 1\,\mathrm{G}$, even a small fraction of their magnetic field would therefore be enough to prevent these instabilities from developing. This possibility is favoured by recent evidence for large magnetic fields in the cores of red giants with strengths $|\mathbf{B}| \gtrsim 10^5\,\mathrm{G}$, obtained from asteroseismology (Fuller et al. 2015).

In the case of a partial disruption, the amplification factor found in our simulations is only a lower limit since higher resolution simulations produce longer-lived vortices due to decreased numerical dissipation, suggesting that at even higher resolution the vortices could result in long-lived hydrodynamic turbulence. An upper limit for the amplification factor can be obtained from equipartition between the core rotational energy and its magnetic energy. This upper limit can be reached only if a sustained dynamo develops which remains unaffected until equipartition. In practice, the dynamo process is likely to be stopped earlier by various physical processes such as internal dissipation within the surviving core. A detailed study of the internal structure of the surviving core is therefore required to determine the exact amount of magnetic field amplification, which is beyond the scope of this paper but could be carried out by means of a stellar evolution code. The core rotational energy is $E_{\mathrm{rot}} \approx M_\star \Delta v^2/2 \approx 10^{48}\,\mathrm{erg}$, sixteen orders of magnitude larger than the magnetic energy for $|\mathbf{B}| = 1\,\mathrm{G}$. Equipartition would therefore induce an amplification of the magnetic field strength of the core up to $|\mathbf{B}| \approx 10^8\,\mathrm{G}$. This implies that strongly-magnetized stellar cores may naturally result from partial tidal disruptions. If, as our simulations find, a sustained dynamo does not develop, a large magnetic field amplification could still be reached if the star experiences a series of several partial disruptions during which its magnetic field is mildly amplified. Starting from a stellar magnetic field of $|\mathbf{B}| = 1\,\mathrm{G}$, the magnetic field strength reached in the stellar core after N_{p} pericentre passages is $|\mathbf{B}| = f_{\mathrm{amp}}^{N_{\mathrm{p}}}\,\mathrm{G}$ which results in

$$N_{\mathrm{p}} = \frac{\log|\mathbf{B}|}{\log f_{\mathrm{amp}}}. \tag{5.3}$$

Using the value $f_{\mathrm{amp}} \approx 10$ found in our simulations for the amplification factor, a star therefore needs to experience $N_{\mathrm{p}} = 8$ pericentre passages for its core to reach a magnetic field strength of $|\mathbf{B}| = 10^8\,\mathrm{G}$. If a star is disrupted after a strong magnetic field amplification, the magnetic field flux brought by the stellar debris could be sufficient to power the relativistic jets detected from a fraction of TDEs. For Swift J1644+57, the required magnetic field strength has been estimated to $|\mathbf{B}| \approx 10^8\,\mathrm{G}$ (Tchekhovskoy et al. 2014) that could be achieved either after a single pericentre passage if a sustained dynamo takes place within the core or after ~ 8 encounters using the lower limit on the amplification factor given by our simulations. However, since the field lines align with the stream longitudinal direction, the newly-formed disc could lack the poloïdal magnetic field component required for jet launching. Theoretically, partial disruptions are expected to represent between $\sim 20\%$ and the large majority of all TDEs depending on the regime of angular momentum relaxation into the loss cone (Stone & Metzger 2016). Such events are also proposed to account for the low value of the total radiated energy obtained from numerous observations of TDEs (e.g. Chornock et al. 2014). Specifically, the scenario of a full tidal disruption following one or multiple partial disruptions is favoured if the star slowly diffuses into the loss cone through small changes of its angular momentum (Strubbe 2011, section 4). However, the remnant may also avoid a subsequent total disruption if it is scattered off its orbit by a two-body encounter (Alexander & Livio 2001). Hydrodynamical effects are also likely to affect this picture. After a partial disruption, the surviving core can get unbound from the black hole due to asymmetric mass loss (Manukian et al. 2013; Gafton et al. 2015). On the other hand, heating of the surviving core at pericentre is done at the expanse of its orbital energy and could make it expand to be more easily disrupted at the next passage close to the black hole (Cheng & Evans 2013). In addition, the stellar core trajectory might be affected by its interaction with the mass lost from previous encounters present close to the black hole. Detailed hydrodynamical simulations of successive partial disruptions are necessary to determine the dominant effect.

For deep-penetrating encounters, the magnetic field strength is found to peak due to compression at pericentre. The associated increase of magnetic pressure could result in an additional support against compression that is likely to impact the subsequent bounce, computed by considering gas pressure only (Stone et al. 2013).

Several investigations of magnetic field amplification during neutron star and white dwarf mergers have been carried out. In this context, both SPH (Price & Rosswog 2006) and moving-mesh (Zhu et al. 2015) simulations tend to result in magnetic field amplifications larger by orders of magnitude than in grid-code simulations (Kiuchi et al. 2014). In Price & Rosswog (2006), the fast growth was an artefact of a boundary condition effect from using the Euler potentials. The method used by Zhu et al. (2015) does not include divergence cleaning which likely explains the large magnetic field amplification seen in their simulations. In the present study, we find an amplification of the magnetic field consistent with the recent grid code simulations performed by Guillochon & McCourt (2017) thanks to the divergence cleaning method used to reduce divergence errors (Tricco & Price 2012; Tricco et al. 2016). We found in some of our early calculations that turning off the divergence cleaning could produce spurious dynamo amplification on timescales similar to those found by Zhu et al. (2015).

We provided a study of the stellar magnetic field evolution during the tidal disruption of a star and early debris evolution. In the future, we aim at investigating the longer-term effect of the magnetic field on the debris, especially its impact on the stream internal structure and dynamical influence during the circularization process.

Acknowledgments

We thank the anonymous referee for useful comments which improved the paper. CB is grateful to the Monash Centre for Astrophysics for hosting him during the completion of this work. He also thanks Mark Avara, Roseanne Cheng, James Guillochon, Yuri Levin, David Liptai, Christopher Matzner, Rebecca Nealon, Josiah Schwab and Nicholas Stone for interesting discussions. CB and EMR acknowledge the help from NOVA. DJP is grateful for funding via Future Fellowship FT130100034 from the Australian Research Council. Finally,

we used the SPH visualization tool SPLASH (Price 2007) for producing all the figures of this paper.

Bibliography

Alexander T., Livio M., 2001, ApJ, 560, L143

Blandford R. D., Znajek R. L., 1977, MNRAS, 179, 433

Bloom J. S., et al., 2011, Science, 333, 203

Bonnerot C., Rossi E. M., Lodato G., 2016, MNRAS, 458, 3324

Bonnerot C., Rossi E. M., Lodato G., 2017, MNRAS, 464, 2816

Burrows D. N., et al., 2011, Nature, 476, 421

Carter B., Luminet J.-P., 1983, A&A, 121, 97

Cheng R. M., Evans C. R., 2013, Phys. Rev. D, 87, 104010

Chornock R., et al., 2014, ApJ, 780, 44

Coughlin E. R., Nixon C., 2015, ApJ, 808, L11

Coughlin E. R., Nixon C., Begelman M. C., Armitage P. J., Price D. J., 2016a, MNRAS, 455, 3612

Coughlin E. R., Nixon C., Begelman M. C., Armitage P. J., 2016b, MNRAS, 459, 3089

Cullen L., Dehnen W., 2010, MNRAS, 408, 669

Fuller J., Cantiello M., Stello D., Garcia R. A., Bildsten L., 2015, Science, 350, 423

Gafton E., Rosswog S., 2011, MNRAS, 418, 770

Gafton E., Tejeda E., Guillochon J., Korobkin O., Rosswog S., 2015, MNRAS, 449, 771

Guillochon J., McCourt M., 2017, ApJ, 834, L19

Guillochon J., Ramirez-Ruiz E., 2013, ApJ, 767, 25

Guillochon J., Ramirez-Ruiz E., 2015, ApJ, 809, 166

Jiang Y.-F., Stone J. M., Davis S. W., 2014, ApJ, 796, 106

Kara E., Miller J. M., Reynolds C., Dai L., 2016, Nature, 535, 388

Kasen D., Ramirez-Ruiz E., 2010, ApJ, 714, 155

Kelley L. Z., Tchekhovskoy A., Narayan R., 2014, MNRAS, 445, 3919

Kiuchi K., Kyutoku K., Sekiguchi Y., Shibata M., Wada T., 2014, Phys. Rev. D, 90, 041502

Kochanek C. S., 1994, ApJ, 436, 56

Krolik J. H., Piran T., 2012, ApJ, 749, 92

Lodato G., Price D. J., 2010, MNRAS, 405, 1212

Lodato G., King A. R., Pringle J. E., 2009, MNRAS, 392, 332

Mandel I., Levin Y., 2015, ApJ, 805, L4

Manukian H., Guillochon J., Ramirez-Ruiz E., O'Leary R. M., 2013, ApJ, 771, L28

McCourt M., O'Leary R. M., Madigan A.-M., Quataert E., 2015, MNRAS, 449, 2

Monaghan J. J., 2005, Reports on Progress in Physics, 68, 1703

Oksala M. E., Wade G. A., Marcolino W. L. F., Grunhut J., Bohlender D., Manset N., Townsend R. H. D., Mimes Collaboration 2010, MNRAS, 405, L51

Piran T., Sądowski A., Tchekhovskoy A., 2015, MNRAS, 453, 157

Price D. J., 2007, Publ. Astron. Soc. Australia, 24, 159

Price D. J., 2012, Journal of Computational Physics, 231, 759

Price D. J., Federrath C., 2010, MNRAS, 406, 1659

Price D. J., Rosswog S., 2006, Science, 312, 719

Price D. J., et al., 2017, preprint (arXiv:1702.03930)

Rees M. J., 1988, Nature, 333, 523

Sądowski A., Narayan R., 2015, MNRAS, 453, 3213

Stone N. C., Metzger B. D., 2016, MNRAS, 455, 859

Stone N., Sari R., Loeb A., 2013, MNRAS, 435, 1809

Strubbe L. E., 2011, PhD thesis, University of California, Berkeley

Svirski G., Piran T., Krolik J., 2017, MNRAS, 467, 1426

Tchekhovskoy A., Metzger B. D., Giannios D., Kelley L. Z., 2014, MNRAS, 437, 2744

Tricco T. S., Price D. J., 2012, Journal of Computational Physics, 231, 7214

Tricco T. S., Price D. J., Bate M. R., 2016, Journal of Computational Physics, 322, 326

Zhu C., Pakmor R., van Kerkwijk M. H., Chang P., 2015, ApJ, 806, L1

6

Nederlandse samenvatting

6.1 Supermassieve zwarte gaten

Zwarte gaten zijn extreem compacte objecten, wiens bestaan voorspeld is door Einstein's algemene relativiteit's theorie. De allerzwaarsten worden supermassieve zwarte gaten genoemd. Deze hemellichamen bevinden zich in het centrum van grote melkwegstelsels en hebben massa's in de orde van een miljoen tot honderden miljarden zonsmassa's. Ook ons eigen melkwegstelsel, de Melkweg, bevat een supermassief zwart gat van ongeveer 4 miljoen zonsmassa's, dat Sagittarius A* wordt genoemd. Hoewel de onderliggende mathematische theorie achter zwarte gaten zeer complex is, zijn zwarte gaten zelf simpel te beschrijven met twee parameters: de massa en de rotatie. Het evalueren van deze eigenschappen voor de zwarte gaten in het Universum is een zeer belangrijke taak. Hoe wordt enorme hoeveelheid materie vergaard in de zwarte gaten? Hoe bereiken sommige zwarte gaten relatief snel een supermassieve status, terwijl anderen dit niet behalen? Met betere en completere metingen van de eigenschappen van supermassieve zwarte gaten kunnen deze en andere mysteries opgelost worden.

Er bestaan verscheidene technieken om de massa en rotatie van een supermassief zwart gat te bepalen. In verafgelegen melkwegstelsels worden supermassieve zwarte gaten, die quasars worden genoemd, zeer snel gevoed met gas, waardoor ze miljoenen jaren lang een ontzettend helder signaal uitzenden. Dit signaal bevat informatie over het zwarte gat en met waarnemingen van dit licht kunnen de eigenschappen van het zwarte gat achterhaald worden. Voor een nabij gelegen melkwegstelsel kunnen de bewegingen van diens sterren rondom het zwarte gat gebruikt worden. Deze waarnemingen bieden een alternatieve meting omdat het pad waarop de sterren zich voortbewegen volledig wordt bepaald door de massa en de rotatie van het zwarte gat. Echter is geen van beide technieken toe te passen op sterrenstelsels in het tussengelegen gebied. Hier kunnen de bewegingen van sterren niet nauwkeurig worden bepaald, noch wordt er genoeg licht uitgezonden door de snelle aanvoer van gas om waar te kunnen nemen. Deze tekortkoming kan worden opgevangen met een derde techniek die gebruik maakt van het korte signaal dat wordt uitgezonden als een ster wordt verstoord door een supermassief zwart gat. Dit soort verstoringen zijn een zeer praktische manier om zwarte gaten in het meerendeel van alle melkwegstelsels te bestuderen, ongeacht de afstand tot de Aarde.

6.2 Verstoring door getijdenwerking

Als een onfortuinlijke ster in de buurt komt van een supermassief zwart gat, dan wordt het uit elkaar getrokken door diens zwaartekracht. Dit proces komt tot stand door het verschil in aantrekkingskracht dat verschillende delen van de ster voelen. Omdat de zwaartekracht afneemt met de afstand tot het zwarte gat, wordt het dichtstbijzijnde deel van de ster sterker aangetrokken dan de andere kant van de ster. Dit zorgt voor een getijdenwerking die de ster uitrekt langs de lijn die de ster en het zwarte gat verbindt. Hetzelfde proces is verantwoordelijk voor de getijden op Aarde: het eb en vloed van de oceanen wordt veroorzaakt door de aantrekking van de Maan. Zwarte gaten oefenen echter veel meer zwaartekracht uit, waardoor de uitrekking extreem is en soms worden sterren er zelfs door uiteengereten. Dit fysische fenomeen is bekend als verstoring door getijdenwerking of VGW.

Na de verstoring wordt het restpuin van de ster opgenomen in het zwarte gat en dit veroorzaakt een sterk signaal dat gedurende maanden tot jaren wordt uitgezonden. De eigenschappen van het uitgezonden signaal kunnen in principe gebruikt worden om de eigenschappen van het zwarte gat en het omliggende gas en stellaire puin te bepalen. Het signaal kan ook meer duidelijkheid verschaffen over de fysische processen rondom deze compacte objecten. Om deze uiteindelijke doelen te bereiken, is het eerst noodzakelijk om de theorie achter de fysische gebeurtenissen te begrijpen. Hoe verandert het stellaire materiaal voordat het opgenomen wordt in het zwarte gat? Wat is de oorzaak van het heldere signaal dat wordt uitgezonden door het gas terwijl het in het zwarte gat valt? Wat zijn de belangrijkste eigenschappen van de uitgezonden straling? Hoe kan nuttige fysische informatie over het zwarte gat of andere processen uit het signaal worden gehaald als het de telescopen op Aarde bereikt? Voordat VGWs gebruikt kunnen worden voor een fysische interpretatie van zwarte gaten, moeten deze vragen eerst beantwoord worden.

De eerste theoretische studies naar het signaal van VGWs zijn uitgevoerd in de jaren ’80. Deze studies hebben de basis gelegd voor het begrijpen van de dynamica van deze gebeurtenissen. Ze hebben aangetoond dat de verstoring van de ster aanleiding is voor de formatie van een uitgerekte stroom gas die rond het zwarte gat heen draait voordat het erdoor opgenomen wordt. Een belangrijke aanname in deze modellen is dat het gas zich snel tot een compacte schijf rond het zwarte gat vormt. In deze zogenoemde accretieschijf beweegt het gas zich snel naar het centrum van de schijf totdat het het zwarte gat bereikt en deze beweging zorgt voor een sterke uitstraling van licht. Met deze aanname voorspelden deze onderzoeken dat er zachte Röntgen straling zou ontstaan met een geleidelijk afnemende helderheid met een bekend patroon. Deze studies hebben ervoor gezorgd dat astronomen de hemel hebben afgespeurd naar licht signalen die aan de voorspellingen voldeden. Met behulp van de Röntgen satelliet ROSAT werden de eerste VGWs ontdekt wiens licht eigenschappen vertoonde die consistent waren met de theoretische voorspellingen.

Het onderzoek is echter nog niet voorbij. Recentelijk zijn er VGWs gevonden wiens eigenschappen niet overeenkomen met de eerste waargenomen gevallen en ook niet met de theoretische voorspellingen. Sommige VGWs zijn waargenomen met optische en ultraviolet licht, waardoor de bijbehorende energie van de verstoring lager is dan verwacht. Ook zijn er enkele waarnemingen geweest van VGWs met een extreem helder signaal, wat waarschijnlijk werd veroorzaakt door een signaal dat direct richting de Aarde werd uitgezonden. Deze bijzondere waarnemingen van VGWs tonen aan dat de oude modellen vernieuwd moeten worden om alle observaties te kunnen verklaren. In deze context zal dit proefschrift theoretisch werk bevatten waarmee de aannames in de oude VGW modellen getest worden en de invloed van verschillende fysische processen, die afwezig waren in eerdere modellen, bepaald worden.

6.3 Dit proefschrift

De studies die in dit proefschrift gepresenteerd worden, hebben als doel om het theoretische begrip over VGWs te vergroten. In het bijzonder, wordt er gekeken naar het stellaire materiaal rond het zwarte gat na de verstoring en hoe dit een licht signaal genereert. Deze studies zijn voornamelijk gericht op de hydrodynamica en magnetohydrodynamica van het stellaire materiaal. Waar het mogelijk is, worden de studies analytisch uitgevoerd en anders met behulp van numerieke methoden.

Zoals boven beschreven is, is het lot van de stroom van stellair materiaal richting het zwarte gat na de verstoring de belangrijkste aanname voor de eerste theoretische modellen voor VGWs. Om voorspellingen te kunnen doen over het uitgezonden licht signaal, werd voor deze modellen aangenomen dat het gas snel een compacte schijf vormt om het zwarte gat heen. Echter was het onderliggende mechanisme waardoor deze schijf zich vormt niet duidelijk benoemd toendertijd en de exacte dynamica van het proces was onbekend. In de eerste twee hoofdstukken van dit proefschrift wordt er gezocht naar een verheldering hiervan. In **Hoofdstuk 2** voeren wij hydrodynamische simulaties van dit proces uit. Onze studie identificeert zichzelf kruisende schokgolven, geïnduceerd door relativistische precessie van de stroom van gas, als een mogelijk mechanisme om een schijf te creeïen. Onze studie toont ook aan dat snelle formatie van de schijf niet kan gebeuren zonder dat de stroom dicht in de buurt van het zwarte gat komt waar grote precessie heerst. Als de stroom zich verder weg van het zwarte gat bevindt, duurt de formatie van de schijf langer. Ook zagen wij dat het stellaire puin significant wordt verhit tijdens de vorming van de schijf. Hierdoor, als het onmogelijk is om efficiënt af te koelen, zet de gas wolk zich uit tot het zich vormt tot een donutvormige wolk rond het zwarte gat. Deze conclusies zijn niet in overeenstemming met de voorspellingen van eerdere theoretische voorspellingen. De vorming van een schijf is niet per se een snel proces en in plaats van een schijf kan ook een donutvormige wolk ontstaan. Deze verschillen met het bestaande concept van de vorming van schijven impliceren dat er materie aanwezig is op grotere afstanden van het zwarte gat dan eerst werd aangenomen. Een interessant punt is dat er gedacht werd dat de straling van het gas op deze grote afstanden verantwoordelijk is voor het recent waargenomen optische en ultraviolette licht, dat niet door de eerdere modellen verklaard werd.

In het hierboven beschreven onderzoek stelde de rekenkracht van computers een limiet aan hoe ver in detail wij de schijf formatie in de meest relevante fysische configuratie konden onderzoeken. Deze tekortkomingen motiveerden een semi-analytische aanpak van het onderzoek, wat gepresenteerd wordt in **Hoofdstuk 3**. In dat model wordt de evolutie van het stellaire materiaal richting het zwarte gat behandeld als opeenvolgende Kepler trajecten. Deze omlooptrajecten rond het zwarte gat variëren doordat de stroom van gas zichzelf kruisende schokgolven ondergaat. Daarnaast nemen we ook de mogelijke magnetische stress in het model aan, wat kan ontstaan als de gasstroom gemagnetiseerd is. Onze resultaten komen overeen met de conclusies van het simpelere numerieke onderzoek in Hoofdstuk 2. Zichzelf kruisende schokgolven kunnen de vorming van de schijf veroorzaken, maar dit proces kan langzamer zijn en leiden tot een meer uitgedijde verdeling van gas dan wat is voorspeld door eerdere modellen. Ons werk laat ook zien dat magnetische stress de formatie van de schijf versneld door de zichzelf kruisende schokgolven te versterken. Vervolgens voorspellen wij de eigenschappen van het laag energetische signaal van VGWs als de schokgolven ervoor verantwoordelijk zijn. Wij vinden dat het signaal niet hetzelfde karakteristieke patroon heeft, wat door eerdere modellen is voorspeld.

In **Hoofdstuk 4** evalueren we de invloed van de gasrijke omgeving van supermassieve zwarte gaten op de evolutie van het stellaire materiaal. Met behulp van een analytische aanpak demonstreren wij dat de Kelvin-Helmholtz instabiliteit ervoor kan zorgen dat de stroom van stellair puin en de omgeving gemixt worden voordat de stroom het zwarte gat bereikt. Dit proces is duidelijker te zien voor stromen met een lage dichtheid aan gas, die worden veroorzaakt door de verstoring van een enorme ster of een zwart gat met een grote massa. In dit geval wordt het stellaire materiaal geheel aangetast door de instabiliteit. Een consequentie hiervan is dat een significante fractie van het stellaire materiaal kan worden verhinderd van het bereiken van het zwarte gat. Hierdoor is het uitgezonden licht signaal waarschijnlijk zwakker in helderheid dan eerder werd aangenomen.

Het effect van een magnetisch veld in de ster tijdens een VGW wordt onderzocht in **Hoofdstuk 5**. Wij maken gebruik van magnetohydrodynamische simulaties om de evolutie van het magnetische veld te onderzoeken tijdens de verstoring van de ster en de vroege evolutie van het stellaire puin. Tijdens de verstoring stroomt het magnetisch veld door het weggetrokken materiaal heen. Terwijl het stellaire materiaal wordt uitgerekt richting het zwarte gat, wordt de richting van het magnetische veld uitgelijnd met de stroom. Dit zorgt voor een verhoging van de magnetische energie van het gas. Voor sterk gemagnetiseerde sterren, kan de magnetische druk voor een significant dikkere schijf zorgen. Daarnaast vinden wij ook een indicatie voor een dynamo proces in het restant van de ster, als deze maar gedeeltelijk wordt verstoord. Dit kan zorgen voor een versterking van het magnetische veld. Dit mechanisme is mogelijk betrokken bij de formatie van relativistische stromen in VGWs, die zou zouden kunnen verklaren waarom er VGWs met sterk geconcentreerde straling zijn waargenomen.

7

Résumé en français

7.1 Trous noirs supermassifs

Les trous noirs sont des objets extrêmement compacts prédits par la théorie de la relativité générale d'Einstein. Les plus massifs d'entre eux sont appelés trous noirs supermassifs. Ils sont localisés au centre des grandes galaxies et ont une masse comprise entre un million et plusieurs centaines de milliards de fois la masse du Soleil. Même notre propre galaxie, la Voie Lactée, contient un trou noir supermassif appelé Sagittarius A* dont la masse est d'environ quatre millions de masses solaires. Bien qu'émergeant d'une théorie mathématique complexe, les trous noirs sont des objets très simples caractérisés par seulement deux propriétés : masse et vitesse de rotation. Évaluer ces propriétés pour la multitude de trous noirs supermassifs de l'Univers est d'une importance capitale. Quelle est la nature des "graines" à partir desquelles les trous noirs supermassifs ont commencé à grossir ? Comment la matière est-elle acheminée dans ces trous noirs pour entraîner une augmentation de leur masse ? Pourquoi certains de ces objets atteignent-ils rapidement des masses extrêmes alors que d'autres non ? Des mesures plus complètes et de meilleure qualité des propriétés des trous noirs supermassifs sont la clé de ces mystères et bien d'autres encore.

Plusieurs techniques existent pour mesurer la masse et vitesse de rotation des trous noirs supermassifs à partir d'observations. Dans les galaxies lointaines, des trous noirs supermassifs appelés quasars sont alimentés en gaz à un rythme soutenu conduisant à l'émission d'un signal très lumineux pour des millions d'années. Des informations sur le trou noir sont encodées dans ce signal qui, quand il atteint nos télescopes, peut par conséquent être utilisé pour déterminer les propriétés de l'objet compact. Pour les galaxies voisines de la nôtre, le mouvement global des étoiles à proximité du trou noir central peut être évalué. Cette observation fournit une autre méthode de mesure puisque les trajectoires des étoiles sont entièrement déterminées par la masse et vitesse de rotation de l'objet compact. Pour les distances intermédiaires, cependant, les deux techniques ci-dessus sont inefficaces : le mouvement des étoiles ne peut pas être détecté par les télescopes et l'émission associée à l'alimentation en gaz est trop faible pour être observable. Cette lacune peut être comblée grâce à une troisième technique qui exploite le court signal émis quand une étoile est détruite par un trou noir supermassif. Ainsi, ces destructions représentent un outil puissant d'exploration des trous noirs dans la majorité des galaxies, qu'elles soient proches ou lointaines.

7.2 Événement de rupture par effet de marée

Quand une étoile malchanceuse s'approche trop près d'un trou noir supermassif, elle est déchirée par la force gravitationnelle de l'objet compact. Plus précisément, ce processus est une conséquence de la différence d'attraction gravitationnelle ressentie par différentes parties de l'étoile. Puisque cette force diminue avec la distance, le côté de l'étoile le plus proche du trou noir est tiré plus fortement que le côté le plus éloigné. Cela résulte en une force appelée force de marée qui étire l'étoile dans la direction connectant l'étoile et le trou noir. Ce mécanisme est exactement le même que celui à l'origine des marées sur Terre pendant lesquelles le niveau d'eau change en raison de l'étirement des océans induit par la force de marée de la Lune. Cependant, comme un trou noir possède une gravité bien plus importante, sa force de marée peut devenir si intense qu'elle ne fait pas que déformer l'étoile mais la détruit complètement. Ce phénomène est appelée événement de rupture par effet de marée ou ERM.

Après la destruction de l'étoile, les débris stellaires alimentent l'objet compact produisant une puissante émission pour une courte durée pouvant aller de quelques mois à plusieurs années. Les caractéristiques du signal émis peuvent en principe être utilisées pour évaluer les propriétés du trou noir impliqué ainsi que de son environnement stellaire et gazeux. Il peut également être exploité pour améliorer notre compréhension des nombreux processus physiques à l'œuvre à proximité de ces objets compacts. Cependant, pour que ces buts ultimes puissent être atteints, il est en premier lieu nécessaire de comprendre théoriquement comment se déroulent ces événements. Comment le matériel stellaire évolue-t-il avant d'être acheminé à l'intérieur du trou noir ? Pendant cette évolution, comment le gaz rayonne-t-il et quels sont les caractéristiques principales de l'émission associée ? Quand ce signal atteint nos télescopes, comment peut-il être utilisé pour extraire les propriétés du trou noir ou avoir un aperçu des phénomènes physiques en jeu pendant l'événement ? Ces questions, parmi d'autres, doivent trouver une réponse pour permettre d'exploiter pleinement le potentiel des ERM.

Les premières études théoriques ayant pour but d'évaluer l'émission provenant des ERM datent des années 80. Elles définissent les bases pour la compréhension de la dynamique de ces événements en montrant que la destruction de l'étoile résulte en la formation d'un long faisceau de gaz qui tourne autour du trou noir avant de retomber dans son voisinage. Il est important de noter que ces modèles adoptent une supposition selon laquelle le gaz retournant vers le trou noir forme rapidement un disque de matière autour de l'objet compact. Dans ce disque dit d'accrétion, le gaz spirale rapidement vers l'intérieur tout en produisant un rayonnement intense avant d'être avalé par le trou noir. Dans cette hypothèse, ces travaux fondateurs prédisent que le signal en provenance des ERM est émis dans la bande des rayons X mous avec une luminosité diminuant à un rythme caractéristique. Sur la base de ces premiers travaux, les astronomes ont scruté le ciel à la recherche de signaux compatibles avec ces premières prédictions. Grâce au télescope spatial ROSAT, les premiers ERM sont découverts avec des caractéristiques correspondant aux prévisions.

Cependant, l'histoire ne s'arrête pas là. Plus récemment, des ERM ont été observés avec des propriétés étonnamment différentes de celles des premiers événements détectés et en désaccord avec les prédictions théoriques des travaux fondateurs. Certains d'entre eux sont observés dans les bandes optiques et ultraviolettes, c'est-à-dire à des énergies plus faibles que prédit précédemment. De plus, quelques autres événements sont détectés avec une très forte luminosité, ce qui correspond probablement à une émission focalisée dans notre ligne de vue. La détection d'ERM aux caractéristiques si curieuses impliquent que les modèles fondateurs doivent être révisés afin de prendre en compte ces nouvelles observations. Écrite dans ce contexte, cette thèse contient des travaux théoriques dont le but est de tester les hypothèses adoptées dans les premiers modèles et d'évaluer l'influence de processus physiques manquants aux études antérieures.

7.3 Cette thèse

Les travaux de recherche présentés dans cette thèse ont pour but d'améliorer la compréhension théorique des ERM, plus particulièrement l'évolution post-destruction de la matière stellaire autour du trou noir et comment elle se traduit en l'émission d'un signal détectable. Ces études se concentrent principalement sur l'hydrodynamique et la magnétohydrodynamique du matériel stellaire. Elles sont effectuées de manière analytique dans la mesure du possible et au moyen de techniques numériques lorsque cela est requis.

Comme expliqué ci-dessus, l'hypothèse principale adoptée dans les modèles fondateurs pour les ERM concerne le sort du faisceau de débris stellaires lorsqu'il retourne vers le trou noir après la destruction. Pour tirer des prédictions sur le signal émis, ces premières études font la supposition que ce gaz forme rapidement un disque d'accrétion compact autour du trou noir. Cependant, le mécanisme conduisant à la formation du disque n'a à l'époque pas été clairement identifié et l'exacte dynamique de ce processus était en grande partie inconnue. Les deux premiers chapitres de cette thèse cherchent à faire la lumière sur cette phase d'évolution. Dans le **Chapitre 2**, nous réalisons des simulations hydrodynamiques de ce processus. Notre étude identifie les chocs d'auto-croisement du faisceau de gaz comme un mécanisme pouvant mener à la formation du disque. Ces chocs ont lieu quand le faisceau de gaz rentre en collision avec lui-même en raison de la modification de sa trajectoire par la précession du périastre, un effet de la relativité générale. Notre travail démontre également qu'une formation de disque rapide requiert que le faisceau passe à une courte distance du trou noir où la précession est forte. Si le faisceau passe plus loin de l'objet compact, le disque peut au contraire mettre plus de temps à se former. De plus, nous trouvons que les débris stellaires sont significativement échauffés pendant la formation du disque. En conséquence, s'il est incapable de se refroidir, le gaz rentre en expansion pour finalement prendre la forme d'un tore épais et étendu autour du trou noir. Ces conclusions sont toutes deux en contradiction avec les prédictions des premiers modèles : la formation du disque n'est pas nécessairement un processus rapide et elle peut résulter en un imposant tore au lieu d'un disque compact. Ces deux écarts par rapport à la compréhension initiale du processus de formation du disque impliquent la présence de matière stellaire à grande distance du trou noir par rapport à ce que l'on pensait auparavant. De récents travaux ont mis en avant la possibilité que le rayonnement de ce gaz soit à l'origine de l'émission dans les bandes optique et ultraviolette détectée en provenance des ERM par les observations les plus récentes alors qu'elle n'était pas prédite par les premières études théoriques.

Dans l'étude numérique ci-dessus, des limitations informatiques intrinsèques au problème étudié nous ont empêché d'étudier le processus de formation du disque dans la configuration physique la plus appropriée. Ces restrictions motivent le modèle analytique présenté dans le **Chapitre 3**. Dans ce modèle, l'évolution de la matière stellaire vers un disque d'accrétion est traitée comme une succession d'orbites kepleriennes qui varient progressivement lorsque le faisceau de gaz subit des chocs d'auto-croisement. De plus, nous prenons en compte la possibilité de contraintes magnétiques qui surgissent si le faisceau est magnétisé. Les résultats sont en concordance avec les conclusions tirées de l'étude numérique du chapitre précédent : la formation du disque peut être entraînée par les chocs d'auto-croisement mais ce processus peut être plus lent et mener à la formation d'une distribution de gaz plus étendue que supposé dans les modèles fondateurs. Notre travail démontre aussi que les contraintes magnétiques accélèrent la formation du disque en renforçant les chocs d'auto-croisement. Nous prédisons également les caractéristiques du signal à basse énergie émis par les ERM s'il provient de ces chocs et trouvons qu'elles peuvent différer des premières prédictions de manière importante.

Dans le **Chapitre 4**, nous évaluons l'impact de l'environnement gazeux des trous noirs supermassifs sur l'évolution du matériel stellaire. En utilisant un traitement analytique, nous démontrons que l'instabilité de Kelvin-Helmholtz peut entraîner le mélange des débris stellaires avec la matière environnante avant qu'ils ne reviennent vers le trou noir. Ce phénomène est plus prononcé pour les faisceaux de gaz de faible densité produits par la destruction d'étoiles géantes et/ou impliquant un trou noir de masse importante. Dans ce cas, le matériel stellaire dans sa totalité est affecté par l'instabilité. En conséquence, une fraction significative de cette matière peut être empêchée de revenir vers le trou noir, ce qui rend probablement le signal associé plus faible que pensé précédemment.

Le champ magnétique stellaire pendant un ERM est examiné dans le **Chapitre 5**. En recourant à des simulations magnétohydrodynamiques, nous suivons l'évolution du champ magnétique pendant la destruction de l'étoile et le début de l'évolution des débris. Suite à la destruction, le champ magnétique stellaire se répand dans le matériel arraché à l'étoile. Alors que la matière stellaire évolue en une structure allongée, le champ magnétique s'oriente dans la direction de l'étirement. Cela résulte en une augmentation de l'énergie magnétique du gaz. Pour les étoiles fortement magnétisées, la pression magnétique associée peut épaissir le faisceau de gaz de manière significative. De plus, si l'étoile est seulement partiellement détruite, nous mettons en évidence un effet dynamo intervenant dans le cœur stellaire survivant à la destruction et pouvant mener à une augmentation de l'intensité de son champ magnétique. Ce mécanisme est potentiellement impliqué dans la formation de jets relativistes pendant les ERM qui peut expliquer l'émission focalisée observée pour certains de ces événements.

Publications

First author:

1. *Magnetic field evolution in tidal disruption events*
   C. Bonnerot, D.J. Price, G. Lodato and E. M. Rossi
   2017, Monthly Notices of the Royal Astronomical Society, Volume 469, Issue 4, p. 4879-4888 (**Chapter 5**)

2. *Long-term stream evolution in tidal disruption events*
   C. Bonnerot, E. M. Rossi and G. Lodato
   2017, Monthly Notices of the Royal Astronomical Society, Volume 464, Issue 3, p. 2816-2830 (**Chapter 3**)

3. *Bad prospects for the detection of giant stars' tidal disruption: effect of the ambient medium on bound debris*
   C. Bonnerot, E. M. Rossi and G. Lodato
   2016, Monthly Notices of the Royal Astronomical Society, Volume 458, Issue 3, p. 3324-3330 (**Chapter 4**)

4. *Disc formation from tidal disruptions of stars on eccentric orbits by Schwarzschild black holes*
   C. Bonnerot, E. M. Rossi, G. Lodato and D. J. Price
   2016, Monthly Notices of the Royal Astronomical Society, Volume 455, Issue 2, p. 2253-2266 (**Chapter 2**)

Contributed:

1. *Phantom: A smoothed particle hydrodynamics and magnetohydrodynamics code for astrophysics*
   D. J. Price, J. Wurster, C. Nixon, T.S. Tricco, S. Toupin, A. Pettitt, C. Chan, G. Laibe, S. Glover, C. Dobbs, R. Nealon, D. Liptai, H. Worpel, **C. Bonnerot**, G. Dipierro, E. Ragusa, C. Federrath, R. Iaconi, T. Reichardt, D. Forgan, M. Hutchison, T. Constantino, B. Ayliffe, D. Mentiplay, K. Hirsh and G. Lodato
   2017, Publications of the Astronomical Society of Australia (submitted)

2. *Recent developments in the theory of tidal disruption events*
   G. Lodato, A. Franchini, **C. Bonnerot** and E.M. Rossi
   2015, Journal of High Energy Astrophysics, Volume 7, p. 158-162

Curriculum Vitae

I was born on 27th April 1989 in Villeneuve-Saint-Georges, located the south-eastern suburbs of Paris. I grew up in the nearby commune, Brunoy, where I went to pre-school, primary school and finally high-school at lycée François-Joseph Talma. After passing my "baccalauréat", I moved to Paris to study in the "classe préparatoire" of lycée Janson de Sailly where I specialized in Mathematics and Physics. After an entrance examination, I was accepted in the "grande école" Centrale of Lille in 2009.

Part of the training in this school includes internships, which I took advantage of in order to gain my first research experiences in astronomy. In the first year, I went to Laboratoire d'Astrophysique de Toulouse-Tarbes in France to work with Prof. Emmanuel Davoust on a phylogenetic method to classify galaxies. At the end of the second year, I spent three months at Lund Observatory in Sweden where I worked under the supervision of Prof. Melvyn Davies on the dynamical evolution of young stellar clusters with a focus on the effects on planetary systems. Feeling a growing interest for fundamental physics and astronomy, I then decided to continue my studies by following a Master in Physics at École Polytechnique Fédérale de Lausanne in Switzerland within a double degree. During the course year, I carried out a project on tidal disruption events, which turned out to become the subject of my PhD at Leiden Observatory. I was also able to attend my first international conference on the topic in Madrid, which was very enriching. Afterwards, I did my Master project on a related topic at the University of Leicester where I developed models for the origin of the G2 cloud under the supervision of Prof. Sergei Nayakshin.

In 2013, I moved to the Netherlands to start a PhD at Leiden Observatory to carry out a theoretical study of tidal disruption events under the supervision of Dr. Elena Maria Rossi and Dr. Giuseppe Lodato. I had the opportunity to travel a lot for my research. I did several month-long visits to the University of Milan, spent one month in Australia to work at the University of Monash with Dr. Daniel Price and two weeks in Switzerland to collaborate with Prof. Lucio Mayer at the University of Zürich. In addition, I presented my work at numerous conferences, workshops and seminars in the Netherlands, Italy, Spain, Israël, Australia, the United States, Switzerland, Germany and England. As part of my PhD, I was teaching assistant for the courses Stellar Structure and Evolution and Computational Astrophysics and helped in the supervision of three students. Finally, together with a fellow PhD student, I was involved in the organization of the PhD talks, during which PhD students have the opportunity to present their work to each other.

Starting this fall, I will pursue my research as a post-doctoral researcher in the United States within the theory network of the Zwicky Transient Facility. I will be mostly based at the Californian Institute of Technology in Pasadena but also spend a significant amount of time at the Kavli Institute for Theoretical Physics in Santa Barbara and at the University of Berkeley.

Acknowledgements

Scientific research is by nature a non-linear process that randomly alternates between periods of intense productivity and creativity resulting in fast advances and moments of profound doubts and confusion during which any real progress seems out of reach. During my PhD, I was very fortunate to be surrounded by individuals whose support and friendliness provided the stable environment necessary for me to most often keep up the enthusiasm and motivation necessary to overcome the obstacles intrinsic to the scientific endeavour.

First of all, I am grateful to all the people who contribute to the excellent working conditions offered by Leiden Observatory and from which I greatly benefited during the past four years. The salary and budget allocated to my PhD research were such that I never had to worry about personal or professional financial difficulties, which nowadays appears to become a rare luxury. In addition, both technical and administrative support at the institute were swift and effective, which allowed me to focus exclusively on my research work.

Of course, this PhD would not have been possible without excellent collaborators. First, it has been a great experience to be the first (exclusive) PhD student of Elena Rossi and to see her group growing from two people to a number of students that her office can almost no longer accommodate. She also showed a constant enthusiasm which I greatly appreciated and made sure that my research work could progress as efficiently as possible in all circumstances. I also thank my co-supervisor Giuseppe Lodato and collaborator Daniel Price whom I visited for extended periods and whose role was essential to the completion of this thesis.

I would also like to thank the member of my research group. Thank you Alex, Tommaso and Valeriya for making our group meetings not only enriching but also pleasant moments. Other shorter-term members of this group have also participated to this nice atmosphere, so thanks to Bart, Isabel, Josh, Mark, Omar, Steven and Zujia. I am also thankful to Alessandro, Ann-Sofie, Caroline and Silvia for sharing their knowledge about various aspects of high-energy astrophysics and providing valuable feedback during our weekly "compact objects" meetings.

I am grateful to David and Fabian for being truly great companions during these years of PhD. I was always happy to spend time with you, both inside and outside the institute, in the Kaiser Lounge or at the Bonte Koe. I am looking forward to share beers with you again, and maybe one day a glass of the real "fée verte". This brings me to thank my office mate Andrej as well as the famous Emanuele who also joined in the quest for this elusive elixir and in other multiple occasions that I always enjoyed very much!

François, j'ai éte très heureux de partager ces quatre ans avec toi. Avoir quelqu'un avec qui blaguer en français au Borrel et autres événements était vraiment cool ! Merci aussi d'avoir partagé ton expertise sur les jets relativistes de M87, que je ne regarderai plus jamais de la même manière. J'ai été honoré d'être ton paranymphe pour ta soutenance de thèse, bon courage pour ton postdoc à Budapest !

It was an honour to be member of the increasingly successful football team successively known as "Messier 5", "Village bike FC", "WTFITDMYT FC" and finally "Supermassive Black Goals". So, thank you Ahmad, Andrea, Andrew, Christos, Duy, Emanuele and your crazy goal-keeping skills, François, Jit, Nicandro, Orchidéa, Pedro, Santiago, Sasha, Sašo, Stephan and Vincenzo. We were right to believe in ourselves!

I also say thank you to all the people from Leiden I have shared good memories with. To name a few: Aayush, Alberto, Anna, Berenice, Chris, Corentin, Cristobál, Darko, Dieuwertje, Edwin (x2), Eleonora, Francesco, Gabriela, Gleb, Irene, Jeroen, Kim, Leah, Luke, Marco, Maria Christina, Marissa, Massimo, Matteo, Mattia, Michael, Mieke, Nicola, Niels, Nikki, Patrick, Ricardo (many thanks for translating the summary of this thesis in Dutch!), Silvia, Tommaso, Tiago, Tiffany and Valeriya.

During my PhD, I was also lucky to make long-term visits to several institutes during which I met very kind and smart people. It has been always a great pleasure to go to Milan thanks to the incredibly friendly fellow students I met during my visits. I would like to thank Marco and Agnese who welcomed me during my early stays. Alessia, Enrico, Giovanni, Manuella and Zeudi, it was awesome to share lunch breaks and evening meals with you. Thank you for giving me a taste of the Italian “beautiful life” which was very much appreciated, especially coming from the rainy Netherlands. A special thank you to Giovanni and Zeudi for showing me their home towns, I will never forget this trip to Puglia! I am also grateful to the people who welcomed me at the University of Zürich: Darren, Davide, Lucio Mayer and Pedro. Finally, thank you to Daniel Price, David, Hayley, Rebecca, Yuri Levin, Paul Lasky, students and faculties at the University of Monash, for making my visit there very pleasant as well as productive.

Je remercie également mes amis français avec lesquels j’ai passé la majorité de mes vacances et qui m’ont souvent permis de complètement me détacher des aléas de la recherche. Donc, merci Adrien (x2), Charles, Fanta, François, Jérémy, Marie, Mamoun, Martine, Mathilde, Olesia, Paul, Thomas, Stéphane et Sylvain.

Finalement, je tiens à remercier ma famille, en particulier mes grands-parents, mes parents et ma soeur Tiphaine, pour m’avoir fourni un soutien nécessaire tout au long de mes études et mon doctorat.